Low Temperature Synthesis of Boron-Based Materials in Molten Salts

Submitted by Ke Bao to the University of Exeter
as a thesis for the degree of
Doctor of Philosophy in Engineering
In June 2017

I certify that all material in this thesis which is not my own work has been identified and that no material has previously been submitted and approved for the award of a degree by this or any other University.

Signature: ……..

Abstract

Compared with conventional synthesis techniques, the so-called molten salt synthesis (MSS) technique has attracted substantial interest and has been used extensively to synthesise a range of advanced materials because it offers several advantages: (1) the synthesis reaction can be completed at a relatively low temperature and within a short time; (2) the resultant product powders are generally well dispersed and have high surface reactivity; (3) the grain shapes (spheroidal, platelet-shaped or rod-like) and sizes (nanoscale to microscale) can be controlled; and (4) the process is easy to perform, scalable and cost effective.

In this thesis, a molten-salt-mediated magnesiothermic reduction technique was used to synthesise high-quality boron-based fine powders, including titanium diboride (TiB_2), hafnium diboride (HfB_2), lanthanum hexaboride (LaB_6), calcium hexaboride (CaB_6), amorphous boron and alumina-titanium diboride (Al_2O_3-TiB_2) nanocomposites, at relatively low temperatures, from relatively cheap oxide-based raw materials. The effects of the processing parameters, such as salt type, starting batch composition, and firing temperature and time, on the reaction extents were investigated, based on which, the synthesis conditions optimised and the responsible underlying mechanisms proposed.

Among the three chloride salts (NaCl, KCl and $MgCl_2$), $MgCl_2$ showed the best accelerating effect on the MSS of amorphous boron, TiB_2, HfB_2 and LaB_6.This finding could be explained by the higher solubility levels of Mg and MgO in molten $MgCl_2$ than in the other two salts. When using appropriately excessive amounts of Mg and/or B_2O_3 to compensate for their evaporation losses at reaction temperatures, phase-pure TiB_2, HfB_2 and LaB_6 fine powders of 100-200

nm were synthesised after 4-6 h firing in $MgCl_2$ at 900-1000°C. In the MSS of amorphous boron, 15 mol% excessive Mg was used. High-purity amorphous boron fine powders with sizes of 100-200 nm were achieved after 6 h firing in $MgCl_2$ at 900°C and further leaching with hot H_2SO_4 solution. In the MSS of CaB_6, $CaCl_2$ facilitated the overall synthesis more effectively than NaCl, KCl or $MgCl_2$. Upon using 20 mol% excessive Mg, phase-pure CaB_6 nanoparticles of ~50 nm were formed in $CaCl_2$ after 6 h at 800°C. Unlike in the molten-salt-mediated magnesiothermic reduction technique, Al_2O_3-TiB_2 nanocomposite powders were synthesised *via* the aluminothermic reduction in molten salt. In this case, NaCl was regarded as the most appropriate reaction medium. When using appropriately excessive amounts of Al and B_2O_3, phase-pure Al_2O_3-TiB_2 nanocomposite powders were synthesised after 4 h at 1150°C or 5 h at 1050°C. These synthesis conditions were much milder than those required by many other techniques reported previously. The “dissolution-precipitation” mechanism was found to be more dominant in the overall MSS processes than the “template-growth” mechanism.

The success of this work indicates that the MSS technique could be a promising alternative approach to low-temperature synthesis of a range of nanomaterials. In addition, the MSS route opens new possibilities for the synthesis of known materials as well as new materials with complex structures, such as new zeolitic materials, metal organic frameworks and polymer chemistry by utilising tailored salt systems.

Contents

Abstract **1**
List of Figures **7**
List of Tables **13**
List of Abbreviations **14**
Chapter 1 Introduction **15**
1.1 Introduction 15
1.2 Objectives 18
1.3 Thesis outline 18
Chapter 2 Literature Review **19**
2.1 Crystal structure, properties and applications 19
2.1.1 Amorphous boron 19
2.1.2 Titanium and hafnium diborides 21
2.1.3 Lanthanum and calcium hexaborides 24
2.1.4 Al_2O_3-TiB_2 nanocomposite 26
2.2 Synthesis of metal boride powders 28
2.2.1 Reduction processes 28
2.2.2 Direct elemental reactions 40
2.2.3 Chemical routes 42
2.2.4 Molten salt electrolysis 47
2.3 Synthesis of amorphous boron powder 49
2.3.1 Moissan's method 51
2.3.2 Combustion synthesis 51
2.3.3 Mechanochemical synthesis 54
2.3.4 Molten salt electrolysis 55
2.4 Synthesis of Al_2O_3-TiB_2 composite powders 56
2.5 MSS technique 60
2.5.1 Molten salt properties 61
2.5.2 Reaction mechanisms 61
2.5.3 MSS of metal boride powders 64
2.5.4 Summary 65
Chapter 3 Experimental Procedures and Characterisation Techniques **67**
3.1 Raw materials 67
3.2 Preparation of samples 68

3.2.1 TiB_2 powder 68
3.2.2 HfB_2 powder 69
3.2.3 B_4C, TiC and HfC coatings on the carbon fibres 70
3.2.4 LaB_6 powder 70
3.2.5 CaB_6 powder 71
3.2.6 Amorphous boron powder 71
3.2.7 Al_2O_3-TiB_2 nanocomposite powder 72
3.2.8 Water washing and acid leaching 72
3.3 Characterisation techniques 72
3.3.1 XRD 72
3.3.2 SEM and EDS 74
3.3.3 TEM and SAED 78
Chapter 4 Low-Temperature Preparation of TiB_2 Fine Powders *via* Magnesiothermic Reduction in Molten Salt 82
4.1 Results and discussion 82
4.1.1 Effect of salt type on TiB_2 formation 82
4.1.2 Effect of firing temperature on TiB_2 formation 83
4.1.3 Effect of excessive Mg on TiB_2 formation 84
4.1.4 Effect of TiO_2 particle shape and size on TiB_2 formation 85
4.1.5 Microstructural characterisation of the TiB_2 product powders 86
4.2 Reaction mechanisms and further discussion 89
4.2.1 Formation of B and Ti in the molten salt 89
4.2.2 Solubility of B and Ti in molten salt 90
4.2.3 Effect of the salt type on the MSS 93
4.3 Conclusion 94
Chapter 5 Low-Temperature Synthesis of HfB_2 Fine Powders *via* Magnesiothermic Reduction in Molten Salt 96
5.1 Results and discussion 96
5.1.1 HfB_2 formation in different salts 96
5.1.2 HfB_2 formation at different temperatures 97
5.1.3 HfB_2 formation using excessive Mg and B_2O_3 98
5.1.4 Effect of time on HfB_2 formation and further optimisation of the reaction conditions 100
5.1.5 Microstructural characterisation of the product powders 103
5.2 Reaction mechanisms and further discussion 104
5.3 Conclusion 108

Chapter 6 Low-Temperature Preparation of LaB_6 Fine Powder *via* Magnesiothermic Reduction in Molten Salt 109
6.1 Results and discussion 109
6.1.1 Effect of salt type on LaB_6 formation 109
6.1.2 Effect of heating temperature on LaB_6 formation 110
6.1.3 Effect of excessive Mg on LaB_6 formation 111
6.1.4 Effect of heating time on LaB_6 formation 112
6.1.5 Microstructures and phase composition of LaB_6 product powders 114
6.2 Reaction mechanism and further discussion 115
6.3 Conclusion 117
Chapter 7 Low-Temperature Synthesis of CaB_6 Nanoparticles *via* Magnesiothermic Reduction in Molten Salt 119
7.1 Results and discussion 119
7.1.1 CaB_6 formation in different salts 119
7.1.2 CaB_6 formation at different temperatures 120
7.1.3 CaB_6 formation using excessive Mg 121
7.1.4 Effect of firing time on CaB_6 formation 122
7.1.5 Microstructure of CaB_6 product powder 124
7.1.6 Further discussion and reaction mechanisms 126
7.2 Conclusion 128
Chapter 8 Preparation and Characterisation of Amorphous Boron Powder *via* Molten-Salt-Assisted Magnesiothermic reduction 130
8.1 Results and discussion 130
8.1.1 Effect of salt type on the magnesiothermic reduction 130
8.1.2 Effect of boron source on the magnesiothermic reduction 131
8.1.3 Effect of heating temperature on the magnesiothermic reduction 132
8.1.4 Effect of excessive Mg on the magnesiothermic reduction and subsequent purification 133
8.1.5 Effect of salt content on the magnesiothermic reduction 136
8.1.6 Microstructural characterisation of the boron powders 137
8.2 Conclusion 141
Chapter 9 Synthesis of Al_2O_3-TiB_2 Nanocomposite Powder *via* Molten-Salt-Assisted aluminothermic reduction 142
9.1 Results and discussion 142
9.1.1 Effect of salt type on Al_2O_3-TiB_2 formation 142
9.1.2 Effect of firing temperature on Al_2O_3-TiB_2 formation 144

9.1.3 Effect of excessive Al on Al_2O_3-TiB_2 formation 145
9.1.4 Effect of excessive B_2O_3 on Al_2O_3-TiB_2 formation 147
9.1.5 Effect of firing time on Al_2O_3-TiB_2 formation and further optimisation of synthesis conditions 147
9.2 Microstructures and phase compositions of the Al_2O_3-TiB_2 product powders 149
9.3 Further discussion and reaction mechanisms 152
9.4 Conclusion 154
Chapter 10 Conclusions and Future Works 155
10.1 Conclusions 155
10.2 Future works 157
Publications 158
Conference Presentations 159
References 160

List of Figures

Figure 2.1 Crystal structures of (a) α-rhombohedral boron and (b) β-rhombohedral boron. Each circle at the lattice point and midpoints of the unit cell edges represents the B_{12} icosahedron. The largest circles represent the B_{28} unit, and the smallest one at the unit cell centre represents an isolated boron atom. 20

Figure 2.2 Side and top-view of the AlB_2-type crystal structure. 22

Figure 2.3 Structural depiction of cubic hexaborides. B-B1 and B-B2 are the inter-octahedral and intra-octahedral boron bond lengths, respectively..... 25

Figure 2.4 Structure of α-Al_2O_3. 27

Figure 2.5 SEM images of the (a) starting HfO_2 particles and (b) HfB_2 particles synthesised from HfO_2-B_4C-C at 1500°C for 1 h using SPS..... 30

Figure 2.6 SEM images of (a) raw material B_4C and (b) CaB_6 synthesised from $CaCO_3$-B_4C-C at 1400°C for 3 h..... 31

Figure 2.7 SEM images of TiB_2 powders by SHS from TiO_2-B_2O_3-Mg-NaCl (1:1:5:n) with (a) n = 0 and (b) n = 2..... 35

Figure 2.8 SEM micrographs of the TiB_2 product powder resulting from 5 h of MA-SHS from (a) TiO_2-H_3BO_3-Mg and (b) TiO_2-H_3BO_3-Mg-NaCl. 38

Figure 2.9 SEM images of LaB_6 prepared from the reaction between La_2O_3 and $NaBH_4$ at (a) 1000°C and (b) 1200°C for 2 h..... 44

Figure 2.10 SEM images of CaB_6 prepared by the reaction of CaO with $NaBH_4$ at various reaction temperatures: (a) 1000°C, (b) 1100°C, and (c) 1150°C..... 44

Figure 2.11 SEM images showing the HfB_2 particle morphology for sol-gel precursors that were heat treated at (a) 1300°C for 25 h and (b)1600°C for 2 h. 46

Figure 2.12 (a) TEM image of the carbon structure resulting from heat treating PPR at 1000°C for 0.1 h, (b) SEM images of the resultant HfB_2 powders after heat treatment at 1600°C for 2 h using PPR (b) and (c-e) formation of HfB_2 powder from PPR. 47

Figure 2.13 SEM images of (a) CaB_2O_4 and electrolytic CaB_6 obtained at (b) 600°C and (c) 700°C. 49

Figure 2.14 SEM images and EDS of amorphous boron powders prepared through the active-dilution SHS method from (a, b) Mg/B_2O_3 and (c, d) Mg/B_2O_3 + 30% KBH_4. 52

Figure 2.15 (a) SEM image and (b) SAED of boron powders obtained from

B_2O_3/Mg + 50 wt%NaCl by salt-assisted SHS synthesis. 53

Figure 2.16 XRD patterns of the (a) combustion-derived sample from B_2O_3+1.2Mg and (b) acid-leached boron powder. 54

Figure 2.17 SEM (a) and TEM (b) images of the Al_2O_3-TiB_2 composite powders synthesised using a mechanochemical method starting from a mixture of TiO_2, HBO_2 and Al powders. 59

Figure 2.18 TEM images of the (a) dried gel/Al powder mixture milled for 30 h and (b) heat treated at 950°C for 1 h. 60

Figure 2.19 SEM images of the (a) as-received α-Al_2O_3 platelets and (b) MA platelets synthesised by heating MgO and Al_2O_3 at 1150°C for 3 h in K_2SO_4... 62

Figure 2.20 TEM images of (a) as-received CNTs and (b) the resultant SiC nanorods from heating CNTs and Si particles for 4 h at 1200°C in NaCl-NaF. . 63

Figure 2.21 SEM images of the as-received raw (a) La_2O_3 and Al_2O_3 powders and (c) $LaAlO_3$ particles synthesised for 3 h at 630°C in KF-KCl. 64

Figure 2.22 SEM images of boride powders obtained after heat treatment for 4 h of (a) $NbCl_5$:$NaBH_4$ = 1:8 at 900°C and (b) $CaCl_2$:$NaBH_4$ = 1:12 at 800°C in LiCl/KCl. 65

Figure 2.23 SEM images of the (a) starting ZrO_2 powder and (b) ZrB_2 particles resultant from firing ZrO_2-$Na_2B_4O_7$-Mg at 1200°C for 3 h in $MgCl_2$. 65

Figure 3.1 Flowchart of the MSS procedures. 69

Figure 3.2 Schematic illustration of Bragg law. 74

Figure 3.3 Schematic diagram of a typical SEM. 75

Figure 3.4 Schematic illustration of (a) the interaction of the primary electron beam with a specimen, showing the depth from the interaction volume that the various signals are generated and (b) the complete energy distribution of electrons emitted. 77

Figure 3.5 Schematic diagram of the layout of JEM-2100 TEM. 79

Figure 3.6 Simplified diagram of the two basic operations of the TEM imaging system involve (a) diffraction mode and (b) image mode. 79

Figure 3.7 Schematic diagram of (a) the geometry of electron diffraction in the TEM and different types of diffraction patterns obtained from (b) amorphous, (c) polycrystalline and (d) single-crystalline sample regions. 81

Figure 4.1 XRD patterns of the samples with stoichiometric compositions after 4 h of firing at 850°C in (a) NaCl, (b) KCl, and (c) $MgCl_2$. 83

Figure 4.2 XRD patterns of the samples with stoichiometric compositions after 4 h of firing in $MgCl_2$ at (a) 750, (b) 850, (c) 950, and (d) 1000°C. 84

Figure 4.3 XRD patterns of samples resultant from firing batch powders for 4 h in $MgCl_2$ at 1000°C with (a) 0, (b) 5, (c) 15, and (d) 20 mol% excessive Mg. ... 85

Figure 4.4 XRD patterns of samples resultant from 4 h firing in $MgCl_2$ at 1000°C using 20 mol% excessive Mg and, respectively (a) TiO_2 I, (b) TiO_2 II, and (c) TiO_2 III. ... 86

Figure 4.5 SEM images of (a) TiO_2 I, (c) TiO_2 II, (e) TiO_2 III, and (b, d, f) the corresponding TiB_2 product powders whose XRD patterns are shown in Figure 4.4. ... 87

Figure 4.6 TEM images and corresponding EDS results of the TiB_2 product powders prepared from (a, b) TiO_2 I, (c, d) TiO_2 II, and (e, f) TiO_2 III. ... 88

Figure 4.7 XRD patterns of the (a) raw CFs and carbide coatings on the CFs: (b) B_4C coating and (c) TiC coating. ... 91

Figure 4.8 SEM images and EDS results of the (a, b) as-received CFs and carbide coatings on the CFs: (c, d) B_4C coating and (e, f) TiC coating. ... 92

Figure 5.1 XRD patterns of samples with stoichiometric compositions after 4 h heating at 850°C in: (a) NaCl, (b) KCl, and (c) $MgCl_2$, respectively. ... 97

Figure 5.2 XRD patterns of samples with stoichiometric compositions after 4 h heating in $MgCl_2$ at: (a) 750, (b) 850, (c) 950, and (d) 1000°C, respectively. ... 98

Figure 5.3 XRD patterns of samples after 4 h heating at 1000°C in $MgCl_2$ using: (a) 0, (b) 20, and (c) 80 wt% excessive Mg, respectively. ... 99

Figure 5.4 XRD patterns of samples resultant from 4 h heating in $MgCl_2$ at 1000°C, using 80 wt% excessive Mg and (a) 0, (b) 10, and (c) 20 wt% excessive B_2O_3. ... 100

Figure 5.5 XRD patterns of samples resultant from heating the batch powders containing respectively 80 and 20 wt% excessive Mg and B_2O_3 in $MgCl_2$ at 1000°C for (a) 3 h and (b) 4 h. ... 101

Figure 5.6 XRD patterns of samples resultant from heating the batch powders containing respectively 80 and 20 wt% excessive Mg and B_2O_3 in $MgCl_2$ at 950°C for (a) 4, (b) 6, and (c) 8 h, respectively. ... 102

Figure 5.7 XRD patterns of samples resultant from 6 h heating in $MgCl_2$ at 950°C, using 80 wt% excessive Mg and (a) 20, (b) 40, and (c) 60 wt% excessive B_2O_3, respectively. ... 102

Figure 5.8 XRD patterns of product samples resulting from (a) 6 h heating at 950°C with 80-60 wt% excessive Mg-B_2O_3 and (b) 4 h at 1000°C with 80-20 wt% excessive Mg-B_2O_3 (after water washing and acid leaching). ... 103

Figure 5.9 SEM/TEM images and EDS results of the HfB_2 product powders corresponding to the XRD patterns shown in Figure 5.8: (a, c and e) 6 h at 950°C and (b, d and f) 4 h at 1000°C. ... 104

Figure 5.10 SEM images of the as-received (a) B_2O_3 and (b) HfO_2 powders, and (c) Hf prepared *via* magnesiothermic reduction of HfO_2 (Reaction (5.2)) in $MgCl_2$ at 950°C for 6 h and (d) corresponding EDS as well as (inset) XRD results. . 106

Figure 5.11 SEM image (a), EDS (b) and (inset) XRD pattern of the product sample resultant from heating the mixture of HfO_2, Mg and CFs in $MgCl_2$ at 950°C for 6 h. 107

Figure 6.1 XRD patterns of samples resultant from heating batch powders with stoichiometric compositions for 4 h at 850°C in (a) KCl, (b) NaCl, and (c) $MgCl_2$. 110

Figure 6.2 XRD patterns of samples resultant from heating batch powders with stoichiometric compositions for 4 h in $MgCl_2$ at (a) 850, (b) 900, and (c) 1000°C. 111

Figure 6.3 XRD patterns of samples resultant from heating batch powders for 4 h in $MgCl_2$ at 1000°C with (a) 0, (b) 10, and (c) 20 mol% excessive Mg. 112

Figure 6.4 XRD patterns of samples resultant from heating batch powders with 20 mol% excessive Mg in $MgCl_2$ at 900°C for (a) 4, (b) 4.5, and (d) 5 h. 113

Figure 6.5 XRD patterns of product samples obtained after (a) 5 h heating at 900°C and (b) 4 h heating at 1000°C in $MgCl_2$ (after water washing and acid leaching).....114

Figure 6.6 SEM images (a, b) and the corresponding EDS spectra (c, d) of the LaB_6 powders, the XRD patterns of which are shown in Figure 6.5: 5 h at 900°C (a, c) and 4 h at 1000°C (b, d) in $MgCl_2$. 115

Figure 6.7 XRD patterns of samples resultant from heating La_2O_3 powder for 4 h in $MgCl_2$ at (a) 850 and (b) 1000°C. 116

Figure 6.8 SEM images of (a) La_2O_3 raw material particles and (b) LaOCl obtained after heating the La_2O_3 powder for 4 h at 1000°C in $MgCl_2$ (after leaching out MgO) and (c, d) EDS spectra of the selected areas in (b).....116

Figure 7.1 XRD patterns of samples of stoichiometric composition after 4 h firing at 850°C in (a) NaCl, (b) KCl, (c) $CaCl_2$, and (d) $MgCl_2$. 120

Figure 7.2 XRD patterns of samples of stoichiometric composition after 4 h firing in $CaCl_2$ at (a) 800, (b) 900, and (c) 1000°C..... 121

Figure 7.3 XRD patterns of samples using (a) 0, (b) 10, and (c) 20 mol% excessive Mg, after 4 h firing in $CaCl_2$ at 1000°C. 122

Figure 7.4 XRD patterns of samples using stoichiometric amount of Mg (i.e., 0 mol% excessive Mg) after firing in $CaCl_2$ at 800°C for (a) 4, (b) 6, or (c) 8 h.. 123

Figure 7.5 XRD patterns of samples using 15 mol% excessive Mg after firing in $CaCl_2$ at 800°C for (a) 4, (b) 6, or (c) 8 h. 123

Figure 7.6 XRD patterns of samples using 20 mol% excessive Mg after firing in

$CaCl_2$ at 800°C for (a) 4, (b) 5, or (c) 6 h. 124

Figure 7.7 SEM images (a, b) and corresponding EDS results (c, d) of CaB_6 powders resultant from (a, c) 6 h firing at 800°C and (b, d) 4 h firing at 1000°C, in $CaCl_2$. 125

Figure 7.8 TEM and corresponding EDS of CaB_6 nanoparticles resultant from 6 h firing in $CaCl_2$ at 800°C (the small C and Cu peaks arose from the carbon film-Cu TEM grid). 126

Figure 7.9 SEM image of as-received CaO powder. 128

Figure 8.1 XRD patterns of samples with stoichiometric compositions after 6 h of heating at 850°C in (a) NaCl, (b) KCl, and (c) $MgCl_2$. 131

Figure 8.2 XRD patterns of samples resultant from heating batch powders for 6 h in $MgCl_2$ at 850°C using (a) $Na_2B_4O_7$ and (b) B_2O_3. 132

Figure 8.3 XRD patterns of samples with stoichiometric composition after 6 h of heating in $MgCl_2$ at (a) 800, (b) 850, (c) 900, and (d) 1000°C. 133

Figure 8.4 XRD patterns of samples resultant from heating batch powders for 6 h in $MgCl_2$ at 1000°C using (a) 0, (b) 10, (c) 15, and (d) 20 mol% excessive Mg. 134

Figure 8.5 XRD patterns of samples resultant from heating batch powders for 6 h in $MgCl_2$ with 20 mol% excessive Mg at (a) 850, (b) 1000, and (c) 1150°C (after water washing and subsequent HCl leaching). 135

Figure 8.6 XRD patterns of samples resultant from heating batch powders for 6 h in $MgCl_2$ with 15 mol% excessive Mg at (a) 800, (b) 900, and (c) 1000°C (after water washing and subsequent HCl leaching). 136

Figure 8.7 XRD patterns of samples resultant from heating batch powders for 6 h in $MgCl_2$ with 15 mol% excessive Mg at (a) 800, (b) 900, and (c) 1000°C (after further H_2SO_4 leaching). 137

Figure 8.8 XRD patterns of samples resultant from heating batch powders containing 15 mol% excessive Mg for 6 h in $MgCl_2$ at 900°C using different S/R ratios: (a) no salt, (b) 3/1, and (c) 5/1. 137

Figure 8.9 EDS results of the samples resultant from heating batch powders for 6 h in $MgCl_2$ with 15 mol% excessive Mg and after leaching with (a) HCl at room temperature for 2 h and (b) subsequent H_2SO_4 leaching at 70-90°C for 2 h. . 138

Figure 8.10 SEM images of the product samples whose XRD patterns are shown in Figure 8.7: (a) 850, (b) 1000, and (c) 900°C, and EDS analysis for the product powder obtained at 900°C (d). 139

Figure 8.11 TEM image (a), EDS spectrum (b), and SAED pattern (c) of the boron powder after 6 h heating at 900°C in $MgCl_2$. HRTEM image of a typical boron particle (d), showing the absence of crystal planes, which further confirmed its amorphous nature. 140

Figure 9.1 XRD patterns of samples of stoichiometric composition after 4 h firing at 850°C in (a) KCl, (b) NaCl, and (c) $MgCl_2$. 143

Figure 9.2 XRD patterns of samples of stoichiometric composition after 4 h firing in NaCl at (a) 850, (b) 950, (c) 1050, and (d) 1150°C. 145

Figure 9.3 XRD patterns of samples using (a) 0, (b) 20, (c) 25, and (d) 30 wt% excessive Al, after 4 h firing in NaCl at 1150°C. 146

Figure 9.4 XRD patterns of samples using 30 wt% excessive Al and respectively: (a) 0, (b) 10, and (c) 20 wt% excessive B_2O_3, after 4 h firing in NaCl at 1150°C. 147

Figure 9.5 XRD patterns of samples using 30 wt% excessive Al and 20 wt% excessive B_2O_3 after firing in NaCl at 1050°C for (a) 4, (b) 5, and (c) 6 h. 148

Figure 9.6 XRD patterns of samples after firing in NaCl at 1050°C for 5 h using 30 wt% excessive Al and (a) 20, (b) 25, and (c) 30 wt% excessive B_2O_3. 149

Figure 9.7 SEM image (a), EDS (b) and X-ray dot mapping of the Al_2O_3-TiB_2 composite powder resultant from firing in NaCl at 1050°C for 5 h. 150

Figure 9.8 SEM images (a, b) and corresponding EDS (c, d) of the Al_2O_3-TiB_2 composite powders resultant from 4 h firing in NaCl at 1150°C..... 151

Figure 9.9 TEM images (a, b) and corresponding EDS (c, d) of the Al_2O_3-TiB_2 composite powders resultant from firing in NaCl at 1050°C for 5 h (the small C and Cu peaks arose from the carbon film-Cu TEM grid). 151

List of Tables

Table 2.1 Some structural, physical and mechanical properties of TiB_2 and HfB_2 compared with those of Al_2O_3 23

Table 2.2 Some structural parameters and properties of LaB_6 and CaB_6..... 26

Table 2.3 Primary synthetic reactions of elemental boron 50

Table 3.1 List of raw materials and their basic properties 67

Table 3.2 List of salts and some of their properties 68

List of Abbreviations

MSS	Molten salt synthesis
SHS	Self-propagating high-temperature synthesis
MSR	Mechanically induced self-sustaining reactions
XRD	X-ray diffraction
SEM	Scanning electron microscope
TEM	Transmission electron microscope
EDS	Energy dispersive X-ray spectroscopy
EELS	Electron energy-loss spectroscopy
BNCT	Boron neutron capture therapy
UHTCs	Ultra-high-temperature ceramics
SPS	Spark plasma sintering
PPR	Powder phenolic resin
CVD	Chemical vapour deposition
ECR	Electron cyclotron resonance
SAED	Selected area electron diffraction
BPR	Ball-to-powder ratio
RS	Rotational speed
TTIP	Titanium isopropoxide
MWCNT	Multi-walled carbon nanotube
CNT	Carbon nanotube
PAN	Polyacrylonitrile
CF	Carbon fibre
FWHM	Half-width at half-maximum
SE/BSE/AE	Secondary electron/Backscattered electron/Auger electron
SEI	Secondary electron imaging

Chapter 1 Introduction

1.1 Introduction

The element boron, the neighbour of carbon in the periodic table, is a non-metallic, hard material that displays structural complexity, electron deficiency and unusual binding situations, and is a constituent of a rich variety of compounds [1]. The reactivity of boron powder depends on its form, i.e., crystalline or amorphous. Of all the chemical elements, amorphous boron has the highest volumetric heat of combustion and the third highest (after H_2 and Be) gravimetric heat of combustion, making it a prime candidate material for use as a fuel or fuel additive in solid propellant formulations and explosives, in airbag igniters, and as an additive in pyrotechnic mixtures [2-6].

The most common methods for producing amorphous boron powder include reducing B_2O_3 with Mg through self-propagating high-temperature synthesis (SHS) [7-9], active-dilution and salt-assisted SHS [10-12], melt-assisted solid flame synthesis [13], mechanically induced self-sustaining reactions (MSR) [14], and mechanochemical synthesis [15-17]. However, the final products obtained from these methods contain many types of impurities (i.e., Mg, O, and their compounds with B), due to the incomplete reduction of B_2O_3. Moreover, the product powders have a large particle size and wide size distribution. Other disadvantages include the requirements for high-cost equipment and long processing times and contamination from milling media.

Titanium and hafnium diborides are important ceramic materials that can potentially withstand extreme environments, such as those associated with the

wing leading edges and nose cones of hypersonic aerospace vehicles, rocket propulsion, scramjet engines, atmospheric re-entry vehicles, impact resistant armour, high-speed cutting tools, refractories for molten metal contact applications, plasma-facing materials for nuclear fusion reactors, and fuel forms for advanced nuclear fission reactors [18]. Lanthanum and calcium hexaborides are a class of boron-rich solids characterised by low thermal expansion coefficients, low work functions, and unique electrochemical behaviour. The current usage of these materials includes the following: field-electron emitters, electrical coatings for resistors, transition metal catalysts, high-energy optical systems, and sensors for high-resolution detectors [19].

Various techniques/methodologies have been investigated to synthesise metal borides with various morphologies and sizes, including direct elemental reaction, carbothermal, borothermal, carbo/borothermal or borocarbide reduction, metallothermic reduction, combustion synthesis, mechanochemical synthesis, solvo/hydrothermal method, molten salt electrolysis, gas-phase synthesis, floating zone method, and aluminium flux method. Unfortunately, these techniques suffer from one or more of the following problems: (1) the use of expensive and/or hazardous raw materials (e.g., elemental boron, metals and $NaBH_4$), (2) the requirement of specialty equipment/vessels, (3) the requirement of high processing temperatures and/or long processing times, (4) heavy agglomeration and contamination in the final products, and (5) high production costs.

Al_2O_3 is one of the most widely used and studied ceramic materials because of its high melting point, superior hardness, chemical inertness and electrical/thermal insulation properties [20]. Its crucially structural applications

are restricted by its low fracture toughness and poor thermal shock resistance [21, 22]. Adding TiB_2 particles to an Al_2O_3 matrix improves hardness, fracture toughness and electrical conductivity and offers benefits in wear behaviour compared to monolithic Al_2O_3 [23-28], making Al_2O_3-TiB_2 composite materials suitable for various applications, such as electrodes, cutting tools, wear parts, lightweight armour, high-temperature/glow-plug heaters, and heat exchangers [26, 29, 30].

Many techniques/methodologies have been investigated to synthesise Al_2O_3-TiB_2 composite powders, including mechanochemical synthesis [31-35], SHS [36-38] or mechanically activated combustion synthesis [39, 40], and milling-assisted sol-gel method [41]. However, these techniques often require a long processing time, and the resulting powders often exhibit heavy agglomeration and/or a relatively large particle size.

Compared with conventional synthesis techniques, the MSS technique shows several advantages: (1) the synthesis reaction can be completed at a relatively low temperature and within a short time; (2) the resultant product powders are generally well-dispersed and have high surface reactivity; (3) the grain shapes (spheroidal, platelet-shaped or rod-like) and sizes (nanoscale to microscale) can be controlled; and (4) the process is easy to perform, scalable and cost-effective. Because of these advantages, MSS has attracted a great deal of research interest and been used extensively to synthesise a range of advanced materials, including inorganic materials (e.g., oxide and non-oxide ceramic powders, semiconductors and carbon nanostructures) and organic solids (e.g., covalent frameworks and polymeric semiconductors) [42].

1.2 Objectives

There are three main objectives of this work. The first is to develop the molten-salt-mediated magnesiothermic reduction technique to prepare high-purity TiB_2, HfB_2, LaB_6, CaB_6, amorphous boron and Al_2O_3-TiB_2 nanocomposite powders. The second objective is to optimise the reaction parameters and investigate the relevant reaction mechanisms. The final objective is to demonstrate the remarkable merits of using the MSS technique over conventional synthesis techniques, with a particular focus on the lower reaction temperature and outstanding control over the shapes and sizes of the as-prepared products.

1.3 Thesis outline

This thesis consists of ten chapters. Chapter 1 provides an overall introduction to the thesis, including the inspiration and innovation of this project and project objectives. Chapter 2 is a comprehensive literature review focusing on the boron-based materials under study and processing techniques used to prepare them, as well as the recent research on MSS. Chapter 3 describes the experimental procedures and various analysis techniques used in this thesis, including powder X-ray diffraction (XRD), scanning electron microscope (SEM), transmission electron microscope (TEM), and energy dispersive X-ray spectroscopy (EDS). Chapters 4-9 contain the results and discussion of the MSS of TiB_2, HfB_2, LaB_6, CaB_6, amorphous boron and Al_2O_3-TiB_2 nanocomposite powders. Finally, Chapter 10 summarises the key findings of the work included in this thesis. Considering the results of this thesis, directions for future work are also proposed.

Chapter 2 Literature Review

2.1 Crystal structure, properties and applications

Crystal chemistry and crystal structure are quintessential in determining the chemical, physical and thermal properties of materials. This section reviews the crystal structure, properties and applications of boron-based materials.

2.1.1 Amorphous boron

Boron is an element of fascinating chemical complexity arising from its unique location in the periodic table: it is situated at the boundary between metals and nonmetals and is the only nonmetal among the Group 13 elements [43]. At least 16 boron modifications have been reported [44]. Among them, two crystalline modifications are well known, namely, α-rhombohedral boron (α-B) and β-rhombohedral boron (β-B) [45]. Most of the reported boron has complicated crystal structures based on icosahedra B_{12} clusters, which can be linked into rigid frameworks [43].

Figure 2.1(a) shows the crystal structure of α-rhombohedral boron consisting of only B_{12} icosahedra located at the vertices of a rhombohedral lattice (space group $R\bar{3}m$; a = 5.057 Å, α = 58.06° [46]). The unit cell contains 12 B atoms. Thus, this modification is sometimes referred to as α-B_{12} [1]. In the case of β-rhombohedral boron, it has 105 B atoms in its idealised unit cell (Figure 2.1(b)) (space group $R\bar{3}m$; a = 10.145 Å, α = 65.28° [46]) consisting of an outer layer of 20 icosahedra-8 at the corners and 12 along the middle of each edge of the cell- and two B_{28} triply fused icosahedra on the body diagonal, which are connected by an interstitial B atom [1]. In addition to these modifications, amorphous boron

gives a characteristic X-ray or electron diffraction pattern of diffuse rings [47]. The structure of amorphous boron is not known. However, transformation of the amorphous boron powder into a crystal modification was identified as β-rhombohedral boron [48], and the electron energy-loss spectroscopy (EELS) result of amorphous boron was shown to be similar to that of β-rhombohedral boron [49], which might be taken to suggest that its structure is similar to that of β-rhombohedral boron. In addition, theoretical calculations by Kobayashi *et al.* [50] indicate that a possible structure of amorphous boron could be simulated using a regular B_{12} icosahedron as a basic structural unit with intra- and inter-icosahedral B-B bonding distances of 1.767 and 1.621 Å.

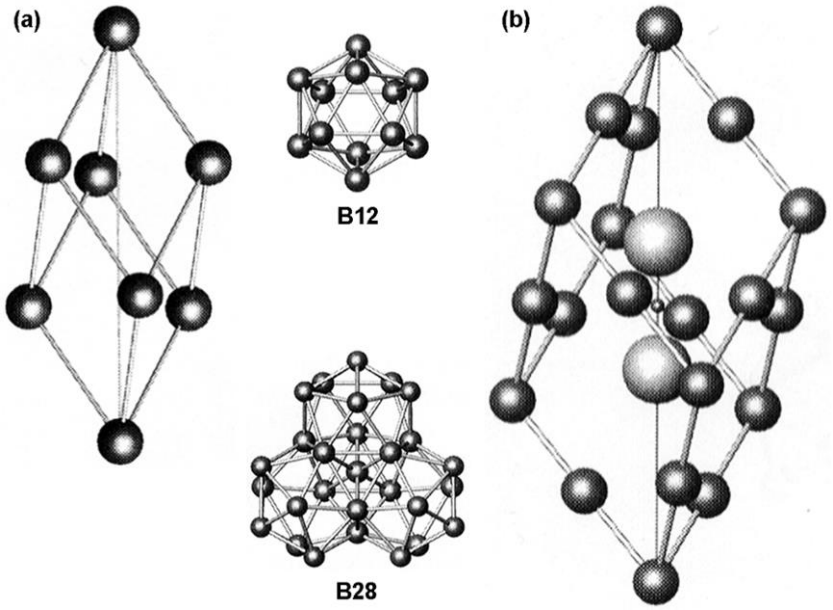

Figure 2.1 Crystal structures of (a) α-rhombohedral boron and (b) β-rhombohedral boron. Each circle at the lattice point and midpoints of the unit cell edges represents the B_{12} icosahedron. The largest circles represent the B_{28} unit, and the smallest one at the unit cell centre represents an isolated boron atom [51].

Elemental boron exhibits a unique combination of properties, such as a high melting point, low density, low volatility, high hardness, and high tensile strength/Young's modulus [52, 53]. Of all the chemical elements, amorphous boron has the highest volumetric heat of combustion (135.8 MJ/L) and the third (after H_2 and Be) highest gravimetric heat of combustion (58.5 MJ/kg) [2]. These

values are over 3 times higher per unit volume, and 1.4 times higher per unit mass, than those of hydrocarbon fuels [54], making amorphous boron a prime candidate material for use as a fuel or fuel additive in solid propellant formulations and explosives [3-5], in airbag igniters, and as an additive in pyrotechnic mixtures [6]. In addition, natural occurring boron consists of two stable isotopes, ^{10}B (19.9%) and ^{11}B (80.1%). Due to the high thermal neutron (0.025 eV) absorption cross-section of the ^{10}B isotope (~3837 barns), boron and its compounds (e.g., boric acid, boron carbide, rare-earth and refractory metal borides) find extensive applications in the nuclear industry as neutron sensors, neutron shielding, nuclear/neutron poison, control/shutoff rods and in nuclear material storage [55]. In nuclear reactors, ^{10}B is used for reactivity control and in emergency shutdown systems. As a part of medical applications, ^{10}B is also used in boron neutron capture therapy (BNCT) [56]. Moreover, as a powerful reducing agent, amorphous boron can be added to certain soldering agents as a flux or additive [57]. Other application areas include the manufacture of high-purity metal borides [58-60], as a sintering additive for silicon carbide high-performance ceramics [61, 62] and in the fields of energy storage and utilisation of solar energy [63, 64].

2.1.2 Titanium and hafnium diborides

Several borides, carbides and nitrides of the group IVB and VB transition metals (TM) are classified as ultra-high-temperature ceramics (UHTCs) based on their melting point in excess of 3000°C and other properties [65]. From this broader family of materials, the refractory diborides, e.g., TiB_2 and HfB_2, have a complex mix of bond types resulting in a remarkable combination of metal-like and ceramic-like properties [66, 67]. The crystal structure of TiB_2 and HfB_2 as well as

that of other transition metal diborides, including ZrB_2, CrB_2, TaB_2 and NbB_2, is primitive hexagonal (AlB_2-type, space group *P*6/*mmm*). As shown in Figure 2.2, the structure is composed of layers of B atoms in 2D graphite-like rings or nets, which alternate with hexagonally close-packed metal (M) layers. Each M atom has 6 equidistant M neighbours in its plane and 12 equidistant B neighbours (6 above and 6 below the M layer). Each B is surrounded by 3 B neighbours in its plane and by 6 M atoms (3 above and 3 below the B layer) [68].

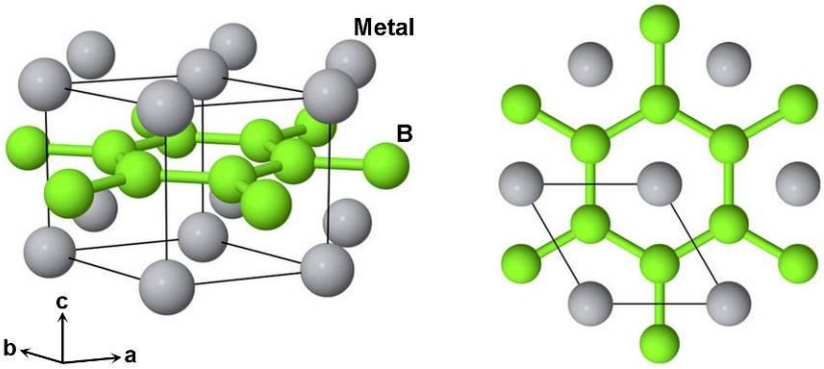

Figure 2.2 Side and top-view of the AlB_2-type crystal structure [69].

Generally, bond strengths and the combination of bond types influence the material properties. Metallic bonding in the M layers leads to high electrical and thermal conductivities, while strong covalent bonding in the B layers gives high hardness and elastic modulus values [18]. The M-B bond strength in diborides depends on the degree of electron localisation around the M atoms. The valence electron configuration in an isolated B atom is $2s^2sp^1$, representing its electron deficient character. In metal borides, the outer electron configurations are sp^2 and sp^3, which promote strong covalent bonding. In diborides, B atoms are electron acceptors, while the M atoms are electron donors. Each M atom donates two electrons (one to each B), which converts M to a doubly charged cation, while B atoms become singly charged anions. Hence, the MB_2 formula can be expressed as $M^{2+}(B^-)_2$ [65]. The M-B bonds have ionic characteristics

because of the donor-acceptor interactions, but they also have covalent characteristics due to partial excitation of *d* electrons and the formation of *spd* hybrid configurations. Some structural, physical and thermal properties of TiB_2 and HfB_2 compared with those of Al_2O_3 are listed in Table 2.1 [65, 70-74].

Table 2.1 Some structural, physical and mechanical properties of TiB_2 and HfB_2 compared with those of Al_2O_3

Diboride	TiB_2	HfB_2	Al_2O_3
Crystal structure	Hexagonal *P6/mmm* AlB_2		Hexagonal $R\bar{3}c$
a (Å)	3.028	3.141	4.756
c (Å)	3.228	3.47	12.99
M-B bond length (Å)	2.38	2.51	-
B-B bond length (Å)	1.748	1.813	-
Density ($g \cdot cm^{-3}$)	4.52	11.21	3.99
Melting point (°C)	3225	3380	2327
Coefficient of thermal expansion ($\alpha;10^{-6}K^{-1}$)	7.4	6.3	8.0
Thermal conductivity ($W \cdot m^{-1}K^{-1}$)	60-120	104	30.1
Electrical conductivity ($S \cdot m^{-1}$)	$\sim 7.6\times10^6$	9.1×10^6	-
Elastic modulus (GPa)	~560	480	400
Hardness (GPa)	25-35	28	18-21
Fracture toughness ($MPa \cdot m^{1/2}$)	4-5	4	3.0
Flexural strength (MPa)	700-1000 (3-point)	350-450 (4-point)	323 (3-point)

Because of desirable properties, i.e., high melting point, relatively low density and thermal expansion coefficient, high elastic modulus/hardness, good electrical/thermal conductivities, and excellent erosion/corrosion resistance, TiB_2 has been extensively investigated as a promising candidate material for several

demanding applications, such as in impact resistant armour, cutting tools, high-temperature wear-resistant parts, electrodes in metal smelting cells, neutron absorbers, and electrocatalysts for renewable energy [70, 75]. Such a unique combination of excellent properties makes HfB_2 suitable for the extreme chemical and thermal environments associated with hypersonic flights, atmospheric re-entry vehicles and rocket propulsion systems [76-78].

2.1.3 Lanthanum and calcium hexaborides

Alkaline-earth metals (e.g., Ca, Sr and Ba) and rare-earth metals (e.g., La, Ce and Sm) form hexaboride MB_6, which crystallise in the CsCl-type cubic structure (space group $Pm\bar{3}m$), where the M atoms occupy the vertices of the cube and the B_6 octahedra lie in the body-centre positions, as shown in Figure 2.3 [79]. Each B atom has four adjacent neighbours in its own octahedron and another neighbour in the direction of one of the cubical main axes, thus giving a homopolar lattice structure with the coordination number 5. The bonding between B_6 octahedron (inter, B-B1) is shorter in distance than that of the B-B bonds forming the B_6 octahedron (intra, B-B2), that forms a three dimensional interconnected cage structure. M atoms trapped in the boron cages have a coordination number of 24 [80]. There are no valence bonds between the M atoms and surrounding B atoms, thus the valence electrons of the M atoms become free electrons, imparting a metallic character to these compounds. Together with the strong bonds between the B atoms in the framework, this property produces a series of MB_6 that has high electrical conductivities, high melting points, low evaporation rate at high temperatures, high hardness, and high thermal/chemical stabilities (see Table 2.2) [80-85].

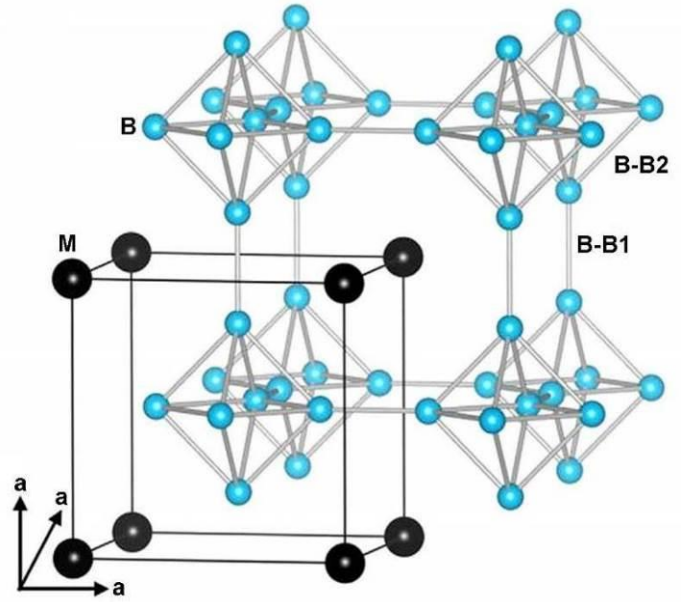

Figure 2.3 Structural depiction of cubic hexaborides [79]. B-B1 and B-B2 are the inter-octahedral and intra-octahedral boron bond lengths, respectively.

LaB_6 is an ideal cathode material possessing many superior properties, including low work function (~2.66 eV), high current density (~29 A/cm^2) and high brightness, low volatility, and long lifetime, as well as good resistance to poisoning in vacuum [80, 86-88]. LaB_6 cathodes are now widely utilised in many branches of modern technology, such as electron microscopes, plasma/ion sources, optical coatings, thermionic converters, electron-beam welders and free-electron lasers, either in the form of small crystal structures or in a geometric form with a heater behind it [89-91]. Moreover, LaB_6 powder can be used as an additive to improve the oxidation resistance of ZrB_2-based UHTCs and mechanical properties of ultrafine grain WC–10Co alloys [92-95].

CaB_6 has the highest specific resistance of all the hexaborides [80] and several other superior properties, such as relatively low density and thermal expansion coefficient, high-temperature weak ferromagnetism, and high neutron absorbability [96-99]. Thanks to its excellent properties, CaB_6 is a highly attractive candidate material for many important applications, e.g., as a boron source in manufacturing boron-alloyed steel, a deoxidising agent for production

of oxygen-free copper, an antioxidant for carbon-containing refractories, an abrasive or wear-resistant material, a neutron absorbent, and a ferromagnetism material [100-106].

Table 2.2 Some structural parameters and properties of LaB_6 and CaB_6

Hexaboride	LaB_6	CaB_6
a (Å)	4.1549	4.1556
B-B1 (inter) (Å)	1.654	1.670
B-B2 (intra) (Å)	1.768	1.745
Melting point (°C)	~2210	2235
Coefficient of thermal expansion (α;$10^{-6}K^{-1}$)	7.0	6.3
Density ($g \cdot cm^{-3}$)	4.72	2.45
Hardness (GPa)	28-30	27
Elastic modulus (GPa)	370-384	379

2.1.4 Al_2O_3-TiB_2 nanocomposite

Al_2O_3 is one of the most widely used and studied ceramic materials because of its high melting point, superior hardness, chemical inertness and electrical/thermal insulation properties [20]. Al_2O_3 has several polymorphs, among which α-Al_2O_3 (or corundum) is the most thermodynamically stable form [73]. The crystal structure of α-Al_2O_3 (space group $R\bar{3}c$) consists of close-packed planes of large O^{2-} anions stacked in the sequence A-B-A-B-…, thus forming a hexagonal close-packed array. The Al^{3+} cations occupy only two-thirds of the octahedral sites of the basic array, forming three different types of Al cation layers, named a, b and c, depending on the sites occupied within the layer. This gives the complete stacking sequence of O and Al layers of the form A-a-B-b-A-c-B-a-A-b-B-c-A-…, (b). One period of this sequence, i.e., from c-A to B-c, forms a hexagonal unit cell of α-Al_2O_3, as depicted in Figure 2.4 [107, 108].

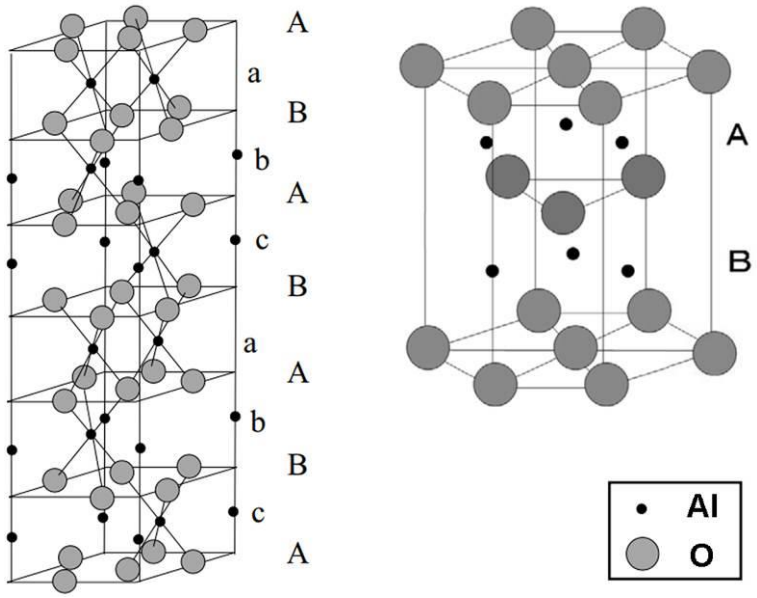

Figure 2.4 Structure of α-Al_2O_3 [108].

Based on its inherent properties and availability in abundance, Al_2O_3 is a strong candidate for a host of functional applications, including wear-resistant components, high-speed cutting tools, armour materials, thermal liners, thermal barrier installations, crucibles, ceramic boards and brackets, electrical and chemical insulators, and biomaterials [73, 109, 110]. However, its crucially structural applications are restricted by its low fracture toughness and poor thermal shock resistance [21, 22]. To date, most attempts to alleviate these problems have involved incorporating second phases such as particles, platelets, fibres or whiskers, CNTs and graphene, into the Al_2O_3 matrix on the basis of Niihara's initial work on ceramic nanocomposites [21]. TiB_2 stands out as a second phase owing to its good structural and thermodynamic compatibility with Al_2O_3 [31, 33] and the unique combination of excellent properties, e.g., high melting point, high hardness/elastic modulus, and high thermal/electrical conductivities [72]. Adding TiB_2 particles to an Al_2O_3 matrix improves hardness, fracture toughness and electrical conductivity and offers benefits in wear behaviour compared to monolithic Al_2O_3 [23-28], making Al_2O_3-TiB_2 composite

materials suitable for a variety of applications, such as electrodes, cutting tools, wear parts, lightweight armour, high-temperature/glow-plug heaters, and heat exchangers [26, 29, 30].

2.2 Synthesis of metal boride powders

Metal boride compounds can be synthesised *via* various routes. This section reviews and evaluates the four main routes used to synthesise TiB_2, HfB_2, LaB_6 and CaB_6 powders: (1) reduction processes, (2) direct elemental reactions, (3) chemical routes, and (4) molten salt electrolysis.

2.2.1 Reduction processes

Several reduction processes are used to synthesise metal boride compounds. Carbon and boron are the most common reducing agents, but boron carbide (B_4C), metals, or combinations of reducing agents can also be used.

2.2.1.1 Carbothermal reduction process

Commercially available TM diboride powders are predominantly synthesised *via* carbothermal reduction of the corresponding TM oxides, Reaction (2.1) is highly endothermic and becomes favourable only at elevated temperatures (above ~1400°C) [111-114].

$$TMO_2 + B_2O_3 + 5C = TMB_2 + 5CO \quad (2.1)$$

Shahbahrami *et al.* [113] studied the mechanism of the carbothermal synthesis of TiB_2 powder and suggested that TiB_2 synthesis is based on a TiC formation mechanism (Reactions (2.2) and (2.3)). The reaction is completed at 1500°C.

$$TiO_2 + 3C = TiC + 2CO \quad (2.2)$$

$$TiC + B_2O_3 + 2C = TiB_2 + 3CO \quad (2.3)$$

Excess B_2O_3 is often added to promote the formation of borides over carbides.

Consequently, the final powders typically contain oxygen and carbon as impurities. In addition, agglomerated products generally result from this process because of the relatively high reaction temperatures required for carbothermal reduction. TiB_2 powders synthesised *via* the carbothermal reduction of TiO_2 at 1786-1791°C contained 5 wt% of carbon [111]. Heat treatment of the product under a H_2 atmosphere at 800°C for 9 h resulted in the carbon content being lowered to 2.9 wt%. Carbothermal reduction of TiO_2 at 1500°C for 20 min with rapid heating and cooling resulted in large agglomerated TiB_2 particles [112]. After planetary milling for 12 h, the product particle sizes were reduced from ~500 nm to ~ 80 nm. However, these further treatments of products have adverse effects, such as contamination from milling media due to prolonged milling and complex processes using H_2 gas.

2.2.1.2 Borocarbide and carbo/borothermal reduction process

Reactions with B_4C have also been used to produce metal boride compounds. Similar to the carbothermal reduction process, the reactions between oxides and B_4C become favourable at elevated temperatures and are highly endothermic. Borocarbide reduction uses B_4C as a reducing agent (Reaction (2.4)), which provides both carbon for the reduction of the oxide and boron as a reactant. In addition, this process offers the benefits of reduced levels of carbon, B_2O_3, and oxide impurities in the products.

$$7TMO_2 + 5B_4C = 7TMB_2 + 3B_2O_3 + 5CO \quad (2.4)$$

$$2TMO_2 + B_4C + 3C = 2TMB_2 + 4CO \quad (2.5)$$

Carbo/borothermal reduction uses the combination of B_4C and carbon as reducing agents (Reaction (2.5)). There have been a few studies on TM boride powders synthesised *via* carbo/borothermal reduction [115-120]. Subramanian

et al. [115] prepared TiB_2 powder by reducing TiO_2 with B_4C and carbon at 1800°C. High temperature-high vacuum treatment and milling of the product powder afforded ~1 μm TiB_2 particles with oxygen, carbon and nitrogen contents all close to 0.5%. Ni *et al.* [117] prepared HfB_2 powder with a particle size of 1 μm at 1500-1600°C. Sonber *et al.* [118] synthesised HfB_2 powder with a size range of 2-3 μm at 1875°C. In addition, the spark plasma sintering (SPS) technique was employed to synthesise HfB_2 powder. The significant features of the SPS process, such as the rapid heating and cooling rates, short processing times and clearing effect of the particle surface, enable the formation of HfB_2 fine powders. HfB_2 powder with a size range of 100-200 nm was prepared *via* the carbo/borothermal reduction of HfO_2 at 1500°C using an SPS apparatus [119]. In addition, the size of the product HfB_2 particles being nearly the same as that of the initial HfO_2 particles indicated that the starting HfO_2 powder acted as the reaction centre during this process (Figure 2.5). Wang *et al.* [120] also used SPS to prepare HfB_2 powder at 1680°C. The synthesised HfB_2 powder was heated at 400°C in a nitrogen flow to eliminate any oxidation and then was quenched into liquid nitrogen, resulting in the refinement of the HfB_2 particles to a size of 1 μm.

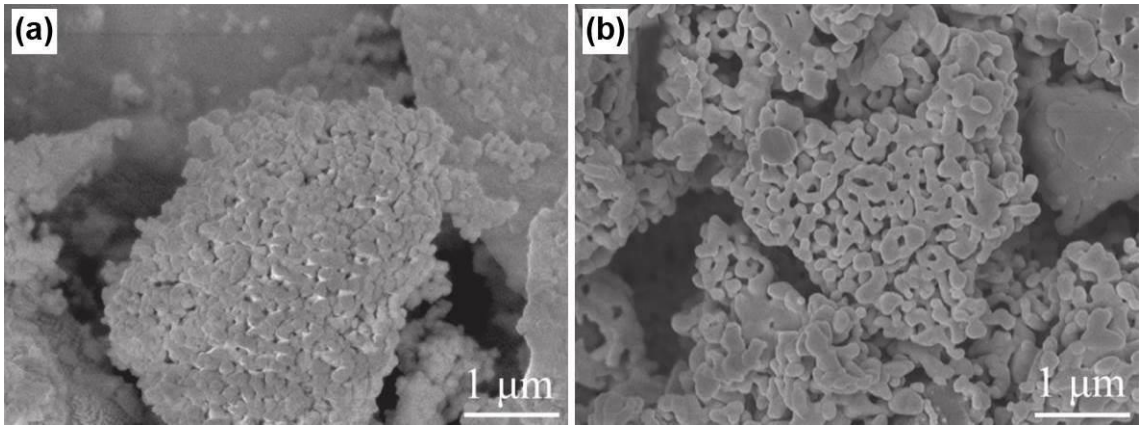

Figure 2.5 SEM images of the (a) starting HfO_2 particles and (b) HfB_2 particles synthesised from HfO_2-B_4C-C at 1500°C for 1 h using SPS [119].

Two synthetic techniques for producing LaB_6 were studied: carbothermal

reduction using La_2O_3-boron-carbon (Reaction (2.6)) and borocarbide reduction using La_2O_3-B_4C blends (Reaction (2.7)) [121]. The carbothermal method conducted at 1350°C was found to produce high-purity LaB_6 with a mean size of 600 nm, whereas a higher temperature of 1450°C was necessary for the borocarbide reduction to provide smaller LaB_6 particles (220 nm). Sonber *et al.* [122] synthesised LaB_6 powder with a size range of 2-10 μm by the borocarbide reduction of La_2O_3 at 1500°C.

$$La_2O_3 + 12B + 3C = 2LaB_6 + 3CO \quad (2.6)$$

$$La_2O_3 + 3B_4C = 2LaB_6 + 3CO \quad (2.7)$$

Zheng *et al.* [123] prepared CaB_6 powder *via* the reaction of calcium carbonate ($CaCO_3$) with B_4C and carbon at 1400°C (Reaction (2.8)). Lin *et al.* [124] also prepared CaB_6 powder at 1400°C using the $CaCO_3$-B_4C-C system. The size distribution and general shape of the CaB_6 particles were found to be similar to those of B_4C (Figure 2.6). Hence, choosing high-quality B_4C was one of the most important aspects to improve the properties of CaB_6 powder.

$$2CaCO_3 + 3B_4C + C = 2CaB_6 + 6CO \quad (2.8)$$

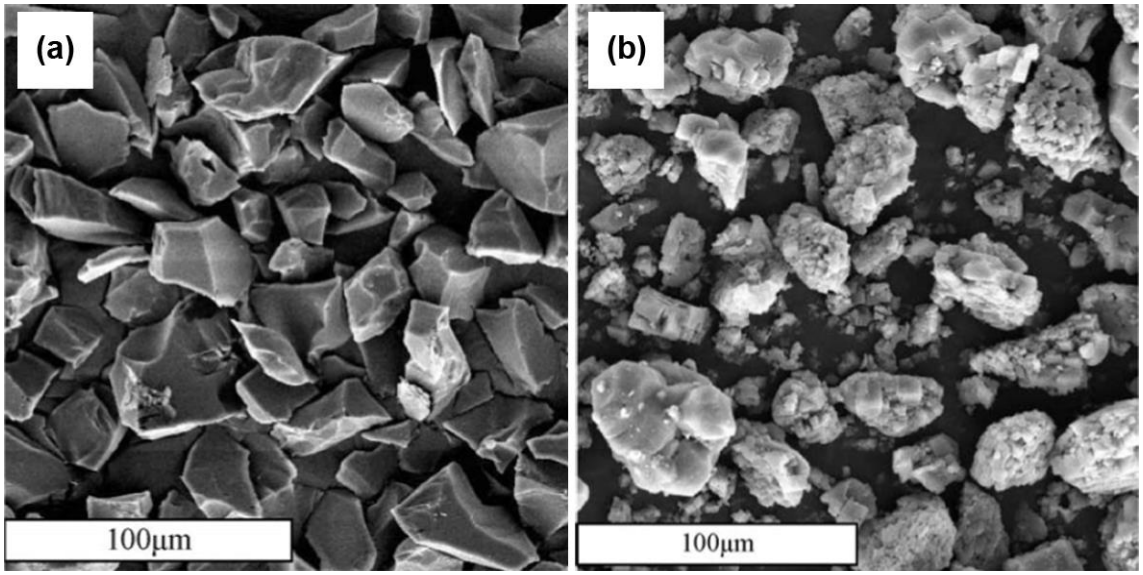

Figure 2.6 SEM images of (a) raw material B_4C and (b) CaB_6 synthesised from $CaCO_3$-B_4C-C at 1400°C for 3 h [124].

Yildiz *et al.* [125] synthesised CaB_6 powder *via* the carbothermal reduction of colemanite ($2CaO{\cdot}3B_2O_3{\cdot}5H_2O$). In this process, B_4C is produced as an intermediate product and becomes the boron source for the formation of CaB_6 at 1700-1850°C. Kakiage *et al.* [126] produced CaB_6 powder by the carbothermal reduction of CaO and B_2O_3, which was generated *via* the transient formation of $Ca_3B_2O_6$ and B_4C at 1400°C (Reaction (2.9)). Cakta *et al.* [127] synthesised CaB_6 *via* carbo/borothermal reduction from a gel precursor that was obtained from $C_6H_{14}O_6$, $CaCO_3$ and H_3BO_3. $Ca_3B_2O_6$, B_4C and $Ca_2B_6O_{11}$ were formed as transitional phases to create CaB_6, and the single-phase CaB_6 powder was obtained at 1400°C for 12 h or at 1500°C for 6 h.

$$Ca_3B_2O_6 + 4B_4C + 2C = 3CaB_6 + 6CO \quad (2.9)$$

2.2.1.3 Borothermal reduction process

Borothermal reduction can also be used to produce boride powders. The main advantage of borothermal reduction is the purity of the final powders and potential for achieving a fine particle size. However, borothermal reduction requires a pure source of boron, which is usually more expensive than carbon and requires a higher reaction temperature, e.g., (1) formation of TiB_2 and HfB_2 at 1700-1750°C (Reaction (2.10)) [128] and (2) formation of LaB_6 (Reaction (2.11)) and CaB_6 at 1500-1800°C [129, 130].

$$3TMO_2 + 10B = 3TMB_2 + 2B_2O_3 \quad (2.10)$$

$$La_2O_3 + 15B \rightarrow 2LaB_6 + \tfrac{3}{2}B_2O_2 \quad (2.11)$$

Guo *et al*. [131] prepared HfB_2 powder by the borothermal reduction of HfO_2 at 1100°C, followed by washing with hot water and removing residual B_2O_3 at 1550°C. The HfB_2 product powders had a low oxygen content (~0.56 wt%) and a particle size in the range of 0.5-1 μm. Guo *et al*. [59] also prepared pure TiB_2

powder with ~1.7 wt% oxygen and a particle size of ~0.9 μm by the direct heat treatment of TiO_2 and B at 1550°C under vacuum for 1 h. HfB_2 powders can also be synthesised *via* a borothermal reduction route from mechanically activated $HfCl_4$ and B powder blends (Reaction (2.12)) [60]. With the addition of 20 wt% excess B, HfB_2 powder with an average particle size of 391 nm and 3.5 wt% oxygen was obtained at 1100-1200°C.

$$3HfCl_4 + 10B = 3HfB_2 + 4BCl_3 \quad (2.12)$$

Hasan *et al.* [132] prepared LaB_6 with particle sizes ranging from submicrons to a few microns *via* the borothermal reduction of La_2O_3 and boron at 1400°C; by contrast, using the borothermal reduction of the high-energy ball milled La_2O_3 and boron allowed the temperature to be reduced to 1300°C and provided a particle size in the range from a few hundred nanometres to 1-2 μm [133].

2.2.1.4 Metallothermic reduction process

Carbothermal, borothermal, carbo/borothermal and borocarbide reduction reactions are highly endothermic, thus, these reduction processes are performed at high temperatures. As a result, the formation of coarse particles is unavoidable. An alternative method for synthesising metal boride compounds is the metallothermic reduction process, which utilises the thermal energy released in the reaction to become self-sustaining. Taking TiB_2 as an example, when Mg, Ca, or Al is used as a metal reduction reagent, the corresponding metallothermic reductions of TiO_2 and B_2O_3 are shown in Reactions (2.13)-(2.15) [134]. Nevertheless, when Al and Ca are used, it is difficult to remove the Al_2O_3 byproduct by acid treatment and to handle Ca in the atmosphere. By contrast, MgO can be leached out easily from the product by an acid leaching process. Therefore, Mg was selected as the most suitable metal reduction reagent. The

metallothermic reduction synthesis of metal boride compounds can be performed *via* combustion synthesis and mechanochemical synthesis.

$$TiO_2 + B_2O_3 + 5Mg = TiB_2 + 5MgO \quad (2.13)$$

$$TiO_2 + B_2O_3 + 5Ca = TiB_2 + 5CaO \quad (2.14)$$

$$3TiO_2 + 3B_2O_3 + 10Al = 3TiB_2 + 5Al_2O_3 \quad (2.15)$$

(1) Combustion synthesis

Combustion synthesis is exceptionally fast, typically on the timescale of seconds, and its important feature is the precise control of composition. The combustion synthesis process is subdivided into two distinct modes of ignition. The first, which is termed thermal explosion, involves the whole volume of the compact being heated to the ignition temperature and all reactant constituents spontaneously reacting to form a final product. However, the purity of the final product obtained from this technique is difficult to control, and multiple phases are often present. The second ignition mode is SHS, in which synthesis is initiated by point-heating a small part (usually the top) of the sample. Once started, a combustion wave passes through the remaining material as the liberated heat of fusion in one section is sufficient to maintain the reaction in the neighbouring section of the compact. Since the combustion wave passes through the sample, it purifies the material and maintains its stoichiometry [135].

In general, SHS can initiate a reaction when its adiabatic temperature (T_{ad}) >1800 K [18]. For Reaction (2.13), the T_{ad} is ~3105 K, indicating that Reaction (2.13) can be used to synthesise TiB_2 by SHS [136]. Demircan *et al*. [136] prepared TiB_2 powder *via* the SHS process with the magnesiothermic reduction of TiO_2 and B_2O_3. However, due to the high T_{ad} and enhanced mass transfer during combustion reaction propagation, the TiB_2 product consisted of

porous agglomerated particles with sizes ranging from less than 1 μm to approximately 30 μm. The use of SHS diluents can reduce the grain growth of the forming products by lowering the T_{ad} and creating an inhibiting layer on the particles. Khanra *et al.* [137] reported the addition of NaCl for the SHS of submicron-sized TiB_2 powder from TiO_2, H_3BO_3 and Mg powders. However, the process using H_3BO_3 as a precursor yielded water as an undesirable high-temperature byproduct, as indicated by the reaction:

$$TiO_2 + 2H_3BO_3 + 5Mg = TiB_2 + 5MgO + 3H_2O \qquad (2.16)$$

Chaichana *et al.* [138] also produced TiB_2 powder by SHS from TiO_2, B_2O_3 and Mg powders using NaCl as a diluent (TiO_2:B_2O_3:Mg:NaCl=1:1:5:n). As the amount of NaCl was increased (n = 0-2 mol), the TiB_2 particle size decreased, reaching 201-167 nm for 2 mol NaCl (Figure 2.7). Nekahi *et al*. [139] produced TiB_2 nanoparticles (~70 nm) through the volume combustion synthesis of TiO_2, B_2O_3 and Mg, employing a ternary mixture of KCl/NaCl/$CaCl_2$ as a low melting temperature diluent.

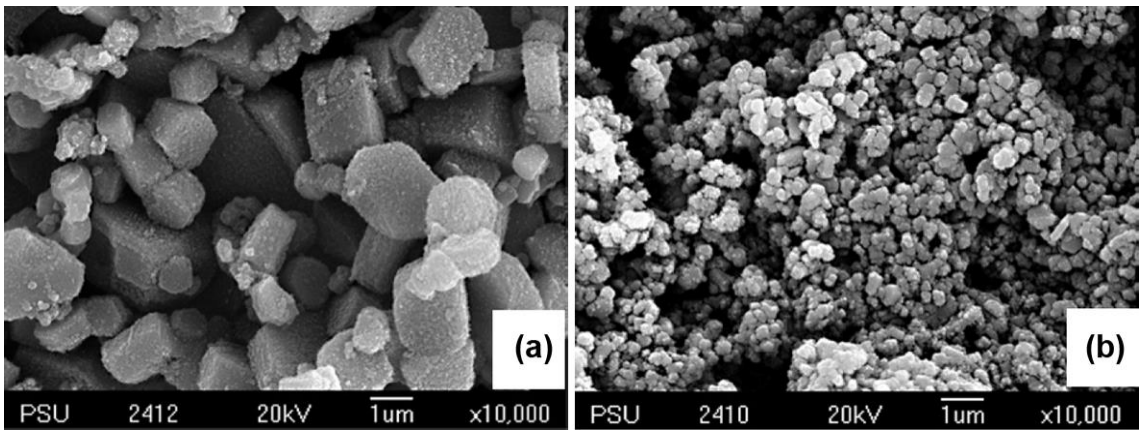

Figure 2.7 SEM images of TiB_2 powders by SHS from TiO_2-B_2O_3-Mg-NaCl (1:1:5:n) with (a) n = 0 and (b) n = 2 [138].

Dou *et al*. [140] synthesised LaB_6 powders from the La_2O_3-B_2O_3-Mg system (Reaction (2.17)) using the combustion synthesis method by applying different molding pressures. The LaB_6 particles became finer as the molding pressure

was increased from 5 to 20 MPa, indicating that LaB_6 grain growth is suppressed at higher pressures.

$$La_2O_3 + 6B_2O_3 + 21Mg = 2LaB_6 + 21MgO \quad (2.17)$$

Huang *et al.* [141] prepared CaB_6 powder through combustion synthesis using CaB_6O_{10} and Mg (Reaction (2.18)) as starting materials.

$$CaB_6O_{10}\ (CaO + 3B_2O_3) + 10Mg = CaB_6 + 10MgO \quad (2.18)$$

Apart from the boride product and MgO byproduct, the combustion products contain different amounts of undesired $Mg_3B_2O_6$ (Reaction (2.19)), Mg_2TiO_4 (Reaction (2.20)), or $Ca_3(BO_3)_2$ (Reaction (2.21)), which cannot be eliminated by acid leaching.

$$B_2O_3 + 3MgO = Mg_3B_2O_6 \quad (2.19)$$

$$TiO_2 + 2MgO = Mg_2TiO_4 \quad (2.20)$$

$$3CaO + B_2O_3 = Ca_3(BO_3)_2 \quad (2.21)$$

The SHS method is energy saving and can be applied to the large-scale production of metal boride compounds. This method has several advantages, including a short processing time, very low environmental impact, simple operation, the generation of fine microstructures due to high cooling rates, and low cost and energy consumption. However, because of the high temperature gradient near the combustion surface and high velocity of the reaction, a non-uniform and non-equilibrium composition is obtained [142].

(2) Mechanochemical synthesis

Mechanochemical synthesis is a solid-state powder processing technique involving repeated welding, fracturing, and rewilding of the reactant powders mixed in a high-energy ball mill, which results in reduction or redox reactions. The chemical precursors typically consist of oxide, chloride and/or metal

mixtures that react during either milling or subsequent heat treatment to form the product powders [143]. Mechanochemical synthesis has the advantages of simplicity, reproducibility and low processing costs. However, the major drawbacks associated with this synthesis method are the inability to produce discrete nanoparticles in the finest size range and the tendency to contaminate powders with the milling media used to grind them, particularly when extensive and repeated milling cycles are performed. In addition, precise control and variation of stoichiometry are not possible with high-energy ball milling. Welham [144] fabricated TiB_2 with a particle size <200 nm by ball milling a mixture of TiO_2, B_2O_3, and Mg in a tumbling mill for 15 h. Ricceri *et al*. [145] reported a similar result using the starting materials of TiO_2, B_2O_3, and Mg and achieved 50 to 100 nm sized TiB_2 particles after milling in a high-energy vibration ball mill for less than 2 h. However, the product particles tended to aggregate. When Si was used instead of Mg as the reducing agent for TiO_2 and B_2O_3, milling for up to 50 h (in a high-energy planetary ball mill) did not lead to the formation of TiB_2 [146]. Furthermore, heat treatment of the milled powders at 1300°C resulted in the formation of TiB_2, Ti_2O_3, Si and SiO_2.

Mechanically-activated/assisted combustion synthesis consists of a short duration high-energy ball milling step followed by a self-sustaining reaction. Mechanical activation of reactants is used as an intermediate step to enhance the kinetics of a reaction during subsequent thermal treatment. The mechanical activation process is known to be able to substantially reduce the reaction temperature required for completing the reactions. In addition, the potential limitation of high-energy ball milling, e.g., contamination effects, can be minimised if the time for intensive mechanical activation is sufficiently short. This

process combines the advantages of mechanochemical synthesis and SHS, and thus has been used to synthesise intermetallics, ceramics and composites [147]. Nasiri-Tabrizi *et al*. [148] prepared TiB_2 powder with a mean particle size of 140 nm using the mechanically induced self-sustaining reaction of a TiO_2-B_2O_3-Mg system with NaCl added as a diluent. Nozari *et al*. [142] synthesised TiB_2 with a mean particle size of 50 nm from TiO_2, H_3BO_3 and Mg powders *via* a mechanically activated SHS route. The authors reported that the addition of NaCl decreased the mean crystallite size of the TiB_2 phase in the final products, but did not prevent the growth of the particles (Figure 2.8).

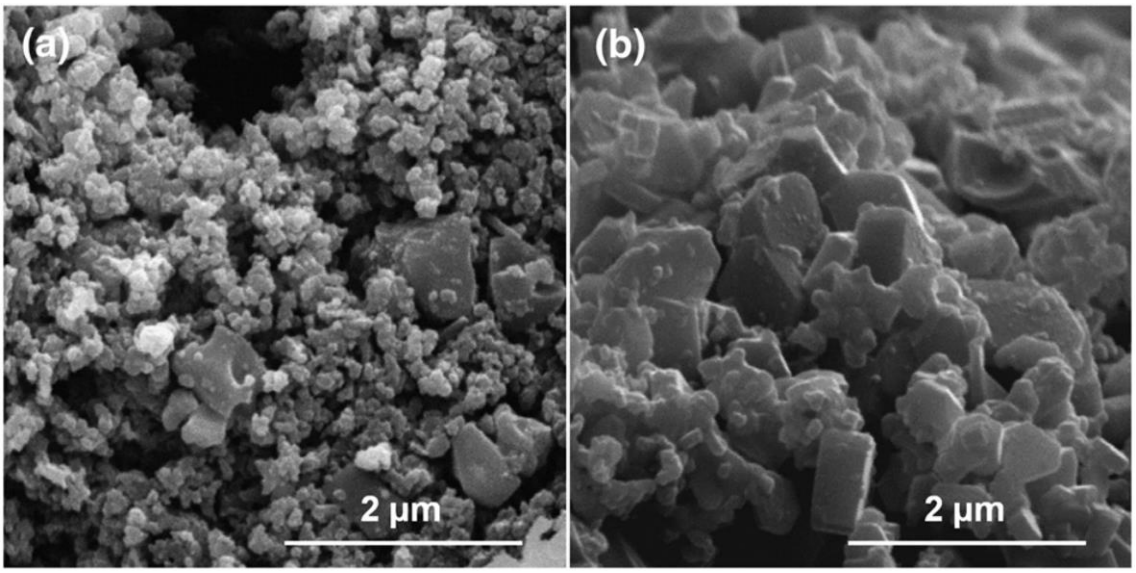

Figure 2.8 SEM micrographs of the TiB_2 product powder resulting from 5 h of MA-SHS from (a) TiO_2-H_3BO_3-Mg and (b) TiO_2-H_3BO_3-Mg-NaCl [142].

E. Barraud *et al.* [149] synthesised HfB_2 from mechanically activated powder mixes of $HfCl_4$-Mg-B (Reaction (2.22)) and $HfCl_4$-B. Mechanical activation for 1 h of the powder mixture of $HfCl_4$-Mg-B followed by annealing under an argon flow for 1 h at 1100°C produced powders mainly consisting of facetted grains of HfB_2 with a size of approximately 300 nm. By contrast, monocrystalline rods of HfB_2 were formed from the mixture of $HfCl_4$-B processed under the same conditions.

$$HfCl_4 + 2B + 2Mg = HfB_2 + 2MgCl_2 \qquad (2.22)$$

Ağaoğulları *et al*. [150] reported a mechanochemical route for the synthesis of LaB_6 powders from La_2O_3-B_2O_3-Mg blends. The formation reactions of the LaB_6 and MgO phases were completed after 5 h of milling. LaB_6 powders with a particle size of 75-300 nm were obtained after subsequent acid leaching. Furthermore, annealing the milled and leached powders at 800°C can improve the purity of LaB_6 powders. Ağaoğulları *et al*. [151] also reported the mechanochemical synthesis of LaB_6 powders from La_2O_3-B_2O_3-Ca blends. After acid leaching, LaB_6 powders were obtained in the presence of a small quantity of $Ca_3(BO_3)_2$. Submicron-sized CaB_6 powders were generated *via* the mechanochemical processing of Ca/B_2O_3 powder blends (Reaction (2.23)) and subsequent leaching [98]. The resultant CaB_6 powders contain spherical particles with sizes between 300 nm and 1 μm.

$$10Ca + 3B_2O_3 = CaB_6 + 9CaO \qquad (2.23)$$

Wang *et al*. [152] reported a versatile route for the synthesis of hexaborides at temperatures of 170-350°C. Single-crystalline cube-like LaB_6 with mean sizes ranging from 450 to 700 nm was prepared through the co-reduction of La_2O_3 and H_3BO_3 by Mg powder with the addition of I_2 at 170-250°C for 12 h in an autoclave. Similarly, CaB_6 nanorods can be produced at 350°C using CaO as the calcium source. When $CaCO_3$ was used instead of CaO, single-crystalline hollow CaB_6 cages were obtained at 400°C. I_2 was vital for the formation of LaI_3, LaOI or similar intermediates and may play a quasi-catalytic role in the synthesis of hexaborides.

Reduction processes are solid-solid reactions that are generally controlled by a slow diffusion mechanism. Therefore, highly reactive precursor powders, high temperatures, and long processing times must be used to complete the

reactions. In addition, the reaction product is often strongly agglomerated. Considerable grinding is required for particle size reduction, which can result in the incorporation of impurities.

2.2.2 Direct elemental reactions

The simplest synthetic method for producing metal boride powders is the reaction of elemental precursor powders. Compared with oxides, starting from pure metals provides the ability to control impurity levels in the product powders.

$$Ti + 2B = TiB_2 \quad (2.24)$$

$$Hf + 2B = HfB_2 \quad (2.25)$$

Reactions (2.24) and (2.25) are both highly exothermic and have extremely high T_{ad} values: T_{ad} = 3190 K for Reaction (2.24) and T_{ad} = 3520 K for Reaction (2.25) [153]. Hence, these reactions are likely to occur in the SHS process [154, 155]. According to several studies, the initiation of SHS reactions between solid elemental powders requires the melting of at least one of the reactants. Radev and Marinov [156] carried out the SHS of TiB_2 from Ti and B powders in a steel reactor under argon. The SHS was initiated by a current pulse of 60 A and 40 V. Due to the high temperature of SHS, most of the TiB_2 product formed aggregates with a mean particle size of 40-60 μm. Hwang and Lee [157] synthesised submicron-sized TiB_2 powders by ball milling Ti and B powders for 280 h. Blum *et al*. [158] used a powder mixture of Hf and B to produce HfB_2 *via* a non-SHS route at 1500°C. They also reported a synthetic route employing metallic Hf strips and elemental B powder. Despite the use of elements, the authors reported the presence of a significant level of unaccounted impurities. Volkova *et al*. [159] synthesised nanosized TiB_2 based on the interaction of Ti and B powders in the ionic melt of sodium tetraborate ($Na_2B_4O_7$). TiB_2 formation

was shown to occur at T≥745°C, which is the melting temperature of $Na_2B_4O_7$. The phenomenon of the transfer of B to Ti in the ionic melt of $Na_2B_4O_7$ was observed and can be explained by the formation of lower valence B^{2+} ions in Reaction (2.26) followed by their disproportionation in the reaction with Ti, which proceeds with the release of energy due to the formation of TiB_2 in Reaction (2.27). Nevertheless, the authors indicated that the proposed mechanism for TiB_2 formation in the $Na_2B_4O_7$ ionic melt requires further verification. The particle size of the TiB_2 powder obtained after heating at 785°C for 10 h was 70-75 nm. The method was extended to synthesise HfB_2 *via* reactions between Hf and B powders in the $Na_2B_4O_7$ ionic melt, and HfB_2 powder with a 50-55 nm particle size was obtained by heating at 850°C for 10 h [160].

$$B + 2B^{3+} \leftrightarrow 3B^{2+} \quad (2.26)$$

$$3B^{2+} + Ti \rightarrow B^{3+} + TiB_2 + Q \quad (2.27)$$

Xin *et al*. [161] synthesised CaB_6 by reacting Ca pellets with B powder under a pressure of 1 GPa and temperatures of 950-1150°C. When the reaction temperature reached the melting point of Ca (~850°C), the Ca melted and formed a molten pool. B was dissolved into the molten Ca and reacted with it to produce CaB_6 crystals (Reaction (2.28)). Their formation and growth were affected by the temperature, pressure gradients, and the ability of B to dissolve and diffuse in the molten Ca. The resulting CaB_6 exhibited three typical morphologies: rods, cubes and plate-like rectangular blocks.

$$Ca(l) + B(s) \rightarrow CaB_6(s) \quad (2.28)$$

The direct elemental reaction method is highly advantageous on the laboratory scale because of the ability to control the purity and particle morphology of the resulting metal boride powders. However, this method is expensive to scale up

due to the use of elemental raw materials.

2.2.3 Chemical routes

A broad range of chemical synthesis methods has been used to produce metal boride powders on the laboratory scale where highly pure and/or extremely fine particles are needed. Most chemical routes involve reactions between metal-containing and boron-containing precursors. For instance, a principal method for synthesising TiB_2 involves the hydrogen reduction of $TiCl_4$ and BCl_3 at 1500°C (Reaction (2.29)), but the solid diboride product requires grinding. The decomposition of $Ti(BH_4)_3$ at ~140°C (Reaction (2.30)) can be used to generate high-purity TiB_2 powder, which was agglomerated with a particle size in the range of 100-200 nm [162]. Axelbaum *et al*. [163] developed a gas-phase combustion process that yielded unagglomerated TiB_2 nanoparticles by the reaction of metallic sodium vapour with $TiCl_4$ and BCl_3. However, this method required sophisticated reactors, and the products were reported to be contaminated with metallic titanium and TiO_2.

$$TiCl_4(g) + 2BCl_3(g) + 5H_2(g) = TiB_2(s) + 10HCl(g) \qquad (2.29)$$

$$2Ti(BH_4)_3 = 2TiB_2 + B_2H_6 + 9H_2 \qquad (2.30)$$

Nanocrystalline TiB_2 and HfB_2 powders were synthesised by reacting anhydrous chlorides with $NaBH_4$ in the temperature range of 500-700°C for 12 h in an autoclave [164, 165]. The overall process can be described by Reaction (2.31). However, the reaction may also proceed by a vapour phase mechanism that involves the decomposition of $NaBH_4$ (i.e., to BH_3 and NaH) and its further reaction with a gaseous chloride. TiB_2 and HfB_2 prepared by these routes can achieve crystalline sizes as fine as 10-30 nm. Bates and co-workers [166] also prepared 5-100 nm nanocrystalline TiB_2 by Reaction (2.31), followed by

annealing the obtained amorphous precursor at 900-1100°C for 24 h under dynamic vacuum. Moreover, Gu *et al.* [167] synthesised TiB_2 *via* a benzene-thermal reaction of metallic sodium with amorphous boron powder and $TiCl_4$ at 400°C for 8 h in an autoclave (Reaction (2.32)). The particle size was reported to be 15-40 nm.

$$TMCl_4(g) + NaBH_4(g) \rightarrow TMB_2(s) + 2NaCl(s) + 3H_2(g) \qquad (2.31)$$

$$TiCl_4 + 2B + 4Na \xrightarrow{\text{Benzene at } 400^oC} TiB_2 + 4NaCl \qquad (2.32)$$

LaB_6 nanoparticles with a mean size of 30 nm were synthesised from Mg, $NaBH_4$ and $LaCl_3$ at 400°C for 4 h in an autoclave. In this case, using B_2O_3 instead of $NaBH_4$, LaB_6 nanocubes of ~200 nm in size were formed at 500°C [168]. To avoid using an autoclave requiring long heating and cooling times, Kelly *et al.* [169] synthesised LaB_6 powders of ~80 nm from $LaCl_3$, B and Li powders (Reaction (2.33)) in quartz tubes using thermal and chemical ignition techniques. Nevertheless, some residual B and/or Li were not fully removed during the washing procedure and so still remained in the product. Yuan *et al*. [170] synthesised LaB_6 nanoparticles *via* the reaction between $LaCl_3$ and $NaBH_4$ (Reaction (2.34)) at 1200°C for 2 h in vacuum. The product powders were composed of cubic particles with sizes ranging from 20 to 100 nm.

$$LaCl_3 + 6B + 3Li = LaB_6 + 3LiCl \qquad (2.33)$$

$$LaCl_3 + 6NaBH_4 = LaB_6 + 3NaCl + 12H_2 + 3Na \qquad (2.34)$$

Bao *et al*. [171] prepared submicron-sized LaB_6 powders by reacting La_2O_3 and $NaBH_4$ using a continuous evacuation process at 1000-1200°C. The LaB_6 powder produced at 1000°C consisted of ultrafine LaB_6 crystallites (~10 nm) and cubic crystals (50-100 nm) (Figure 2.9(a)). By contrast, when the temperature was elevated to 1200°C, the LaB_6 powder exhibited good dispersion and

favourable growth behaviour with an average size of 300-400 nm (Figure 2.9(b)).

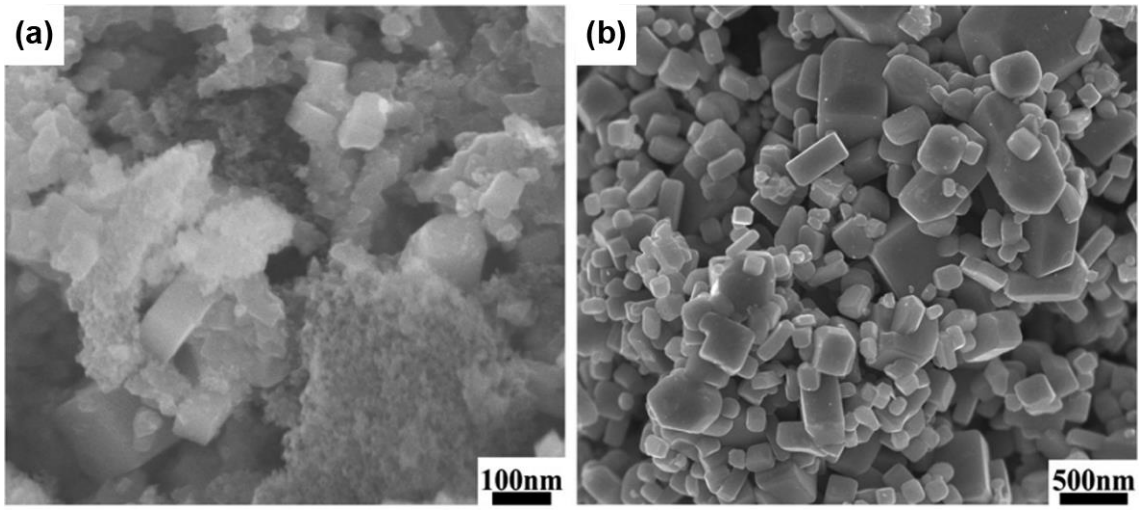

Figure 2.9 SEM images of LaB_6 prepared from the reaction between La_2O_3 and $NaBH_4$ at (a) 1000°C and (b) 1200°C for 2 h [171].

CaB_6 powder was also synthesised at 500°C in an autoclave using $CaCl_2$ and $NaBH_4$ as the reactants [172]. Bao *et al*. [173] synthesised ultrafine CaB_6 powders *via* the reaction of CaO with $NaBH_4$ at 1000-1150°C for 2 h (Figure 2.10). At 1000°C, the CaB_6 product consisted primarily of agglomerated nanoparticles with a mean size less than 10 nm. A large quantity of nanoparticles was converted into small crystalline nanocubes with a size of 20 nm when the reaction temperature was increased to 1100°C. After the temperature was increased to 1150°C, perfect nanocubes formed with a clear increase in grain size, which reached 150 nm.

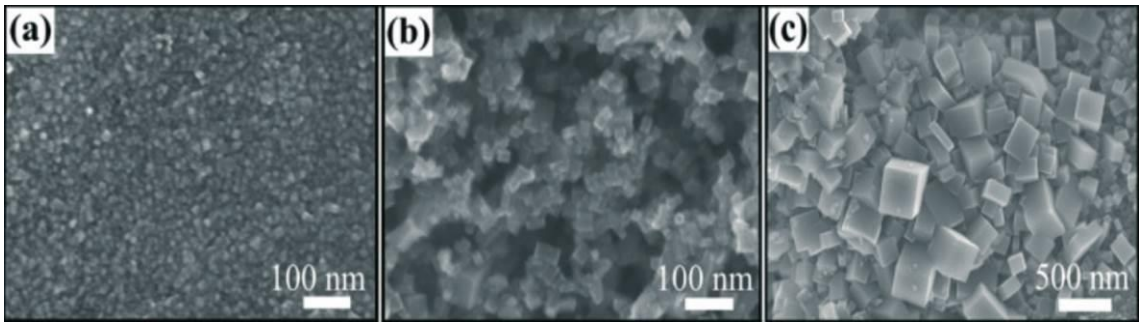

Figure 2.10 SEM images of CaB_6 prepared by the reaction of CaO with $NaBH_4$ at various reaction temperatures: (a) 1000°C, (b) 1100°C, and (c) 1150°C [173].

Boride powders were also synthesised by sol-gel processing followed by

carbothermal reduction. Compared with many other synthetic routes, molecular level mixing in the liquid phase allows transformation to the final product at lower temperatures with improved homogeneity of the final product. Wang *et al*. [174] prepared ultrafine HfB_2 powder using inorganic-organic hybrid precursors of $HfOCl_2{\cdot}8H_2O$, B_4C, and phenolic resin as sources of hafnium, boron and carbon, respectively. The reactions were substantially completed over a temperature range of 1300-1500°C for 1 h using SPS. The synthesised powder had a small crystalline size <500 nm. Ultrafine TiB_2 powders were also prepared by sol-gel processing with tetrabutyl titanate, H_3BO_3 and phenolic resin as the solution-derived precursors. The carbothermal reduction reactions were largely completed at temperatures below 1400°C. At temperatures below 1100°C, TiC was the predominant phase, and the resulting products consequently had a fine average crystalline size <200 nm [175]. A sol-gel mixture of $HfCl_4$, H_3BO_3, and phenolic resin was used to obtain intimately mixed (yet unreacted) HfO_2, B_2O_3, and C, which was then subjected to the carbothermal reduction reaction *via* heat treatment [176]. Typically, this approach yields HfC and B_4C as side products in unpredictable amounts. In this study, the ratios of the different precursors were optimised to produce HfB_2 powder with negligible impurities. Calcination at 1300°C produced HfB_2, but required 25 h to form phase-pure HfB_2. The long heating time resulted in a significant fraction of rod-shaped particles, with the screw dislocation driven growth occurring along the *c*-axis (Figure 2.11(a)). The use of a higher calcination temperature avoided this problem (Figure 2.11(b)).

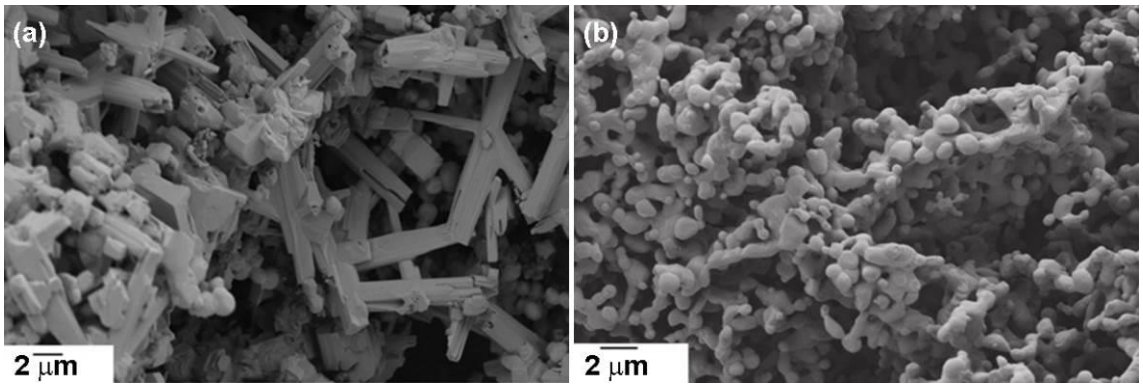

Figure 2.11 SEM images showing the HfB_2 particle morphology for sol-gel precursors that were heat treated at (a) 1300°C for 25 h and (b)1600°C for 2 h [176].

Venugopal *et al.* [177] studied carbon sources with different structures to produce HfB_2 particles with different morphology using $HfCl_4$ and H_3BO_3 as the elemental precursors. The carbon sources included liquid and powder phenolic resin (PPR), pitch, sucrose, graphite, carbon black, and CNTs. In general, the final particle size of HfB_2 was influenced by the structure and level of agglomeration of the carbon source. For example, HfB_2 particles resulting from the use of ~20 nm carbon black were coarser than those resulting from the use of ~150 nm carbon black because the former carbon source was more heavily agglomerated. Similarly, heavily entangled CNTs produced HfB_2 particles of 0.8-1 μm in size, although their diameter was only 10-20 nm. The finest HfB_2 particles with sizes from 30 to 150 nm were obtained using the PPR as the carbon source, which yielded tiny and well-dispersed particles of carbon on pyrolysis (Figure 2.12).

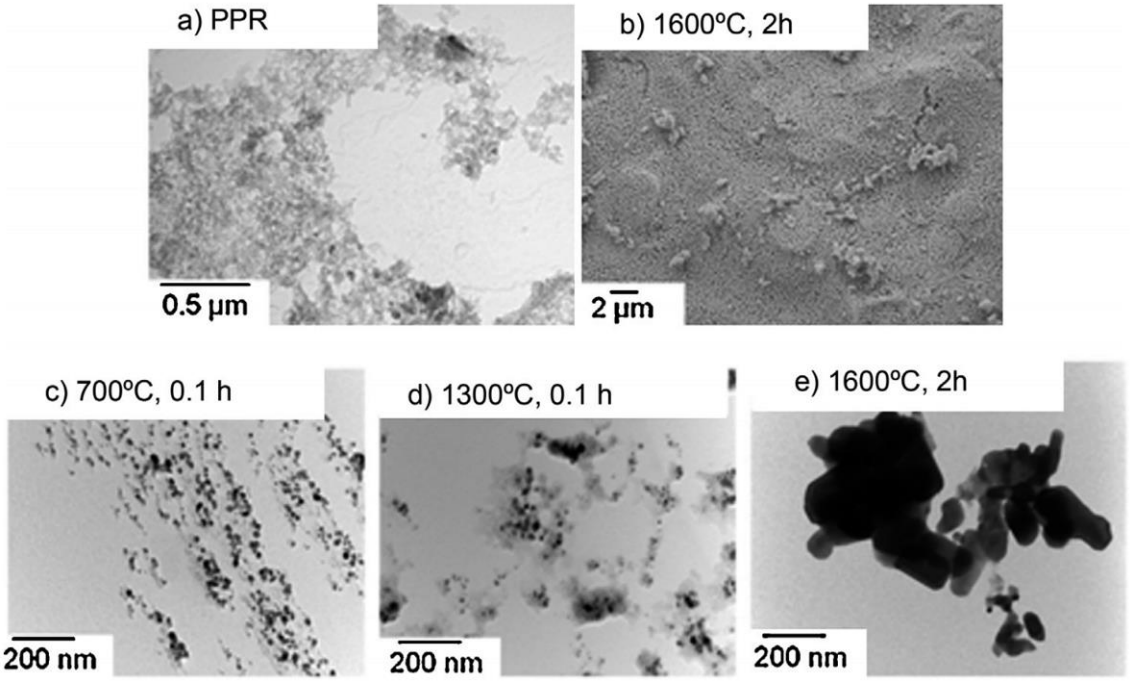

Figure 2.12 (a) TEM image of the carbon structure resulting from heat treating PPR at 1000°C for 0.1 h, (b) SEM images of the resultant HfB_2 powders after heat treatment at 1600°C for 2 h using PPR (b) and (c-e) formation of HfB_2 powder from PPR [177].

Metal boride powders prepared by sol-gel processes are pure, homogeneous, and highly reactive. However, these processes still suffer from several drawbacks. Metal borohydride and polymer-based synthetic routes use chemicals that are toxic and unstable in air or moisture, making them undesirable as large-scale processing methods. Methods that are based on metal chlorides offer atmospheric stability, but are more expensive than using oxide-based raw materials. In addition, these processing techniques require multiple processing steps to form the final precursor liquid system, and the processing parameters are relatively complex. Another vital disadvantage of the sol-gel method is that Cl^- cannot be completely removed, which can impede the densification of the bulk materials.

2.2.4 Molten salt electrolysis

Alternatively, molten salt electrolysis can be regarded as a promising method for the deposition of metal borides because of its applicability to complex

geometries, simplicity and use of cheap raw materials. In an electrolysis cell, electrons are employed as reductants, and their activity can be tuned by controlling the electrode potential.

The electrochemical synthesis of metal borides is basically described as co-deposition of metal and boron to form metal borides on a cathode material because of simultaneous and/or sequential reactions occurring in a molten electrolyte containing both metal- and boron-components [178]. The electrolytes employed in the synthesis of TiB_2 can essentially be divided into two groups according to the type of electroactive components: (i) molten systems consisting of oxygen-containing compounds of Ti and B, e.g., $Me_2B_4O_7$-TiO_2 or $MeBO_2$-TiO_2 (where Me donates alkali metal), and (ii) systems using Me_2TiF_6 and $MeBF_4$ (can also be applied to HfB_2 by replacing Me_2TiF_6 as Me_2HfF_6) as electroactive components that are dissolved in a supporting electrolyte, generally consisting of a mixture of alkali metal fluorides and/or chlorides (reduction mechanisms: Ti^{4+} + $e^- \leftrightarrow Ti^{3+}$; $Ti^{3+} + 3e^- \rightarrow Ti$; $B^{3+}+ 3e^- \rightarrow B$; $Ti + 2B \rightarrow TiB_2$ on the cathode surface). Compared to the pure fluoride melt, the chloro-fluoride melt exhibits some advantages, such as low corrosion of construction materials and easy separation of the cathodic product from the quenched salt [179, 180]. Graphite or steel rods are often used as the cathode material. Depending on the electrolyte used, the working temperature covers a wide range from 540 to 1100°C.

Electrodeposition of TiB_2 from cryolite-based electrolytes at 960°C and KF-KCl melts at 800°C on molybdenum substrates was performed. The results showed that electrolysis in KF-KCl electrolytes containing KBF_4-K_2TiF_6 provided coherent TiB_2 coatings with good adhesion to the substrate, whereas coatings prepared at

960°C from cryolite-based electrolytes containing KBF_4-K_2TiF_6 or B_2O_3-TiO_2 were either not successful or not coherent [181]. Ozkalafat *et al.* [178] investigated the electrochemical co-deposition of TiB_2 on nickel substrates at temperatures ranging from 800 to 1000°C, from an oxide-type electrolyte ($Na_2B_4O_7$-$Na_{16}Ti_{10}O_{28}$) added with CaF_2 (1 wt%) to adjust the viscosity of the melt and to activate the deposition of Ti and B.

Wang and Zhai [182] prepared CaB_6 powder from CaO-B_2O_3-sintered samples by electrolysis using a $CaCl_2$-NaCl electrolyte at 750°C. Angappan *et al*. [183] synthesised CaB_6 crystals *via* electrolytic synthesis in a CaO-B_2O_3-LiF melt at 900°C. Yin *et al*. [105] prepared CaB_6 by the one-step electroreduction of solid CaB_2O_4 in molten $CaCl_2$-NaCl. Before electrolysis, the CaB_2O_4 was not uniform, and some particles were larger than 10 μm (Figure 2.13(a)). After electrolysis at 600°C, solid CaB_2O_4 was converted to CaB_6 nanoparticles that ranged in size from 20 to 100 nm (Figure 2.13(b)). When the electrolytic temperature was increased to 700°C, needle-like CaB_6 with diameters ranging from 0.2 to 1 μm were obtained (Figure 2.13(c)).

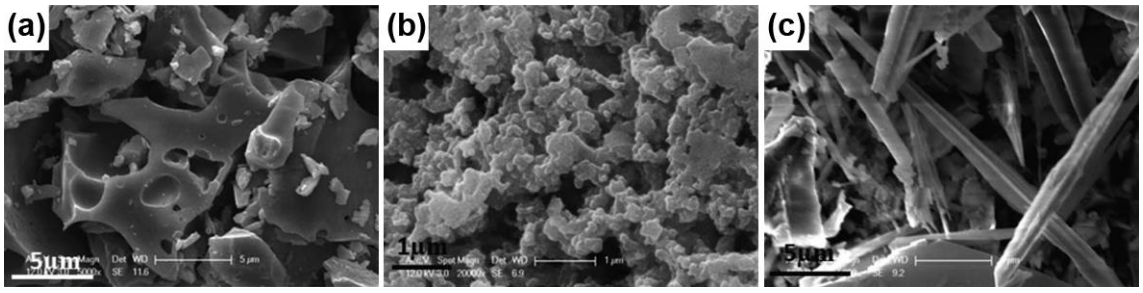

Figure 2.13 SEM images of (a) CaB_2O_4 and electrolytic CaB_6 obtained at (b) 600°C and (c) 700°C [105].

2.3 Synthesis of amorphous boron powder

The known methods for synthesising elemental boron from boron-containing compounds can be divided into four groups: (1) reduction of boron compounds

(oxides, halogenides, and fluoroborates) by metals (metallothermic method) [7-12, 184-188], (2) electrolytic reduction of boron compounds (potassium fluoroborate, magnesium borate, and mixed alloys) [189-197], (3) reduction of boron halogenides by hydrogen [198-206] and (4) thermal decomposition of boranes and boron halogenides [54, 207-213]. The primary synthetic reactions of elemental boron are listed in **Table 2.3**.

Table 2.3 Primary synthetic reactions of elemental boron

Method	Reaction	Product
Hydrogen reduction	$2BX_{3(g)} + 3H_{2(g)} \rightarrow 2B_{(s)} + 6HX_{(g)}$ (with X = F, Cl, Br, I)	Crystalline boron
Thermal decomposition	$2BX_{3(g)} \rightarrow 2B_{(s)} + 3X_{2(g)}$ (with X = Br, I)	Crystalline boron
	$B_nH_{m(g)} \rightarrow B_{(s)} + H_{2(g)}$ (B_2H_6, $B_{10}H_{14}$)	Crystalline and amorphous boron
Metallothermic reduction	$B_2O_3 + 6X \rightarrow 2B + 3X_2O$ (X = Na, K) $B_2O_3 + 3Y \rightarrow 2B + 3YO$ (Y = Ca, Mg) $2B_2O_3 + 3Z \rightarrow 4B + 3ZO_2$ (Y = Ti, Hf) $B_2O_3 + 2Al \rightarrow 2B + Al_2O_3$	Amorphous boron

Under standard conditions, the gas routes produce pure crystalline boron (≥99%), whereas the metallothermic reduction yields amorphous boron powders with lower purity (~90%). Although B_2H_6 pyrolysis can also produce amorphous boron powders with high purity, highly demanding working conditions and severe pollution problems limit the applications of this method. In addition, different forms of amorphous boron (films, whiskers, fibres or nanowires) can be fabricated by chemical vapour deposition (CVD) [47, 214], laser-assisted CVD, and electron cyclotron resonance (ECR) plasma CVD using gas mixtures of BCl_3+H_2 or B_2H_6+H_2 as precursors [47, 214-216]. However, these processes are hazardous due to the use of reactive, corrosive, poisonous and inflammable

reagents, e.g., H_2, BCl_3, BBr_3, B_2H_6 and $B_{10}H_{14}$, and the generation of a large amount of toxic waste.

2.3.1 Moissan's method

The most common method for producing amorphous boron is *via* the exothermic reduction of B_2O_3 with Mg, which was first proposed by Moissan in 1892 [184, 185]. In this method, B_2O_3 and Mg powders are mixed and heated. The exothermic reaction occurs and causes an increase in temperature, which exceeds 800°C. The product is a mixture of B and MgO. The byproduct MgO and unreacted reactants can be removed by acid leaching, and the resulting boron is impure (usually <90%) and has an amorphous structure. Considerable effort has been dedicated to the development of techniques to improve the purity of the amorphous boron based on Moissan's process [186-188]. The initial reactant ratio, impurity content of the raw materials, reaction temperature and purification method are crucial factors to produce high-purity amorphous boron powders. Vignolo *et al*. [217] described a novel procedure that can be applied prior to Moissan's process to produce fine amorphous boron powders. This procedure comprised the solubilisation, cryogenic freezing, and freeze-drying of B_2O_3 to reduce the boron precursor size to the nanometre scale. The lyophilised B_2O_3 shows a porous structure, which provides a higher reaction surface to Mg during the B_2O_3 reduction. Amorphous boron powder was also produced by reacting $Na_2B_4O_7$ with different reductants (e.g., carbon, hydrocarbons, alkali/alkaline earth/TMs, and metal hydrides) [218].

2.3.2 Combustion synthesis

Wu *et al*. [7] prepared amorphous boron powder using an SHS process based on the exothermic reaction of a Mg and B_2O_3 mixture. Irregular ultrafine

amorphous boron powder with a purity of 94.6% and a size of 0.36 μm was obtained when w(B_2O_3)/w(Mg) was 3.0. After acid leaching, the predominant impurities found in the products were acid-insoluble substances, such as MgB_x, B_xO, Mg_2SiO_4, FeB_x and $xMgO{\cdot}B_2O_3$. Kim *et al*. [8] also used this route to synthesise fine amorphous boron powder with a mean particle size of ~350 nm and a purity of 95.0%. The leached product still contained some magnesium boride. Wang *et al*. [10] prepared nanosized amorphous boron powders through an active-dilution SHS method using Mg, B_2O_3 and KBH_4 as the raw materials. Without the KBH_4 diluent, the sample showed a random structure, non-uniform particle sizes in the range of 0.2-3.0 μm and a purity of 87.33% (Figure 2.14(a)). When KBH_4 was increased to 30%, the boron powders showed a smaller particle size of 50 nm and a higher purity of 95.64% (Figure 2.14(b)).

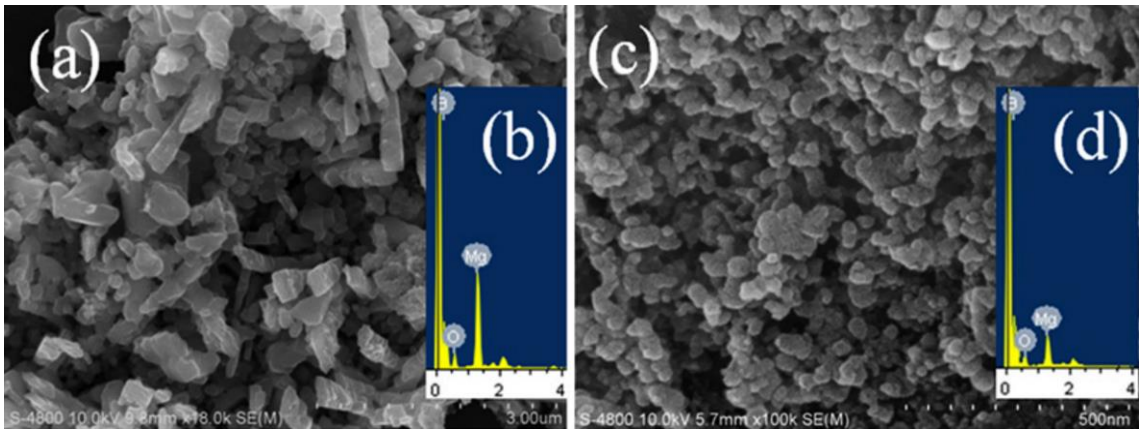

Figure 2.14 SEM images and EDS of amorphous boron powders prepared through the active-dilution SHS method from (a, b) Mg/B_2O_3 and (c, d) Mg/B_2O_3 + 30% KBH_4 [10].

Ou *et al*. [12] prepared amorphous boron powders from B_2O_3/Mg/kNaCl (k is the number of moles of NaCl) using a salt-assisted SHS technique. When the NaCl content was increased from 10 wt% to 50 wt%, the average particle size of the resulting boron powders decreased from 2.07 μm to 0.69 μm (Figure 2.15(a)), and the purity was greater than 96%. The selected area electron diffraction (SAED) pattern of the leached product revealed that the prepared boron powder

was amorphous (Figure 2.15(b)).

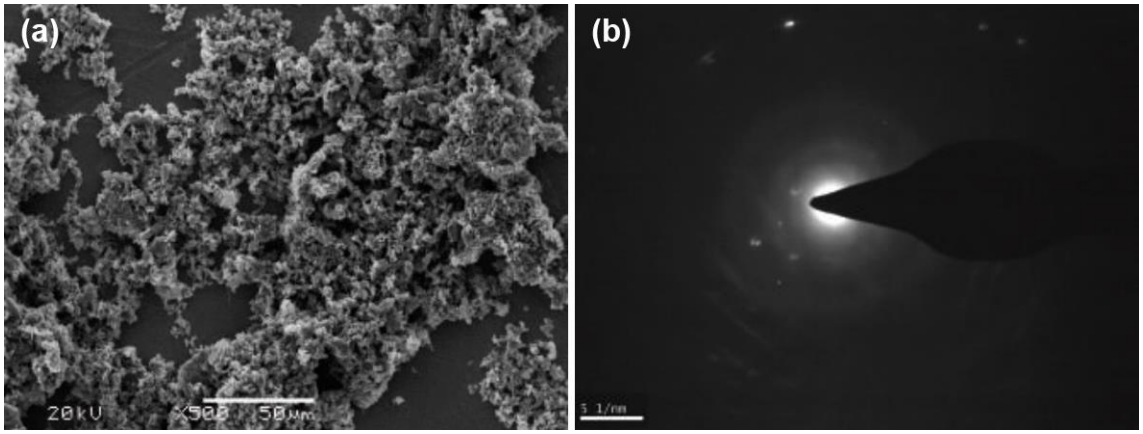

Figure 2.15 (a) SEM image and (b) SAED of boron powders obtained from B_2O_3/Mg + 50 wt%NaCl by salt-assisted SHS synthesis [12].

Yoo *et al*. [11] also prepared amorphous boron nanoparticles by heating a B_2O_3/Mg/kNaCl exothermic mixture at 800°C under an argon flow. They found that the particle size of the acid-leached boron particles ranged from 30 nm to 300 nm when the k values were adjusted from 1 to 5. However, several issues related to the synthesis process and boron purity remain unresolved. The first issue is the energy consumption associated with preheating the initial mixture to begin the combustion process. The second is the relatively large oxygen content in the final boron nanoparticle, which negatively affects the volumetric energy content and combustion efficiency. For these reasons, Nersisyan *et al*. [13] researched a self-sustaining combustion process from an initial mixture of B_2O_3+αMg ($0.8 \leq \alpha \leq 2.0$ mol). Using B_2O_3+1.2Mg resulted in the formation of $Mg_2B_2O_5$ in the product material (Figure 2.16(a)). After acid leaching, the purity of the boron powder was approximately 95% (Figure 2.16(b)).

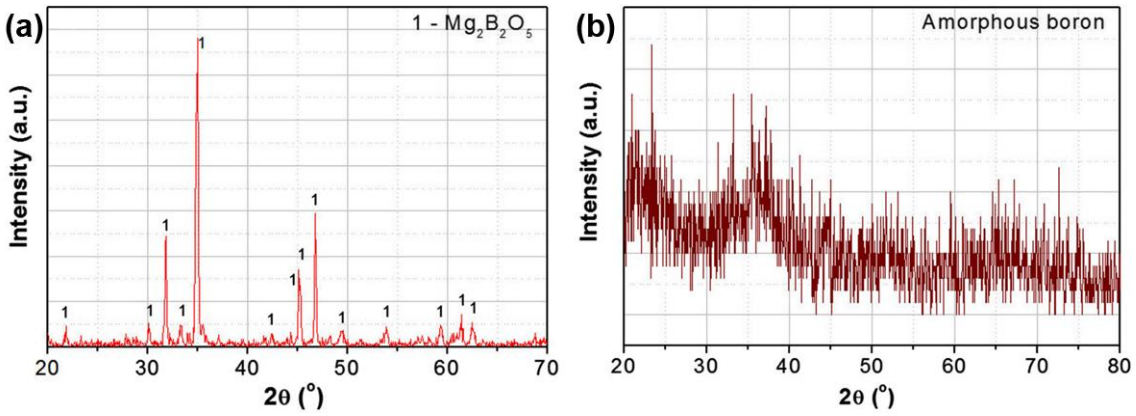

Figure 2.16 XRD patterns of the (a) combustion-derived sample from B_2O_3+1.2Mg and (b) acid-leached boron powder [13].

2.3.3 Mechanochemical synthesis

In addition to the SHS method, mechanochemical synthesis is an alternative technique for the preparation of boron powders with high purity and small particle sizes. This process subjects a mixture of a reducible boron compound (B_2O_3, H_3BO, HBO_2, $NaBO_3$-$4H_2O$ or $Na_2B_4O_7$) and a reducing agent (Al, Mg or Ca) to mechanical activation, whereby the boron compound is reduced to elemental boron by the reducing agent [16]. Mechanochemical synthesis was also attempted using B_2O_3+3Ca, B_2O_3+3Mg and B_2O_3+3Al powder mixtures [17]. The formation of the elemental boron, CaO and $Ca_3(BO_3)_2$ phases was accomplished after 1 h of milling, whereas the elemental boron, MgO and $Mg_3(BO_3)_2$ phases were obtained after 6 h of milling. The reduction of B_2O_3 with Al was not successful after up to 6 h of milling. Seifolazadeh and Mohammadi [15] introduced a low-cost method for the preparation of nanoboron powders with a purity of approximately 91 wt% B (~32 nm) *via* a two-stage process that involves (a) a mechanochemical reaction of an exothermic mixture consisting of B_2O_3 and Mg powders and (b) the extraction of boron powders from the final milled product by leaching with hydrochloric acid (28 wt%, at 60-70°C for 4 h) and washing (deionised water, at 100°C for 4 h). Dou and co-workers [219]

developed a new method that combined high-energy ball milling and combustion synthesis to prepare amorphous boron powder from a B_2O_3/Mg/$KClO_3$ precursor mixture. The purity of the amorphous boron powder was 94.8%, and the particle sizes were less than 100 nm. They concluded that the high-energy ball milling pretreatment was effective in obtaining nanometre and smaller particle sizes. Nevertheless, the addition of $KClO_3$ can disturb the efficient performance of the reactants and purity of the products. Masih and Maisam [14] presented an efficient route for the combustion mechanosynthesis of amorphous boron from B_2O_3/Mg in a short time without the use of dilutent materials.

2.3.4 Molten salt electrolysis

The production of elemental boron by electrolysis has been investigated for nearly a century. The molten salt system must be capable of dissolving a boron precursor at an adequate concentration and must provide suitable fluidity and electrical conductivity. However, satisfying these requirements cannot guarantee the high purity of the produced boron or cathode adhesion. Commonly used molten salt systems are molten chlorides, molten fluorides, and mixed molten chloride-fluorides. In addition, B_2O_3 and KBF_4 are widely used as boron precursors to produce elemental boron.

Cooper [220] reported the electrolysis of B_2O_3 in the molten salts of KCl-KBF_4. In this melt system, KBF_4 acted as an electrically conductive inert vehicle, whereas B_2O_3 was the main material that was consumed in the process. The purity of the deposited boron was ~98.68%. Nies [221] indicated that the optimal electrochemical production of elemental boron occurred in KCl-KF-B_2O_3 mixtures. The electrolysis was conducted at 850°C, and the highest product purity obtained was 97.5%. Using B_2O_3 as the boron precursor instead of KBF_4

could prevent KBF_4 decomposition at high temperatures, thereby reducing the corrosion of the container and product. Yukin [189] reported the formation of elemental boron by electrolysing $Na_2B_4O_7$. The electrolysis produced Na, which reacted with $B_4O_7^{2-}$ to produce elemental boron. Nair *et al*. [222] developed two different electrolytic methods to obtain elemental boron with satisfactory purity. The first process involved electrowinning from a KCl-KF-KBF_4/B_2O_3 electrolyte at 775°C, which resulted in less than 96% pure B. In the second process, boron was electroextracted from the soluble B_4C anode in a NaCl-KCl-KBF_4 bath at the same temperature, yielding 99.8% pure B. The latter was found to be more efficient from the viewpoint of product purity and energy consumption. Taylor and Gomez [195] invented an approach for recovering elemental boron in which a molten boron-containing electrolyte (at least one alkaline earth fluoride salt and two alkali earth fluoride salts) was electrolysed to recover the elemental boron. The recovered boron was at least 50% pure.

Electrolysis equipment represents a substantial technical obstacle. Moreover, removing carbon impurities (primarily resulting from the corrosion of the graphite crucible) from the deposited boron and producing electrolytic boron continuously are challenging. The current efficiency is also a crucial metric for electrolysis because it affects the output and powder consumption of the elemental boron [12].

2.4 Synthesis of Al_2O_3-TiB_2 composite powders

In most cases, Al_2O_3-TiB_2 composites were prepared by simply mixing commercial TiB_2 and Al_2O_3 powders in a ball mill and subsequent high-temperature sintering [23, 24, 26-29, 223, 224]. Unfortunately, such composites often exhibited poor characteristics arising from an inadequate

dispersion process and inhomogeneous distribution of TiB_2 in Al_2O_3. Thus, it is necessary to improve the processing route to prepare composites with a better distribution of components. A preferable alternative is the *in situ* formation of the second phase to obtain optimum properties [225]. For this reason, simultaneous synthesis (*via* SHS reactions of compacted powder mixtures of Al, TiO_2 or Ti, and B_2O_3, B, or H_3BO_3) and densification were developed to fabricate Al_2O_3-TiB_2 composites [30, 226-236]. To improve the economic perspective, Ti and B were substituted with inexpensive TiO_2 and B_2O_3 precursors [31]. Therefore, the Al-TiO_2-B_2O_3 reaction system has been highlighted. Thermodynamic evaluations indicate that the reaction of TiO_2, B_2O_3 and Al (Reaction (2.15)) is highly exothermic and should be self-sustainable [32]. Nevertheless, the composites so prepared had porous structures due to very little diffusion and sintering involved during SHS reactions [227]. In addition, the control over composition and phase was challenging. Apart from Al_2O_3 and TiB_2, impurity phases such as TiO_2, Al_3Ti, and/or Al_5BO_9 were found in the bulk composites.

Many techniques/methodologies were investigated to synthesise Al_2O_3-TiB_2 composite powders, including mechanochemical synthesis [31-35], SHS [36-38] or mechanically activated combustion synthesis [39, 40], and milling-assisted sol-gel method [41]. However, these techniques often required a long processing time, and the resulting powders often exhibited heavy agglomeration and/or a relatively large particle size.

Yu and Yang [36] prepared Al_2O_3-TiB_2 composite powders with a mean particle size of 2-4 μm by the SHS method with a reductive process from the Al-TiO_2-B_2O_3 system. Montakhab and Hadian [38] produced Al_2O_3-TiB_2 composite powders by the SHS method from the TiO_2-H_3BO_3-Al system and

investigated the effects of different Al content on the reaction progress. The authors found that the highest conversion ratio was obtained from the sample containing a 1.2 stoichiometric amount of Al. Sharifi *et al*. [31] synthesised Al_2O_3-TiB_2 nanocomposite powders *via* the mechanochemical reaction of Al-TiO_2-B_2O_3. The authors reported that ball milling a mixture of Al, TiO_2 and B_2O_3 powders for up to 50 h led to no phase change, whereas 60 h of milling resulted in a combustion reaction that formed an Al_2O_3 matrix composite containing TiB_2 particulates. The ball-to-powder ratio (BPR) and rotational speed (RS) of the vials were 10:1 and 500 rpm, respectively. In another study [32], an Al_2O_3-TiB_2 nanocomposite was synthesised from an Al, TiO_2 and H_3BO_3 mixture, and the products were formed after 1.5 h of milling time due to the high energy of the milling media (BRP = 20:1 and RS = 600 rpm). Based on these two studies, Abdellahi *et al*. [34] investigated the influence of boron source materials (i.e., B_2O_3 and H_3BO_3) on the synthesis of Al_2O_3-TiB_2 nanocomposite powders *via* mechanochemical synthesis under the same conditions (BRP = 10:1 and RS = 250 rpm). The results showed that complete formation of the product was achieved after 15 h of milling time for the Al-TiO_2-B_2O_3 system, whereas 30 h were required for the Al-TiO_2-H_3BO_3 system. The authors stated that additional milling energy was required for the composite formation in the Al-TiO_2-H_3BO_3 system because of the lubricant properties of H_3BO_3 and its decomposition into HBO_2 and B_2O_3 during milling. Sharifi *et al.* [33] also produced Al_2O_3-TiB_2 nanocomposite powders by high-energy ball milling of a mixture of Al, B_2O_3 and Ti powders. In this study, the composite powders were formed after 32 h of milling at 500 rpm (BRP = 10:1). Sayagués *et al*. [40] synthesised Al_2O_3-TiB_2 nanocomposite powders by high-energy ball milling of a mixture of TiO_2, HBO_2 and Al powders. The ignition of the combustion reaction occurred after a short

milling time (15-30 min), which mitigated contamination problems. However, the synthesised Al_2O_3-TiB_2 nanocomposite powders exhibited a high affinity for agglomeration. Thus, distinguishing between the Al_2O_3 and TiB_2 phases in the images (Figure 2.17) was almost impossible. Yang *et al.* [35] explored the effect of adding Ni on the preparation of Al_2O_3-TiB_2 nanocomposite powders *via* a mechanochemical method from starting powders containing Al, TiO_2 and B_2O_3 (BRP = 10:1 and RS = 500 rpm). The results showed that an intermediate product, NiAl, was formed by a gradual exothermic reduction and that the presence of the ductile Ni phase and brittle NiAl phase facilitated the mechanochemical reaction among Al, TiO_2 and B_2O_3.

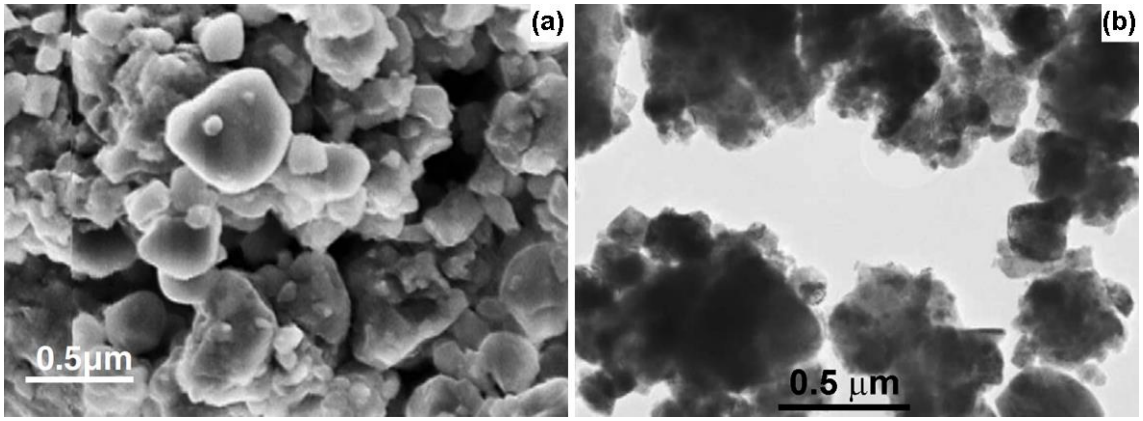

Figure 2.17 SEM (a) and TEM (b) images of the Al_2O_3-TiB_2 composite powders synthesised using a mechanochemical method starting from a mixture of TiO_2, HBO_2 and Al powders [40].

In the past few decades, the sol-gel technique has been utilised to synthesise ceramic composite powders successfully. Sol-gel approaches have been found to provide extensive composite homogeneity and dispersion, which improve both the physical and mechanical properties of the products [237]. Rabiezadeh *et al*. [41] proposed an approach to combine the sol-gel process and mechanochemical route to prepare Al_2O_3-TiB_2 nanocomposite powders. In this study, a gel derived from titanium isopropoxide (TTIP) and B_2O_3 was used and was followed by a mechanochemical reduction in the presence of Al powder.

The reaction between dried gel and Al occurred after 30 h of milling at 300 rpm, and the milled product had a wide range of particle sizes between 100 nm and 2 μm. The milled product was found to contain amorphous phases, requiring high-temperature calcination, which can generate agglomerates that may coarsen the microstructure (Figure 2.18).

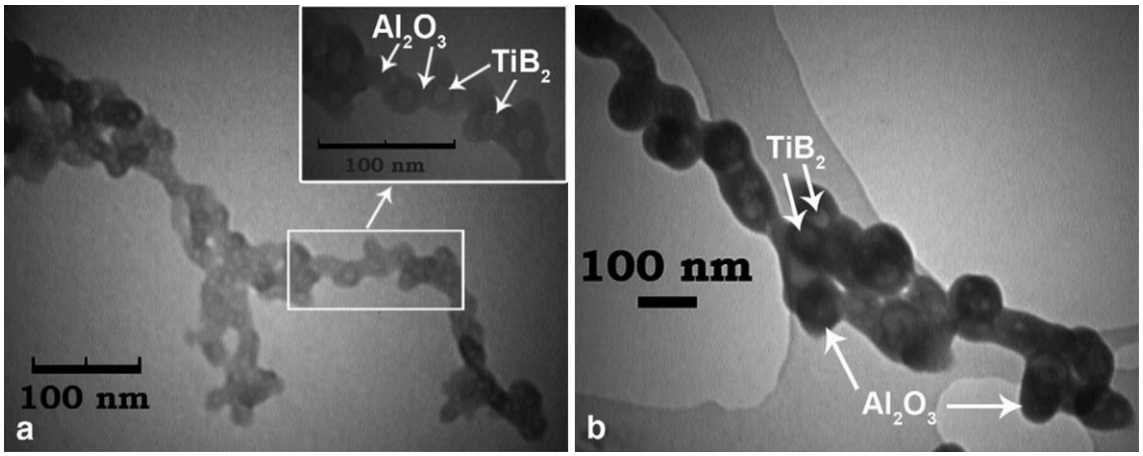

Figure 2.18 TEM images of the (a) dried gel/Al powder mixture milled for 30 h and (b) heat treated at 950°C for 1 h [41].

2.5 MSS technique

Salt was used in combustion synthesis as a diluent that effectively absorbs the reaction heat through melting and evaporation over a long period [137-139]. The amount of salt used in this route is small, typically a few percent of the total weight. By contrast, in the MSS technique, a large amount of salt is introduced into a reactant mixture and forms a melt when heated above the melting point of the salt. Molten salt behaves as a reaction medium, i.e., a pool of ionised cations and anions. Compared with solid-state reactions, the rates of which are usually seriously limited by the slow diffusion of the reactants, the MSS technique lowers the reaction temperature because it allows faster mass transport in the liquid phase *via* convection and diffusion. In addition, the MSS technique has several advantages, such as low temperature, high chemical and phase purity, excellent

control of particle morphology, low aggregation levels and narrow crystallite size distribution in the products, minimal energy consumption, low-cost and large-scale production.

2.5.1 Molten salt properties

Salt used for MSS must meet certain requirements, such as stability, availability (or abundant supply), cost efficiency and water solubility. In addition, a low melting point is desirable, depending on the chemical characteristics. The useful molten salt systems can be roughly categorised into inert systems (e.g., metal chlorides) and reactive systems (e.g. oxides). To obtain a lower melting point, mixtures of two or more salts are used, which can provide a wider operating temperature range. Other requirements are that they have a low vapour pressure at the heating temperatures and do not cause undesirable reactions with either the reactants or products [238].

Molten salt properties have great effects on the MSS process, especially the salt viscosity and solubility of reactants in the respective salts. On the one hand, salts with low viscosity at the reaction temperature are favoured to promote the diffusion rate of the reactant species in the melt. A lower viscosity of the reaction medium results in a more rapid species transport. On the other hand, the solubility determines how much precursor the salt melts can accommodate, thus controlling the rate of reaction. A higher solubility of the reactant in the molten salt leads to a quicker formation of the product phase [239-241].

2.5.2 Reaction mechanisms

Depending on the solubility values of the reactants in the molten salt, two mechanisms, “dissolution-precipitation” and “template-growth”, generally function in an MSS process. In the first case, the reactants dissolve in the salt

melt, followed by formation of the product in the salt melt and finally the precipitation of the product above its solubility limit. In the second case, the more soluble reactant dissolves in the salt melt, diffuses onto the surface of the insoluble or less soluble reactant, and then reacts to form the product, which retains the morphology/size of the insoluble or less soluble reactant [239].

2.5.2.1 Template-growth mechanism

The MSS template mechanism involves: (1) reactant dissolution, (2) reactant transport through the melt, (3) nucleation of the product, and (4) growth of the product on existing nuclei [242]. For example, Jayaseelan *et al.* [240] synthesised $MgAl_2O_4$ (MA) platelets by reacting MgO and α-Al_2O_3 platelets in a K_2SO_4 salt. Figure 2.19 shows the SEM images of the as-received α-Al_2O_3 platelets and MA platelets obtained by MSS in molten K_2SO_4. The MA platelets retained the typical hexagonal plate morphology, indicating that MgO is the fast dissolving component of the constituent oxides in molten K_2SO_4 and that the formation of MA initiates on the Al_2O_3 platelet surfaces, i.e., the "template-growth" mechanism has dominated the MSS process.

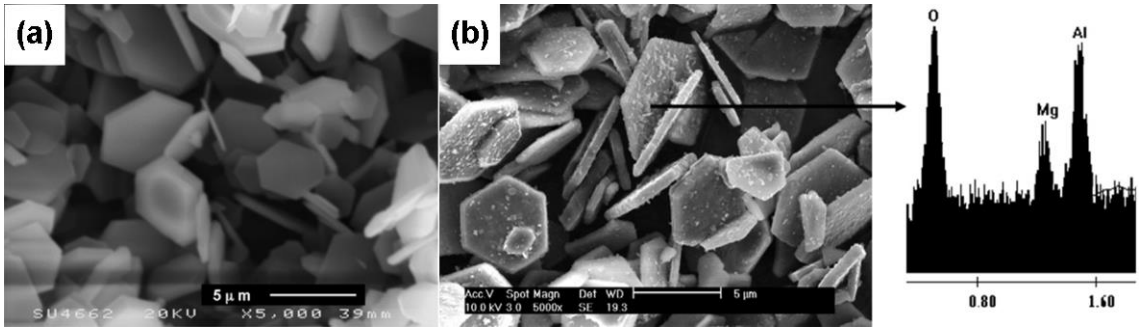

Figure 2.19 SEM images of the (a) as-received α-Al_2O_3 platelets and (b) MA platelets synthesised by heating MgO and Al_2O_3 at 1150°C for 3 h in K_2SO_4 [240].

Another example is the preparation of SiC nanorods by reacting multi-walled carbon nanotubes (MWCNTs) with Si particles in a NaCl-NaF binary salt [243]. The morphologies of the resultant SiC nanorods mostly corresponded to those of

as-received CNTs (Figure 2.20), indicating that the CNTs not only served as the carbon source but also acted as the templates for the nanorod growth.

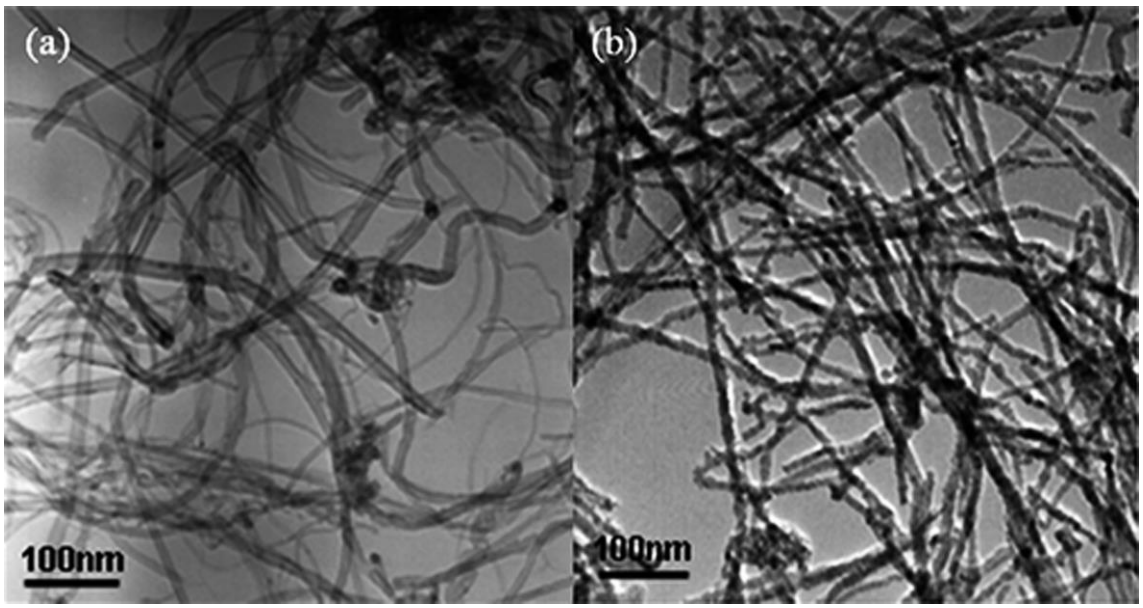

Figure 2.20 TEM images of (a) as-received CNTs and (b) the resultant SiC nanorods from heating CNTs and Si particles for 4 h at 1200°C in NaCl-NaF [243].

2.5.2.2 Dissolution-precipitation mechanism

A typical example of the “dissolution-precipitation” mechanism is the synthesis of $LaAlO_3$ powder by reacting La_2O_3 and Al_2O_3 in a molten KF-KCl eutectic salt [244]. Figure 2.21 shows SEM images of the as-received raw La_2O_3 and Al_2O_3 powders and $LaAlO_3$ particles synthesised at 630°C for 3 h in KF-KCl. Although spheroidal La_2O_3 and Al_2O_3 starting powders were used, the synthesised $LaAlO_3$ particles showed well-crystallised euhedral shapes, indicating that the “dissolution-reaction-precipitation” mechanism is dominant in this case. Both La_2O_3 and Al_2O_3 are reported to be soluble in molten potassium fluoride/chloride salts. The whole MSS process can be described as follows: La_2O_3 and Al_2O_3 dissolved in the molten salt are mixed homogeneously at the atomic level, and diffusion in the molten salt is more rapid than that in the solid state. Consequently, the dissolved La_2O_3 and Al_2O_3 react rapidly to form $LaAlO_3$ in the molten salt. Once the molten salt is oversaturated with $LaAlO_3$, $LaAlO_3$ crystals

start to precipitate from the salt. The precipitation of $LaAlO_3$ from the oversaturated salt leads to further dissolution and reaction between La_2O_3 and Al_2O_3, and then more $LaAlO_3$ precipitates. This cycle is repeated until all of the starting La_2O_3 and Al_2O_3 are consumed to form $LaAlO_3$.

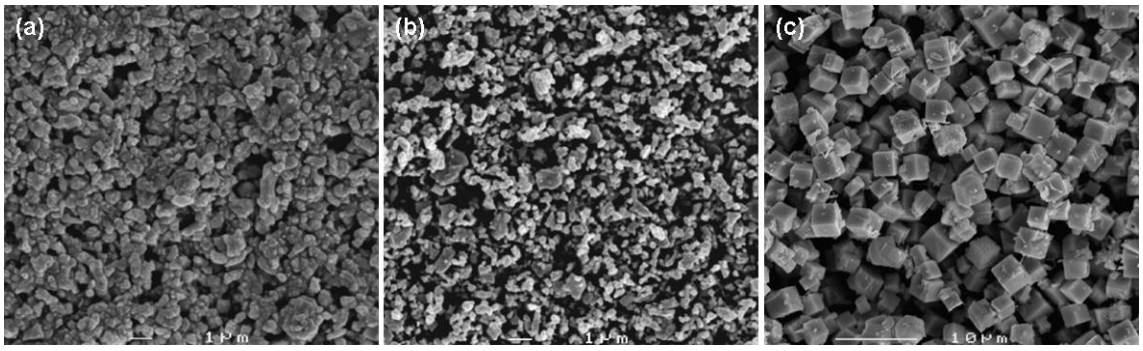

Figure 2.21 SEM images of the as-received raw (a) La_2O_3 and Al_2O_3 powders and (c) $LaAlO_3$ particles synthesised for 3 h at 630°C in KF-KCl [244].

2.5.3 MSS of metal boride powders

Recently, the MSS technique has been applied to synthesise metal boride materials. Portehault *et al.* [245] prepared several metal boride nanocrystals by the reaction of the corresponding metal chlorides and $NaBH_4$ in a eutectic LiCl/KCl melt (argon flow, at 700-900°C for 4 h). Using this synthesis process, nanocrystals of NbB_2 and CaB_6 as examples were obtained under a temperature of 800-900°C (Figure 2.22). However, expensive and hazardous $NaBH_4$ was used as the boron source and reducing agent in this process. NbB_2 and CrB_2 powders were successfully synthesised by the borothermal reduction of metal oxides in NaCl/KCl salt at 800-1000°C [246, 247]. However, expensive amorphous boron powders were used in these processes.

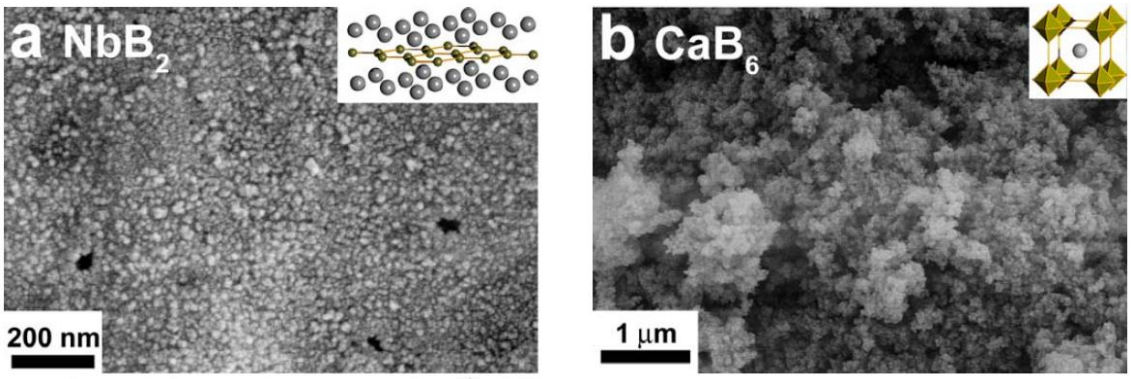

Figure 2.22 SEM images of boride powders obtained after heat treatment for 4 h of (a) $NbCl_5$:$NaBH_4$ = 1:8 at 900°C and (b) $CaCl_2$:$NaBH_4$ = 1:12 at 800°C in LiCl/KCl [245].

Zhang *et al*. [248] synthesised submicron ZrB_2 powder *via* a molten-salt-mediated reduction route using ZrO_2, $Na_2B_4O_7$ and Mg powders as the starting raw materials. SEM images (Figure 2.23) revealed that the resultant ZrB_2 particles appeared similar to the original ZrO_2 particles in terms of shapes and sizes (300-400 nm).

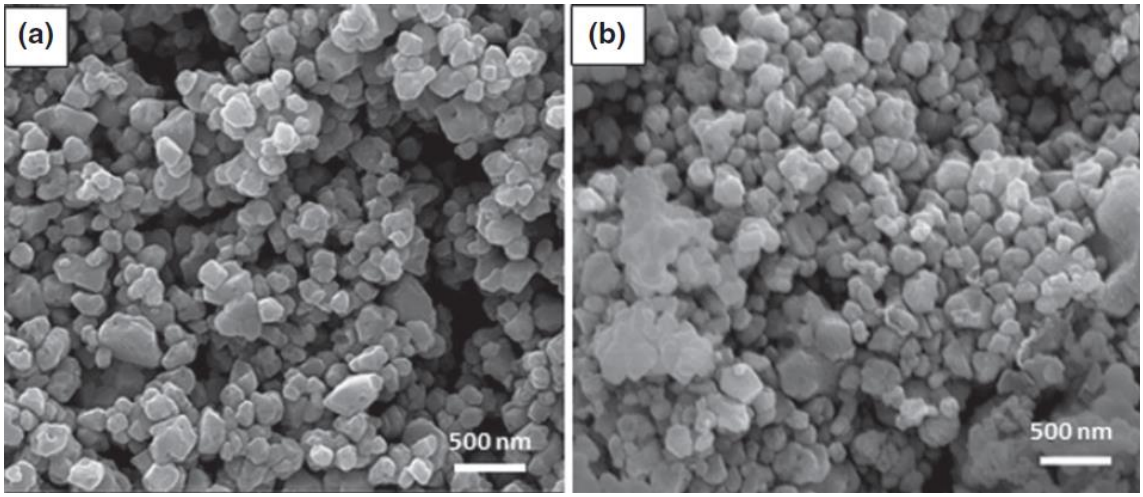

Figure 2.23 SEM images of the (a) starting ZrO_2 powder and (b) ZrB_2 particles resultant from firing ZrO_2-$Na_2B_4O_7$-Mg at 1200°C for 3 h in $MgCl_2$ [248].

2.5.4 Summary

In this chapter, the crystal chemistry, properties, applications, and synthesis methods of boron-based materials, including boron, TiB_2, HfB_2, LaB_6, CaB_6 and Al_2O_3-TiB_2 nanocomposites, have been thoroughly reviewed. Metal borides are known to have a particular combination of properties because of their special

crystal structure, atomic bonding, and microstructure formed during sintering. These features result in metal borides with high melting temperatures, high hardness and elastic modulus, chemical inertness and excellent thermal/electrical characteristics. The choice of methods for synthesis can be made based on a balance of cost with the properties of the resulting powders with the most important properties being initial particle size, particle size distribution, agglomeration and purity. In the future, continued research into synthesis methods will be driven by the need for materials that exhibit improved performance in extreme environments, higher purity for improved properties, or smaller particle size for enhanced densification and control of final microstructure.

In this thesis, the molten-salt-mediated magnesiothermic reduction technique developed previously for synthesis of ZrB_2 powder was further extended and modified, aiming to provide an alternative approach to low-temperature synthesis of high-quality boron-based fine powders from cost-effective oxide-based precursors.

Chapter 3 Experimental Procedures and Characterisation Techniques

3.1 Raw materials

The raw materials included B_2O_3, $Na_2B_4O_7$, TiO_2, HfO_2, La_2O_3, CaO, and Mg powders from Sigma-Aldrich (Gillingham, UK), Al powder from Alfa Aesar (Lancashire, UK), and polyacrylonitrile (PAN)-based carbon fibres (CFs) from Toho Tenax Europe (Wuppertal, Germany). Their basic properties are listed in Table 3.1.

Table 3.1 List of raw materials and their basic properties

Raw materials	Product No.	Purity (%)	Size	Melting/Boiling point (°C)
B_2O_3	221740	99.98	-	450/1860
$Na_2B_4O_7$	221732	99	-	741/1575
TiO_2 I	637254	99.7	<25 nm	1825/2972
TiO_2 II (nanowires)	774529	-	L ~10 μm × ø 10 nm	>350/2972
TiO_2 III	248576	≥99	~ 300 nm	1825/2972
HfO_2	202118	98	-	2758/5400
La_2O_3	L4000	>99.9	-	2305/4200
CaO	208159	99.9	-	2614/2850
Mg	13112	≥99	~250 μm	648/1090
Al	11067	99.5	~44 μm	660/2470
PAN-based CFs	-	-	L 2 cm × ø ~7, 8 μm	~3652/4200

The salts used (Table 3.2) were NaCl, KCl and anhydrous $MgCl_2$ from Sigma-Aldrich (Gillingham, UK) and $CaCl_2$ from Fisher Scientific (Loughborough,

UK). In addition, the solvents used in the experiment included ethanol absolute (99.8%), HCl (0.3-1 M) and H_2SO_4 (0.5 M) from Fisher Scientific (Loughborough, UK) and $AgNO_3$ (0.1 M) from Sigma-Aldrich (Gillingham, UK).

Table 3.2 List of salts and some of their properties [249, 250]

Salt	Product No.	Purity (%)	Melting/Boiling point (°C)	Viscosity (~850°C)
NaCl	S9888	≥99	801/1413	1.22
KCl	P9541	≥99	770/1420	0.94
$MgCl_2$	M8266	≥98	714/1412	1.63
$CaCl_2$	12664987	≥96	782/>1600	2.31

3.2 Preparation of samples

Figure 3.1 illustrates the flowchart of the MSS procedures. The experimental details are provided below.

3.2.1 TiB_2 powder

TiO_2 (TiO_2 I, TiO_2 II, and TiO_2 III), B_2O_3 and Mg powders were used as the starting materials, and KCl, NaCl and anhydrous $MgCl_2$ were used to form a molten salt medium. TiO_2 (0.01 mol/~0.8 g) and B_2O_3 (0.01 mol/~0.7 g) were mixed with Mg in stoichiometric (corresponding to Reaction (3.1), i.e., 0.05 mol/~1.22 g) or nonstoichiometric ratios (with 5-20 mol% more Mg) using a mortar and pestle (250 ml), and further combined with 15 g of NaCl, KCl, or $MgCl_2$. The resultant powder mixture was added to an alumina crucible (L82 mm × W40 mm × H24 mm) covered with a lid, heated in an argon-protected alumina tube furnace (I/D 60 mm) at 3°C/min to a given temperature between 750 and 1000°C and then held for 4 h before cooling the furnace to room temperature.

$$TiO_2 + B_2O_3 + 5Mg = TiB_2 + 5MgO \quad (3.1)$$

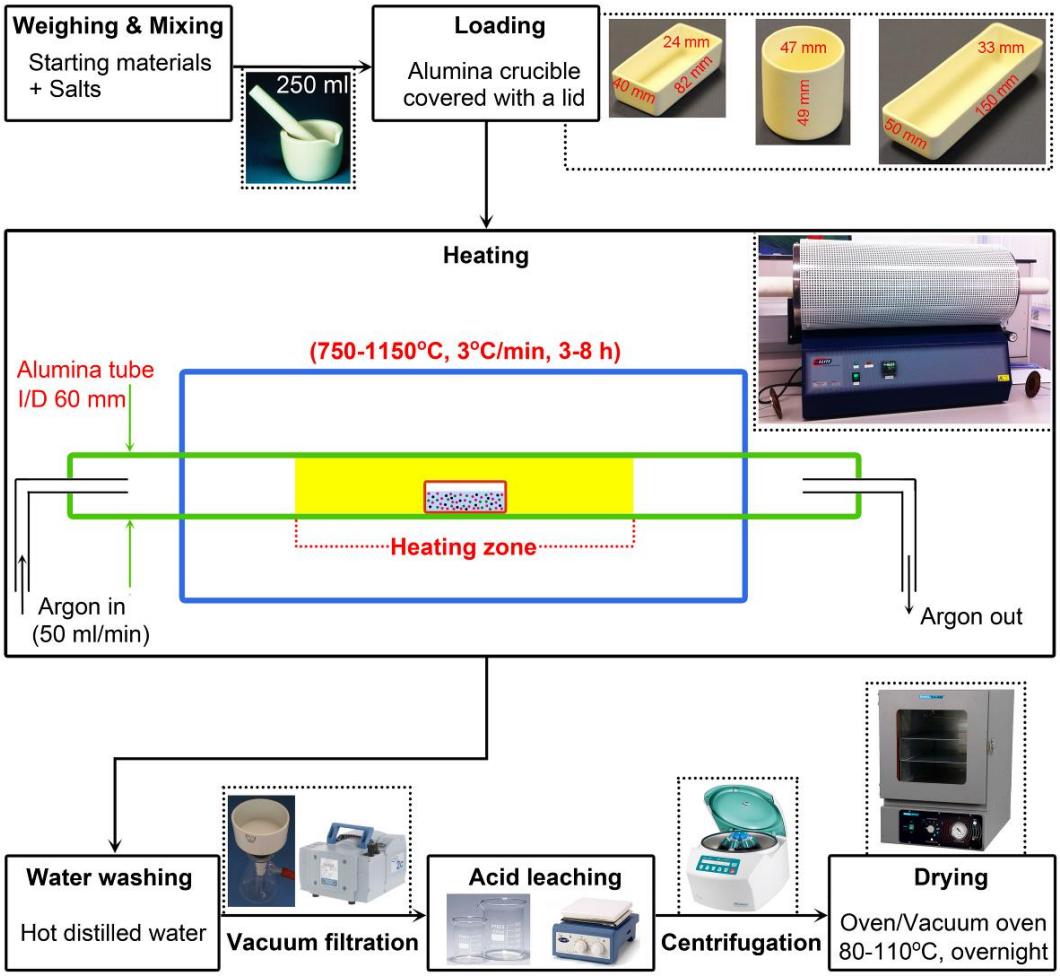

Figure 3.1 Flowchart of the MSS procedures.

3.2.2 HfB_2 powder

HfO_2 (0.005 mol/~1.05 g), B_2O_3 (0.005 mol/~0.35 g) and Mg (0.025 mol/~0.61 g) in stoichiometric (corresponding to the overall reaction, Reaction (3.2)) or nonstoichiometric ratios (with excessive amounts of Mg and B_2O_3) were mixed and further combined with a 1-5 times the weight of NaCl, KCl or $MgCl_2$ using a mortar and pestle. The resultant batch powder was placed in a lid-covered alumina crucible (L82 mm × W40 mm × H24 mm) and heated at a rate of 3°C/min until a target temperature between 750 and 1000°C under an Ar atmosphere in an alumina tube (I/D 60 mm) furnace. The temperature was maintained for 4-8 h, and then the furnace was cooled to room temperature.

$$HfO_2 + B_2O_3 + 5Mg = HfB_2 + 5MgO \qquad (3.2)$$

3.2.3 B_4C, TiC and HfC coatings on the carbon fibres

To better understand the formation mechanism, samples of B_4C-, TiC- and HfC-coated CFs were prepared in molten $MgCl_2$. Powders and CFs were mixed in a mortar with a pestle and further combined with 15 g of $MgCl_2$ at the following ratios: (1) 0.07 g of B_2O_3, 0.97 g of Mg and 0.06 g of CFs (corresponding to Reaction (3.3)) [251]; (2) 0.8 g of TiO_2 III, 0.73 g of Mg and 0.12 g of CFs (corresponding to Reaction (3.4)) [252]; and (3) 1.05 g of HfO_2, 1.22 g of Mg and 0.24 g of CFs (corresponding to Reaction (3.5)).

$$2B_2O_3 + 6Mg + C = B_4C + 6MgO \quad (3.3)$$

$$TiO_2 + 2Mg + C = TiC + 2MgO \quad (3.4)$$

$$HfO_2 + 2Mg + C = HfC + 2MgO \quad (3.5)$$

The resultant mixture was loaded into a lid-topped alumina crucible (L 49 mm × Ø 47 mm), heated in an argon-protected alumina tube furnace at 3°C/min until 1000-1100°C (the mixture of B_2O_3, Mg, CFs and $MgCl_2$ was heated to 1100°C because of the higher reaction temperature needed for B_4C formation) and then held for 4 h before cooling the furnace to room temperature.

3.2.4 LaB_6 powder

La_2O_3 (0.002 mol/~0.65 g) and B_2O_3 (0.012 mol/~0.84 g) were mixed with stoichiometric (corresponding to Reaction (3.6), i.e., 0.042 mol/~1.02 g) or nonstoichiometric (with 10-20 mol% excessive Mg) Mg using a mortar and pestle and further combined with 15 g of KCl, NaCl, or $MgCl_2$. Each resultant powder mixture was placed in a covered alumina crucible (L82 mm × W40 mm × H24 mm), heated in an argon-protected alumina tube (I/D 60 mm) furnace at 3°C/min to a temperature between 800 and 1000°C and then held at this temperature for 4-5 h before cooling the furnace to room temperature.

$$La_2O_3 + 6B_2O_3 + 21Mg = 2LaB_6 + 21MgO \quad (3.6)$$

3.2.5 CaB_6 powder

CaO (0.003 mol/~0.17 g) and B_2O_3 (0.009 mol/~0.63 g) were pre-mixed with the stoichiometric (corresponding to the overall Reaction (3.7), i.e., 0.03 mol/~0.73 g) or nonstoichiometric amounts (10-20 mol% extra) of Mg, in a mortar and pestle, before being further combined with 15 g of KCl, NaCl, $MgCl_2$ or $CaCl_2$. Each resultant powder mixture was placed in a covered alumina crucible (L82 mm × W40 mm × H24 mm) that was heated in an alumina tube (I/D 60 mm) furnace in flowing argon (50 ml/min) at 3°C/min to a target temperature between 800 and 1000°C and held for 4-8 h before furnace-cooling to room temperature.

$$CaO + 3B_2O_3 + 10Mg = CaB_6 + 10\ MgO \quad (3.7)$$

3.2.6 Amorphous boron powder

B_2O_3 (0.015 mol/~1.04 g) was mixed with Mg in stoichiometric (corresponding to Reaction (3.8), 0.045 mol/~1.09 g) or nonstoichiometric ratios (with 10-20 mol% excessive Mg) using a mortar and pestle (250 ml), and further combined with 1-5 times the weight of NaCl, KCl or $MgCl_2$. $Na_2B_4O_7$ (0.005 mol/~1.01 g) was mixed with stoichiometric Mg (corresponding to Reaction (3.9)) and then combined with 5 times the weight of $MgCl_2$. The resultant powder mixture was placed in an alumina crucible (L 82 mm × W 40 mm × H 24 mm), topped with a lid and placed in an alumina tube (I/D 60 mm) furnace. The furnace was heated up to 800-1150°C in flowing argon at a 3°C/min rate and held at the target temperature for 6 h (the $Na_2B_4O_7$ sample was subjected to only 6 h heating at 850°C). The furnace was allowed to cool to room temperature.

$$B_2O_3 + 3Mg = 2B + 3MgO \quad (3.8)$$

$$Na_2B_4O_7 + 6Mg = 4B + Na_2O + 6MgO \quad (3.9)$$

3.2.7 Al_2O_3-TiB_2 nanocomposite powder

TiO_2 III (0.72 g) was mixed with B_2O_3 and Al in stoichiometric (corresponding to Reaction (3.10), i.e., 0.63 g of B_2O_3 and 0.81 g of Al) or nonstoichiometric ratios (with 10-30 wt% excessive B_2O_3 and 10-30 wt% excessive Al) using a mortar and pestle and further combined with NaCl, KCl or $MgCl_2$ in a 1:5 weight ratio. The resultant powder mixture was added to an alumina crucible (L82 mm × W40 mm × H24 mm) covered with a lid, heated in an argon-protected alumina tube (I/D 60 mm) furnace at 3°C/min to a target temperature between 850 and 1150°C and held for 4-5 h before cooling the furnace to room temperature.

$$3TiO_2 + 3B_2O_3 + 10Al = 3TiB_2 + 5Al_2O_3 \quad (3.10)$$

3.2.8 Water washing and acid leaching

The reacted mass was washed with hot distilled water, followed by filtration to remove the salts. The process could be repeated several times. The resulting powders were oven-dried overnight at 80°C prior to further characterisation. Furthermore, the dried product powders were subjected to acid leaching for 2 h using a 0.3-1 M HCl solution to remove the MgO byproduct and/or with 0.5 M H_2SO_4 for 2-6 h at 70-90°C to eliminate any residual $Mg_3B_2O_6$ (Reaction (3.11)) [253]. The remaining product powder was collected *via* centrifugation and further rinsed with deionised water several times (until no Cl^- was detected by $AgNO_3$ in the centrifugal liquid) before oven-drying (the amorphous boron product powders were dried in a vacuum oven) overnight at 80°C.

$$Mg_3B_2O_6 + 3H_2SO_4 = 3MgSO_4 + 2H_3BO_3 \quad (3.11)$$

3.3 Characterisation techniques

3.3.1 XRD

XRD is a non-destructive technique primarily used for phase identification of a

crystalline material. Atoms in a crystalline material are situated in a repeating or periodic array over large atomic distances, i.e., long-range order exists. X-rays are electromagnetic waves with a much shorter wavelength than visible light, typically on the order of 0.1 nm (1 Å), i.e., the same order as the interatomic distances in a crystalline lattice, thus, X-ray scattering can be used to study atomic structure [254]. A monochromatic X-ray beam with wavelength λ incident on a crystal will be scattered in all directions by the electrons surrounding the atomic nuclei. In some directions, an increased intensity is observed due to the constructive interference of the scattered X-rays, which occurs when the path length difference between X-rays scattered from parallel lattice planes is an integer number of λ (Figure 3.2). This condition is summarised in Bragg's law:

$$2d_{hkl}\sin\theta = n\lambda \qquad (3.12)$$

where d_{hkl} is the interplanar spacing, θ is the incident angle and n is an integer. The angle between the diffraction beam and the transmitted one is 2θ, and this angle is known as the diffraction angle [255, 256]. A diffraction pattern includes information about peak positions, intensities and profiles. The peak positions are indicative of the crystal structure and symmetry of the contributing phase. The peak intensities reflect the total scattering from each plane in the phase's crystal structure, and are directly dependent on the distribution of particular atoms in the structure. Therefore, the intensities are ultimately related to both the structure and composition of the phase [257]. The peak profiles are broadened inversely proportional to the crystalline size (size effect). The peak width β in radians (often measured as the half-width at half-maximum, FWHM) can be related to the mean crystalline size (τ) *via* the Scherrer equation [258]:

$$\tau = \frac{K\lambda}{\beta\cos\theta} \quad \text{(K is a dimensionless shape factor)} \qquad (3.13)$$

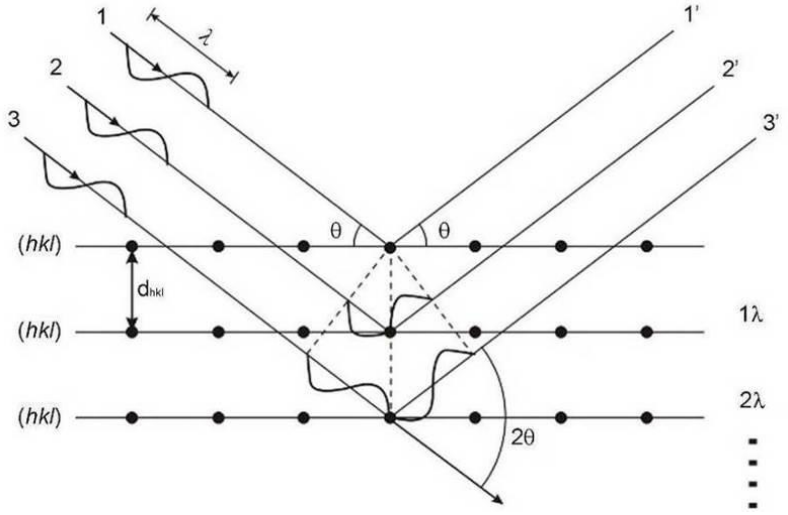

Figure 3.2 Schematic illustration of Bragg law [259].

In this thesis, XRD characterisation was performed with a Bruker D8 Advance X-ray diffractometer (Bruker, Germany) using Cu*K*α radiation source (λ=1.5418 Å). The operating voltage and current of the instrument were 40 kV and 40 mA, respectively. A scan rate of 2° (2θ)/min and a step size of 0.03° were used. To prepare an XRD sample, approximately 0.05 g of dried and homogenised sample powder was pressed in the centre of a glass slide to obtain a smooth, flat surface. Diffraction patterns were analysed using X'Pert HighScore Plus software (PANalytical, Almelo, The Netherlands) with the ICDD (International Centre for Diffraction Data) database. ICDD cards used for phase identification were TiB_2 (35-741), MgO (65-476), Mg_2TiO_4 (25-1157), $Mg_3B_2O_6$ (38-1475), B_4C (35-798), TiC (32-1383), C (graphite) (75-2078), HfB_2 (38-1398), HfO_2 (34-104), Hf (38-1478), HfC (39-1491), LaB_6 (34-427), La_2O_3 (54-213), LaOCl (8-477), $LaBO_3$ (12-762), CaB_6 (35-741), MgB_4 (15-299)&(73-1014), B (12-377), MgB_6 (15-298), Al_2O_3 (10-173), Al_3Ti (37-1449), Ti_2O_3 (43-1033), $Al_{18}B_4O_{33}$ (32-3), and $MgAl_2O_4$ (21-1152).

3.3.2 SEM and EDS

SEM is one of the most versatile instruments available for the examination and

analysis of the microstructure morphology and chemical composition of materials. In a typical SEM system, an electron beam produced from an electron gun is focused through a series of electromagnetic lenses to form a fine probe, which is scanned across the specimen surface continuously with the help of scanning coils (Figure 3.3) [88].

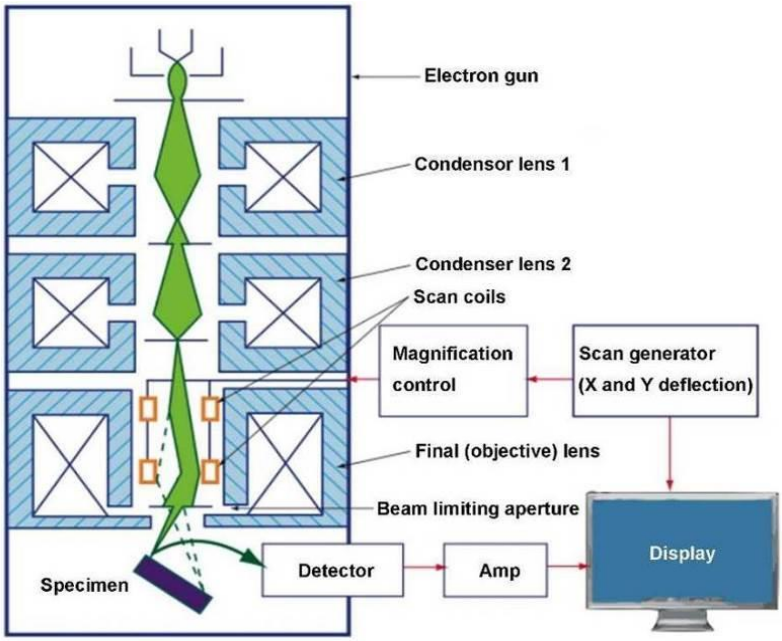

Figure 3.3 Schematic diagram of a typical SEM [260].

When the primary beam electrons strike a specimen they penetrate into the solid for some distance (~1 μm) and interact both elastically and inelastically with the solid, forming a limiting interaction volume from which various signals are produced, including secondary electrons (SEs), backscattered electrons (BSEs), X-rays and Auger electrons (AEs) (Figure 3.4(a)) [261, 262]. Among these signals, SEs and BSEs are generally used to produce SEM images. SEs are produced as a result of inelastic scattering interactions between the incident electrons and weakly bound electrons of the atoms in specimen that have sufficient energy to overcome the work function and escape the solid. SEs are represented by a peak at low energies of 3-5 eV (Figure 3.4(b)). The depth of emission of SE is approximately 5λ (λ is ~1 nm for metals and up to 10 nm for

insulators). SEs are used principally for topographic contrast in the SEM, i.e., for the visualisation of surface texture and roughness. BSEs with a broad range energy spectrum between 50 eV and the primary electron energy (E = eU) (Figure 3.4(b)) are caused by the deceleration of electrons that have suffered multiple energy losses and have undergone multiple scattering through large angles. Elements with higher atomic numbers have more positive charges on the nucleus, so more electrons are backscattered, causing the resulting backscattered signal to be higher. Therefore, the yield of BSE increases with the atomic number of the specimen, providing atomic number contrast in the SEM images [263]. The maximum information depth of BSEs is greater than that of SEs, thus, the resolution of a BSF image is considerably worse (1.0 μm) than it is for a SE image (10 nm) [261].

When the primary beam strikes the specimen, a high-energy beam electron penetrates through the outer conduction/valence bands and interacts with the inner-shell (or core) electrons. If more than a critical amount of energy is transferred to an inner-shell electron, that electron is ejected, i.e., it escapes the attractive field of the nucleus, leaving a hole in the inner shell. The ionised atom can return to its lowest energy (ground state) by filling in the hole with an electron from an outer shell. The de-excitation energy released can be emitted as an X-ray, or transferred to another atomic electron, which will then eject as an AE. In both the X-ray and Auger cases, the energy of the emission is characteristic of the difference in energy between the two electron shells involved and this energy difference is unique to the atom. The difference between the two shell energies equals the energy of the characteristic X-ray. An EDS measures the energy of the characteristic X-ray [263-266]. Each element

has characteristic X-ray peaks allowing the elemental composition of a sample to be identified. Since lower atomic number elements have fewer filled shells, they have fewer X-ray peaks. Moreover, the distribution of elements over a particular area of the sample can be viewed by acquiring element specific maps. Elemental mapping based on the counts of a single characteristic line can be performed with an EDS by scanning the electron beam [267].

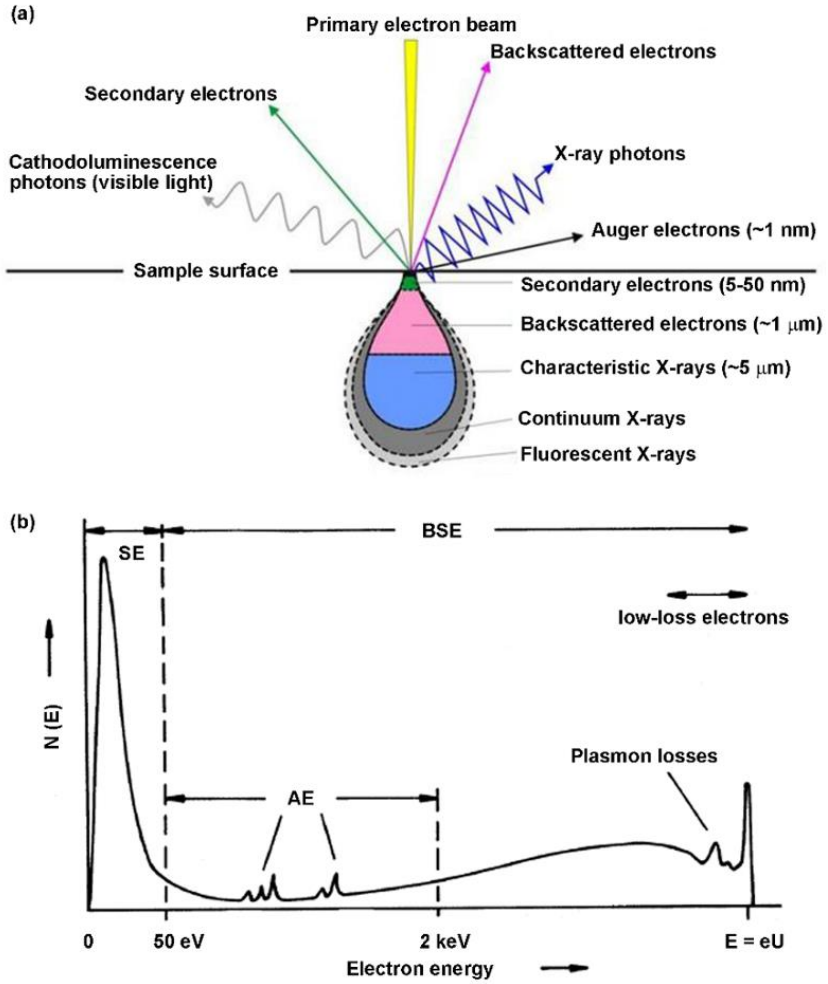

Figure 3.4 Schematic illustration of (a) the interaction of the primary electron beam with a specimen, showing the depth from the interaction volume that the various signals are generated [268] and (b) the complete energy distribution of electrons emitted [265].

In this thesis, the microstructures and morphologies of the samples were examined in the secondary electron imaging (SEI) mode using an FEI Nova 600 SEM (FEI, USA) operated at 15 kV. To prepare the SEM specimen, the synthesised powders were sprinkled directly onto conductive carbon tape that

sticks to a sample stub. Prior to SEM, all samples were sputter-coated with Au/Pd (~10 nm thickness) to avoid the charging effect. Elemental analysis was performed using an Oxford INCA EDS (Oxford Instruments, Oxford, UK) installed on a Hitachi S3200N SEM (Hitachi, Japan) operated at 10-15 kV. Samples for EDS were not sputter-coated to avoid the influence of the coating elements.

3.3.3 TEM and SAED

TEM is the premier tool to examine the internal microstructure of electron transparent specimens (<100 nm thick) at a resolution approaching the atomic level. A conventional TEM can be divided into three components: the illumination system, objective lens/stage and imaging system (Figure 3.5) [269]. The objective lens takes the electrons emerging from the exit surface of the specimen, disperses them to create a diffraction pattern in the back focal plane, and recombines them to form an image in the image plane [270]. To adjust the imaging-system lenses to that the back focal plane of the objective lens acts as the object plane for the intermediate lens, then the diffraction pattern is projected onto the viewing screen as shown in Figure 3.6(a). To readjust the intermediate lens so that its object plane is the image plane of the objective lens, then an image is projected onto the viewing screen as shown in Figure 3.6(b) [271]. In the diffraction mode, the objective aperture is removed, thus, the diffraction pattern contains electrons from the whole area of the specimen illuminated with the beam. An SAED pattern will be created by inserting an SAD aperture into the image plane of the objective lens [272].

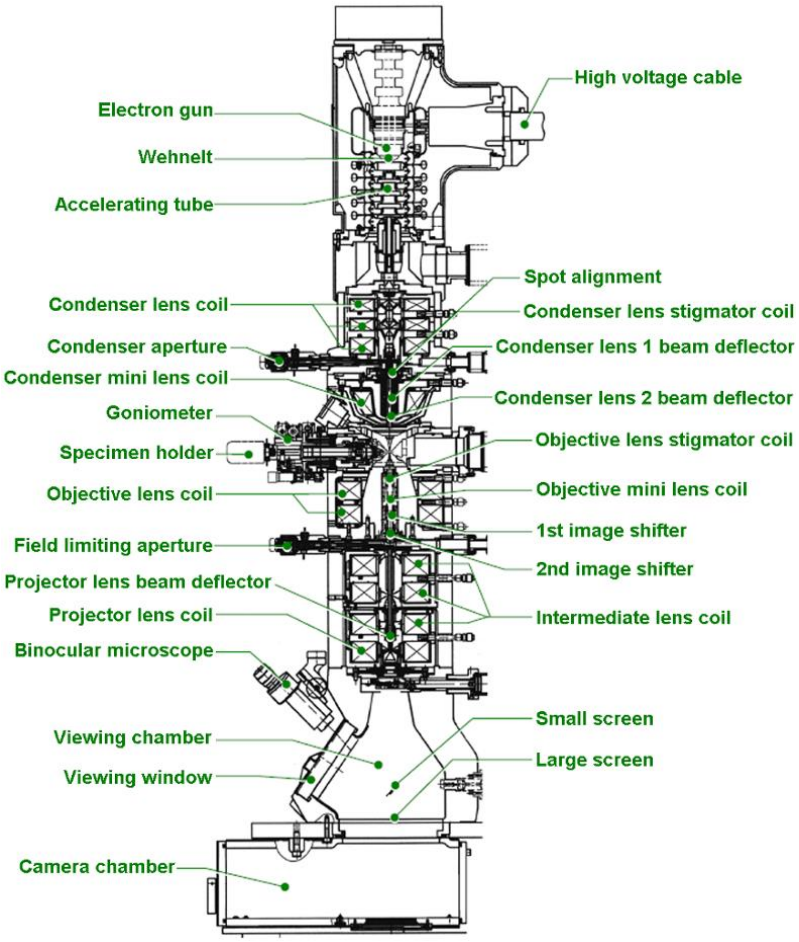

Figure 3.5 Schematic diagram of the layout of JEM-2100 TEM [273].

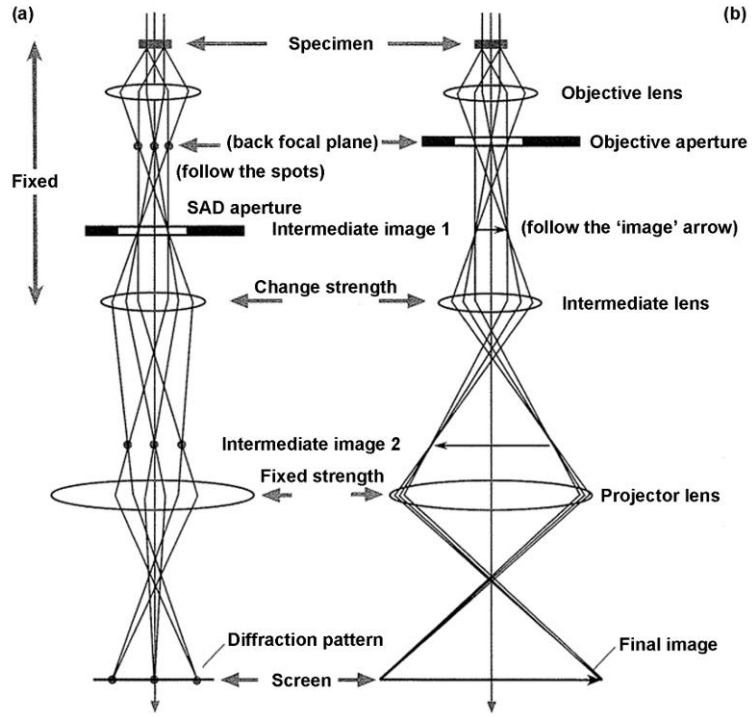

Figure 3.6 Simplified diagram of the two basic operations of the TEM imaging system involve (a) diffraction mode and (b) image mode [271].

SAED pattern can provide information on the crystal structure and orientation of the specimen. Since the wavelength of high-energy electrons is very small (e.g., λ = 0.0037 nm for 100 eV electrons), the diffraction angles are generally small (of the order of 10^{-3} radians), $\sin\theta \approx \theta$, resulting in a small distance between the transmitted electron beam and diffraction spots, R, which is related to the camera length (the effective distance between the specimen and recording plane), L, as illustrated in Figure 3.7(a). In view of this, Bragg's equation can be simplified:

$$\lambda = 2d\theta \tag{3.14}$$

From Figure 3.7(a), the geometric equation is obtained:

$$\frac{R}{L} = \tan 2\theta \sim 2\theta \tag{3.15}$$

Combining Equations (3.14) and (3.15) gives

$$Rd = \lambda L \tag{3.16}$$

λL is termed the camera constant and can be obtained using a reference sample of known lattice parameter under the same electron-optic conditions. Thus, R is directly proportional to 1/d.

Amorphous materials exhibit diffuse diffraction rings related to the average interatomic separations and hence the radial distribution function (Figure 3.7(b)). If the specimen area is polycrystalline, then the electron diffraction produces a pattern of concentric rings of radii R that exhibit virtually all possible d spacings, because the crystallites are randomly oriented (Figure 3.7(c)). For a single-crystal specimen, the diffraction pattern consists of points, spaced at a distance proportional to 1/d, aligned in a direction perpendicular to the orientation of the (hkl) planes (Figure 3.7(d)) [274].

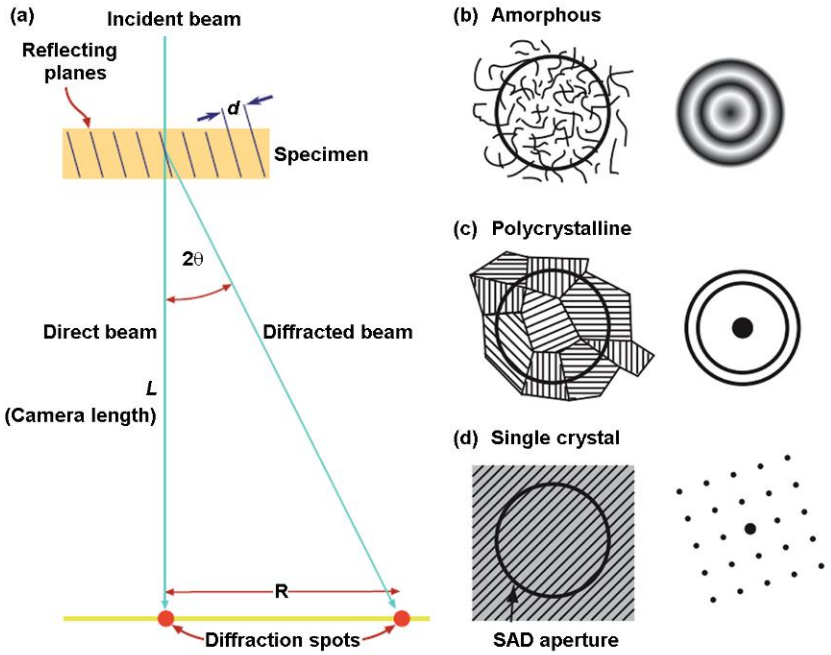

Figure 3.7 Schematic diagram of (a) the geometry of electron diffraction in the TEM [271] and different types of diffraction patterns obtained from (b) amorphous, (c) polycrystalline and (d) single-crystalline sample regions [274].

In this thesis, a JEM2100 TEM (JEOL, Tokyo, Japan) at an acceleration voltage of 200 kV was selected to further characterise the microstructures and morphologies of the samples. EDS (Oxford Instruments, Oxford, UK) linked with TEM was used to semi-quantitatively determine elemental compositions in the product sample. To prepare the TEM specimen, the synthesised powders were dispersed in ethanol under moderate sonication, pipetted onto a holey carbon Cu grid, and dried by exposure to ambient conditions for 24 h.

Chapter 4 Low-Temperature Preparation of TiB_2 Fine Powders *via* Magnesiothermic Reduction in Molten Salt

TiB_2 fine powder was prepared from TiO_2 and B_2O_3 using a molten-salt-mediated magnesiothermic reduction technique. The effects of the morphology/size of the raw material TiO_2, salt type, firing temperature, and Mg amount on the synthesis process were examined. Based on these studies, the reaction conditions were optimised, and the relevant synthesis mechanisms were proposed.

4.1 Results and discussion

4.1.1 Effect of salt type on TiB_2 formation

Figure 4.1 shows XRD patterns of the samples with stoichiometric compositions after 4 h of firing at 850°C in different salts (here and in the cases of Figures 4.2 and 4.3 below, nanosized TiO_2 I was used, and the samples were after water washing but before acid leaching). When NaCl was used (Figure 4.1(a)), some amount of TiB_2 was formed, along with the MgO byproduct (Reactions (4.1) and (4.2)) and intermediates $Mg_3B_2O_6$ and Mg_2TiO_4 from Reactions (4.3) and (4.4) [275], indicating the overall low extent of TiB_2 formation under these conditions.

$$B_2O_3 + 3Mg = 2B + 3MgO \quad (4.1)$$

$$TiO_2 + 2Mg = Ti + 2MgO \quad (4.2)$$

$$B_2O_3\ (\text{unreduced}) + 3MgO = Mg_3B_2O_6 \quad (4.3)$$

$$TiO_2\ (\text{unreduced}) + 2MgO = Mg_2TiO_4 \quad (4.4)$$

The same four phases were also identified when KCl was used (Figure 4.1(b)). However, compared to the sample obtained using NaCl, the TiB_2 and MgO peaks were higher, and the $Mg_3B_2O_6$ and Mg_2TiO_4 peaks were lower, revealing

greater TiO_2 and B_2O_3 reduction and TiB_2 formation when using KCl. When $MgCl_2$ was used, the peaks of TiB_2 and MgO further increased, whereas the peaks of $Mg_3B_2O_6$ and Mg_2TiO_4 further decreased (Figure 4.1(c)), suggesting that $MgCl_2$ was the most effective of the three salts in accelerating the magnesiothermic reduction and TiB_2 formation.

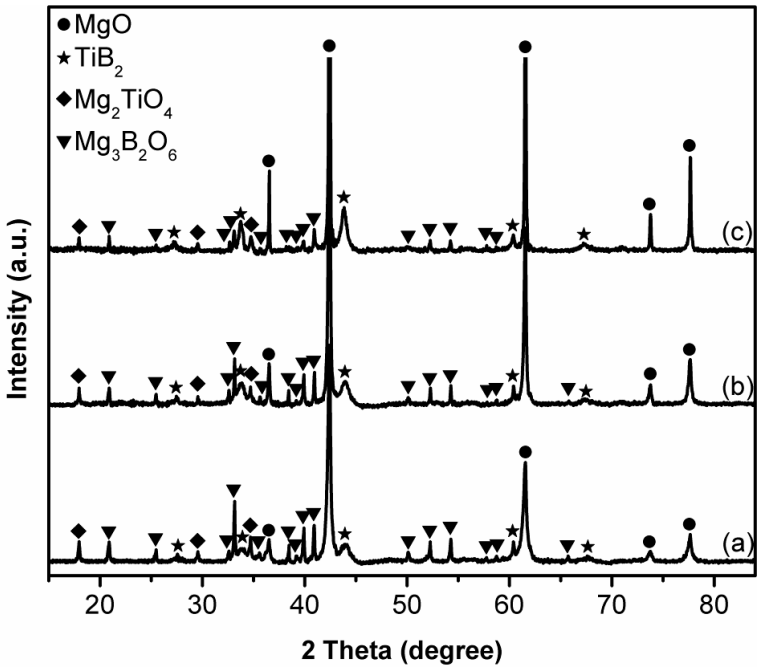

Figure 4.1 XRD patterns of the samples with stoichiometric compositions after 4 h of firing at 850°C in (a) NaCl, (b) KCl, and (c) $MgCl_2$.

4.1.2 Effect of firing temperature on TiB_2 formation

Figure 4.2 shows XRD patterns of the samples with stoichiometric compositions after 4 h of firing in $MgCl_2$ at different temperatures. At 750°C, TiB_2 was evidently already formed, along with MgO, $Mg_3B_2O_6$ and Mg_2TiO_4 (Figure 4.2(a)). Upon increasing the temperature to 850°C (Figure 4.2(b)/Figure 4.1(c)) and 950°C (Figure 4.2(c)), the peaks of TiB_2 and MgO increased, whereas the peaks of $Mg_3B_2O_6$ and Mg_2TiO_4 decreased, showing enhanced reaction extents. Conversely, upon further increasing the temperature to 1000°C, the peaks of $Mg_3B_2O_6$ and Mg_2TiO_4 increased (Figure 4.2(d)), indicating a decreased extent of magnesiothermic reduction and TiB_2 formation. This was caused by Mg

evaporation loss at this relatively high temperature [139, 144, 275]. Hence, excessive Mg had to be used to push the TiB_2 formation reaction to completion.

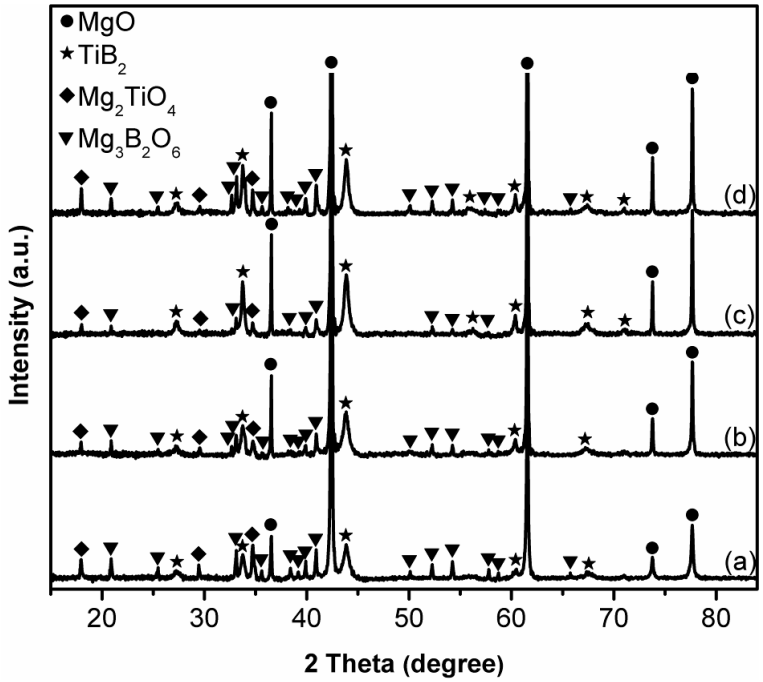

Figure 4.2 XRD patterns of the samples with stoichiometric compositions after 4 h of firing in $MgCl_2$ at (a) 750, (b) 850, (c) 950, and (d) 1000°C.

4.1.3 Effect of excessive Mg on TiB_2 formation

Figure 4.3 illustrates the effects of excessive amounts of Mg on the phase evolution in samples resultant from 4 h of firing in $MgCl_2$ at 1000°C. $Mg_3B_2O_6$ and Mg_2TiO_4 remained when 5 mol% excessive Mg was used (Figure 4.3(b)) but were present at significantly smaller amounts than when a stoichiometric amount of Mg was used (Figure 4.3(a)), indicating improved B_2O_3 and TiO_2 reduction and TiB_2 formation. With 15 mol% excessive Mg, TiB_2 became the primary phase, and minor $Mg_3B_2O_6$ and Mg_2TiO_4 phases were present (Figure 4.3(c)). When the excessive amount of Mg was increased to 20 mol%, only the TiB_2 and MgO byproduct phases were detected, confirming the completion of the TiB_2 formation reaction (Figure 4.3(d)).

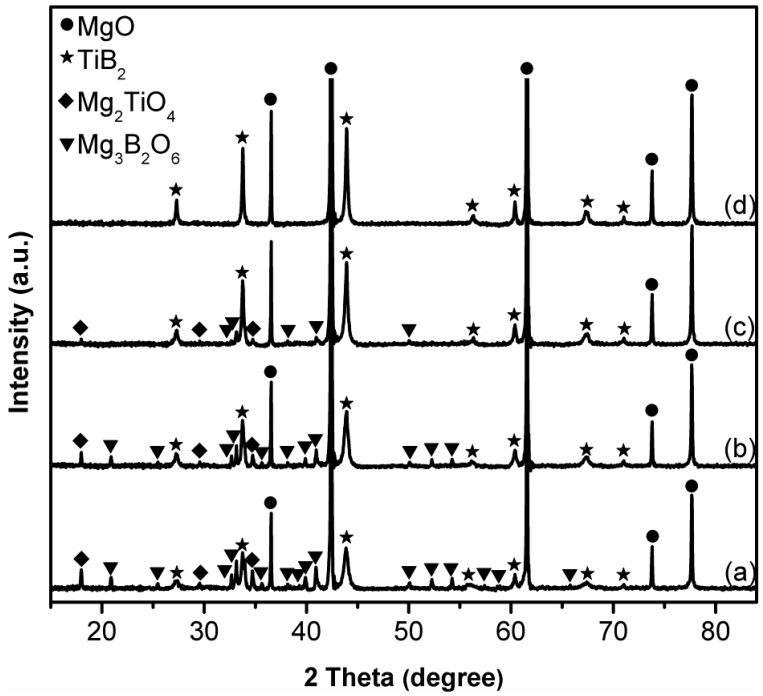

Figure 4.3 XRD patterns of samples resultant from firing batch powders for 4 h in $MgCl_2$ at 1000°C with (a) 0, (b) 5, (c) 15, and (d) 20 mol% excessive Mg.

4.1.4 Effect of TiO_2 particle shape and size on TiB_2 formation

As shown in Figure 4.3(d) and described above, when nanosized TiO_2 I and 20 mol% excessive Mg were used, the TiB_2 formation reaction was completed after 4 h of firing in $MgCl_2$ at 1000°C, so only TiB_2 and MgO were formed in the fired sample (Figure 4.3(d)). Leaching out the MgO byproduct resulted in phase-pure TiB_2, as shown by Figure 4.4(a). Interestingly, when the nanosized TiO_2 I powders were replaced by TiO_2 II nanowires or coarser TiO_2 III powders, TiB_2 formation could still be completed under the identical firing conditions, and phase-pure TiB_2 was still obtained in both cases after acid leaching (Figures 4.4(b) and (c)). These results indicated that TiO_2 particle shape and size had little effect on the MSS of TiB_2. The reason for this finding and its practical significance will be discussed shortly.

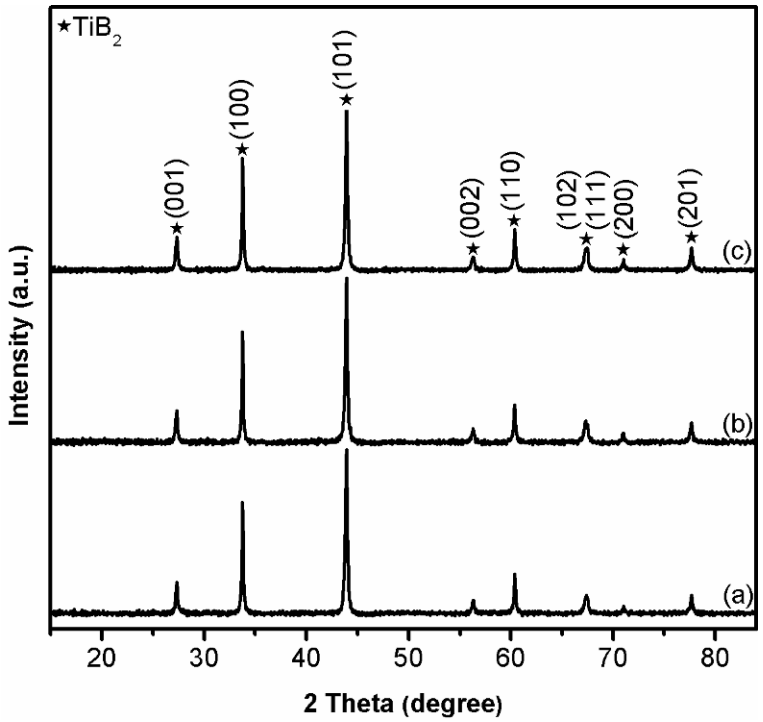

Figure 4.4 XRD patterns of samples resultant from 4 h firing in $MgCl_2$ at 1000°C using 20 mol% excessive Mg and, respectively (a) TiO_2 I, (b) TiO_2 II, and (c) TiO_2 III.

4.1.5 Microstructural characterisation of the TiB_2 product powders

Figure 4.5 presents SEM images of the TiO_2 raw materials and the corresponding TiB_2 product powders whose XRD patterns are shown in Figure 4.4. Despite the great shape/size differences between TiO_2 I (Figure 4.5(a)), TiO_2 II (Figure 4.5(c)) and TiO_2 III (Figure 4.5(e)), the corresponding TiB_2 product powders exhibited similar shapes/sizes (100-200 nm) (Figures 4.5(b), (d) and (f)). This can be seen more clearly from their TEM images given in Figure 4.6. These results, in addition to the XRD results (Figure 4.4), further confirmed that TiO_2 particle morphology/size had little effect on the overall TiB_2 formation in terms of the reaction conditions and product morphology/size. This interesting finding can have great practical significance, as it suggests that using expensive nanosized TiO_2 raw materials for the MSS of fine TiB_2 particles is unnecessary. Regarding the purity of the TiB_2 product powders, EDS (Figures 4.6(b), (d) and (f)) only detected negligible O in addition to Ti and B (the small Cu peak originated from

the Cu grid used for TEM) in all three samples, confirming that the as-prepared TiB_2 powders were of high purity. The presence of free oxygen in this specimen could be due to handling the samples in non-inert laboratory conditions.

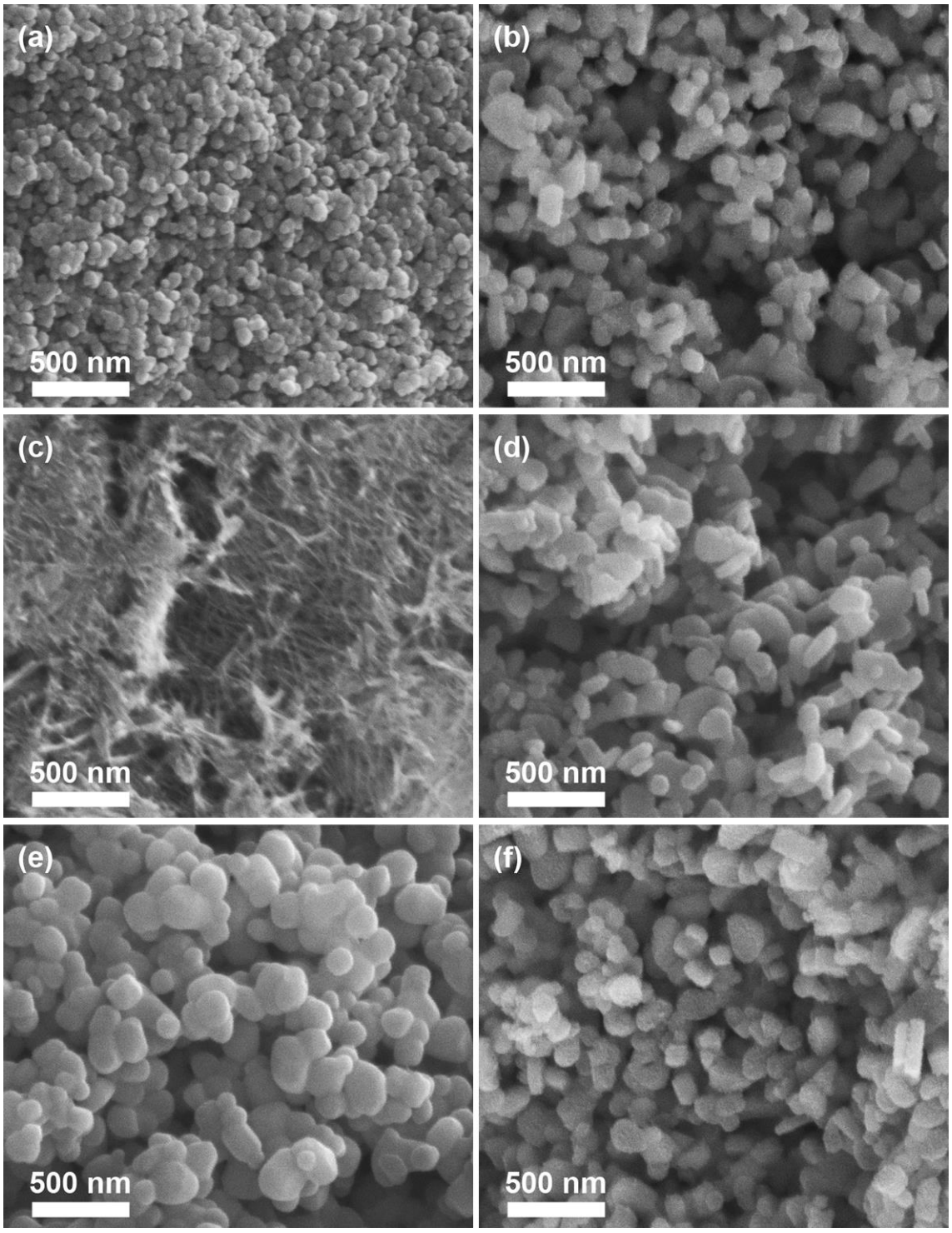

Figure 4.5 SEM images of (a) TiO_2 I, (c) TiO_2 II, (e) TiO_2 III, and (b, d, f) the corresponding TiB_2 product powders whose XRD patterns are shown in Figure 4.4.

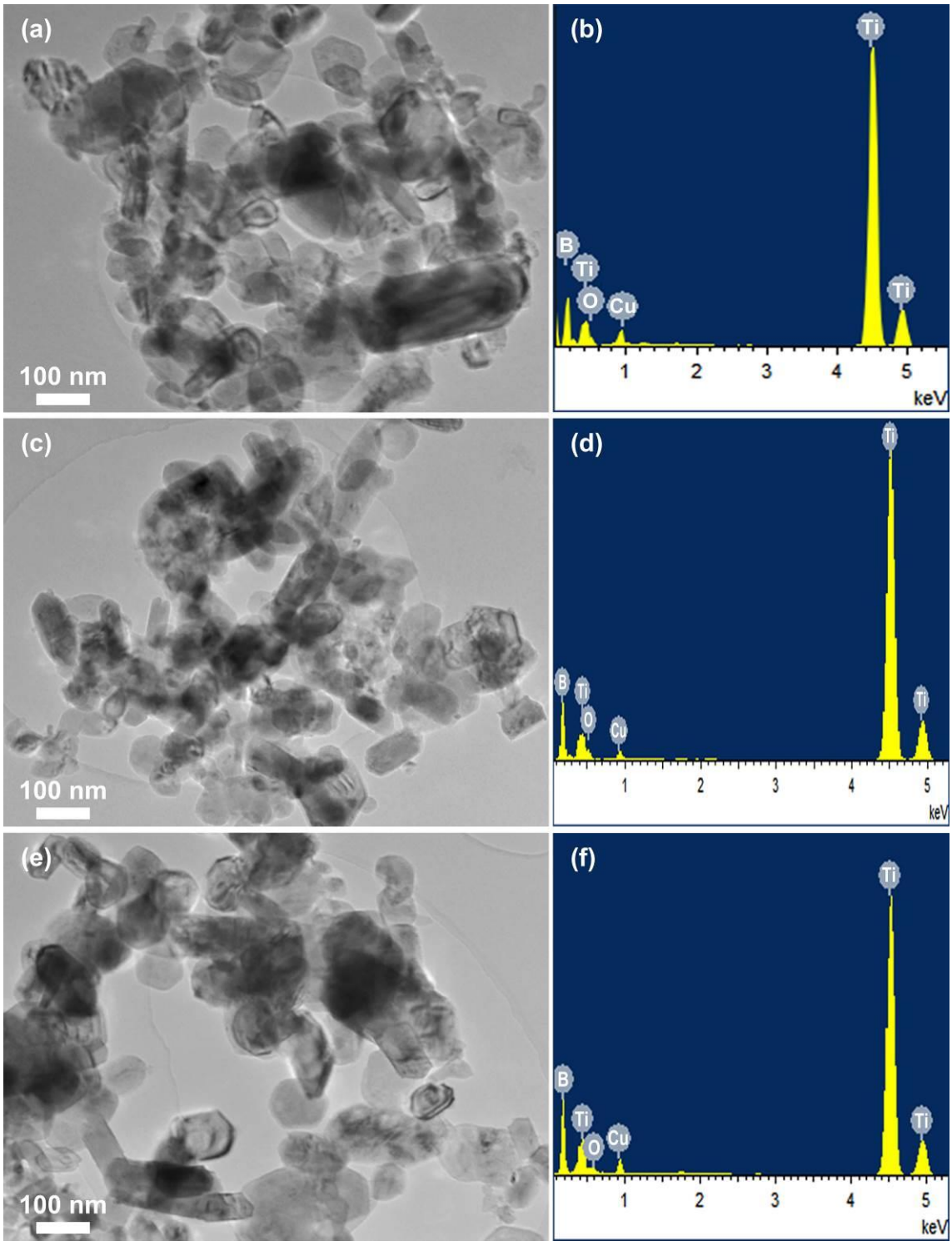

Figure 4.6 TEM images and corresponding EDS results of the TiB_2 product powders prepared from (a, b) TiO_2 I, (c, d) TiO_2 II, and (e, f) TiO_2 III.

Product yield of TiB_2 was calculated based on the quantity of TiB_2 product after acid leaching and the theoretical quantity of TiB_2 according to Reaction (3.1). It was calculated to be >86 wt%. Some TiB_2 was lost due to probably the repeated water washing, filtration, acid leaching and centrifuge. So the actual figure

should be higher than this.

4.2 Reaction mechanisms and further discussion

According to the results shown in Figures 4.1-4.6 and the preliminary discussion above, the reaction mechanism of the present MSS can be further considered as follows.

4.2.1 Formation of B and Ti in the molten salt

A firing temperature of 850°C, which is above the melting points of the three chloride salts, was used to investigate the effect of the salt type on the synthesis (Figure 4.1). Therefore, at the test temperature, the chloride salt initially melts, forming the desired liquid medium. For example, in the case of using $MgCl_2$ as the liquid medium, Mg slightly dissolved [276]. On the other hand, part of the TiO_2 interacted with B_2O_3, forming a eutectic liquid [277], whereas the remaining part was still present as a solid phase in the molten salt. The dissolved Mg diffused rapidly through the molten $MgCl_2$ salt to the B_2O_3-TiO_2 (B-T) eutectic liquid and the remaining TiO_2 particles and then reduced B_2O_3 and TiO_2 to B and Ti, respectively (Reactions (4.5)-(4.7)).

$$B_2O_3 \text{ (in B-T eutectic liquid)} + 3Mg \text{ (dissolved)} = 2B + 3MgO \quad (4.5)$$

$$TiO_2 \text{ (in B-T eutectic liquid)} + 2Mg \text{ (dissolved)} = Ti + 2MgO \quad (4.6)$$

$$TiO_2 \text{ (in the salt as a solid)} + 2Mg \text{ (dissolved)} = Ti + 2MgO \quad (4.7)$$

In addition to the TiB_2 product and MgO byproduct, the intermediates $Mg_3B_2O_6$ and Mg_2TiO_4 were formed in some of the reacted samples (Figures 4.1-4.3). Interestingly, because of the molten salt medium, these intermediate phases could be well dispersed in the salt and further reduced by the dissolved Mg, forming additional B and Ti according to Reactions (4.8) and (4.9). This was

verified by the test results. With improving reaction conditions (using $MgCl_2$ salt, increasing the temperature and using excessive Mg), the $Mg_3B_2O_6$ and Mg_2TiO_4 content gradually decreased and eventually disappeared. In addition to advantages such as low synthesis temperature and finer size/better dispersion of the final product powders, this outcome is an “unexpected” advantage of the MSS technique over other previously reported conventional magnesiothermic reduction techniques.

$$Mg_3B_2O_6 + 3Mg\ (dissolved) = 6MgO + 2B \quad (4.8)$$

$$Mg_2TiO_4 + 2Mg\ (dissolved) = 4MgO + Ti \quad (4.9)$$

4.2.2 Solubility of B and Ti in molten salt

As reviewed in Section 2.5, depending on the solubility of the reactants in molten salt, two main mechanisms, “template-growth” and “dissolution and precipitation”, generally function in MSS. The exact solubility values of B and Ti in molten chloride salts are not known. However, according to the findings from other MSS studies [278, 279], the results from the firing systems of B_2O_3-Mg-CFs and TiO_2-Mg-CFs in $MgCl_2$ could give some useful clues.

Figure 4.7 shows XRD patterns of the as-received CFs, resultant sample from firing B_2O_3-Mg-CFs for 4 h at 1150°C in $MgCl_2$, and resultant sample from firing TiO_2-Mg-CFs for 4 h at 1000°C in $MgCl_2$. Figure 4.7(a) revealed two broad peaks at 2θ (25.2) (002) and 43.6 (101), indicating that the uncoated CFs might have a poor degree of graphitisation. By contrast, in the fired samples, phases other than the broad peaks from the CFs were detected, i.e. B_4C resultant from B_2O_3-Mg-CFs-$MgCl_2$ at 1150°C (Figure 4.7(b)) and TiC from TiO_2-Mg-CFs-$MgCl_2$ at 1000°C (Figure 4.7(c)), confirming the formation of B_4C and TiC.

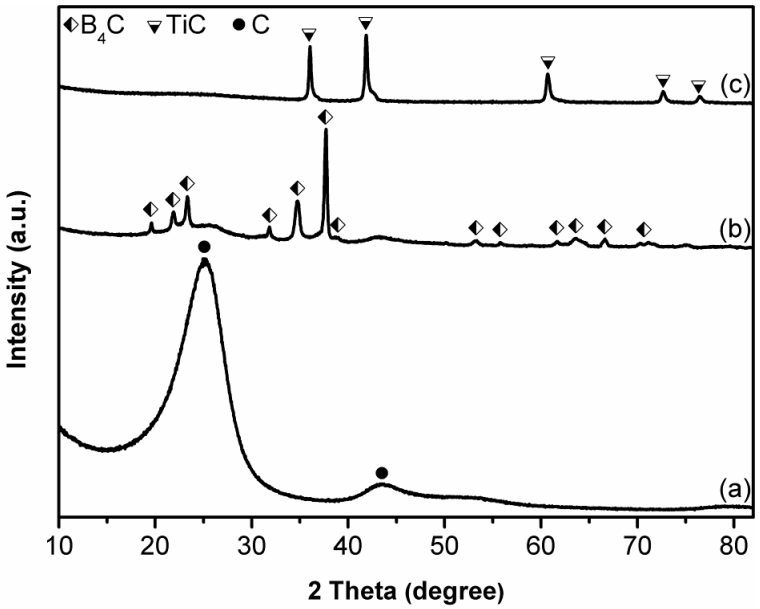

Figure 4.7 XRD patterns of the (a) raw CFs and carbide coatings on the CFs: (b) B_4C coating and (c) TiC coating.

Figure 4.8 displays the typical microstructures of the as-received CFs and the B_4C-coated and TiC-coated CFs. The resulting coated CFs (Figure 4.8(c, e)) retained the fibrous shape of the precursor CFs (Figure 4.8(a)). However, unlike the smooth and clean surfaces of the uncoated CFs, the surfaces of the product CFs exhibited coating fragments and missing areas in the coatings, implying that cracks were formed in the coatings and that they could peel away from the CF surfaces. Compared to the EDS of the uncoated CFs, which only revealed the presence of C (Figure 4.8(b)), B (Figure 4.8(d)) and Ti (Figure 4.8(f)) were detected in selected areas of the product samples (along with small amounts of O contamination). The EDS results, together with the XRD results (Figure 4.7), verified the formation of the B_4C and TiC coatings on the CFs.

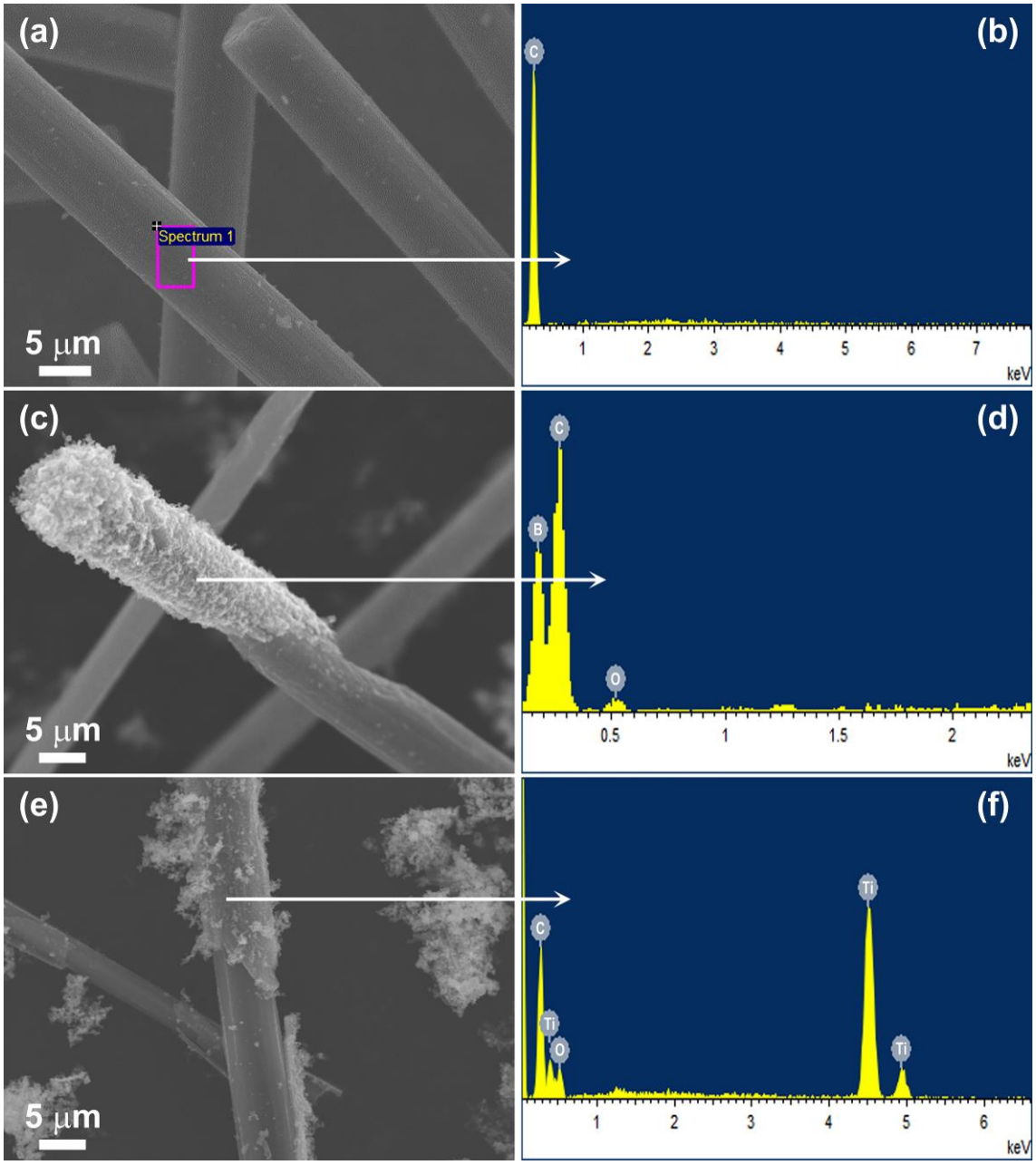

Figure 4.8 SEM images and EDS results of the (a, b) as-received CFs and carbide coatings on the CFs: (c, d) B_4C coating and (e, f) TiC coating.

During the process of forming the carbide coatings, several individual reaction steps, i.e. Reactions (4.10)-(4.13), were most likely involved. As discussed previously [241, 278-280], the resultant B or Ti reacted with the CFs in the molten salt to form B_4C or TiC on the CFs, following a "template-growth" mechanism, in which the CFs acted as not only carbon sources but also templates for B_4C or TiC growth. Therefore, it became evident that the resultant B and Ti could at least partially dissolve in molten chloride salts (although the

actual solubility was probably quite small).

$$B_2O_3 + 3Mg = 2B + 3MgO \quad (4.10)$$

$$TiO_2 + 2Mg = Ti + 2MgO \quad (4.11)$$

$$4B + C = B_4C \quad (4.12)$$

$$Ti + C = TiC \quad (4.13)$$

Therefore, in the MSS of TiB_2, B and Ti from Reactions (4.5)-(4.9) would slightly dissolve in the molten salt and then react with each other rapidly, forming the TiB_2 product according to Reaction (4.14) *via* a "dissolution-precipitation" mechanism. The TiB_2 product particles did not retain the morphology/size of any of the "parent" reactants (B or Ti) because of this operative reaction mechanism, which also explains the minimal effect of the morphology/size of the raw material TiO_2 particles on the final TiB_2 product powder.

$$Ti\ (dissolved) + 2B\ (dissolved) = TiB_2 \quad (4.14)$$

4.2.3 Effect of the salt type on the MSS

Although the "dissolution-precipitation" mechanism proposed above remained the same in the other two cases of using KCl and NaCl, the reaction rates/extents in the three cases were different. As shown in Figure 4.1 and described in Section 4.1.1, among the three salts, $MgCl_2$ had the best accelerating effect on the formation of TiB_2. The reasons for this contrast are discussed below.

As reviewed in Section 2.5, the salt viscosity and reactant solubility greatly affect MSS. At a given temperature, the viscosity of molten $MgCl_2$ is close to (only slightly higher than) that of molten NaCl or KCl [249, 250], but Mg is much more soluble in molten $MgCl_2$ than in the other two molten salts [276]. Thus the magnesiothermic reduction as well as the subsequent TiB_2 formation would

proceed more rapidly in molten $MgCl_2$ than in the other two molten salts. In addition, another factor might have been partially responsible for the differences in the accelerating effects of the salts. As indicated by Reactions (4.7), (4.8) and (4.9), when solid TiO_2, $Mg_3B_2O_6$ and Mg_2TiO_4 were reduced by the dissolved Mg in the molten salt, a product barrier layer (composing MgO+Ti/B) initially formed on their surfaces. If such a barrier layer remained, it could inhibit further reduction reactions, i.e., slow down the overall formation of Ti and B and thus TiB_2 formation. Fortunately, MgO, the main component of this barrier layer, could be removed through its partial dissolution in the molten salt, making the barrier layer less continuous and thinner and thus avoiding otherwise significant delays in Reactions (4.7), (4.8) and (4.9) [281]. Considering that MgO in $MgCl_2$ is also more soluble in molten $MgCl_2$ than in molten NaCl or KCl [282, 283], the MgO in the initially formed barrier layer should be removed more efficiently in molten $MgCl_2$ than in molten NaCl or KCl, which could also explain the superior accelerating effect of $MgCl_2$ on the MSS.

4.3 Conclusion

TiB_2 fine powders were prepared from TiO_2 and B_2O_3 *via* a molten-salt-mediated magnesiothermic reduction route. The effects of salt type, excessive Mg, firing temperature, and TiO_2 particle shape/size on the formation process were examined. Of the three chloride salts, $MgCl_2$ showed the best accelerating effect. By using 20 mol% excessive Mg to compensate for its evaporation loss at the test temperatures, phase-pure TiB_2 fine particles of 100-200 nm were synthesised after 4 h of firing in $MgCl_2$ at 1000°C. In addition, the formation of the intermediates Mg_2TiO_4 and $Mg_3B_2O_6$, which are difficult to leach out, was avoided by optimising the reaction conditions. Another interesting finding was

that under the optimal reaction conditions (i.e., firing batch powders for 4 h in $MgCl_2$ at 1000°C with 20 mol% excessive Mg), the shape/size of the raw material TiO_2 had little effect on the reaction extent and shape/size of the TiB_2 product particles, suggesting that it was unnecessary to use expensive nanosized TiO_2 as a starting raw material for the MSS of TiB_2 fine particles. The “dissolution-precipitation” mechanism dominated the overall MSS process.

Chapter 5 Low-Temperature Synthesis of HfB_2 Fine Powders *via* Magnesiothermic Reduction in Molten Salt

HfB_2 fine powder was synthesised in molten NaCl, KCl or $MgCl_2$ at a relatively low temperature using HfO_2 and B_2O_3 powders as the main starting materials. The effects of key processing factors, such as salt type, initial batch composition, heating temperature/time, on the synthesis were investigated. Based on the results, the synthesis conditions were optimised, and the main mechanisms governing the synthesis clarified.

5.1 Results and discussion

5.1.1 HfB_2 formation in different salts

Figure 5.1 presents XRD results of the samples with stoichiometric compositions after 4 h heating in different salts at 850°C (here and in Figures 5.2-5.7 below, the samples were subjected to only water washing). When NaCl was used (Figure 5.1(a)), both HfB_2 and MgO were identified, indicating the occurrence of Reaction (3.2). However, large amounts of unreacted HfO_2 remained, along with some intermediate $Mg_3B_2O_6$, indicating the low extents of the magnesiothermic reduction and HfB_2 formation. Hence, NaCl produced a limited accelerating effect in this case. When NaCl was replaced with KCl, the HfB_2 and MgO peaks became higher, whereas those of HfO_2 and $Mg_3B_2O_6$ became lower (Figure 5.1(b)), suggesting that KCl improved the reaction extents and had a better accelerating effect than NaCl. Upon replacing KCl with $MgCl_2$, the HfB_2 and MgO peaks further increased, whereas those of HfO_2 and $Mg_3B_2O_6$ further decreased (Figure 5.1 (c)), revealing further enhanced reaction extents and an even better

accelerating effect due to $MgCl_2$. These results suggested that among the three salts, $MgCl_2$ was the most effective at facilitating the magnesiothermic reduction and HfB_2 formation. This result was similar to the one observed in the previous MSS work on TiB_2, and can be explained based on the similar reasons: Mg and MgO were more soluble in molten $MgCl_2$ than in molten KCl or NaCl. The greater solubility of Mg in molten $MgCl_2$ than in the other two molten salts caused the magnesiothermic reduction and subsequent HfB_2 formation to proceed more rapidly. Moreover, the higher solubility of MgO in molten $MgCl_2$ led to more effective removal of the MgO byproduct from the barrier layer initially formed on the remaining unreacted solid reactants, avoiding otherwise significantly delayed/inhibited magnesiothermic reduction and HfB_2 formation.

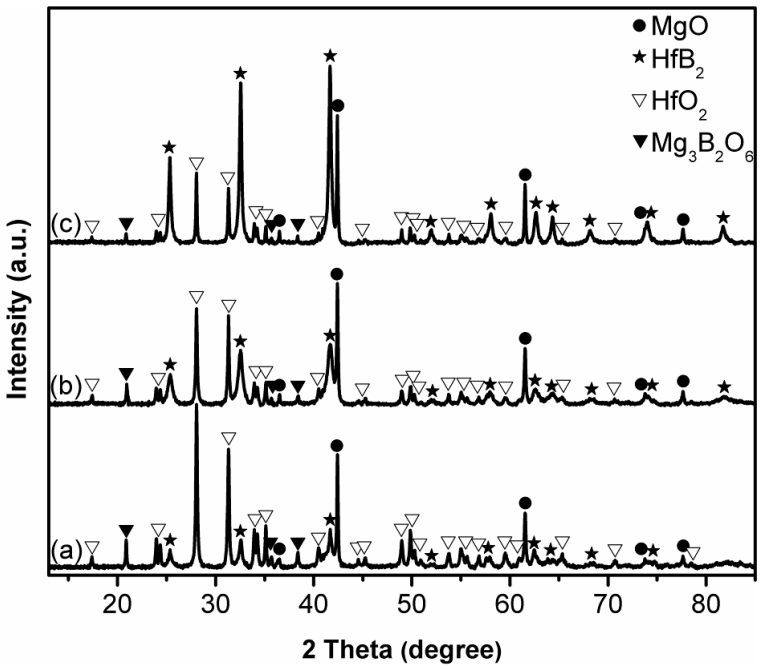

Figure 5.1 XRD patterns of samples with stoichiometric compositions after 4 h heating at 850°C in: (a) NaCl, (b) KCl, and (c) $MgCl_2$, respectively.

5.1.2 HfB_2 formation at different temperatures

Figure 5.2 shows the effects of different heating temperatures on the phase evolution in the samples with stoichiometric compositions after 4 h heating in $MgCl_2$. At 750°C (Figure 5.2(a)), despite the evident formation of HfB_2, large

amounts of HfO_2, along with some intermediate $Mg_3B_2O_6$, remained. Upon increasing the temperature to 850°C (Figure 5.2 (b)/Figure 5.1(c)) and 950°C, the HfB_2 and MgO peaks increased, while those of HfO_2 and $Mg_3B_2O_6$ decreased (Figure 5.2(c)), revealing that reaction had gone closer to completion. Nevertheless, increasing the temperature further to 1000°C caused the HfO_2 and $Mg_3B_2O_6$ content to increase (Figure 5.2(d)), implying a reduced extent of the magnesiothermic reduction and HfB_2 formation. This was attributable to the evaporation loss of Mg at the relatively high reaction temperature, as similarly observed and discussed in the MSS of TiB_2 (Section 4.1.2). Therefore, the effect of using excessive Mg on HfB_2 formation was further investigated, as described and discussed next.

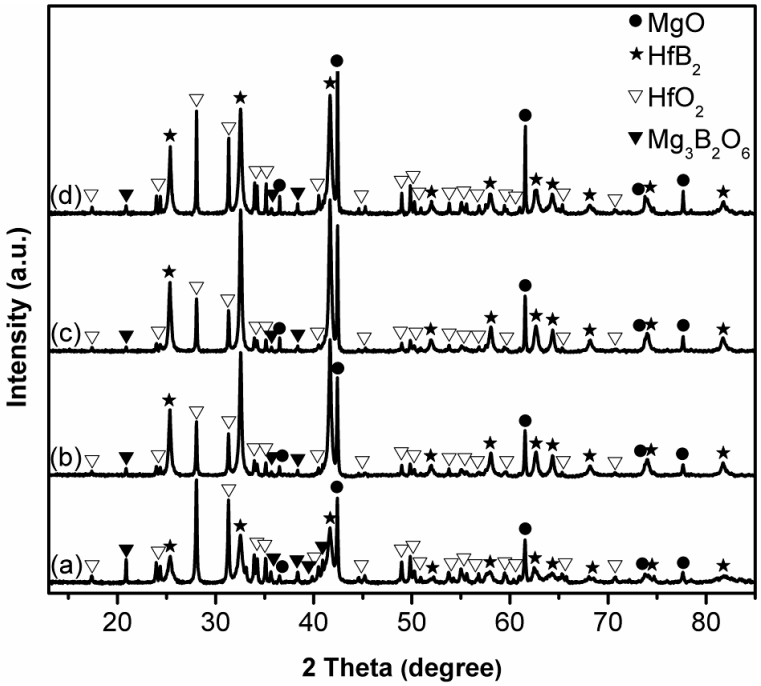

Figure 5.2 XRD patterns of samples with stoichiometric compositions after 4 h heating in $MgCl_2$ at: (a) 750, (b) 850, (c) 950, and (d) 1000°C, respectively.

5.1.3 HfB_2 formation using excessive Mg and B_2O_3

Figure 5.3 illustrates the effect of using excessive amounts of Mg on the phase evolution in HfB_2 samples obtained from 4 h heating in $MgCl_2$ at 1000°C. When

20 wt% excessive Mg was used (Figure 5.3(b)), the HfO_2 and $Mg_3B_2O_6$ peaks decreased substantially compared to the case of using a stoichiometric amount of Mg (Figure 5.3(a)). When 80 wt% excessive Mg was used (Figure 5.3(c)), $Mg_3B_2O_6$ disappeared, and both the HfB_2 and MgO peaks increased. However, a considerable amount of residual HfO_2 still remained due to the absence of B_2O_3, which was lost through evaporation [117, 176]. This was verified by later experiment results shown in Figure 5.4.

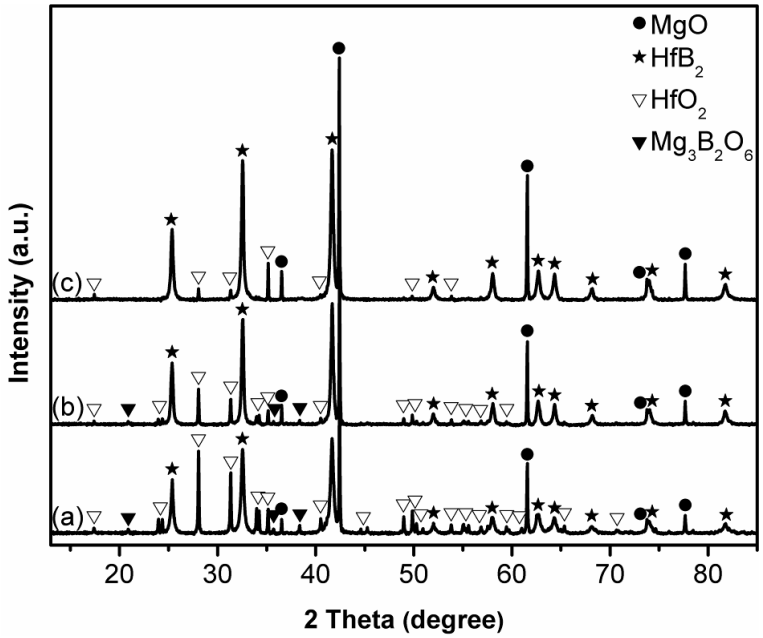

Figure 5.3 XRD patterns of samples after 4 h heating at 1000°C in $MgCl_2$ using: (a) 0, (b) 20, and (c) 80 wt% excessive Mg, respectively.

It can be seen from Figure 5.4 that, 10 wt% excessive B_2O_3, in conjunction with 80 wt% excessive Mg, led to an increase in both the HfB_2 and MgO peaks and to minor HfO_2 remaining. Furthermore, when 20 wt% excessive B_2O_3 was used, HfO_2 disappeared completely, and only HfB_2 and the byproduct MgO were formed, suggesting that using appropriately excessive amounts of B_2O_3, along with excessive Mg, was necessary to complete the magnesiothermic reduction and HfB_2 formation.

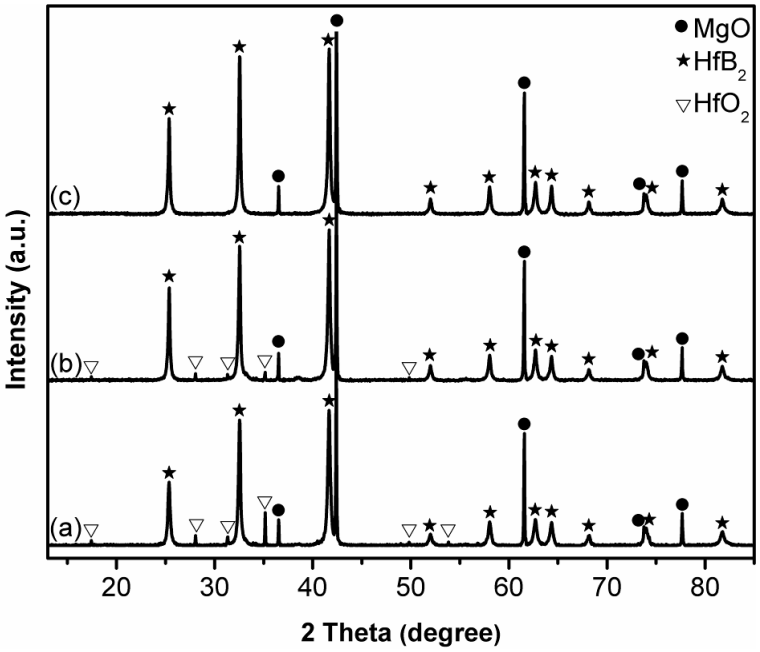

Figure 5.4 XRD patterns of samples resultant from 4 h heating in $MgCl_2$ at 1000°C, using 80 wt% excessive Mg and (a) 0, (b) 10, and (c) 20 wt% excessive B_2O_3.

5.1.4 Effect of time on HfB_2 formation and further optimisation of the reaction conditions

As discussed above, the HfB_2 formation reaction could be completed in $MgCl_2$ after heating for 4 h at 1000°C using 80 wt% excessive Mg and 20 wt% excessive B_2O_3 (Figure 5.5(b)/Figure 5.4(c)). When the time was reduced to 3 h, as shown in Figure 5.5 (a), a significant amount of residual HfO_2, along with a small amount of $Mg_3B_2O_6$ remained, indicating that the magnesiothermic reduction and HfB_2 formation were incomplete. Hence, a heating time of 4 h was essential for completing the HfB_2 formation reaction under these conditions.

Shown in Figure 5.6 are XRD patterns of samples with 80 wt% excessive Mg and 20 wt% excessive B_2O_3 after heating in $MgCl_2$ at 950°C for different times. Increasing the reaction time from 4 to 6 h (Figures 5.6(a)&(b)) resulted in much increased HfB_2 and MgO, decreased HfO_2 and complete disappearance of $Mg_3B_2O_6$. Unfortunately, further extending the time to 8 h (Figure 5.6(c)) did not provide any further improvement in the reaction extents, and some HfO_2

remained, which was related to the evaporation loss of B_2O_3 upon prolonged heating. This was verified by the XRD results shown in Figure 5.7, which revealed that in addition to 80 wt% excessive Mg, using 20 to 60 wt% excessive B_2O_3 led to significantly reduced HfO_2 peaks (until they disappeared) and to the completion of the HfB_2 formation reaction (Figure 5.7(c)).

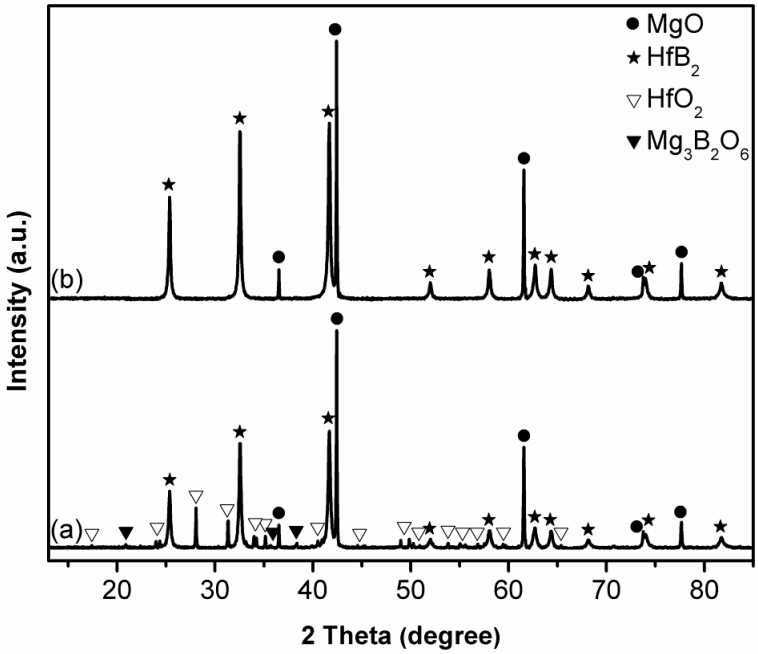

Figure 5.5 XRD patterns of samples resultant from heating the batch powders containing respectively 80 and 20 wt% excessive Mg and B_2O_3 in $MgCl_2$ at 1000°C for (a) 3 h and (b) 4 h.

According to Figure 5.4(c), Figure 5.7(c) and the above discussion, the HfB_2 formation reaction could be completed in $MgCl_2$ after 4 h at 1000°C using 80 wt% excessive Mg and 20 wt% excessive B_2O_3 or after 6 h at 950°C using 80 wt% excessive Mg and 60 wt% excessive B_2O_3. In both cases, HfB_2 was formed along with the MgO byproduct. Thus, after MgO was removed through acid leaching, phase-pure HfB_2 powders were obtained (Figure 5.8).

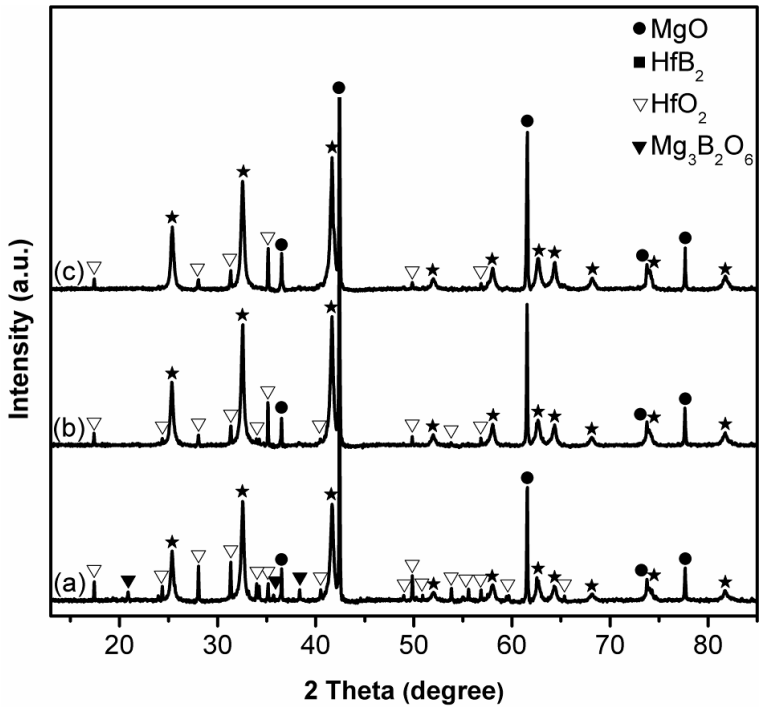

Figure 5.6 XRD patterns of samples resultant from heating the batch powders containing respectively 80 and 20 wt% excessive Mg and B_2O_3 in $MgCl_2$ at 950°C for (a) 4, (b) 6, and (c) 8 h, respectively.

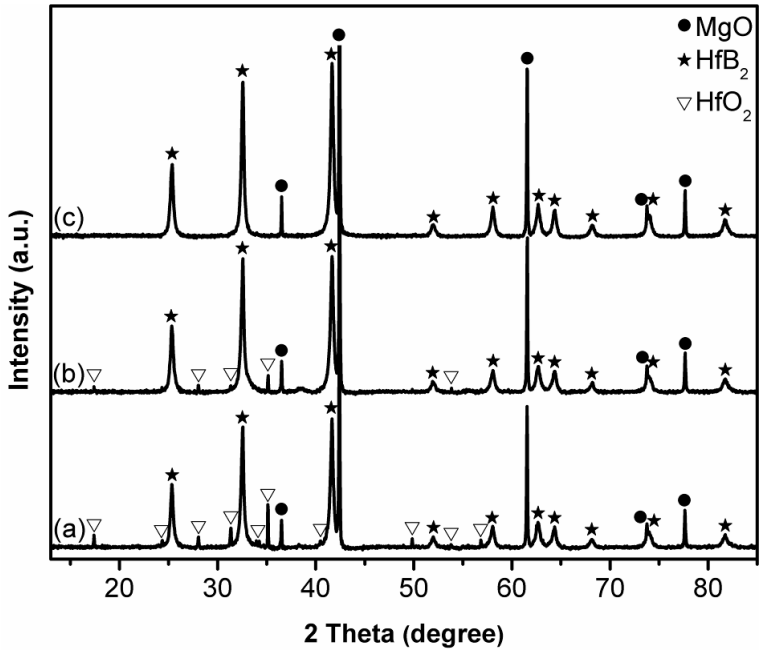

Figure 5.7 XRD patterns of samples resultant from 6 h heating in $MgCl_2$ at 950°C, using 80 wt% excessive Mg and (a) 20, (b) 40, and (c) 60 wt% excessive B_2O_3, respectively.

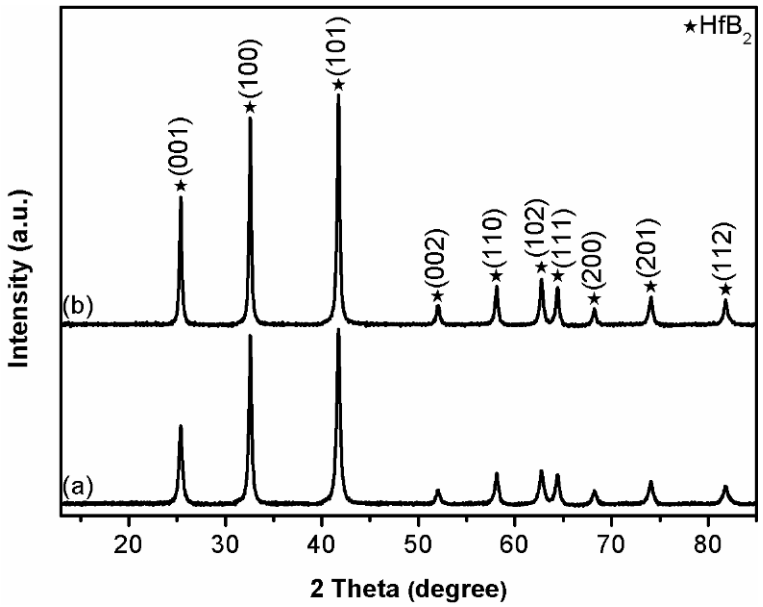

Figure 5.8 XRD patterns of product samples resulting from (a) 6 h heating at 950°C with 80-60 wt% excessive Mg-B_2O_3 and (b) 4 h at 1000°C with 80-20 wt% excessive Mg-B_2O_3 (after water washing and acid leaching).

5.1.5 Microstructural characterisation of the product powders

Figure 5.9 displays SEM and TEM images and EDS results of the HfB_2 product powders corresponding to the XRD results given in Figure 5.8. Spheroidal HfB_2 particles with an average size of approximately 100 nm were produced after 6 h heating at 950°C (Figure 5.9(a)), whereas angular particles with a larger average size of 100-200 nm were produced after 4 h heating at 1000°C (Figure 5.9(b)). The morphology and size differences can be observed more clearly in the corresponding TEM images (Figures 5.9(c)&(d)). These results indicated that the reaction temperature had a greater effect on the morphology and size of the HfB_2 particles than the reaction time. To prepare HfB_2 particles with fine sizes, a lower reaction temperature (in this case, 950°C) is preferred. Regarding the purity level of the product powder, EDS detected Hf and B along with tiny O contamination (the Cu and C peaks were due to the carbon film/Cu grid used for TEM) in both cases, further confirming the formation of phase-pure HfB_2, as previously confirmed by the XRD results (Figure 5.8).

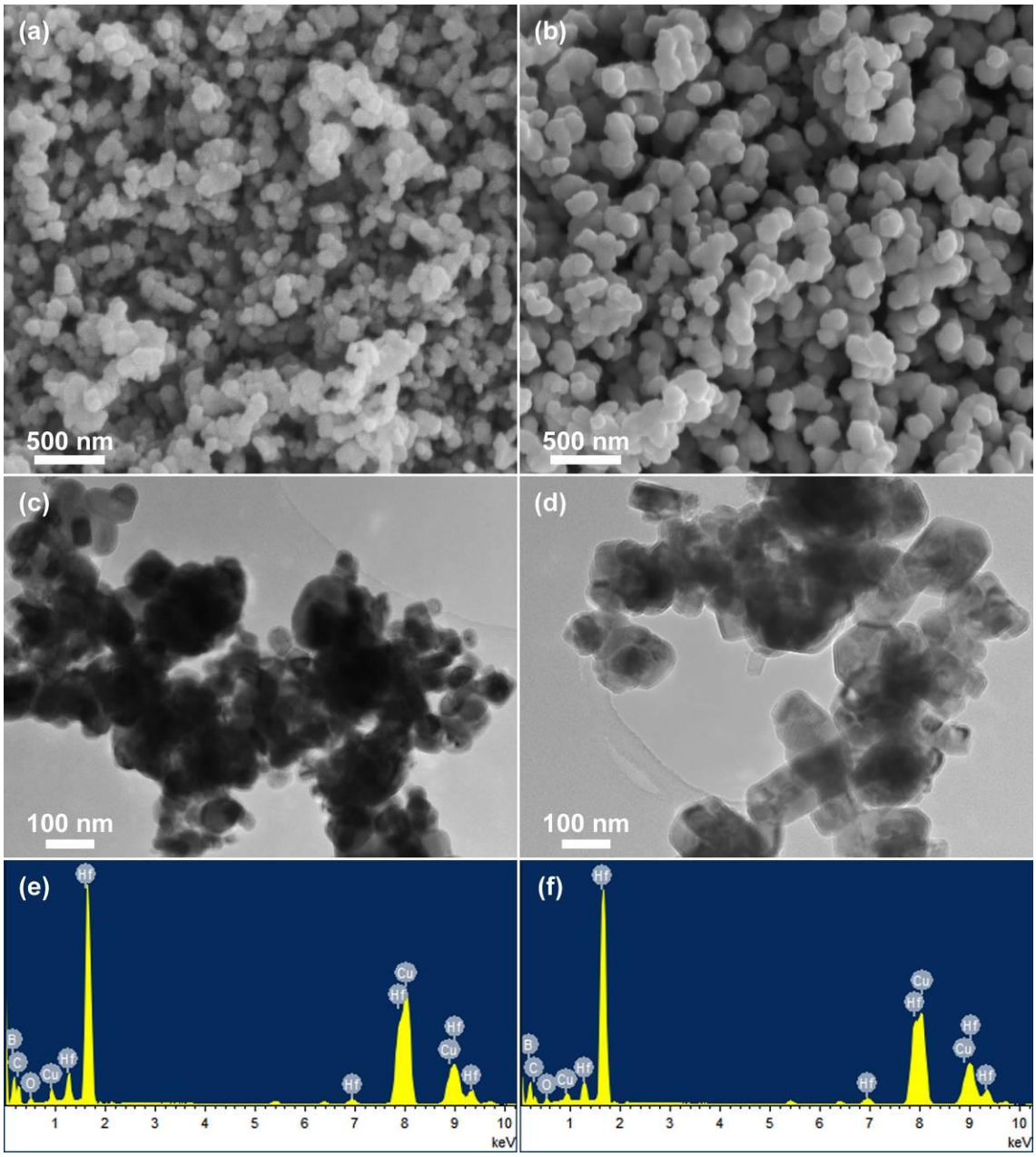

Figure 5.9 SEM/TEM images and EDS results of the HfB_2 product powders corresponding to the XRD patterns shown in Figure 5.8: (a, c and e) 6 h at 950°C and (b, d and f) 4 h at 1000°C.

5.2 Reaction mechanisms and further discussion

Reaction (3.2) indicates the overall reaction process. However, several individual reaction steps were most likely involved, which, based on Figures 5.1-5.9, could be considered as follows (using $MgCl_2$ as an example).

At the test temperatures, $MgCl_2$ melted initially, forming a liquid pool in which Mg slightly dissolved, diffused to the two reactants, B_2O_3 and HfO_2, and

subsequently reduced them to B (Reaction (5.1)) and Hf (Reaction (5.2)), respectively. In the case of Reaction (5.1), the reactant B_2O_3 was in a liquid state (due to its low melting point: ~450°C), thus, Reaction (5.1) was essentially a liquid-liquid reaction. In this case, the resultant B would not retain the morphologies and sizes of the original B_2O_3 or Mg.

$$B_2O_3 \text{ (melt)} + 3Mg \text{ (dissolved)} = 2B + 3MgO \quad (5.1)$$

$$HfO_2 + 2Mg \text{ (dissolved)} = Hf + 2MgO \quad (5.2)$$

In the case of Reaction (5.2), however, the reactant HfO_2 could be in a solid and/or a liquid state, depending on its solubility in the molten salt used. Therefore, for Reaction (5.2), two parallel reactions could occur simultaneously, as indicated by Reactions (5.3) and (5.4). Unfortunately, the exact solubility values of HfO_2 in the three molten salts are not available in the literature. Hf powder was prepared under the same heating conditions from the magnesiothermic reduction of HfO_2 (corresponding to Reaction (5.2)) in molten chloride salts (e.g. $MgCl_2$).

$$HfO_2 \text{ (solid)} + 2Mg \text{ (dissolved)} = Hf + 2MgO \quad (5.3)$$

$$HfO_2 \text{ (dissolved)} + 2Mg \text{ (dissolved)} = Hf + 2MgO \quad (5.4)$$

As shown in Figure 5.10(a), the raw material B_2O_3 powder consisted of micron-sized flake-like particles. As discussed above, since B_2O_3 melted at the test temperatures, its morphology/size would not affect the morphology/size of the product powders. The morphology and size of the as-synthesised Hf particles (Figures 5.10(c)&(d)) appeared to be quite different from those of the raw material HfO_2 particles (Figure 5.10(b)), indicating that HfO_2 did exhibit some solubility in the molten chloride salts. Therefore, in this work, Reaction (5.4) controlled by the “dissolution-precipitation” mechanism, was much more

dominant than Reaction (5.3) controlled by the “template-growth” mechanism.

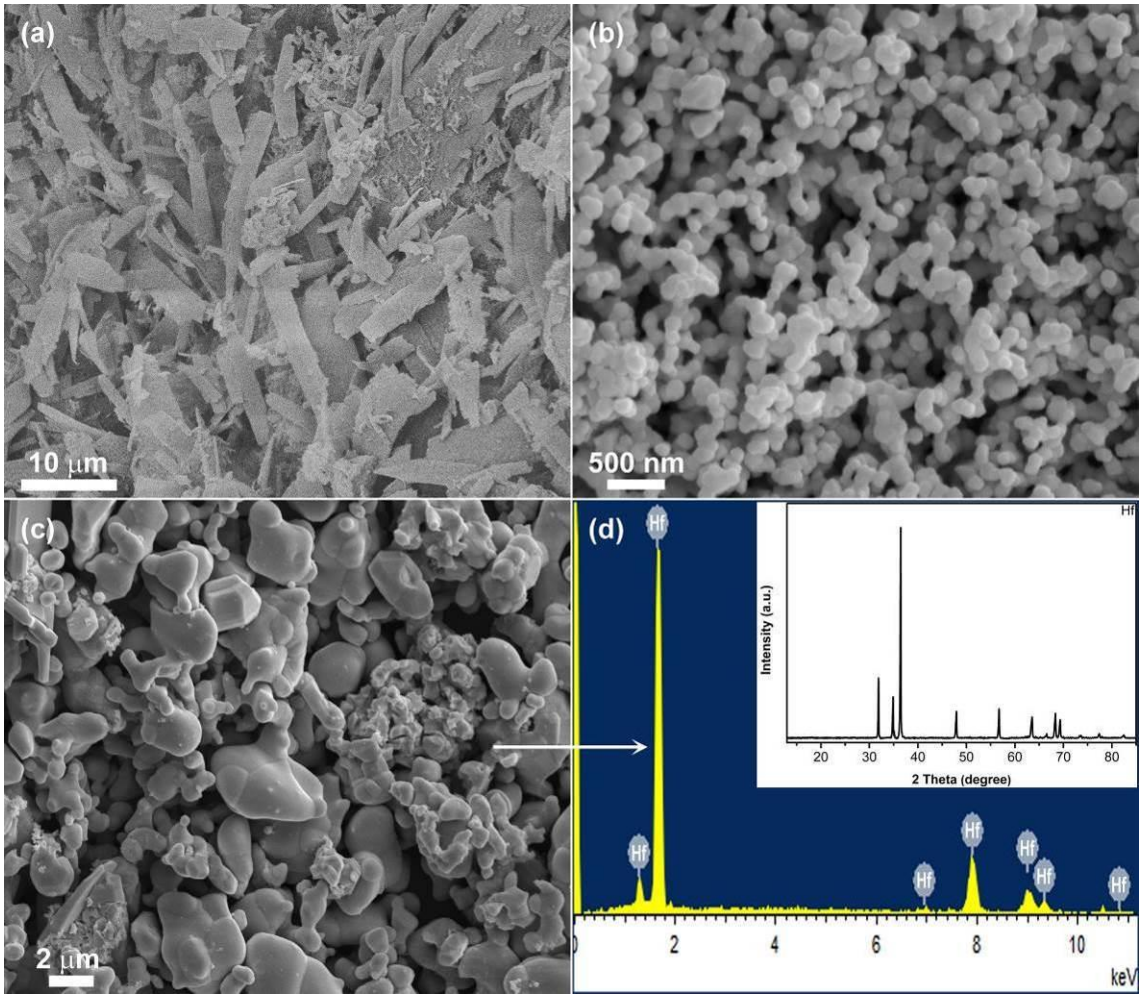

Figure 5.10 SEM images of the as-received (a) B_2O_3 and (b) HfO_2 powders, and (c) Hf prepared *via* magnesiothermic reduction of HfO_2 (Reaction (5.2)) in $MgCl_2$ at 950°C for 6 h and (d) corresponding EDS as well as (inset) XRD results.

The solubility values of Hf in molten chloride salts are not known. Sample of HfC coating on the CFs was prepared in the molten $MgCl_2$. As shown in Figure 5.11, the product sample retained the fibrous shape of the uncoated CFs but with rougher surfaces (Figure 5.11(a)). The composition of the product sample was further revealed to be HfC from the EDS measurements and XRD pattern (Figure 5.11(b)). As discussed in Section 4.2.2, in the HfO_2-Mg-CFs system, the resultant Hf (Reaction (5.5)/Reaction (5.2)) reacted with the CFs in the molten salt to form HfC on the fibres (Reaction (5.6)), following a “template-growth” mechanism, in which the CFs acted as not only a carbon source but also a

template for HfC growth. Similarly to the findings from the MSS study on B_4C and TiC coatings on CFs, Hf was considered to be able to at least partially dissolve in molten chloride salts (although the actual solubility might be very low).

$$HfO_2 + 2Mg\ (dissolved) = Hf + 2MgO \quad (5.5)$$

$$Hf + C = HfC \quad (5.6)$$

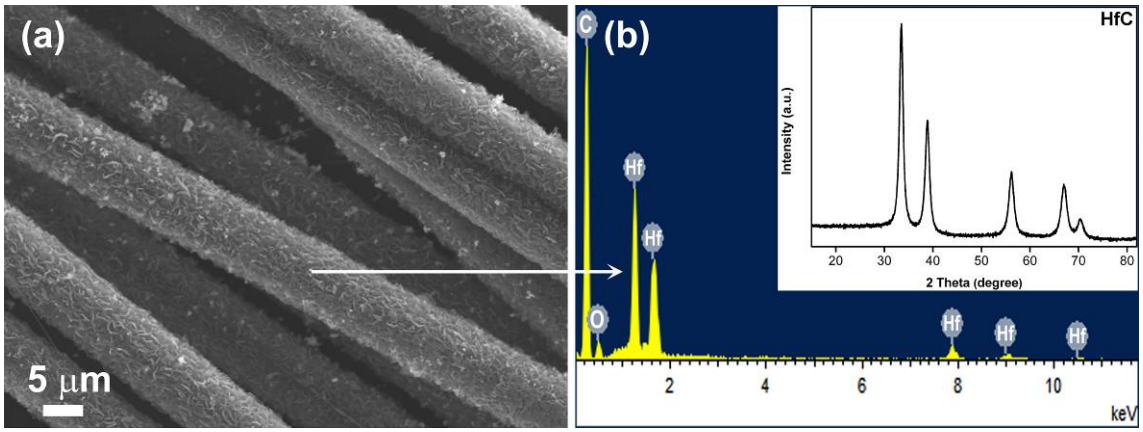

Figure 5.11 SEM image (a), EDS (b) and (inset) XRD pattern of the product sample resultant from heating the mixture of HfO_2, Mg and CFs in $MgCl_2$ at 950°C for 6 h.

Therefore, during the reaction process, the resultant B and Hf would partially dissolve in the molten salt medium, diffuse through it and finally react with each other to form HfB_2 *via* the "dissolution-precipitation" mechanism (Reaction (5.7)).

$$Hf\ (dissolved\ in\ the\ salt) + 2B\ (dissolved\ in\ the\ salt) = HfB_2 \quad (5.7)$$

Additionally, according to previous findings from a study on the borothermal reduction of HfO_2 [131], the reduction of HfO_2 by B at the test temperatures was thermodynamically favourable. Hence, the resultant B could also partially dissolve in the molten salt and react directly with the portions of HfO_2 dissolved in the molten salt and unreduced solid HfO_2 to form additional HfB_2 according to Reactions (5.8) and (5.9), which were controlled by the "dissolution-precipitation" mechanism and "template-growth" mechanism, respectively.

$$3HfO_2\ (dissovled) + 10B\ (dissolved) = 3HfB_2 + 2B_2O_3 \quad (5.8)$$

$$3HfO_2\ (solid) + 10B\ (dissolved) = 3HfB_2 + 2B_2O_3 \qquad (5.9)$$

According to the individual reaction steps indicated by Reactions (5.1)-(5.9) and discussed above, the “dissolution-precipitation” mechanism was more dominant than the “template-growth” mechanism in the whole MSS process.

5.3 Conclusion

Submicron-sized HfB_2 powder was successfully synthesised in chloride salts *via* the magnesiothermic reduction of HfO_2 and B_2O_3. The effects of salt type, initial batch composition, and heating temperature/time on the synthesis process were examined. Compared to NaCl and KCl, $MgCl_2$ accelerated the overall reaction process more effectively. Phase-pure HfB_2 powder with particle size of 100-200 nm could be prepared in $MgCl_2$ after 6 h heating at 950°C using respectively 80 and 60 wt% excessive Mg and B_2O_3 or 4 h heating at 1000°C using respectively 80 and 20 wt% excessive Mg and B_2O_3. The yield of phase-pure HfB_2 after acid leaching was calculated to be ~92 wt%. The “dissolution-precipitation” mechanism was found to be more dominant than the “template-growth” mechanism in the overall MSS process.

Chapter 6 Low-Temperature Preparation of LaB_6 Fine Powder *via* Magnesiothermic Reduction in Molten Salt

LaB_6 fine powder was synthesised from La_2O_3 and B_2O_3 using the molten-salt-assisted magnesiothermic reduction technique. In this chapter, the effects of salt type, Mg amount, heating temperature and holding time on the synthesis were investigated, and the relevant reaction mechanisms were discussed.

6.1 Results and discussion

6.1.1 Effect of salt type on LaB_6 formation

Figure 6.1 shows XRD patterns of samples with stoichiometric compositions after 4 h heating at 850°C in different salts (here, and in the cases of Figures 6.2-6.4 below, the samples had been water-washed but not acid-leached). When KCl was used (Figure 6.1(a)), LaB_6 was clearly already formed, together with the MgO byproduct resulting from the redox reactions between the oxide reactants and Mg (see Section 6.2 below). However, a small amount of intermediate $LaBO_3$ (Reaction (6.1)) and $Mg_3B_2O_6$ remained.

$$La_2O_3 + B_2O_3 = 2LaBO_3 \quad (6.1)$$

Upon using NaCl instead of KCl, the LaB_6 and MgO peaks increased, whereas the $Mg_3B_2O_6$ and $LaBO_3$ peaks decreased (Figure 6.1(b)), revealing enhanced extents of the magnesiothermic reduction and LaB_6 formation. Nevertheless, another intermediate phase, LaOCl, was formed under these conditions, as a result of the chlorination of La_2O_3 by molten NaCl (Reaction (6.2)) [284, 285]. When $MgCl_2$ was used to replace NaCl (Figure 6.1(c)), the LaB_6 and MgO peaks

further increased, whereas the $Mg_3B_2O_6$ and LaOCl (Reaction (6.3)) [284, 285] peaks further decreased. Moreover, no $LaBO_3$ was detected. Hence, the extents of magnesiothermic reduction and LaB_6 formation further increased when using $MgCl_2$. Unlike when KCl and NaCl were used, minor La_2O_3 was detected in this case, indicating the incomplete reaction between La_2O_3 and $MgCl_2$ at this temperature (see Section 6.2 below). $MgCl_2$ having the best accelerating effect on LaB_6 formation among the three chloride salts was due to the same reaction discussed previously in the MSS studies on TiB_2 and HfB_2.

$$La_2O_3 + 2NaCl = 2LaOCl + Na_2O \quad (6.2)$$

$$La_2O_3 + MgCl_2 = 2LaOCl + MgO \quad (6.3)$$

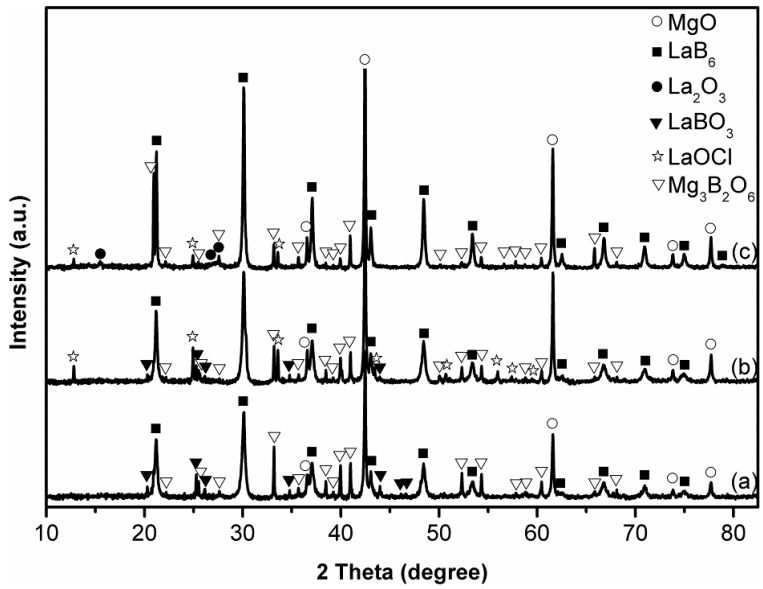

Figure 6.1 XRD patterns of samples resultant from heating batch powders with stoichiometric compositions for 4 h at 850°C in (a) KCl, (b) NaCl, and (c) $MgCl_2$.

6.1.2 Effect of heating temperature on LaB_6 formation

Figure 6.2 shows XRD patterns of the stoichiometric samples after 4 h heating in $MgCl_2$ at different temperatures. At 850°C, as described above, LaB_6 was already formed evidently, though MgO, $Mg_3B_2O_6$, La_2O_3 and LaOCl were also present (Figure 6.2(a)/Figure 6.1(c)). When the temperature increased to 900°C (Figure 6.2(b)), La_2O_3 disappeared, and the LaB_6 and MgO peaks increased

concomitantly with the decrease in the $Mg_3B_2O_6$ and LaOCl peaks, indicating enhanced reaction extents. However, upon further increasing the temperature to 1000°C (Figure 6.2(c)), the $Mg_3B_2O_6$ and LaOCl peaks started to increase again, indicating reduced extents of the magnesiothermic reduction and LaB_6 formation. As discussed in the MSS studies on TiB_2 and HfB_2, this was related to the evaporation loss of Mg at this relatively high temperature, suggesting that excessive Mg had to be used to complete the LaB_6 formation reaction.

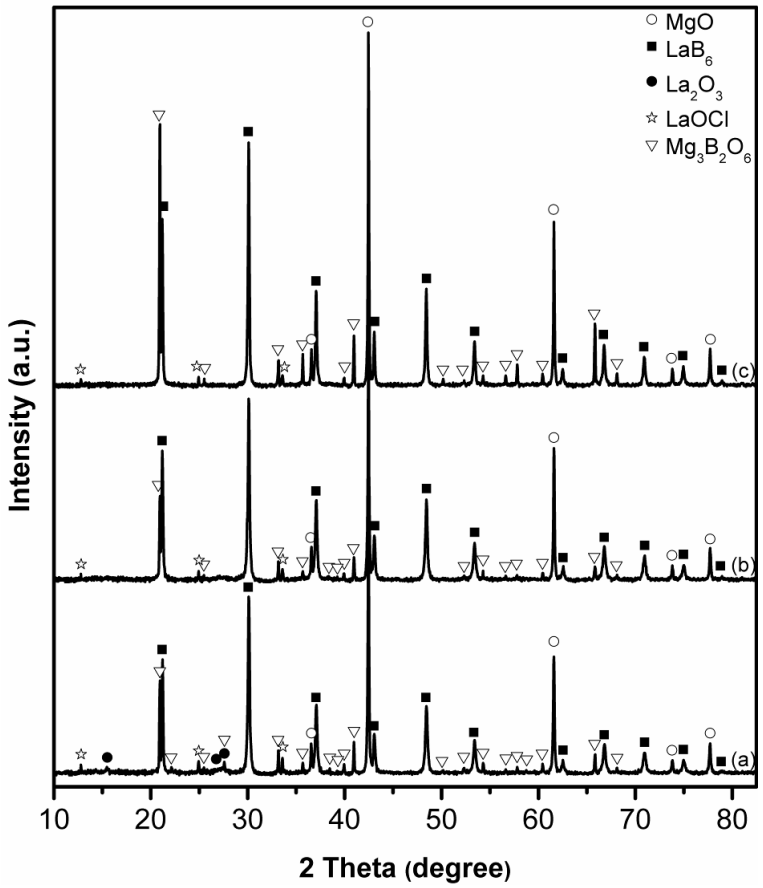

Figure 6.2 XRD patterns of samples resultant from heating batch powders with stoichiometric compositions for 4 h in $MgCl_2$ at (a) 850, (b) 900, and (c) 1000°C.

6.1.3 Effect of excessive Mg on LaB_6 formation

Figure 6.3 illustrates the effects of excessive amounts of Mg on the magnesiothermic reduction and LaB_6 formation in samples resultant from heating in $MgCl_2$ at 1000°C for 4 h. When 10 mol% excessive Mg was used, $Mg_3B_2O_6$ and LaOCl remained (Figure 6.3(b)), but their contents were

substantially lower than when a stoichiometric amount of Mg was used (Figure 6.3(a)), indicating enhanced La_2O_3 and B_2O_3 reductions and LaB_6 formation. When the excessive amount of Mg was increased to 20 mol%, only LaB_6 and MgO were detected while no other phases could be observed (Figure 6.3(c)), confirming the completion of the LaB_6 formation reaction.

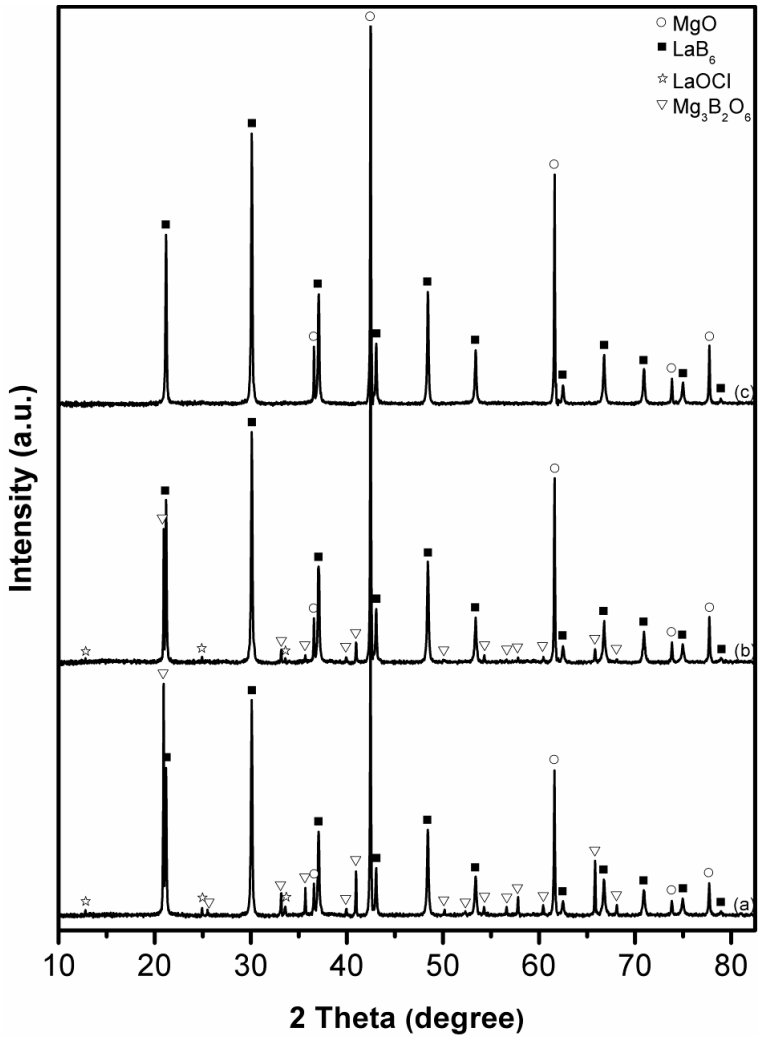

Figure 6.3 XRD patterns of samples resultant from heating batch powders for 4 h in $MgCl_2$ at 1000°C with (a) 0, (b) 10, and (c) 20 mol% excessive Mg.

6.1.4 Effect of heating time on LaB_6 formation

Figure 6.4 presents XRD patterns of the samples with 20 mol% excessive Mg after heating in $MgCl_2$ at 900°C for different durations. When the time was increased from 4 to 4.5 h, the LaB_6 and MgO peaks increased, whereas the $Mg_3B_2O_6$ and LaOCl peaks decreased. After further increasing the time to 5 h,

only the LaB_6 and MgO peaks were detected, as all other peaks of the impurity/intermediate phases had disappeared.

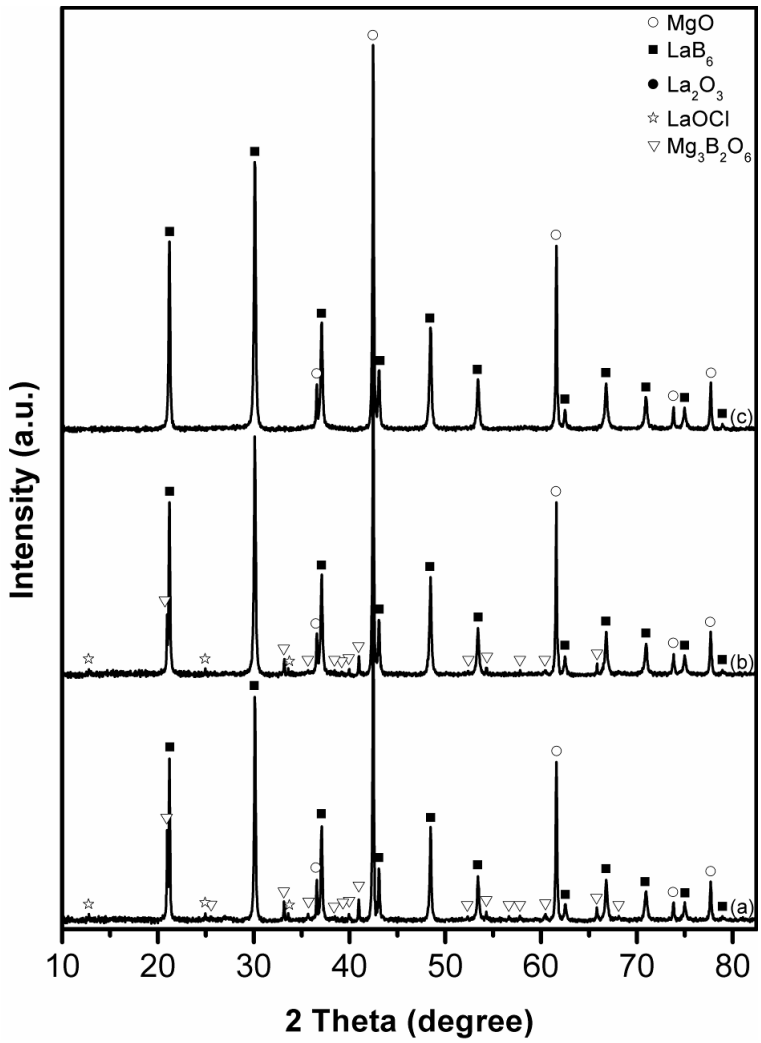

Figure 6.4 XRD patterns of samples resultant from heating batch powders with 20 mol% excessive Mg in $MgCl_2$ at 900°C for (a) 4, (b) 4.5, and (d) 5 h.

According to Figure 6.3(c) and Figure 6.4(c) and described above, when 20 mol% excessive Mg was used, the LaB_6 formation reactions were completed in $MgCl_2$ after heating for 4 h at 1000°C or 5 h at 900°C. Under both conditions, only LaB_6 and MgO byproduct were formed. After MgO was leached out with acid, phase-pure LaB_6 powders were finally obtained (Figure 6.5).

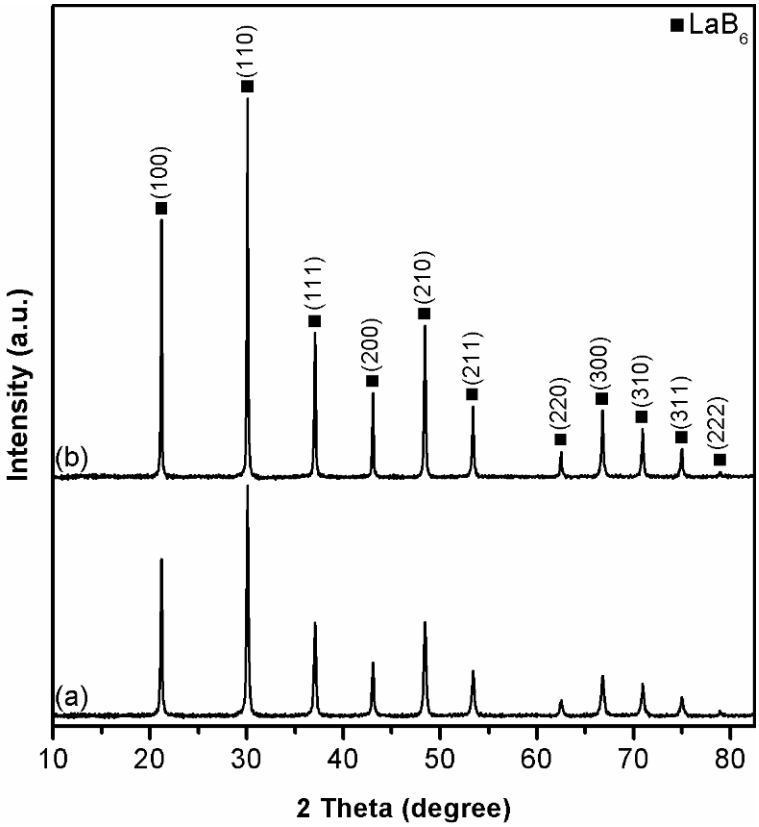

Figure 6.5 XRD patterns of product samples obtained after (a) 5 h heating at 900°C and (b) 4 h heating at 1000°C in $MgCl_2$ (after water washing and acid leaching).

6.1.5 Microstructures and phase composition of LaB_6 product powders

Figure 6.6 displays SEM images and EDS results of the as-prepared LaB_6 powders, the XRD patterns of which are shown in Figure 6.5. The LaB_6 particles obtained after heating at 900°C for 5 h were spheroidal with an average size of ~100 nm (Figure 6.6(a)), whereas those obtained from heating at 1000°C for 4 h were angular with a relatively larger average size of ~200 nm (Figure 6.6(b)). In both cases, EDS revealed with presence of only La and B (along with tiny O contaminant) (Figures 6.6(c)&(d)), further confirming the formation of phase-pure LaB_6 in both cases, as already revealed by XRD (Figure 6.5).

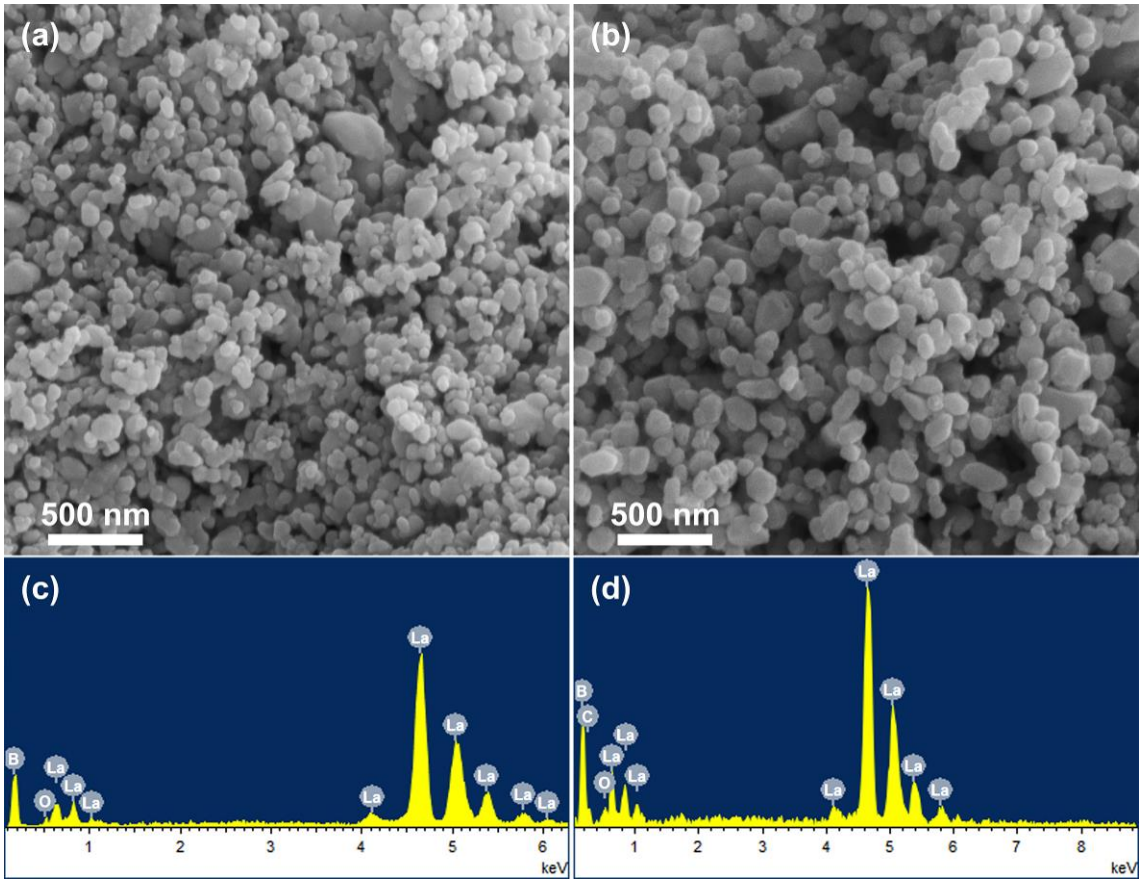

Figure 6.6 SEM images (a, b) and the corresponding EDS spectra (c, d) of the LaB_6 powders, the XRD patterns of which are shown in Figure 6.5: 5 h at 900°C (a, c) and 4 h at 1000°C (b, d) in $MgCl_2$.

6.2 Reaction mechanism and further discussion

As shown in Figures 6.1-6.4, the intermediate LaOCl appeared in the fired samples, which was attributed to the initial reaction between La_2O_3 and $MgCl_2$ (Reaction (6.3)). To better understand the formation mechanism, La_2O_3 powder was heated for 4 h in $MgCl_2$ at 850 or 1000°C and similarly water-washed and further characterised using XRD and SEM. As shown in Figure 6.7(a), at 850°C, LaOCl and MgO were formed, along with minor residual La_2O_3. However, when the temperature was increased to 1000°C (Figure 6.7(b)), the La_2O_3 peak disappeared, and the LaOCl and MgO peaks increased, indicating the complete conversion of La_2O_3 to LaOCl.

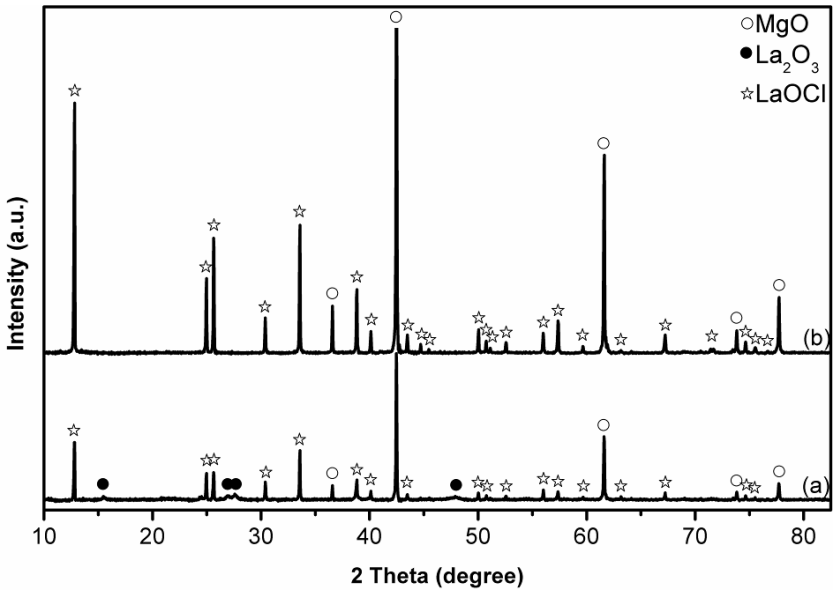

Figure 6.7 XRD patterns of samples resultant from heating La_2O_3 powder for 4 h in $MgCl_2$ at (a) 850 and (b) 1000°C.

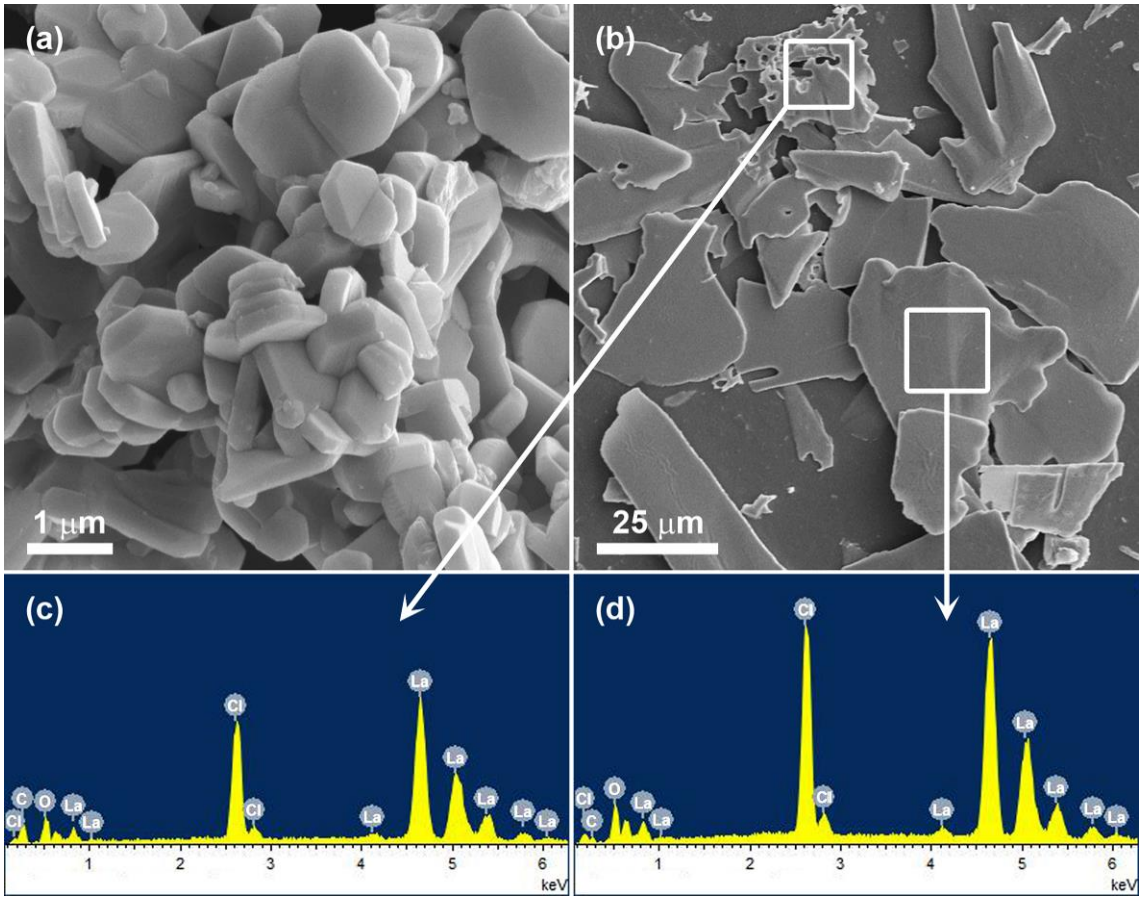

Figure 6.8 SEM images of (a) La_2O_3 raw material particles and (b) LaOCl obtained after heating the La_2O_3 powder for 4 h at 1000°C in $MgCl_2$ (after leaching out MgO) and (c, d) EDS spectra of the selected areas in (b).

Figure 6.8, as an example, compares the microstructural morphologies of the as-received La_2O_3 particles and the LaOCl obtained after heating La_2O_3 powder

for 4 h at 1000°C in $MgCl_2$. As shown in Figure 6.8(a), the raw La_2O_3 particles had a hexagonal morphology with an average size of ~1 μm. By contrast, after being heated for 4 h at 1000°C in $MgCl_2$, the particles changed to irregular platelet-shaped LaOCl particles (as confirmed by the EDS results, Figures 6.8(c)&(d), along with the XRD patterns in Figure 6.7(b)). A comparison between Figure 6.8 and Figure 6.6 revealed that the as-synthesised LaB_6 particles not only had different morphologies from the La_2O_3 and LaOCl particles but also were much smaller than them, indicating that neither La_2O_3 nor LaOCl had acted as a direct template for the MSS of LaB_6. Based on these and other results presented above (Figures 6.1-6.8), the reaction mechanisms during the present MSS (using $MgCl_2$ as an example) can be discussed as follows.

At the test temperatures, $MgCl_2$ initially melted, forming a molten salt pool in which La_2O_3 reacted with $MgCl_2$ to form LaOCl (Reaction (6.3)), which partially dissolved in the molten chloride salts [286]. The dissolved Mg in the molten $MgCl_2$ salt [276] reacted with the dissolved LaOCl and molten B_2O_3 according to Reactions (6.4) and (6.5), respectively, forming elemental La and B, which further reacted with each other to form the final LaB_6 product according to Reaction (6.6).

$$2LaOCl + 3Mg = 2La + 3MgCl_2 + MgO \quad (6.4)$$

$$B_2O_3 + 3Mg = 2B + 3MgO \quad (6.5)$$

$$La + 6B = LaB_6 \quad (6.6)$$

6.3 Conclusion

LaB_6 fine powder was successfully synthesised from La_2O_3 and B_2O_3 *via* molten-salt-mediated magnesiothermic reduction. The effects of salt type, Mg amount, and heating temperature/time on the formation process were examined.

Of the three chloride salts, $MgCl_2$ showed the best accelerating effect. When 20 mol% excessive Mg was used, phase-pure LaB_6 fine particles were synthesised after heating at 900°C for 5 h (~100 nm) or at 1000°C for 4 h (~200 nm). These conditions are much less harsh than those required by most other techniques reported to date.

Chapter 7 Low-Temperature Synthesis of CaB_6 Nanoparticles *via* Magnesiothermic Reduction in Molten Salt

Calcium hexaboride (CaB_6) nanoparticles were prepared *via* low temperature magnesiothermic reduction of CaO and B_2O_3 in molten NaCl, KCl or $CaCl_2$. The effects of salt type, Mg amount, and firing temperature and time on the reaction extents were examined, and the responsible reaction mechanisms discussed. Under an identical firing condition, $CaCl_2$ facilitated the overall synthesis more effectively than the other two salts. In the case of using 20 mol% excessive Mg, phase-pure CaB_6 nanoparticles of ~50 nm were formed in $CaCl_2$ after 6 h at 800°C. The “dissolution-precipitation” mechanism is believed to be responsible for the MSS of high quality nanosized CaB_6 particles at such a low temperature.

7.1 Results and discussion

7.1.1 CaB_6 formation in different salts

Figure 7.1 shows XRD patterns of samples of stoichiometric composition after 4 h firing in different salts at 850°C. In the case of using NaCl or KCl (Figures 7.1(a)&(b)), the intermediate $Mg_3B_2O_6$ appeared as the primary phase, along with a little CaB_6, indicating the overall low extents of the magnesiothermic reduction and CaB_6 formation in either of these two salts. $Mg_3B_2O_6$ was also identified with CaB_6 in the case of using $CaCl_2$ (Figure 7.1(c)), however, the former decreased whereas the latter increased substantially, compared to the cases of using the other two salts, revealing the enhanced reaction extents. When $MgCl_2$ was used, no $Mg_3B_2O_6$ was detected, but significant amounts of

MgB_4 were formed, along with small amounts of CaB_6. The formation of MgB_4 was considered to be related to the reaction of Mg with B formed in the molten salt (Reaction (7.1)) [287, 288]. These results suggested the best effect of $CaCl_2$ among the four salts in accelerating the magnesiothermic reduction as well as CaB_6 formation.

$$Mg + XB = MgB_X \ (X = 2, 4, 6) \qquad (7.1)$$

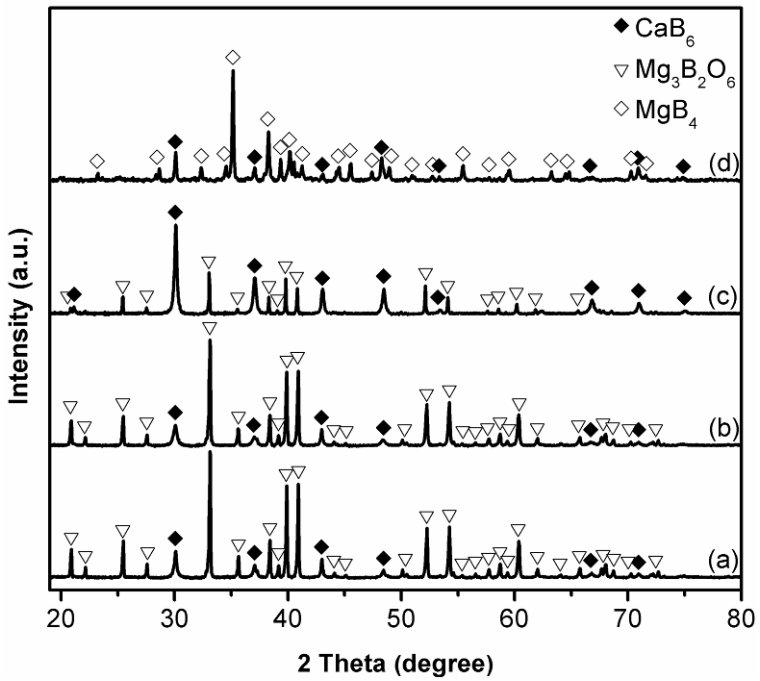

Figure 7.1 XRD patterns of samples of stoichiometric composition after 4 h firing at 850°C in (a) NaCl, (b) KCl, (c) $CaCl_2$, and (d) $MgCl_2$.

As confirmed by our previous studies on MSS of other borides, the solubility of a reactant in the molten salt medium is key in the MSS process. The best accelerating effect of molten $CaCl_2$ demonstrated by Figure 7.1 and described above was attributable mainly to the greater solubility values of CaO and Mg in it than in the other salts [276, 289], which facilitated the magnesiothermic reduction and other reactions involved in CaB_6 formation.

7.1.2 CaB_6 formation at different temperatures

Given in Figure 7.2 are XRD patterns of samples of stoichiometric composition

after 4 h firing in $CaCl_2$ at different temperatures. CaB_6 already started to form evidently at 800°C (Figure 7.2(a)), but much $Mg_3B_2O_6$ still remained. Increasing the temperature to 900°C led to considerable decrease in $Mg_3B_2O_6$ and increase in CaB_6, suggesting much improved reaction extents (Figure 7.2(b)). However, further increasing the temperature to 1000°C adversely caused the increase in $Mg_3B_2O_6$ but decrease in CaB_6, i.e., reduced extents of the magnesiothermic reduction and CaB_6 formation (Figure 7.2(c)). This was due to the evaporation loss of Mg at this relatively high temperature [139, 144, 275], as similarly observed and discussed in our previous MSS studies, and further verified below.

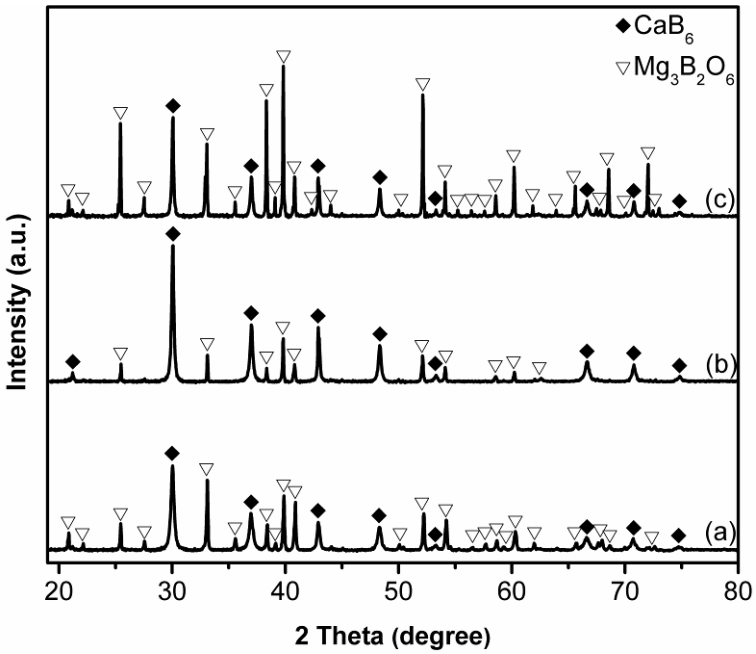

Figure 7.2 XRD patterns of samples of stoichiometric composition after 4 h firing in $CaCl_2$ at (a) 800, (b) 900, and (c) 1000°C.

7.1.3 CaB_6 formation using excessive Mg

To address the issue of Mg evaporation loss mentioned above, the effect of using more Mg than the stoichiometric amount, on the CaB_6 formation was further investigated. Figure 7.3, as an example, illustrates phase evolution in samples after 4 h firing in $CaCl_2$ at 1000°C, with excessive amount of Mg. Use of 10 mol% more Mg resulted in substantial decrease in $Mg_3B_2O_6$ and increase in

CaB_6, revealing quite positive effects from the Mg compensation (Figure 7.3(a)-(b)). Upon using 20 mol% excessive Mg (Figure 7.3(c)), $Mg_3B_2O_6$ disappeared completely, and only CaB_6 was formed, confirming the completion of the magnesiothermic reduction and CaB_6 formation reaction.

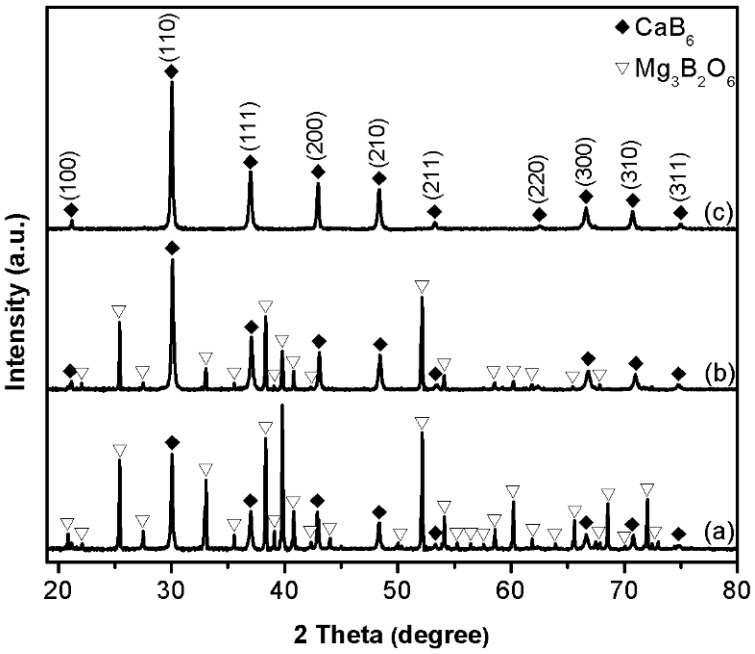

Figure 7.3 XRD patterns of samples using (a) 0, (b) 10, and (c) 20 mol% excessive Mg, after 4 h firing in $CaCl_2$ at 1000°C.

7.1.4 Effect of firing time on CaB_6 formation

Figures 7.4-7.6 illustrate phase formation in samples with different amounts of Mg, after firing in $CaCl_2$ at 800°C for different times. In samples of stoichiometric composition (i.e., with 0 mol% excessive Mg) (Figure 7.4), CaB_6 slightly increased, whereas $Mg_3B_2O_6$ slightly decreased, upon increasing the firing time from 4 to 6 h (Figure 7.4(a)-(b)). On further extending the time to 8 h, however, the former only marginally increased and the latter marginally decreased (Figure 7.4(c)). On the other hand, in the samples fired with 15 mol% excessive Mg (Figure 7.5), $Mg_3B_2O_6$ decreased and CaB_6 increased more evidently with increasing the time. After 8 h, CaB_6 was formed as the primary phase and only small amounts of $Mg_3B_2O_6$ remained (Figure 7.5(c)). These results indicated that

the increase in firing time had more significant effects on the CaB_6 formation in samples using excessive Mg than in samples using the stoichiometric amount of Mg. Nevertheless, phase-pure CaB_6 was still not obtained under either of these conditions, which was addressed by further optimizing the firing conditions.

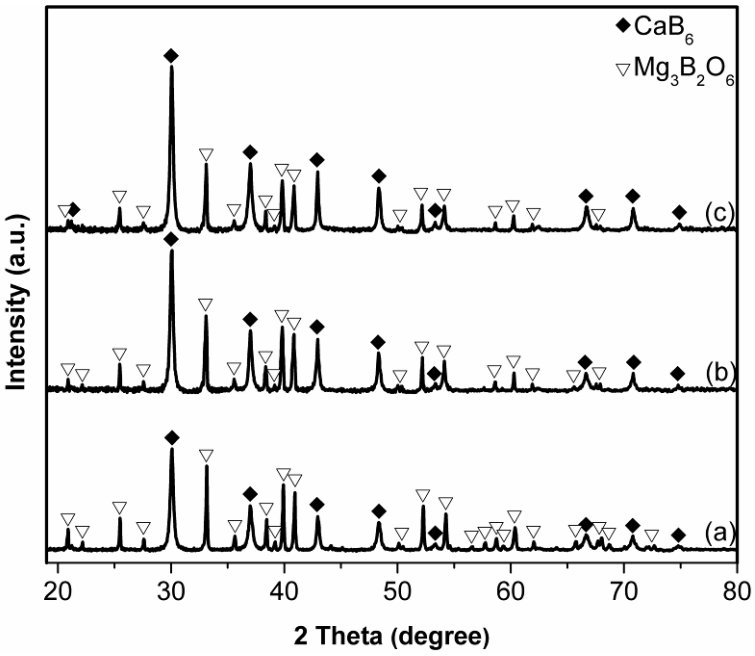

Figure 7.4 XRD patterns of samples using stoichiometric amount of Mg (i.e., 0 mol% excessive Mg) after firing in $CaCl_2$ at 800°C for (a) 4, (b) 6, or (c) 8 h.

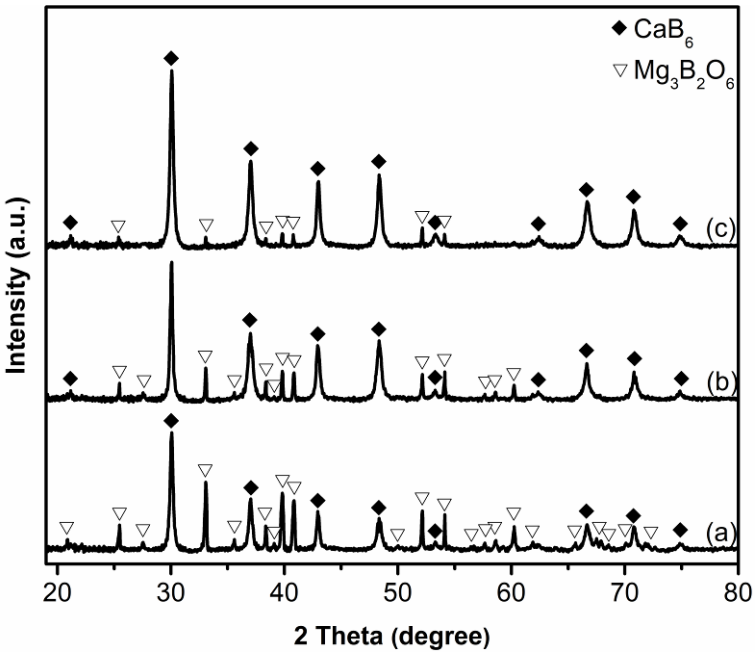

Figure 7.5 XRD patterns of samples using 15 mol% excessive Mg after firing in $CaCl_2$ at 800°C for (a) 4, (b) 6, or (c) 8 h.

As shown in Figure 7.6, upon further increasing the excessive amount of Mg to

20 mol%, the firing time showed much more sensitive effect on the reaction extents. For instance, by increasing the firing time from 4 h by just 1 h (Figure 7.6(a)-(b)), CaB_6 increased and $Mg_3B_2O_6$ decreased considerably. Furthermore, after another 1 h, $Mg_3B_2O_6$ completely disappeared, and only phase-pure CaB_6 was formed (Figure 7.6(c)).

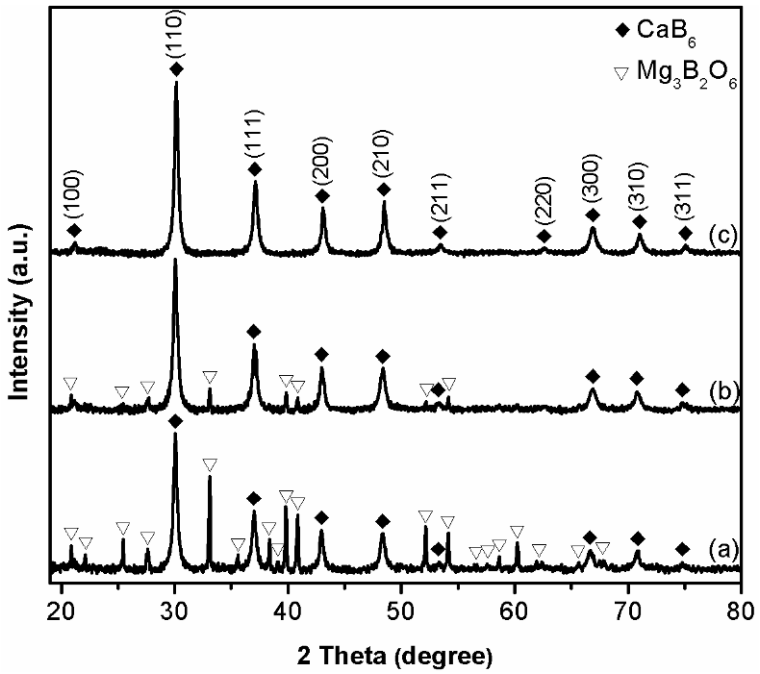

Figure 7.6 XRD patterns of samples using 20 mol% excessive Mg after firing in $CaCl_2$ at 800°C for (a) 4, (b) 5, or (c) 6 h.

7.1.5 Microstructure of CaB_6 product powder

As demonstrated in Figures 7.3(c)&7.6(c) and discussed above, when 20 mol% excessive Mg was used with $CaCl_2$, phase-pure CaB_6 could be prepared after either 4 h firing at 1000°C or 6 h at 800°C. Figure 7.7 presents SEM images and EDS of product powders synthesised under these two conditions. In the sample resultant from 6 h firing at 800°C (Figure 7.7(a)), nanosized particles <100 nm were formed, though they were loosely agglomerated together. By contrast, in the sample resultant from 4 h firing at 1000°C (Figure 7.7(b)), nanosized particles (<100 nm) coexisted with submicron-sized particles (up to 500 nm), indicating significant grain growth at this temperature, despite the shorter firing

time. The size change with the grain growth also suggested that the product particle's size could be controlled at least to certain extents by using the present MSS method. Only Ca and B, along with a trace of O contamination, were detected by EDS (Figures 7.7(c)&(d)) in the samples fired under both conditions, this, in addition to the XRD results in Figures 7.3(c)&7.6(c), further confirmed the formation of essentially phase-pure CaB_6. TEM examination further revealed that CaB_6 particles resultant from 6 h firing at 800°C had an average size of ~50 nm (Figure 7.8(a)). Moreover, EDS only detected Ca and B in these particles, along with tiny O contamination (Figure 7.8(b)), revealing additionally their high purity.

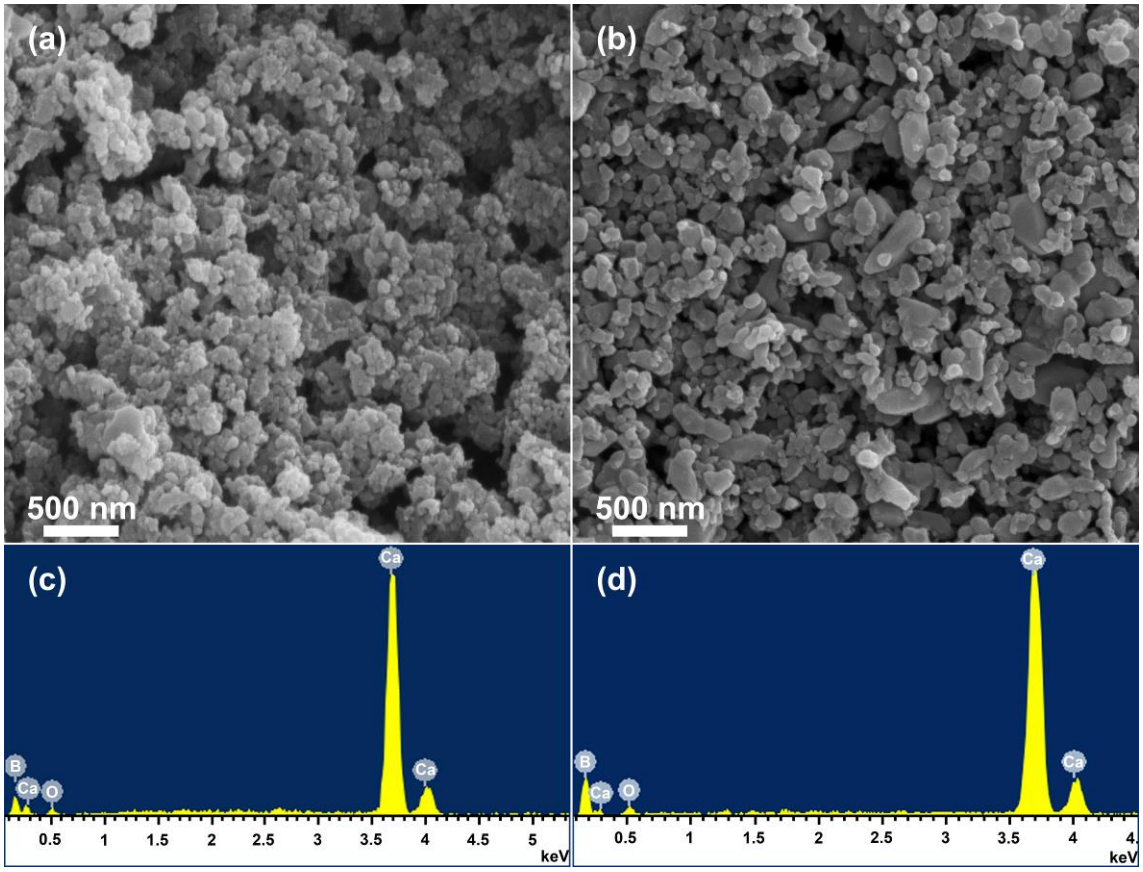

Figure 7.7 SEM images (a, b) and corresponding EDS results (c, d) of CaB_6 powders resultant from (a, c) 6 h firing at 800°C and (b, d) 4 h firing at 1000°C, in $CaCl_2$.

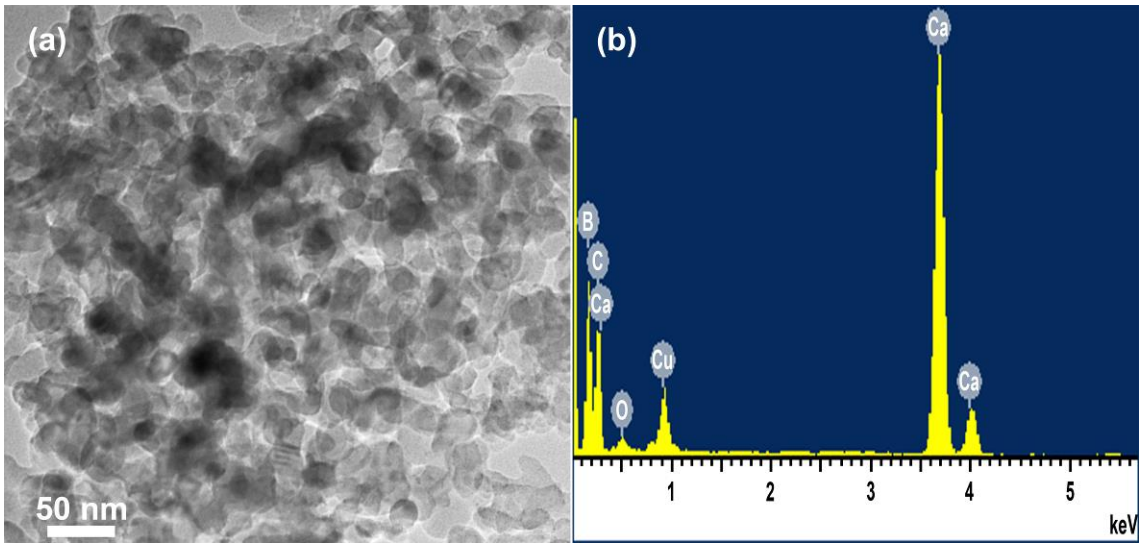

Figure 7.8 TEM and corresponding EDS of CaB_6 nanoparticles resultant from 6 h firing in $CaCl_2$ at 800°C (the small C and Cu peaks arose from the carbon film-Cu TEM grid).

7.1.6 Further discussion and reaction mechanisms

As mentioned earlier, the overall synthesis process of CaB_6 can be indicated by Reaction (3.7). Nevertheless, the actual formation process should be involved with several individual steps. Based on reaction extents and phase formation in different samples fired under different conditions (Figures 7.1-7.8), and previous MSS studies on other borides, the main reactions involved in each individual step can be detailed as follows.

At testing temperatures (800-1000°C), $CaCl_2$ initially melted, forming a desirable molten salt medium in which both Mg and CaO partially dissolved [276, 289], and subsequently reacted, forming a Ca-Mg binary liquid (Ca in this liquid is indicated by (Ca)) and MgO (Reaction (7.2)) [290, 291]. On the other hand, the dissolved Mg also diffused through the molten salt medium to the liquid (dissolved or undissolved in $CaCl_2$) B_2O_3 and then reduced it to B (Reaction (7.3)).

$$CaO\ (dissolved) + Mg\ (dissolved) = (Ca) + MgO \qquad (7.2)$$

$$3Mg\ (dissolved) + B_2O_3\ (l) = 2B + 3MgO \qquad (7.3)$$

Before all of the B_2O_3 was consumed, the unreduced B_2O_3 would react with the MgO from Reactions (7.2) and (7.3) forming the intermediate $Mg_3B_2O_6$ (Reaction (7.4)) (Figures 7.1-7.6). With improving/optimizing the synthesis conditions, e.g., increasing firing temperature or time, and using excessive Mg (Figures 7.1-7.6), the formed $Mg_3B_2O_6$ would be further reduced by Mg dissolved in $CaCl_2$, producing more B and releasing MgO (Reaction (7.5)). Finally, B resultant from Reactions (7.3) and (7.5) reacted with (Ca) from Reaction (7.2), in molten $CaCl_2$, forming the desired CaB_6 (Reaction (7.6)).

$$B_2O_3 \text{ (unreduced)} + 3MgO = Mg_3B_2O_6 \quad (7.4)$$

$$Mg_3B_2O_6 + 3Mg \text{ (dissolved)} = 2B + 6MgO \quad (7.5)$$

$$(Ca) + 6B = CaB_6 \quad (7.6)$$

According to the $CaO\text{-}B_2O_3$ binary phase diagram [292], unreacted CaO could also react with unreduced B_2O_3, forming intermediate calcium borates such as $Ca_3B_2O_6$ (Reaction (7.7)). However, no such a borate phase was detected by XRD (Figures 7.1-7.6), which, along with the detection of $Mg_3B_2O_6$, implied that in the molten salt unreduced B_2O_3 had reacted preferentially with MgO (Reaction (7.4)).

$$3CaO + B_2O_3 = Ca_3B_2O_6 \quad (7.7)$$

Since (Ca) and B were formed from reductions of dissolved CaO and liquid B_2O_3 (or intermediate $Mg_3B_2O_6$) (Reactions (7.2), (7.3)&(7.5)), they would not retain the shapes/sizes of their “parent” precursors. Therefore, CaB_6 product particles from Reaction (7.6) would also lose the original shapes/sizes of raw materials CaO and B_2O_3. This explained the quite different shapes and sizes between as-prepared CaB_6 particles (Figures 7.7&7.8) and raw material CaO (Figure 7.9). These results suggested that the overall formation process of CaB_6 (Reaction

(3.7)) was not dominated by the “template-growth” mechanism, rather, it was essentially completed in the molten salt medium *via* mainly the “dissolution-precipitation” mechanism.

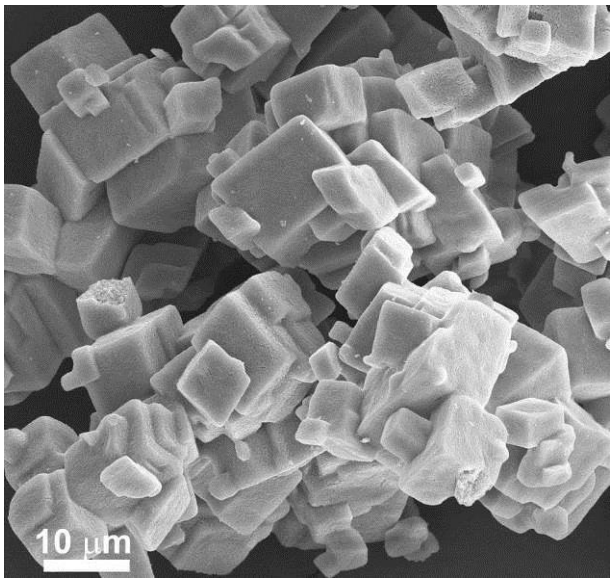

Figure 7.9 SEM image of as-received CaO powder.

The successful preparation of phase-pure CaB_6 nanoparticles at as low as 800°C (Figures 7.3(c)&7.6(c)) was mainly ascribed to the accelerated magnesiothermic reduction (Reactions (7.2), (7.3)&(7.5)) and CaB_6 formation (Reaction (7.6)) in the molten salt medium, and the complete reduction and elimination of $Mg_3B_2O_6$. In the latter case, the intermediate $Mg_3B_2O_6$, after formation, was still separated by and well dispersed in the molten salt, and so still readily accessible and reducible by the dissolved Mg, in particular, when excessive Mg was used (Figures 7.3-7.6). This, as discussed in our previous studies on MSS of other borides, was especially beneficial to the purification of product powder, in view of that it is very difficult to remove $Mg_3B_2O_6$ *via* acid leaching with HCl.

7.2 Conclusion

CaB_6 nanoparticles were synthesized *via* magnesiothermic reduction of CaO

and B_2O_3 in a molten chloride salt (NaCl, KCl or $CaCl_2$). Factors including salt type, Mg amount, and firing temperature/time showed significant effects on the MSS process. Among the three tested chloride salts, $CaCl_2$ formed the most effective reaction medium for the magnesiothermic reduction and subsequent CaB_6 formation. When 20 mol% excessive Mg was used, phase-pure CaB_6 nanoparticles of ~50 nm, were synthesized after 6 h firing in $CaCl_2$ at 800°C. By increasing the temperature to 1000°C, phase-pure CaB_6 powder could also be prepared in $CaCl_2$ after a shorter time period of 4 h. Nevertheless, significant grain growth occurred in this case, resulting in a mixture of nanosized (<100 nm) and submicron-sized (up to 500 nm) particles. The “dissolution-precipitation” mechanism is considered to be responsible for the overall MSS process and low temperature formation of nanosized CaB_6 particles.

Chapter 8 Preparation and Characterisation of Amorphous Boron Powder *via* Molten-Salt-Assisted Magnesiothermic reduction

In this chapter, the molten-salt-assisted magnesiothermic reduction technique was used to synthesise high-purity amorphous boron fine powder. Effects of the processing conditions, such as salt type, boron source, heating temperature, Mg amount and salt content, on the synthetic process were also studied, and the reaction conditions were subsequently optimised.

8.1 Results and discussion

8.1.1 Effect of salt type on the magnesiothermic reduction

Figure 8.1 shows XRD patterns of samples with stoichiometric compositions after 6 h of heating at 850°C in different salts (here and for the samples shown in Figures 8.2-8.4 below, the samples were water-washed but not acid-leached). When NaCl was used (Figure 8.1(a)), in addition to the MgO byproduct, significant amounts of $Mg_3B_2O_6$ were formed, indicating a low reaction extent. When KCl was used (Figure 8.1(b)), the MgO peaks gradually increased, whereas the $Mg_3B_2O_6$ peaks gradually decreased. These phenomena were extended when $MgCl_2$ was used (Figure 8.1(c)), revealing that $MgCl_2$ was the most effective of the three salts in accelerating the magnesiothermic reduction. As discussed in our previous MSS studies on borides, this superior effect of $MgCl_2$ was due to Mg and MgO being more soluble in molten $MgCl_2$ than in molten NaCl or KCl.

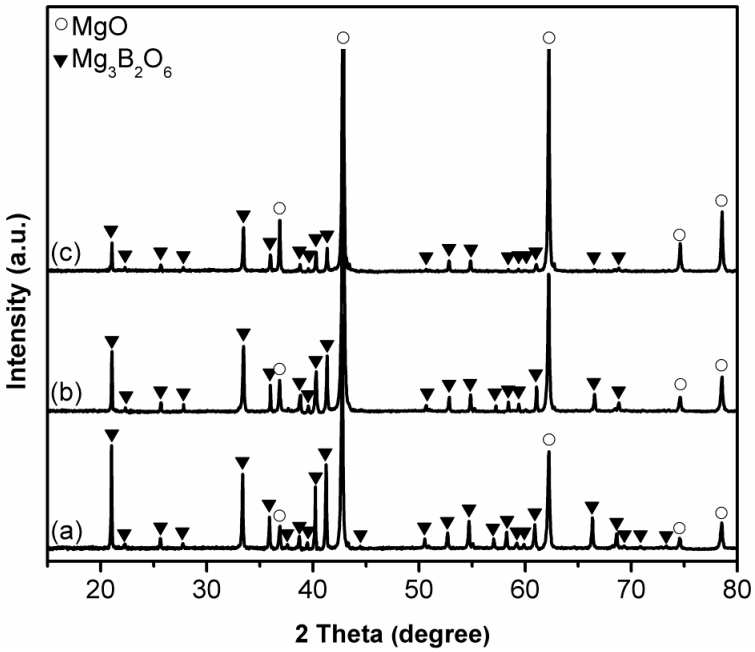

Figure 8.1 XRD patterns of samples with stoichiometric compositions after 6 h of heating at 850°C in (a) NaCl, (b) KCl, and (c) $MgCl_2$.

8.1.2 Effect of boron source on the magnesiothermic reduction

Because $Na_2B_4O_7$ has been used by some investigators for synthesising amorphous boron powders and various boron compounds [218, 248, 293], it was also used as a boron source in this work. Figure 8.2 shows XRD patterns of stoichiometric samples with different boron precursors after heating in $MgCl_2$ at 850°C for 6 h. Figure 8.2(a) reveals that in the sample prepared using $Na_2B_4O_7$, MgO and $Mg_3B_2O_6$ were formed. However, replacing $Na_2B_4O_7$ with B_2O_3 caused the intensity of the MgO peaks to increase and the intensity of the $Mg_3B_2O_6$ peaks to decrease (Figure 8.2(b)). These results suggested that as a boron source, B_2O_3 possessed better reactivity than $Na_2B_4O_7$.

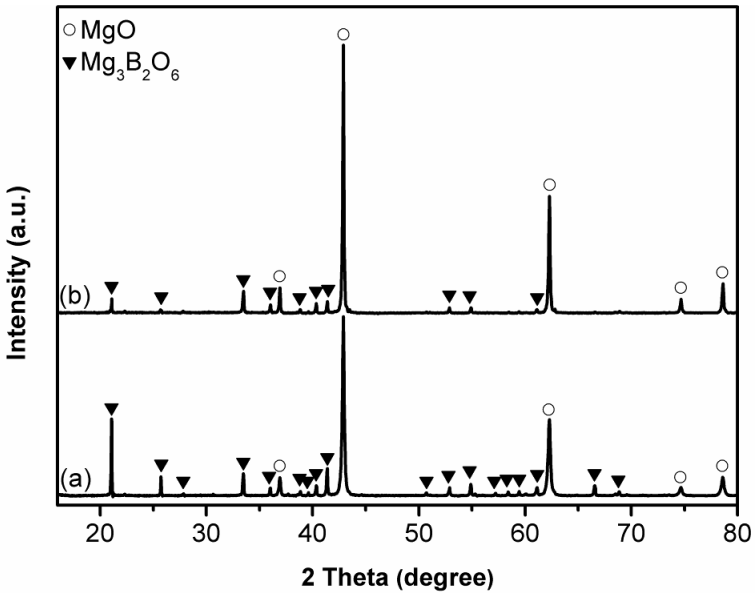

Figure 8.2 XRD patterns of samples resultant from heating batch powders for 6 h in $MgCl_2$ at 850°C using (a) $Na_2B_4O_7$ and (b) B_2O_3.

8.1.3 Effect of heating temperature on the magnesiothermic reduction

XRD patterns of stoichiometric samples after 6 h heating in $MgCl_2$ at different temperatures are plotted in Figure 8.3. At 800°C (Figure 8.3(a)), large amounts of $Mg_3B_2O_6$ were formed, but the $Mg_3B_2O_6$ content decreased as the temperature was increased to 900°C (Figures 8.3(b)&(c)). Meanwhile, the MgO peaks increased, indicating improved magnesiothermic reduction. Nevertheless, when the temperature was increased to 1000°C, the $Mg_3B_2O_6$ peaks adversely increased (Figure 8.3(d)), which was caused by the evaporation loss of Mg at this relatively high temperature.

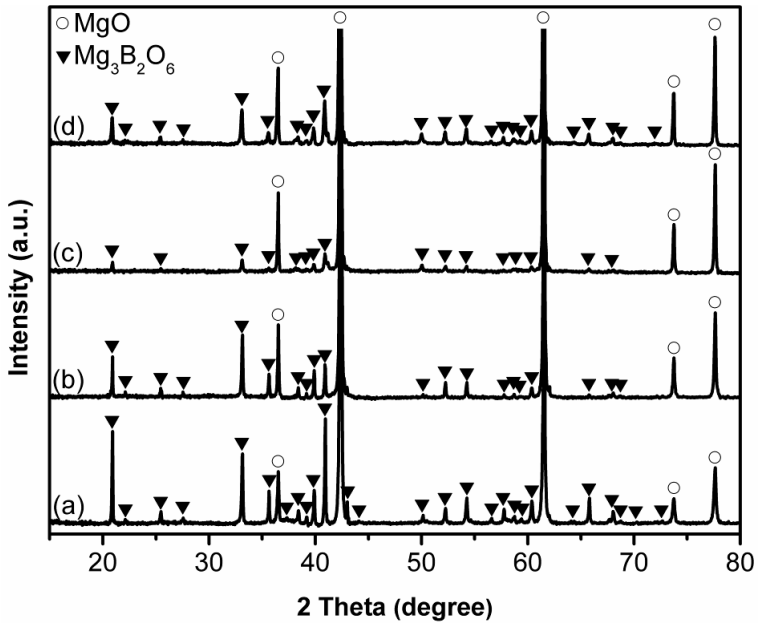

Figure 8.3 XRD patterns of samples with stoichiometric composition after 6 h of heating in $MgCl_2$ at (a) 800, (b) 850, (c) 900, and (d) 1000°C.

8.1.4 Effect of excessive Mg on the magnesiothermic reduction and subsequent purification

Figure 8.4 illustrates the effects of excessive amounts of Mg on the phase evolution in samples resultant from 6 h of heating at 1000°C in $MgCl_2$. The intensity of the $Mg_3B_2O_6$ peaks gradually decreased as excessive amount of Mg was added until 15 mol% was reached (Figures 8.4(a)-(c)). As discussed previously, this result was attributed to the further reduction of $Mg_3B_2O_6$ by the excessive Mg according to Reaction (8.1).

$$Mg_3B_2O_6 + 3Mg = 6MgO + 2B \quad (8.1)$$

When the excessive amount of Mg was increased to 20 mol% (Figure 8.4(d)), the $Mg_3B_2O_6$ peaks disappeared, but small amounts of MgB_6 were detected. The reaction of Mg remnants with amorphous B occurred to form MgB_6, as indicated in Reaction (7.1) [7, 294, 295].

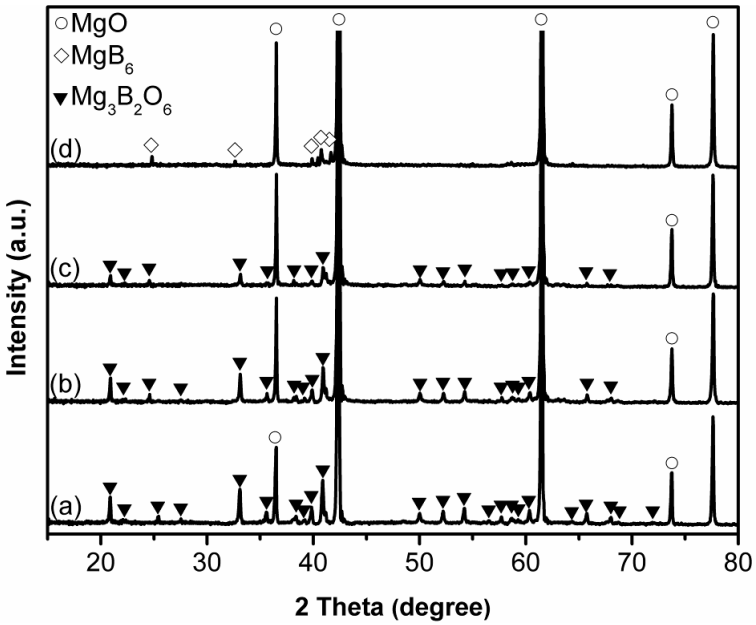

Figure 8.4 XRD patterns of samples resultant from heating batch powders for 6 h in $MgCl_2$ at 1000°C using (a) 0, (b) 10, (c) 15, and (d) 20 mol% excessive Mg.

Figure 8.5 shows XRD patterns of samples with 20 mol% excessive Mg after 6 h of heating in $MgCl_2$ at temperatures ranging from 850 to 1150°C. The patterns exhibited broad peaks that were ascribed to amorphous boron obtained after leaching out MgO. At 850°C (Figure 8.5(a)), both $Mg_3B_2O_6$ and MgB_6 were detected, indicating that at this relatively low temperature, the B_2O_3 reduction was incomplete and that the formation of MgB_6 resulted from using excessive Mg. When the temperature was increased to 1000°C (Figure 8.5(b)), the $Mg_3B_2O_6$ peaks disappeared, whereas a large amount of MgB_6 was formed. This result was consistent with the XRD pattern of the sample before HCl leaching (Figure 8.4(d)). Upon increasing the temperature to 1150°C (Figure 8.5(c)), the MgB_6 peaks decreased compared to those of the sample heated at 1000°C (Figure 8.5(b)). Considering that formation of acid-insoluble MgB_6 would inevitably decrease the B content and accordingly increase the Mg content in the products powders [7], the reaction conditions were optimised on the basis of the case using 15 mol% excessive Mg.

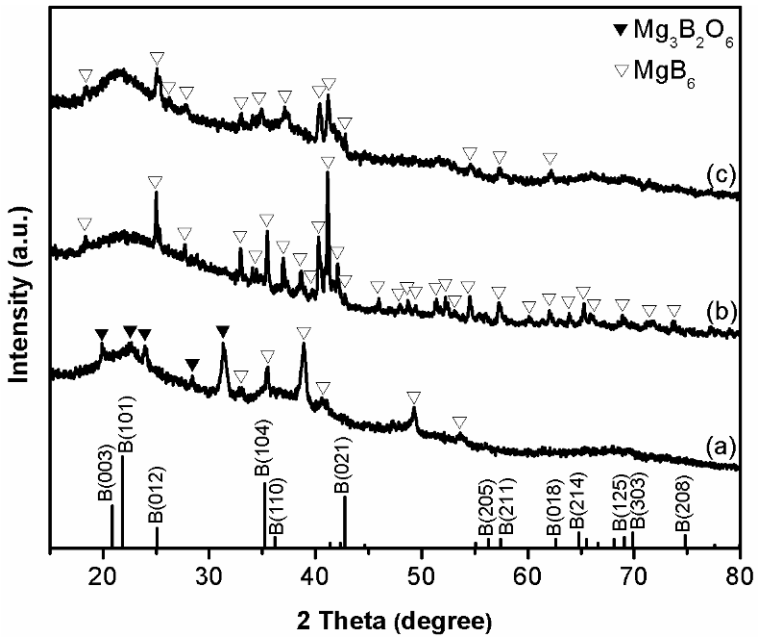

Figure 8.5 XRD patterns of samples resultant from heating batch powders for 6 h in $MgCl_2$ with 20 mol% excessive Mg at (a) 850, (b) 1000, and (c) 1150°C (after water washing and subsequent HCl leaching).

Figure 8.6 shows XRD patterns of samples with 15 mol% excessive Mg after 6 h of heating in $MgCl_2$ between 850 and 1000°C. At 1000°C (Figure 8.6(c)), small amounts of $Mg_3B_2O_6$ remained, which was consistent with the XRD pattern of the sample before HCl leaching (Figure 8.4(c)). When the temperature was decreased to 900°C (Figure 8.6(b)), the $Mg_3B_2O_6$ peaks disappeared, and only the amorphous boron peaks were observed, which indicated that the B_2O_3 reduction was likely to complete under these conditions owing to the minimised Mg evaporation loss at this temperature. Nevertheless, $Mg_3B_2O_6$ was formed again when the temperature decreased to 850°C (Figure 8.6(a)), implying that the reduction at a lower temperature was insufficient compared to the reduction at 900°C (Figure 8.6(b)). The samples were further subjected to H_2SO_4 leaching. As shown in Figure 8.7, no $Mg_3B_2O_6$ peaks can be observed in the resultant samples, suggesting the effective removal of $Mg_3B_2O_6$ *via* the H_2SO_4 leaching process.

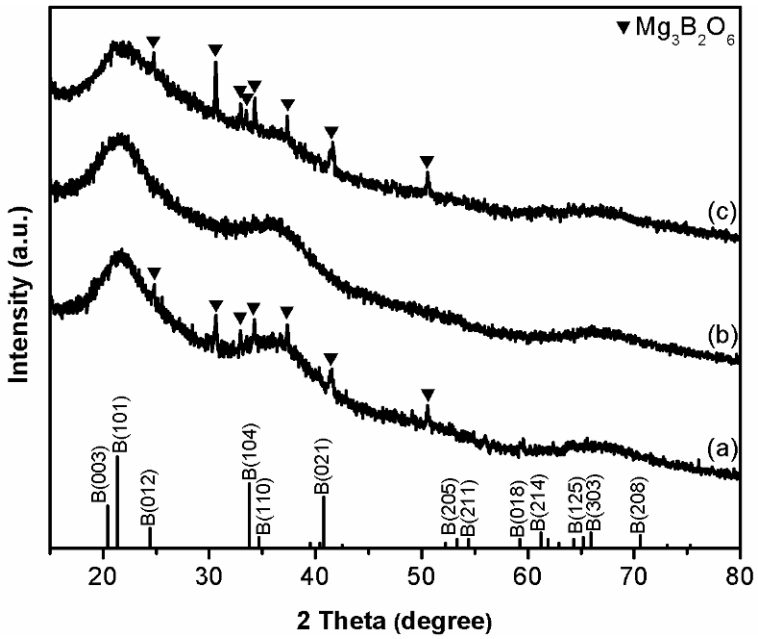

Figure 8.6 XRD patterns of samples resultant from heating batch powders for 6 h in $MgCl_2$ with 15 mol% excessive Mg at (a) 800, (b) 900, and (c) 1000°C (after water washing and subsequent HCl leaching).

8.1.5 Effect of salt content on the magnesiothermic reduction

Figure 8.8 shows XRD patterns of samples with 15 mol% excessive Mg after 6 h of heating at 900°C using various salt-to-reactant (S/R) ratios. For the sample heated without salt (Figure 8.8(a)), large amounts of $Mg_3B_2O_6$ were formed, indicating a low reaction extent of the solid-state magnesiothermic reduction. Using the salt at an S/R ratio of 3/1 caused the $Mg_3B_2O_6$ peaks to dramatically decrease, indicating that the magnesiothermic reduction in molten salt was greatly accelerated (Figure 8.8(b)). When the S/R ratio was increased to 5/1, the $Mg_3B_2O_6$ peaks disappeared, and only the amorphous boron peaks were observed (Figure 8.8(c)/Figure 8.6(c)). Increasing the amount of salt decreased the viscosity of the medium, which facilitated the diffusion of Mg towards B_2O_3 [296].

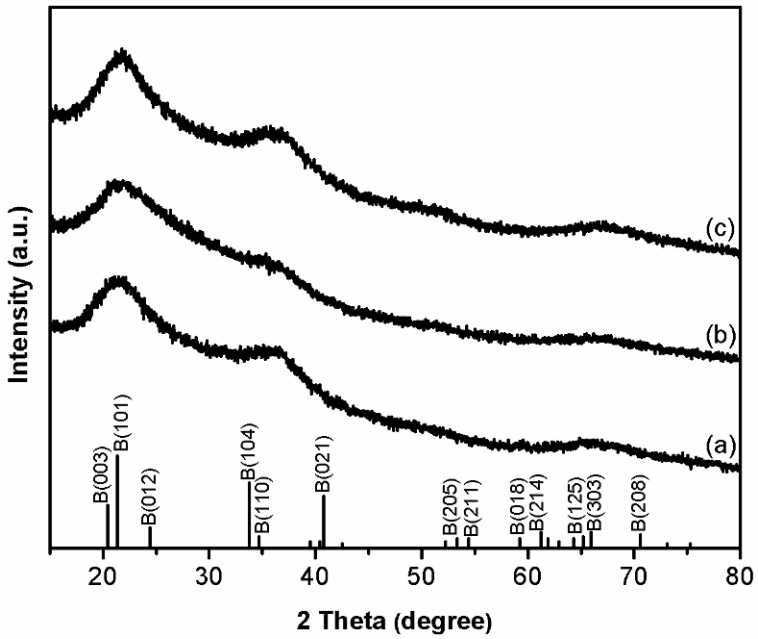

Figure 8.7 XRD patterns of samples resultant from heating batch powders for 6 h in $MgCl_2$ with 15 mol% excessive Mg at (a) 800, (b) 900, and (c) 1000°C (after further H_2SO_4 leaching).

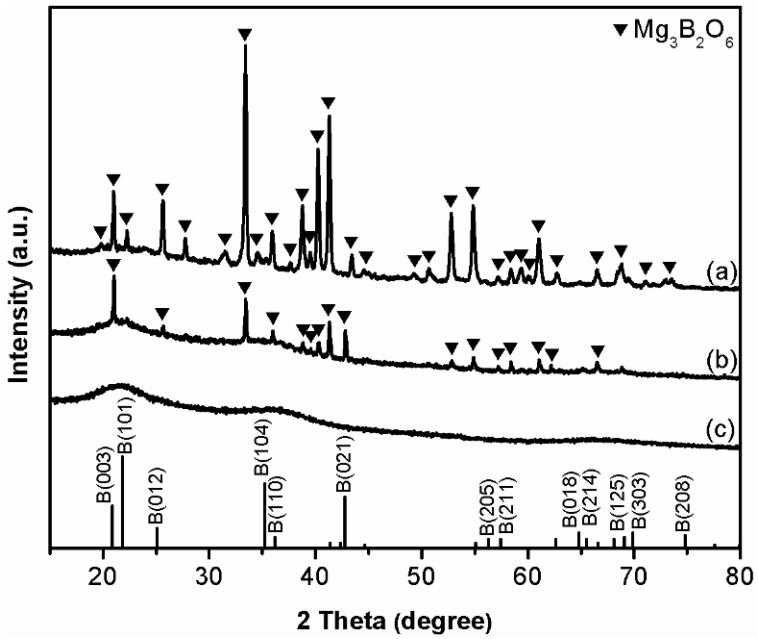

Figure 8.8 XRD patterns of samples resultant from heating batch powders containing 15 mol% excessive Mg for 6 h in $MgCl_2$ at 900°C using different S/R ratios: (a) no salt, (b) 3/1, and (c) 5/1.

8.1.6 Microstructural characterisation of the boron powders

Figure 8.9 shows the EDS results of the product samples resultant from 6 h of heating at 1000°C in $MgCl_2$ after HCl leaching and subsequent H_2SO_4 leaching. This figure revealed that the product powders comprised B, O and Mg. As shown

in Figure 8.9(a), in the HCl-leached powder, the O and Mg contents were 9.35 and 3.12 wt%, respectively. Mg and O originated from the residual $Mg_3B_2O_6$ in the resultant powder, as indicated in the corresponding XRD pattern (Figure 8.6(c)).

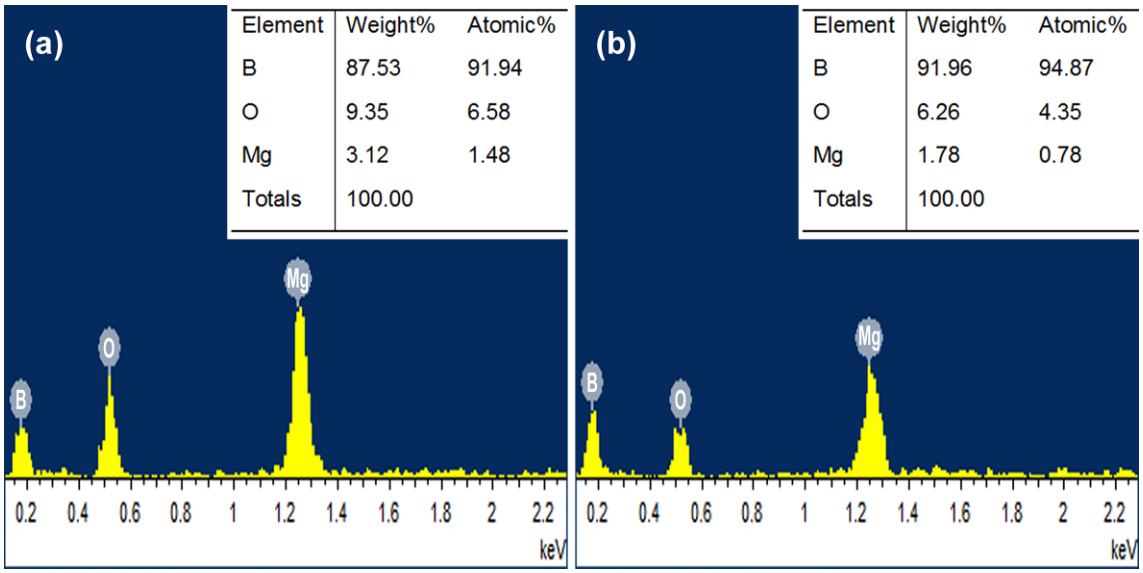

Figure 8.9 EDS results of the samples resultant from heating batch powders for 6 h in $MgCl_2$ with 15 mol% excessive Mg and after leaching with (a) HCl at room temperature for 2 h and (b) subsequent H_2SO_4 leaching at 70-90°C for 2 h.

After further H_2SO_4 leaching (Figure 8.9(b)), the O and Mg contents decreased to 6.26 and 1.78 wt%, respectively, indicating that a certain amount of $Mg_3B_2O_6$ was successfully removed *via* this leaching process, consistent with the XRD result (Figure 8.7(c)). Unfortunately, this sample still contained some impurities associated with Mg, B and O elements, which could not be fully eliminated *via* the leaching processes in this work. XRD (Figure 8.7(c)) was not able to detect these phases due to their minor amounts and/or their amorphous structure. These results implied that despite the effectiveness of purifying the product through acid leaching, the formation of $Mg_3B_2O_6$ should be avoided in the fired samples to achieve high purity amorphous boron powders.

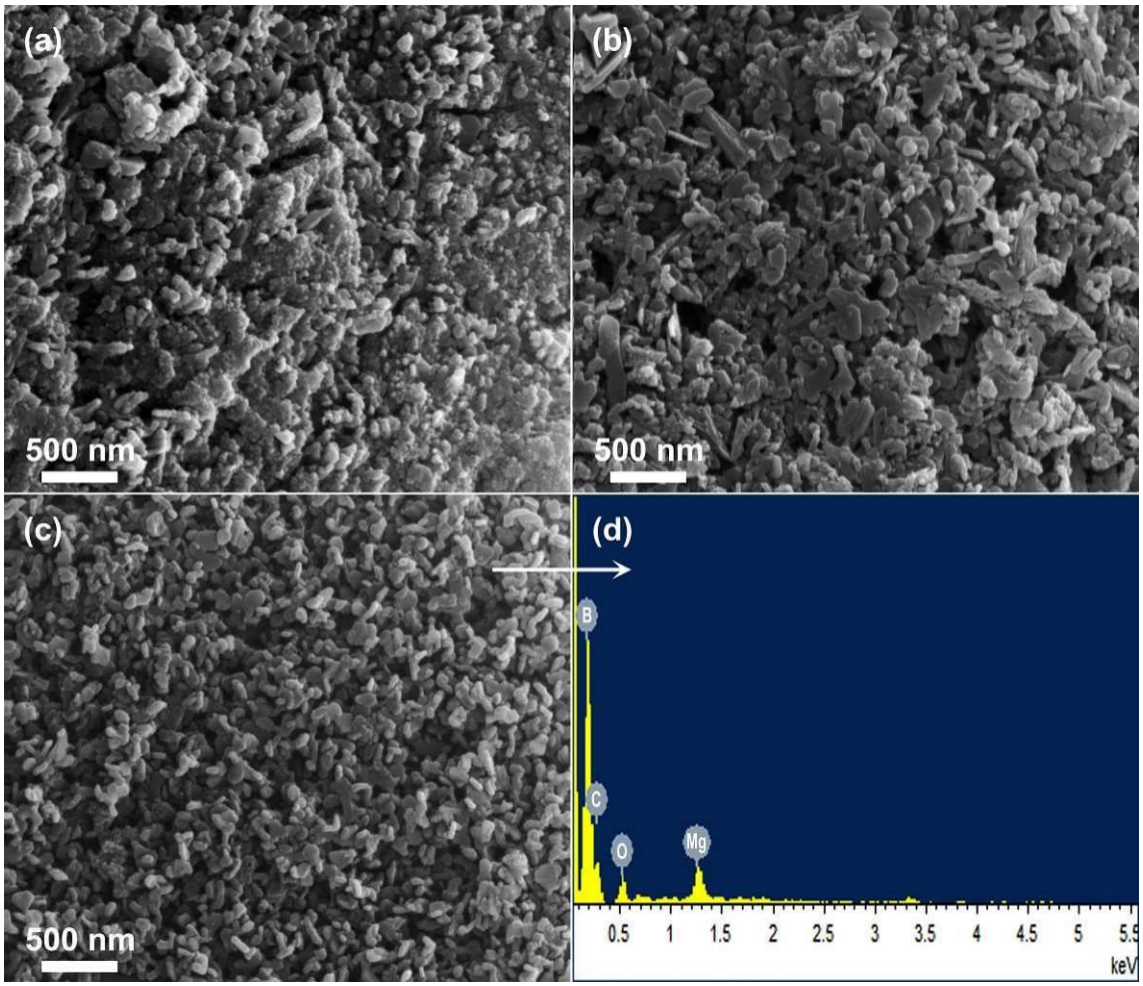

Figure 8.10 SEM images of the product samples whose XRD patterns are shown in Figure 8.7: (a) 850, (b) 1000, and (c) 900°C, and EDS analysis for the product powder obtained at 900°C (d).

Figure 8.10 presents SEM images of the product powders obtained at different temperatures (whose XRD patterns are shown in Figure 8.7), revealing the considerable effects of the reaction temperature on the morphology/size of the product powders. The product powder resulting from 6 h at 850°C in $MgCl_2$ exhibited dense agglomerates (Figure 8.10(a)), whereas raising the temperature to 1000°C afforded a product powder with larger and elongated features (Figure 8.10(b)). The synthesised amorphous boron powder from 6 h at 900°C had a rounded morphology with a mean particle size of ~100 nm (Figure 8.10(c)). The EDS results of the amorphous boron powder at 900°C (Figure 8.10(d)) exhibited only B and trace amounts of O and Mg (apart from the C from the carbon tape on

the SEM stub), indicating that the magnesiothermic reduction of B_2O_3 was almost complete after 6 h heating at 900°C in $MgCl_2$, which was in agreement with the XRD results (Figures 8.6-8.8). The trace amounts of oxygen were associated with the presence of the inevitable water moisture and oxygen absorbed on the boron particles [11, 297].

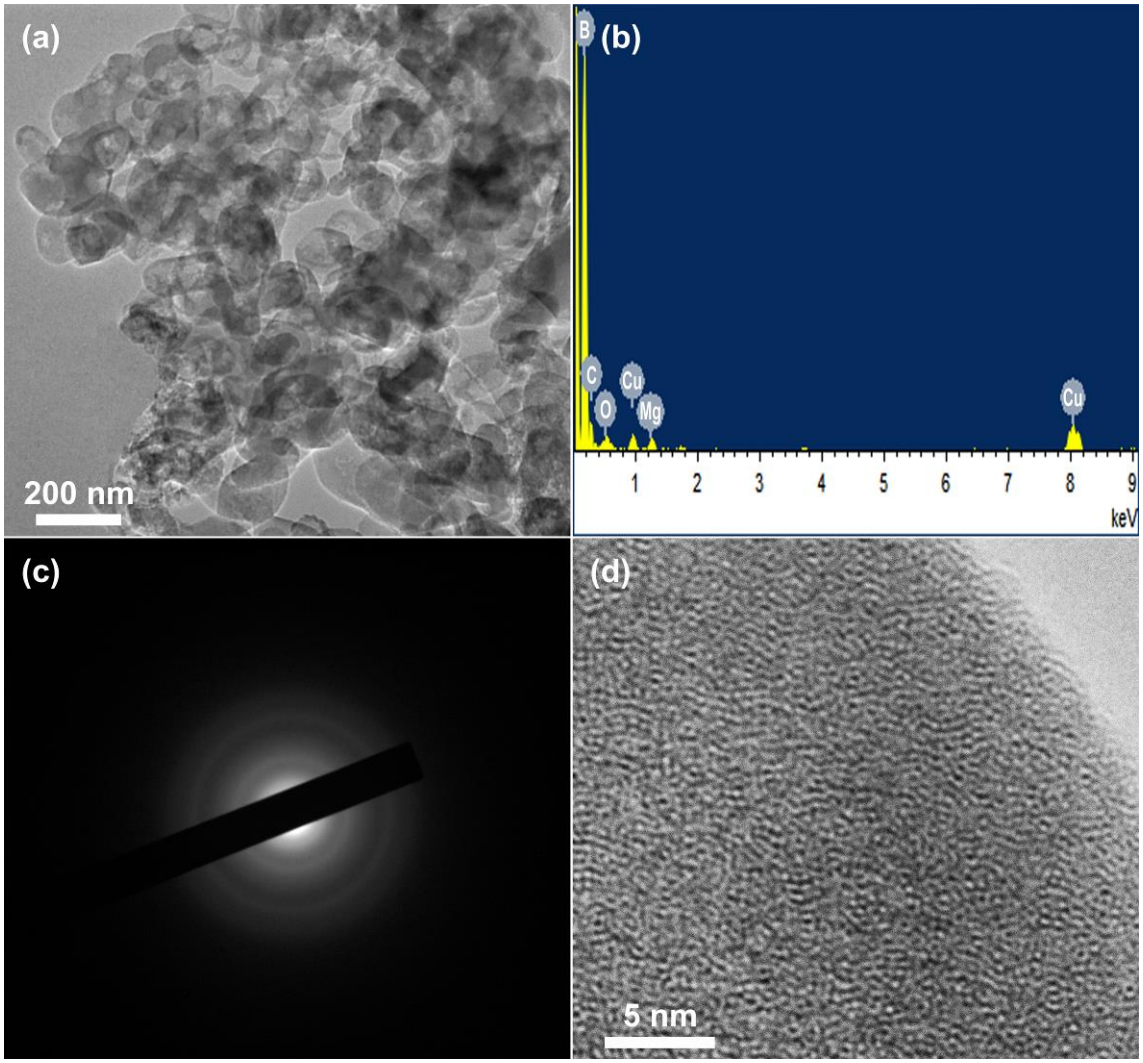

Figure 8.11 TEM image (a), EDS spectrum (b), and SAED pattern (c) of the boron powder after 6 h heating at 900°C in $MgCl_2$. HRTEM image of a typical boron particle (d), showing the absence of crystal planes, which further confirmed its amorphous nature.

Further characterisation of the amorphous boron powder synthesised at 900°C was conducted using TEM and electron diffraction. TEM image revealed rounded particle morphology in the range of 100-200 nm (Figure 8.11(a)), which was roughly in agreement with the SEM observations (Figure 8.10(b)). The

SAED pattern (Figure 8.11(b)) of the boron particles revealed some diffusive rings and no diffraction spots, indicating that the product boron powder had an amorphous structure, consistent with the XRD analysis (Figure 8.7(b)). EDS detected B and tiny O and Mg (apart from the C and Cu peaks from the carbon film/Cu grid used for TEM), confirming the high purity of the amorphous boron powder. In addition, no crystalline fringes were identified in the high-resolution transmission electron microscopy (HTEM) image of a typical boron particle at the lattice-resolved scale (Figure 8.11(b)), further confirming the amorphous structure of the boron particles.

8.2 Conclusion

In conclusion, amorphous boron powder was prepared by the molten-salt-assisted magnesiothermic reduction of B_2O_3. The effects of salt type, boron source, reaction temperature, Mg amount and salt content on the synthetic process were investigated. High-purity amorphous boron fine particles (100-200 nm) were prepared in $MgCl_2$ after 6 h of heating at 900°C using 15 mol% excessive Mg and leaching with 1 M HCl at room temperature and with 0.5 M H_2SO_4 at 70-90°C.

Chapter 9 Synthesis of Al_2O_3-TiB_2 Nanocomposite Powder *via* Molten-Salt-Assisted aluminothermic reduction

In this chapter, high-quality Al_2O_3-TiB_2 nanocomposite powders were synthesised from inexpensive oxide-based precursors by aluminothermic reduction with the advantages of lower reaction temperature and shorter reaction time. Investigation of the effects of salt type, initial batch composition, and firing temperature/time on the Al_2O_3-TiB_2 formation was undertaken for optimizing the synthesis conditions, based on which, the dominant reaction mechanisms were clarified.

9.1 Results and discussion

9.1.1 Effect of salt type on Al_2O_3-TiB_2 formation

Figure 9.1 shows XRD patterns of samples of stoichiometric composition after 4 h firing in different salts at 850°C. In the case of using KCl (Figure 9.1(a)), both Al_2O_3 and TiB_2 were identified, indicating the occurrence of the overall Reaction (3.10), which involved three main sequential reactions, i.e., Reactions (9.1)-(9.3) [31]. Apart from these, some amounts of intermediate $Al_{18}B_4O_{33}$ from Reaction (9.4) [298] and Al_3Ti from Reaction (9.5) [229] were formed, along with a trace of Ti_2O_3 which signified the incomplete reduction of TiO_2 with Al [299], implying the overall low extents of Al_2O_3-TiB_2 formation in this case.

$$B_2O_3 + 2Al = 2B + Al_2O_3 \quad (9.1)$$

$$3TiO_2 + 4Al = 3Ti + 2Al_2O_3 \quad (9.2)$$

$$Ti + 2B = TiB_2 \quad (9.3)$$

$$2B_2O_3\ (\text{unreduced}) + 9Al_2O_3 = Al_{18}B_4O_{33} \quad (9.4)$$

$$Ti + 3Al = Al_3Ti \quad (9.5)$$

Upon replacing KCl with NaCl (Figure 9.1(b)), although $Al_{18}B_4O_{33}$ and Ti_2O_3 marginally increased, Al_2O_3 and TiB_2 substantially increased while Al_3Ti decreased, suggesting enhanced extents of Al_2O_3-TiB_2 formation. These results indicated that KCl had better effect than NaCl on accelerating the aluminothermic reduction of B_2O_3 (Reaction (9.1)) and TiO_2 (Reaction (9.2)), so less unreduced B_2O_3 (or $Al_{18}B_4O_{33}$) and Ti_2O_3 remained. In addition, the formation of Al_3Ti (Reaction (9.5)) was more preferential than that of TiB_2 (Reaction (9.3)) in KCl, which may explain why more Al_3Ti was formed in the case of using KCl than that of NaCl.

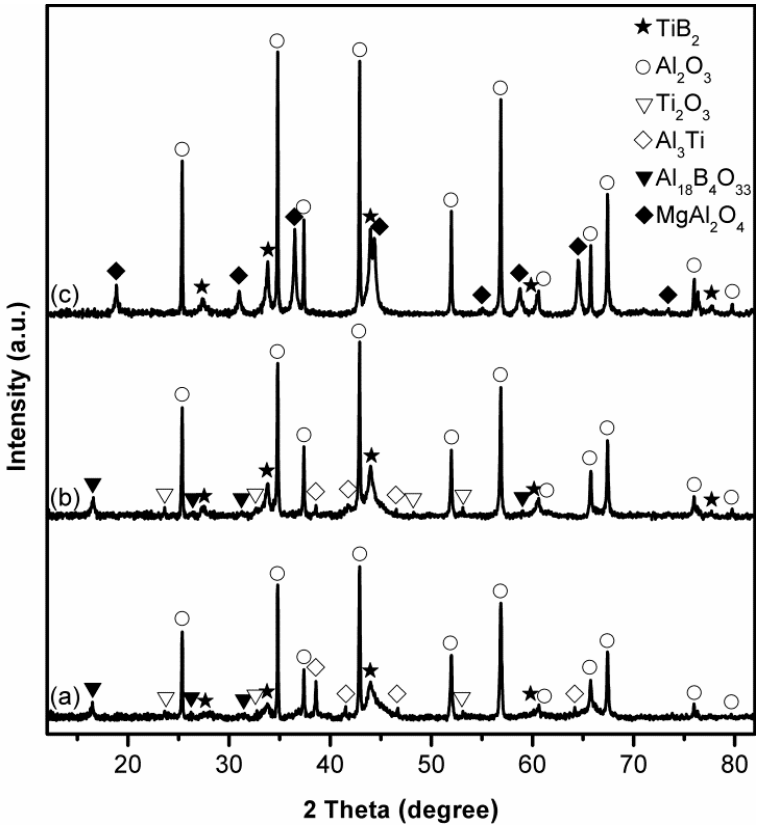

Figure 9.1 XRD patterns of samples of stoichiometric composition after 4 h firing at 850°C in (a) KCl, (b) NaCl, and (c) $MgCl_2$.

Upon replacing NaCl with $MgCl_2$ (Figure 9.1(c)), Al_2O_3 and TiB_2 further increased, and no $Al_{18}B_4O_{33}$, Al_3Ti or Ti_2O_3 was detected, revealing much improved reaction extents. Nevertheless, another intermediate phase, $MgAl_2O_4$, was formed in this

case, which was considered to be related to the reaction between Al_2O_3 and $MgCl_2$ (Reaction (9.6)) [300]. Therefore, among the three chloride salts attempted, NaCl was regarded as the most appropriate reaction medium for the MSS of Al_2O_3-TiB_2 nanocomposite powders.

$$4Al_2O_3 + 3MgCl_2\ (l) = 3MgAl_2O_4 + 2AlCl_3\ (l) \qquad (9.6)$$

9.1.2 Effect of firing temperature on Al_2O_3-TiB_2 formation

Given in Figure 9.2 are XRD patterns of samples of stoichiometric composition after 4 h firing in NaCl at different temperatures. At 850°C (Figure 9.2(a)/Figure 9.1(b)), as described above, Al_2O_3 and TiB_2 were formed evidently, along with some $Al_{18}B_4O_{33}$, Al_3Ti and Ti_2O_3. Upon increasing the temperature to 950 (Figure 9.2(b)) and 1050°C (Figure 9.2(c)), Al_2O_3 and TiB_2 increased significantly and no Al_3Ti was detected, but $Al_{18}B_4O_{33}$ and Ti_2O_3 also gradually increased, implying that the firing temperature had little effect on achieving the completion of aluminothermic reduction and Al_2O_3-TiB_2 formation under these conditions. Upon further increasing the temperature to 1150°C (Figure 9.2(d)), $Al_{18}B_4O_{33}$ and Ti_2O_3 further increased, whereas Al_2O_3 and TiB_2 decreased adversely, indicating negative effect of firing temperature on the Al_2O_3-TiB_2 formation reactions in this case. According to our previous studies on MSS of borides [248, 301, 302], partial sublimation and/or volatilization of Al at reaction temperatures [303] may account for these results. Hence, the effect of using excessive Al on the Al_2O_3-TiB_2 formation was further investigated, as described and discussed next.

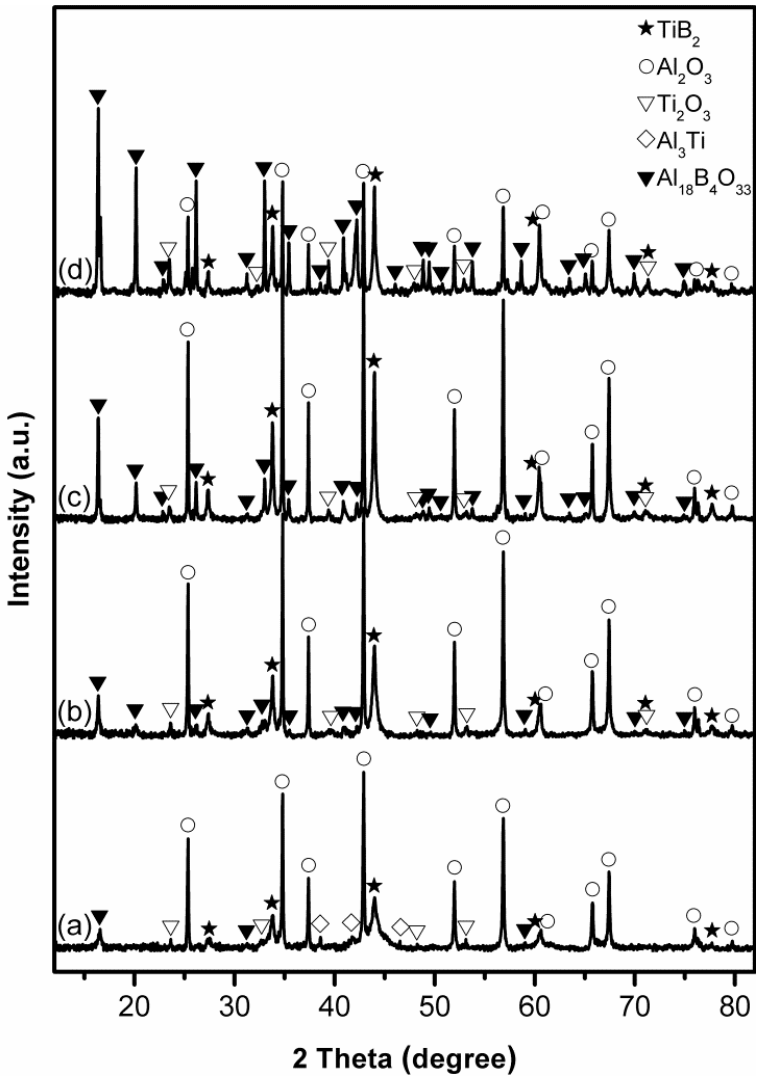

Figure 9.2 XRD patterns of samples of stoichiometric composition after 4 h firing in NaCl at (a) 850, (b) 950, (c) 1050, and (d) 1150°C.

9.1.3 Effect of excessive Al on Al_2O_3-TiB_2 formation

Figure 9.3 illustrates the phase evolution in samples after 4 h firing in NaCl at 1150°C, with excessive amount of Al. Use of 20 wt% more Al (Figures 9.3 (a)-(b)) led to considerable increase in Al_2O_3 and TiB_2 while decrease in $Al_{18}B_4O_{33}$ and Ti_2O_3, and upon using 25 wt% excessive Al (Figure 9.3(c)), Al_2O_3 and TiB_2 further increased, Ti_2O_3 completely disappeared, and only minor $Al_{18}B_4O_{33}$ remained, suggesting quite positive effects from the Al compensation. However, phase-pure Al_2O_3-TiB_2 was still not obtained under these conditions. Upon using 30 wt% excessive Al (Figure 9.3(d)), $Al_{18}B_4O_{33}$ was entirely absent, yet some

amounts of Al_3Ti were formed. Thus, it was reasonable to consider that there would be residual TiO_2 (might exist as Ti_2O_3 and/or Ti) in the sample using 25 wt% excessive Al, which were not shown in the XRD pattern (Figure 9.3(c)), indicating that these phases were present in amorphous form or in amounts too small to be detected by XRD. Moreover, the presence of Al_3Ti implied that there was an insufficient quantity of B to completely react with all of Ti (Reaction (9.3)) caused by the evaporation loss of B_2O_3 [37, 304]. This was verified by the XRD results shown in Figure 9.4.

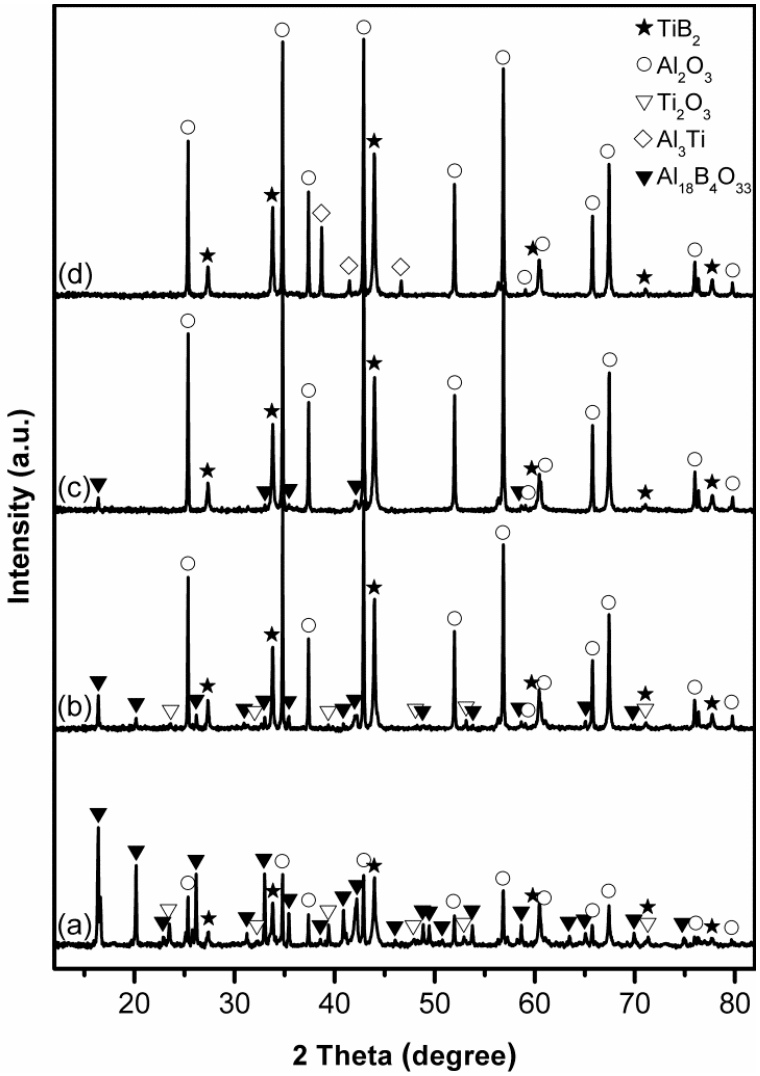

Figure 9.3 XRD patterns of samples using (a) 0, (b) 20, (c) 25, and (d) 30 wt% excessive Al, after 4 h firing in NaCl at 1150°C.

9.1.4 Effect of excessive B_2O_3 on Al_2O_3-TiB_2 formation

To address the issue of B_2O_3 evaporation loss mentioned above, the effect of using excessive B_2O_3 (along with 30 wt% excessive Al) on the Al_2O_3-B_2O_3 formation was further investigated. As shown in Figure 9.4, when 10 wt% excessive B_2O_3 was used, both Al_2O_3 and TiB_2 increased, and only a little Al_3Ti remained, and when 20 wt% excessive B_2O_3 was used, Al_3Ti disappeared completely, and only Al_2O_3 and TiB_2 were formed, providing an explanation as to why excessive B_2O_3 was needed, along with excessive Al, to promote and complete the Al_2O_3-TiB_2 formation reactions.

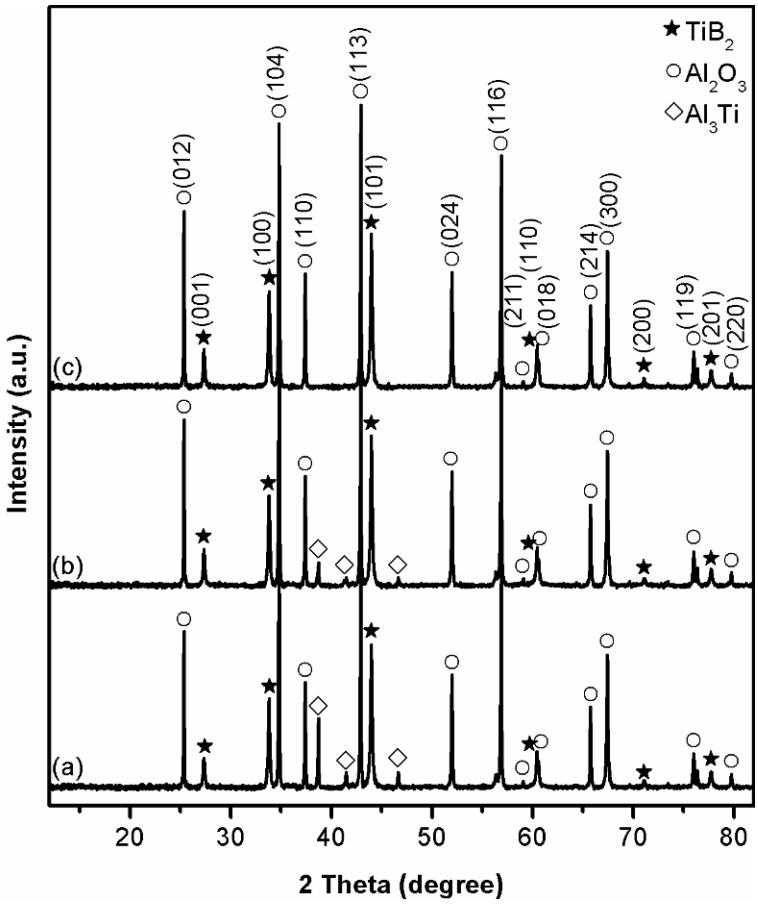

Figure 9.4 XRD patterns of samples using 30 wt% excessive Al and respectively: (a) 0, (b) 10, and (c) 20 wt% excessive B_2O_3, after 4 h firing in NaCl at 1150°C.

9.1.5 Effect of firing time on Al_2O_3-TiB_2 formation and further optimisation of synthesis conditions

According to the findings from the previous MSS of HfB_2 and LaB_6, the firing time

could also have pronounced effects on the reaction extents. To further examine this, Figure 9.5, as an example, illustrates phase formation in samples using 30 wt% excessive Al and 20 wt% excessive B_2O_3, after firing in NaCl at 1050°C for different times. Increasing the firing time from 4 to 5 h (Figures 9.5(a)-(b)) resulted in disappearance of $Al_{18}B_4O_{33}$, but slightly decreased Al_2O_3 and TiB_2 and increased Al_3Ti. Further extending the time to 6 h did not give any favourable result, and small amounts of Al_3Ti still remained, which was related to the evaporation loss of B_2O_3 upon prolonged firing at this temperature. This was verified by the results shown in Figure 9.6 revealing that in addition to 30 wt% excessive Al, using 20 to 30 wt% excessive B_2O_3 led to markedly reduced Al_3Ti and its eventual disappearance, and the completion of the Al_2O_3-TiB_2 formation reactions.

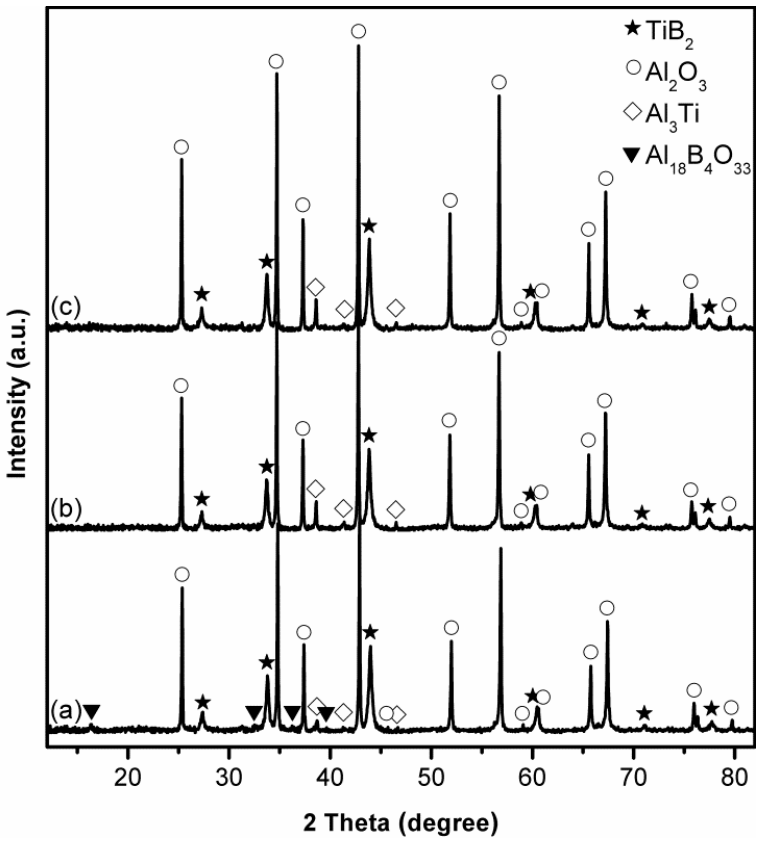

Figure 9.5 XRD patterns of samples using 30 wt% excessive Al and 20 wt% excessive B_2O_3 after firing in NaCl at 1050°C for (a) 4, (b) 5, and (c) 6 h.

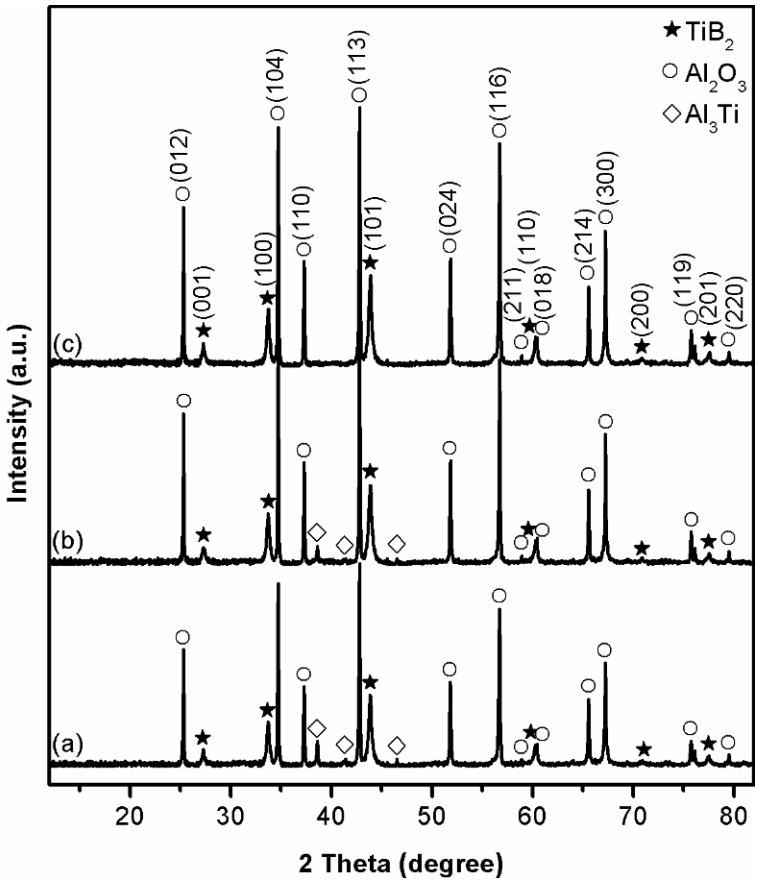

Figure 9.6 XRD patterns of samples after firing in NaCl at 1050°C for 5 h using 30 wt% excessive Al and (a) 20, (b) 25, and (c) 30 wt% excessive B_2O_3.

9.2 Microstructures and phase compositions of the Al_2O_3-TiB_2 product powders

As demonstrated in Figures 9.4(c) and 9.6(c) and discussed above, when 30 wt% excessive Al was used with NaCl, the Al_2O_3-TiB_2 formation reactions could be completed after 4 h firing at 1150°C using 20 wt% excessive B_2O_3 or 5 h firing at 1050°C using 30 wt% excessive B_2O_3, and the synthesized powder consisted of only Al_2O_3 and TiB_2 in both cases. A representative SEM image of the composite powder resultant from 5 h firing at 1050°C is shown in Figure 9.7(a) revealing the formation of spheroidal particle aggregates. The X-ray dot mapping showed reasonably uniform distribution of the elements, suggesting that the Al_2O_3 and TiB_2 were intimately mixed. By contrast, in the sample resultant from 4 h firing at 1150°C, the particles were evidently coarser (Figures 9.8(a)&(b)), with

Al_2O_3 (confirmed by EDS, Figure 9.8(c)) adopting a “block-shaped” morphology (1-2 μm), while the TiB_2 [confirmed by EDS, Figure 9.8(d)) remained spheroidal (100-200 nm). TEM imaging of the synthesised powder resultant from 5 h firing at 1050°C (Figure 9.9) revealed two different particle morphologies confirming the SEM observations of intimately mixed submicron-sized Al_2O_3 particles (0.3-0.6 μm) (Figures 9.9(a)&(c)) and nanosized TiB_2 particles (30-60 nm) (Figures 9.9(b)&(d)). TEM examination of the composite powder revealed no evidence of the presence of any other impurities consistent with the results obtained from the XRD (Figure 9.6(c)) that the synthesized sample was composed of Al_2O_3-TiB_2 crystals only.

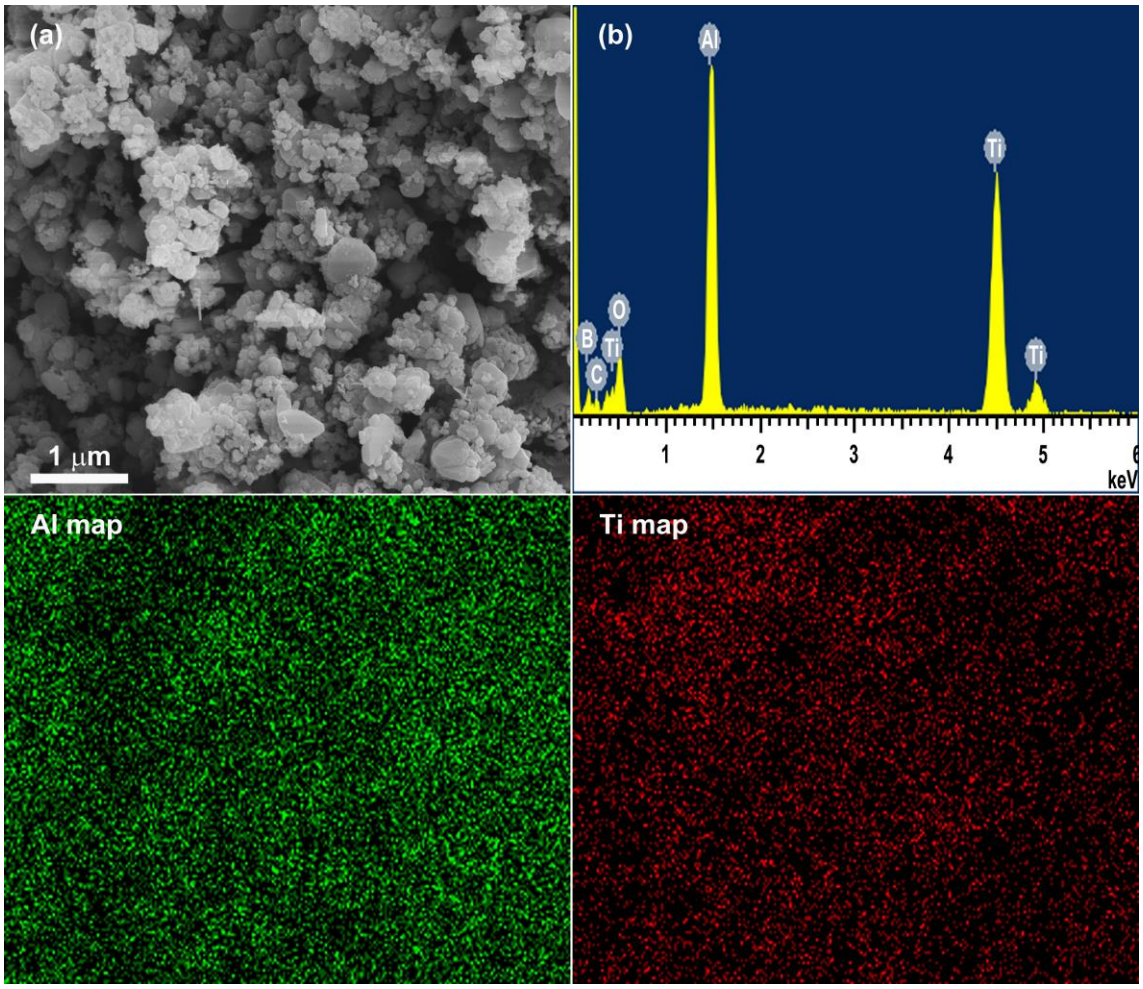

Figure 9.7 SEM image (a), EDS (b) and X-ray dot mapping of the Al_2O_3-TiB_2 composite powder resultant from firing in NaCl at 1050°C for 5 h.

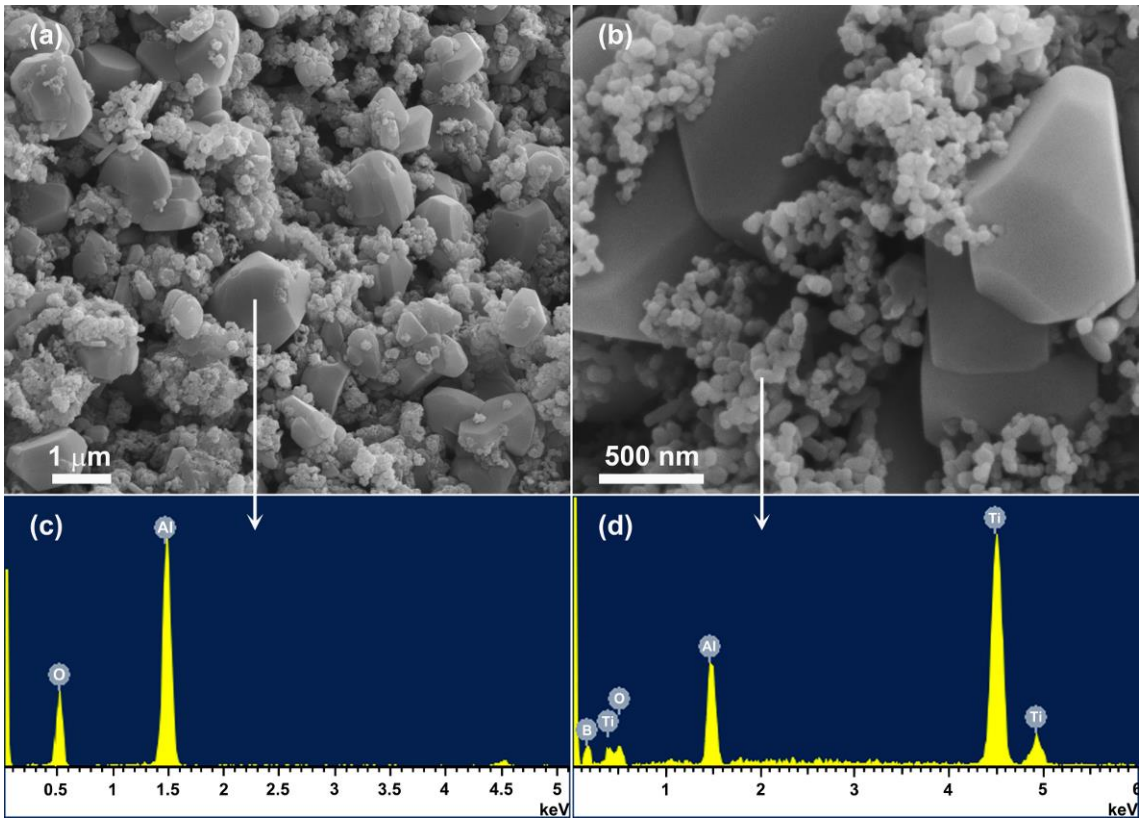

Figure 9.8 SEM images (a, b) and corresponding EDS (c, d) of the Al_2O_3-TiB_2 composite powders resultant from 4 h firing in NaCl at 1150°C.

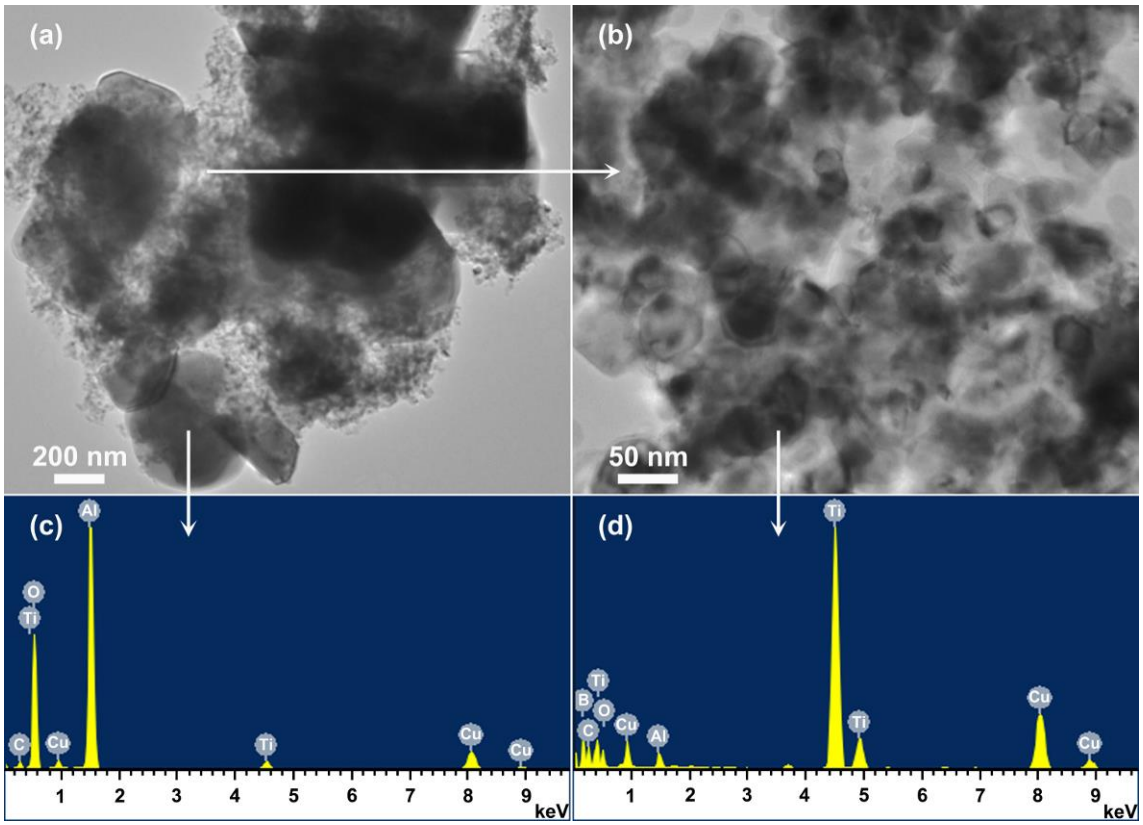

Figure 9.9 TEM images (a, b) and corresponding EDS (c, d) of the Al_2O_3-TiB_2 composite powders resultant from firing in NaCl at 1050°C for 5 h (the small C and Cu peaks arose from the carbon film-Cu TEM grid).

9.3 Further discussion and reaction mechanisms

Based on the results shown in Figures 9.1-9.9 and the preliminary discussion above, the reaction mechanisms in the present MSS (taking the case of using NaCl as an example) could be further considered as follows.

The firing temperatures (850-1150°C) were above the melting points of the chloride salts as well as the raw materials B_2O_3 and Al. Hence, at a test temperature, they all melted, forming a desirable liquid medium. Although B_2O_3 and Al had negligible solubility in molten NaCl [305-307], they would not act as "templates" during the overall MSS due to their liquid states. Therefore, Reaction (9.1) was essentially a liquid-liquid reaction, and the resultant B and Al_2O_3 would not retain the sizes/morphologies of the original B_2O_3 or Al (Reaction (9.7)).

$$B_2O_3\ (l) + 2Al\ (l) = 2B + Al_2O_3 \qquad (9.7)$$

As discussed in our previous MSS of TiB_2 [302], part of the TiO_2 would interact with B_2O_3 forming a eutectic liquid [277], whereas the remaining part would present in the liquid medium as a solid phase. Thus, for Reaction (9.2), two parallel reactions might occur simultaneously, as indicated by Reactions (9.8) and (9.9). Reaction (9.8) was also a liquid-liquid reaction, so the resultant Ti and Al_2O_3 would also lose the sizes/morphologies of their precursors.

$$3TiO_2\ (\text{in } B_2O_3\text{-}TiO_2 \text{ eutectic liquid}) + 4Al\ (l) = 3Ti + 2Al_2O_3 \qquad (9.8)$$

$$3TiO_2\ (\text{in salt as a solid}) + 4Al\ (l) = 3Ti + 2Al_2O_3 \qquad (9.9)$$

In the case of Reaction (9.9), after initial reaction, a protective barrier layer comprising Al_2O_3 and Ti would be formed on the unreduced solid TiO_2, causing some delay in the further reduction reaction [228]. Fortunately, Al_2O_3 is slightly soluble in molten chloride salts [308-311], so Al_2O_3 in the initially formed barrier could be removed *via* its dissolution in the molten NaCl, making the barrier layer

less continuous and less “protective”, and avoiding otherwise significant delay in Reaction (9.9).

Upon the formation of Al_2O_3, it would in turn act as a reactant with unreduced B_2O_3 to form intermediate $Al_{18}B_4O_{33}$ (Reaction (9.4), Figures 9.1-9.3&9.5), which has a relatively high melting point (~1440°C) [312] and is difficult to be removed. Nevertheless, due to the presence of a molten salt medium, it could be well dispersed (dissolved or undissolved) in the salt, and further reduced by Al to form additional B and Al_2O_3 according to Reaction (9.10), and its final disappearance could be accomplished by using appropriately excessive amount of Al (Figure 9.3(c)) and/or increasing firing (Figure 9.5(b)). The sizes/morphologies of the resultant B and Al_2O_3 would be linked to the solid $Al_{18}B_4O_{33}$. Similarly to the case of Reaction (9.9), Reaction (9.10) also would not be delayed much by the barrier layer possibly formed on $Al_{18}B_4O_{33}$, as the Al_2O_3 in the Al_2O_3 in the barrier layer also would be removed *via* its dissolution in the molten salt.

$$Al_{18}B_4O_{33}\ \text{(in salt as a solid)} + 4Al\ (l) = 4B + 11Al_2O_3 \qquad (9.10)$$

As discussed and confirmed in our previous MSS studies, both B and Ti could partially dissolve in the molten chloride salts (though the actual solubility values might be quite small). Therefore, it was considered that the Ti resultant from Reactions (9.8) and (9.9) dissolved in the molten salt would diffuse through the liquid medium and react with B resultant from Reactions (9.7) and (9.10) dissolved in the salt, forming TiB_2 *via* the “dissolution-precipitation” mechanism (Reaction (9.11)).

$$Ti\ \text{(dissolved in salt)} + 2B\ \text{(dissolved in salt)} = TiB_2 \qquad (9.11)$$

Moreover, intermetallic Al_3Ti was formed in some reacted samples (Reaction

(9.5), Figures 9.1-9.6), which was thought to be related to the reaction between the dissolved Ti and the liquid Al according to Reaction (9.12).

$$Ti\ (dissolved\ in\ salt) + 3Al\ (l) = Al_3Ti \qquad (9.12)$$

Based on the individual reaction steps indicated by Reactions (9.7)-(9.12) and further discussion above, it can be considered that the “dissolution-precipitation” mechanism played a dominant role in the TiB_2 formation (Reactions (9.11)), whereas the formation of Al_2O_3 might involve the “template-growth” mechanism (Reactions (9.9) and (9.10)). This may explain the quite different sizes and morphologies between as-prepared Al_2O_3 and TiB_2 particles (Figures 9.7-9.9) and raw materials B_2O_3 (Figure 5.10(a)) and TiO_2 (Figure 4.5(e)).

9.4 Conclusion

Homogeneous and phase-pure Al_2O_3-TiB_2 nanocomposite powders were synthesised *via* aluminothermic reduction of TiO_2 and B_2O_3 in molten NaCl. Factors including salt type, initial batch composition, and firing temperature/time showed significant effects on the MSS process. The size of the composite powder was found to be 0.3-0.6 μm/30-60 nm for Al_2O_3/TiB_2 phases after 5 h firing in NaCl at 1050°C, using 30 wt% excessive Al and 30 wt% excessive B_2O_3. By increasing the temperature to 1150°C, Al_2O_3-TiB_2 nanocomposite powder could also be prepared in NaCl after a shorter dwell time of 4 h using 30 wt% excessive Al and 20 wt% excessive B_2O_3, but the crystals grew large, with 1-2 μm for the blocky Al_2O_3 particles and 100-200 nm for the spherical TiB_2 particles.

Chapter 10 Conclusions and Future Works

10.1 Conclusions

The conclusions of the thesis are as follows.

(1) TiB_2 fine powder was prepared from TiO_2 and B_2O_3 *via* a molten-salt-assisted magnesiothermic reduction route. Among the three chloride salts (NaCl, KCl, and $MgCl_2$), $MgCl_2$ had the best accelerating effect. To synthesise phase-pure TiB_2, 20 mol% excessive Mg was used to compensate for its evaporation loss at the test temperatures. The MSS technique developed in this work enabled the synthesis of phase-pure TiB_2 fine particles of 100-200 nm in size at temperatures as low as 1000°C, which is much lower than the temperatures required by many other techniques reported to date. In addition, under the optimal reaction conditions, the shape/size of the raw material TiO_2 had little effect on the reaction extent and the shape/size of the TiB_2 product particles, suggesting that it was unnecessary to use expensive nanosized TiO_2 as a starting raw material for the MSS of TiB_2 fine particles. The "dissolution-precipitation" mechanism dominated the overall MSS process.

(2) HfB_2 fine powder was prepared *via* the magnesiothermic reduction of HfO_2 and B_2O_3 in molten $MgCl_2$. Phase-pure HfB_2 powder could be prepared in $MgCl_2$ after 4 h heating at 1000°C using 80 and 20 wt% excessive Mg and B_2O_3, respectively. In addition, to promote the completion of the HfB_2 formation reaction after the temperature was decreased to 950°C, the heating time was increased to 6 h and the excessive amount of B_2O_3 was increased to 60 wt% (due to the prolonged duration). Spheroidal HfB_2

particles with an average size of ~100 nm were obtained after 6 h heating at 950°C, whereas angular particles with a larger average size of 100-200 nm were obtained after 4 h heating at 1000°C. The “dissolution-precipitation” mechanism was more dominant than the “template-growth” mechanism in the overall MSS process.

(3) LaB_6 powder was successfully synthesised from La_2O_3 and B_2O_3 *via* magnesiothermic reduction in molten $MgCl_2$. When 20 mol% excessive Mg was used, phase-pure LaB_6 fine particles with a size of ~200 nm were obtained after 4 h of heating at 1000°C in $MgCl_2$, whereas smaller LaB_6 particles (~100 nm) were generated after 5 h of heating at 900°C.

(4) CaB_6 powder was synthesised from CaO and B_2O_3 *via* the molten-salt-mediated magnesiothermic reduction. Compared with NaCl and KCl, $CaCl_2$ facilitated the synthesis more effectively. When 20 mol% excessive Mg was used, phase-pure CaB_6 nanoparticles (~50 nm) were formed after heating at 800°C for 6 h. The “dissolution-precipitation” mechanism is considered to be responsible for the overall MSS process and low temperature formation of nanosized CaB_6 particles.

(5) Al_2O_3-TiB_2 composite powders were produced *via* the aluminothermic reduction of TiO_2 and B_2O_3 in molten NaCl. When appropriately excessive amounts of Al and B_2O_3 were used to compensate for their evaporation losses at the test temperatures, phase-pure Al_2O_3-TiB_2 nanocomposite powders were successfully synthesised in NaCl after 5 h of heating at 1050°C. The size of the Al_2O_3 particles was in the range of 0.3-0.6 μm, whereas that of the TiB_2 particles was between 30 and 60 nm.

(6) The molten-salt-mediated magnesiothermic reduction technique was used to

synthesise amorphous boron powders. Upon using 15 mol% excessive Mg, high-purity amorphous boron fine particles (100-200 nm) were prepared after 6 h of heating at 900°C in $MgCl_2$ and subsequent leaching using 1 M HCl at room temperature and 0.5 M H_2SO_4 at 70-90°C.

10.2 Future works

Unfortunately, because of the limitations of the current experimental conditions, a few works were not carried out that must be completed in the future.

(1) The oxygen content should be examined using a more reliable method/tool, such as an oxygen elemental analyser, to provide a comparable result for other research.

(2) The preparation of high-purity and dense diborides without any additives is desirable. Therefore, the sintering behaviour of prepared diboride ultrafine powders and that of Al_2O_3-TiB_2 nanocomposite powder should be studied. Furthermore, the microstructures and physical properties of the fabricated ceramic samples should be evaluated.

(3) Examination of the optical, thermal or electrochemical properties of the as-synthesised hexaboride nanoparticles should be carried out.

(4) The MSS technique offers new possibilities for the synthesis of known advanced materials as well as new material development. The research on MSS controlled by the “dissolution and precipitation” mechanism can be applied to prepare many different metal borides with fine particle sizes using oxide-based metal sources. The research on MSS governed by the “template-growth” mechanism can be modified to fabricate novel materials with 2D-nanostructure or 3D-interconnected networks.

Publications

1. **Ke. Bao**, Cheng Liu, Bahareh Yazdani Damavandi, and Shaowei Zhang, "Low-temperature preparation of lanthanum hexaboride fine powder *via* magnesiothermal reduction in molten salt," Journal of Ceramic Science and Technology 7[4] 403-08 (2016).
2. Jianke. Ye, **Ke. Bao**, Yan. Wen, and Jiangtao. Li, "Improvement of the oxidation resistance of TiC-coated carbon black by high-temperature annealing in N_2," RSC Advances, vol. 6, pp. 25601-25604, 2016.
3. **Ke. Bao**, Yan. Wen, Matthana. Khangkhamano, and Shaowei Zhang, "Low-temperature preparation of titanium diboride fine powder *via* magnesiothermal reduction in molten salt," Journal of the American Ceramic Society, 100[5] 2266-72 (2017).
4. **Ke. Bao**, Joseph Massey, Juntong Huang, and Shaowei Zhang, "Low-temperature synthesis of hafnium diboride powder *via* magnesiothermal reduction in molten salt," Ceramic Engineering and Science Proceedings (2017) (accepted).
5. **Ke Bao**, Liangxu Lin, Hong Chang and Shaowei Zhang, “Low-temperature synthesis of calcium hexaboride nanoparticles *via* magnesiothermic reduction in molten salt,” Journal of the Ceramic Society of Japan (2017) (accepted).
6. **Ke Bao**, Jacob Black, Yanqiu Zhu and Shaowei Zhang, “Synthesis of alumina-titanium diboride nanocomposite powders *via* molten-salt-assisted aluminothermic reduction,” Journal of Materials Science (2017) (submitted).

Conference Presentations

1. **Ke Bao**, “Low Temperature Preparation of Lanthanum Hexaboride Fine Powder *via* Magnesiothermal Reduction in Molten Salt”, 6th International Congress on Ceramics (ICC6), August 21-25, 2016, Dresden, Germany.
2. **Ke Bao**, “Low-temperature synthesis of hafnium diboride powder *via* magnesiothermal reduction in molten salt”, 41st International Conference and Expo on Advanced Ceramics and Composites (ICACC 17), January 22-27, 2017, Daytona Beach, Florida, USA.

References

[1] B. Albert and H. Hillebrecht, "Boron: Elementary Challenge for Experimenters and Theoreticians," *Angewandte Chemie International Edition,* vol. 48, pp. 8640-8668, 2009.

[2] B. Van Devener, J. P. L. Perez, J. Jankovich, and S. L. Anderson, "Oxide-Free, Catalyst-Coated, Fuel-Soluble, Air-Stable Boron Nanopowder as Combined Combustion Catalyst and High Energy Density Fuel," *Energy & Fuels,* vol. 23, pp. 6111-6120, 2009.

[3] C. Perut and B. Mahe, "BORON PROPELLANTS FOR DUCTED ROCKET APPLICATION," vol. 2, pp. 361-374, 1993.

[4] C. L. Yeh and K. K. Kuo, "Ignition and combustion of boron particles," *Progress in Energy and Combustion Science,* vol. 22, pp. 511-541, 1996.

[5] R. O. Foelsche, R. L. Burton and H. Krier, "Boron particle ignition and combustion at 30–150 atm," *Combustion and Flame,* vol. 117, pp. 32-58, 1999.

[6] J. C. Poret and J. J. Sabatini, "Comparison of Barium and Amorphous Boron Pyrotechnics for Green Light Emission," *Journal of Energetic Materials,* vol. 31, pp. 27-34, 2013.

[7] J. J. Wu, W. H. Ma, G. L. Zhang, Y. C. Zhai, B. Yang, and Y. N. Dai, "Preparation of ultra-fine amorphous boron powder by magnesiothermic reduction," *Chinese Journal of Nonferrous Metals,* vol. 17, pp. 2034-2039, 2007.

[8] Y.-K. Kim, K. Chung, J. Yoo, I.-H. Song, J. Ko, W.-H. Chung, D.-H. Kim, X. Wang, S. X. Dou, and P.-W. Shin, "Effect of fine boron powders prepared with a self-propagating high temperature synthesis on flux pinning properties of the MgB_2/Fe composite wires," *Journal of Alloys and Compounds,* vol. 485, pp. L44-L46, 2009.

[9] Z.-h. Dou, T.-a. Zhang, J.-c. He, and Y. Huang, "Preparation of amorphous nano-boron powder with high activity by combustion synthesis," *Journal of Central South University,* vol. 21, pp. 900-903, 2014.

[10] J. Wang, Y. Gu, Z. Li, W. Wang, and Z. Fu, "Synthesis of nano-sized amorphous boron powders through active dilution self-propagating high-temperature synthesis method," *Materials Research Bulletin,* vol. 48, pp. 2018-2022, 2013.

[11] B. U. Yoo, H. H. Nersisyan, H. Y. Ryu, J. S. Lee, and J. H. Lee, "Structural and thermal properties of boron nanoparticles synthesized from

B2O3+3Mg+kNaCl mixture," *Combustion and Flame,* vol. 161, pp. 3222-3228, 2014.

[12] Y. Ou, P. La, D. Zhu, and Y. Zhu, "Preparation and Characterization of Amorphous B Powders by Salt-Assisted SHS Technique," *Advances in Materials Science and Engineering,* vol. 2015, p. 7, 2015.

[13] H. H. Nersisyan, S. H. Joo, B. U. Yoo, Y. H. Cho, H. M. Kim, and J.-H. Lee, "Melt-assisted solid flame synthesis approach to amorphous boron nanoparticles," *Combustion and Flame,* vol. 162, pp. 3316-3323, 2015.

[14] S. Masih and J. Maisam, "Combustion synthesis of amorphous boron in a very-short-term magnesiothermic reduction," *Materials Research Express,* vol. 3, p. 115018, 2016.

[15] A. SEIFOLAZADEH and S. MOHAMMADI, "Synthesis and characterization of nanoboron powders prepared with mechanochemical reaction between B_2O_3 and Mg powders," *Bulletin of Materials Science,* vol. 39, pp. 479-486, 2016.

[16] S. Boily, H. D. Alamdari, R. DUBUC, and J. Gaudet, "Process for the production of elemental boron by solid state reaction," WIPO Patent 2003051773, 2003.

[17] D. AĞAOĞULLARI, Ö. BALCI and İ. DUMAN, "Mechanisms and effects of various reducing agents on the fabrication of elemental Boron," in *19th International Conference on Metallurgy and Materials, Roznov Pod Radhostem, Czech republic*, pp. 748-752, 2010.

[18] W. G. Fahrenholtz, J. Binner and J. Zou, "Synthesis of ultra-refractory transition metal diboride compounds," *Journal of Materials Research,* vol. 31, pp. 2757-2772, 2016.

[19] K. M. Schmidt, O. A. Graeve and V. R. Vasquez, "Ab Initio and Molecular Dynamics-Based Pair Potentials for Lanthanum Hexaboride," *The Journal of Physical Chemistry C,* vol. 119, pp. 14288-14296, 2015.

[20] M. Munro, "Evaluated Material Properties for a Sintered alpha-Alumina," *Journal of the American Ceramic Society,* vol. 80, pp. 1919-1928, 1997.

[21] K. Niihara, "New design concept of structural ceramics. Ceramic nanocomposites," *Journal of the Ceramic Society of Japan,* vol. 99, pp. 974-982, 1991.

[22] W. M. Rainforth, "The wear behaviour of oxide ceramics-A Review," *Journal of Materials Science,* vol. 39, pp. 6705-6721, 2004.

[23] I. Kimura, N. Hotta, Y. Hiraoka, N. Saito, and Y. Yokota, "Sintering and characterization of Al_2O_3-TiB_2 composites," *Journal of the European Ceramic Society,* vol. 5, pp. 23-27, 1989.

[24] J. Liu and P. D. Ownby, "Enhanced Mechanical Properties of Alumina by

Dispersed Titanium Diboride Particulate Inclusions," *Journal of the American Ceramic Society,* vol. 74, pp. 241-243, 1991.

[25] S. Ranganath and J. Subrahmanyam, "Impact response of Al_2O_3 and Al_2O_3-TiB_2 ceramic composites," *Journal of Materials Science Letters,* vol. 10, pp. 1297-1298, 1991.

[26] A. Bellosi, G. De Portu and S. Guicciardi, "Preparation and properties of electroconductive Al_2O_3-based composites," *Journal of the European Ceramic Society,* vol. 10, pp. 307-315, 1992.

[27] D. Jianxin, A. Xing and L. Zhaoqian, "Friction and wear behavior of Al_2O_3/TiB_2 composite against cemented carbide in various atmospheres at elevated temperature," *Wear,* vol. 195, pp. 128-132, 1996.

[28] D. Jianxin, C. Tongkun and L. Lili, "Self-lubricating behaviors of Al_2O_3/TiB_2 ceramic tools in dry high-speed machining of hardened steel," *Journal of the European Ceramic Society,* vol. 25, pp. 1073-1079, 2005.

[29] A. Tampieri and A. Bellosi, "Oxidation of monolithic TiB_2 and of Al_2O_3-TiB_2 composite," *Journal of Materials Science,* vol. 28, pp. 649-653, 1993.

[30] R. H. Plovnick and E. A. Richards, "New combustion synthesis route to TiB_2-Al_2O_3," *Materials Research Bulletin,* vol. 36, pp. 1487-1493, 2001.

[31] E. Mohammad Sharifi, F. Karimzadeh and M. H. Enayati, "Synthesis of titanium diboride reinforced alumina matrix nanocomposite by mechanochemical reaction of Al–TiO_2–B_2O_3," *Journal of Alloys and Compounds,* vol. 502, pp. 508-512, 2010.

[32] M. A. Khaghani-Dehaghani, R. Ebrahimi-Kahrizsangi, N. Setoudeh, and B. Nasiri-Tabrizi, "Mechanochemical synthesis of Al_2O_3–TiB_2 nanocomposite powder from Al–TiO_2–H_3BO_3 mixture," *International Journal of Refractory Metals and Hard Materials,* vol. 29, pp. 244-249, 2011.

[33] E. M. Sharifi, F. Karimzadeh and M. H. Enayati, "Preparation of Al_2O_3–TiB_2 nanocomposite powder by mechanochemical reaction between Al, B_2O_3 and Ti," *Advanced Powder Technology,* vol. 22, pp. 526-531, 2011.

[34] M. Abdellahi, J. Heidari and R. Sabouhi, "Influence of B source materials on the synthesis of TiB_2-Al_2O_3 nanocomposite powders by mechanical alloying," *International Journal of Minerals, Metallurgy and Materials,* vol. 20, pp. 1214-1220, 2013.

[35] W. Yang, S. Dong, P. Luo, A. Yangli, Q. Liu, and Z. Xie, "Effect of Ni addition on the preparation of Al_2O_3–TiB_2 composites using high-energy ball milling," *Journal of Asian Ceramic Societies,* vol. 2, pp. 399-402, 2014.

[36] Z. Yu and Z. Yang, "Self-propagating high-temperature reductive

synthesis of TiB_2-Al_2O_3 composite powders," *Journal of Wuhan University of Technology-Materials Science Edition,* vol. 22, pp. 48-51, 2007.

[37] B. Shahbahrami, R. Sarraf Maamoori and N. Ehsani, "Self-spreading high-temperature synthesis of TiB_2 powder," *Materials Science Poland,* vol. 25, pp. 719-731, 2007.

[38] E. Montakhab and A. M. Hadian, "Combustion synthesis and sintering of TiB_2-Al_2O_3 composites; investigating the effects of different Al-content as a precursor," *Advanced Materials Research,* vol. 829, pp. 549-553, 2014.

[39] R. T. Mousavian, S. Sharafi, M. R. Roshan, and M. H. Shariat, "Effect of mechanical activation of reagents' mixture on the high-temperature synthesis of Al_2O_3-TiB_2 composite powder," *Journal of Thermal Analysis and Calorimetry,* vol. 104, pp. 1063-1070, 2011.

[40] M. J. Sayagués, M. A. Avilés, J. M. Córdoba, and F. J. Gotor, "Self-propagating combustion synthesis *via* an MSR process: An efficient and simple method to prepare (Ti, Zr, Hf)B_2-Al_2O_3 powder nanocomposites," *Powder Technology,* vol. 256, pp. 244-250, 2014.

[41] A. Rabiezadeh, A. M. Hadian and A. Ataie, "Preparation of alumina/titanium diboride nano-composite powder by milling assisted sol-gel method," *International Journal of Refractory Metals and Hard Materials,* vol. 31, pp. 121-124, 2012.

[42] X. Liu, N. Fechler and M. Antonietti, "Salt melt synthesis of ceramics, semiconductors and carbon nanostructures," *Chemical Society Reviews,* vol. 42, pp. 8237-8265, 2013.

[43] C. Fan, J. Li and L. Wang, "Phase transitions, mechanical properties and electronic structures of novel boron phases under high-pressure: A first-principles study," *Scientific Reports,* vol. 4, p. 6786, 2014.

[44] A. R. Oganov and V. L. Solozhenko, "Boron: a hunt for superhard polymorphs," *Journal of Superhard Materials,* vol. 31, pp. 285-291, 2009.

[45] A. R. Oganov, J. Chen, C. Gatti, Y. Ma, Y. Ma, C. W. Glass, Z. Liu, T. Yu, O. O. Kurakevych, and V. L. Solozhenko, "Ionic high-pressure form of elemental boron," *Nature,* vol. 457, pp. 863-867, 2009.

[46] E. D. Jemmis and D. L. V. K. Prasad, "Icosahedral B_{12}, macropolyhedral boranes, β-rhombohedral boron and boron-rich solids," *Journal of Solid State Chemistry,* vol. 179, pp. 2768-2774, 2006.

[47] M. Kobayashi, "Structure of amorphous boron," *Journal of Materials Science,* vol. 23, pp. 4392-4398, 1988.

[48] J. S. Gillespie, "Crystallization of Massive Amorphous Boron," *Journal of the American Chemical Society,* vol. 88, pp. 2423-2425, 1966.

[49] M. Terauchi, Y. Kawamata, M. Tanaka, M. Takeda, and K. Kimura,

"Electron Energy-Loss Spectroscopy Study of the Electronic Structure of α-Rhombohedral Boron," *Journal of Solid State Chemistry,* vol. 133, pp. 156-159, 1997.

[50] M. Kobayashi, I. Higashi and M. Takami, "Fundamental Structure of Amorphous Boron," *Journal of Solid State Chemistry,* vol. 133, pp. 211-214, 1997.

[51] I. Higashi and T. Ishii, "Two-Dimensional Icosahedral B_{12} Networks in Boron-Rich Crystals," *Forma,* vol. 16, pp. 187-207, 2001.

[52] C. P. Talley, L. E. Line and Q. D. Overman, "Preparation and Properties of Massive Amorphous Elemental Boron," in *Boron Synthesis, Structure, and Properties: Proceedings of the Conference on Boron*, Edited by J. A. Kohn*, et al.*, Springer US, Boston, MA, pp. 94-104, 1960.

[53] A. Masago, K. Shirai and H. Katayama-Yoshida, "Crystal stability of -and -boron," *Physical Review B,* vol. 73, p. 104102, 2006.

[54] B. J. Bellott, W. Noh, R. G. Nuzzo, and G. S. Girolami, "Nanoenergetic materials: boron nanoparticles from the pyrolysis of decaborane and their functionalisation," *Chemical Communications,* pp. 3214-3215, 2009.

[55] C. Subramanian, A. K. Suri and T. S. R. Ch Murthy, "Development of boron–based materials for nuclear applications," *BARC Newsletter,* pp. 14-22, 2010.

[56] G. E. Laramore, P. Wootton, J. C. Livesey, D. S. Wilbur, R. Risler, M. Phillips, J. Jacky, T. A. Buchholz, T. W. Griffin, and S. Brossard, "Boron neutron capture therapy: A mechanism for achieving a concomitant tumor boost in fast neutron radiotherapy," *International Journal of Radiation Oncology*Biology*Physics,* vol. 28, pp. 1135-1142, 1994.

[57] I. Boustani, "Towards novel boron nanostructural materials," in *Chemical Modelling: Applications and Theory Volume 8*. vol. 8, Edited by M. Springborg, The Royal Society of Chemistry, pp. 1-44, 2011.

[58] S. Ran, O. Van der Biest and J. Vleugels, "ZrB_2 Powders Synthesis by Borothermal Reduction," *Journal of the American Ceramic Society,* vol. 93, pp. 1586-1590, 2010.

[59] W. M. Guo, G. J. Zhang, Y. You, S. H. Wu, and H. T. Lin, "TiB_2 Powders Synthesis by Borothermal Reduction in TiO_2 Under Vacuum," *Journal of the American Ceramic Society,* vol. 97, pp. 1359-1362, 2014.

[60] N. Akçamlı, D. Ağaoğulları, Ö. Balcı, M. L. Öveçoğlu, and İ. Duman, "Synthesis of HfB_2 powders by mechanically activated borothermal reduction of HfCl4," *Ceramics International,* vol. 42, pp. 3797-3807, 2016.

[61] S. Prochazka and R. M. Scanlan, "Effect of Boron and Carbon on Sintering of SiC," *Journal of the American Ceramic Society,* vol. 58, pp.

72-72, 1975.

[62] K. Kawahara, S. Tsurekawa and H. Nakashima, "Effect of boron and carbon addition on high temperature deformation behavior of β-silicon carbide," *Materials Science Forum,* vol. 304-306, pp. 519-524, 1999.

[63] P. Wang, S. Orimo and H. Fujii, "Characterization of hydrogenated amorphous boron by a combination of infrared absorption spectroscopy and thermal analyses," *Journal of Alloys and Compounds,* vol. 359, pp. L1-L3, 2003.

[64] T. Abu-Hamed, J. Karni and M. Epstein, "The use of boron for thermochemical storage and distribution of solar energy," *Solar Energy,* vol. 81, pp. 93-101, 2007.

[65] W. G. Fahrenholtz, G. E. Hilmas, I. G. Talmy, and J. A. Zaykoski, "Refractory Diborides of Zirconium and Hafnium," *Journal of the American Ceramic Society,* vol. 90, pp. 1347-1364, 2007.

[66] P. Vajeeston, P. Ravindran, C. Ravi, and R. Asokamani, "Electronic structure, bonding, and ground-state properties of AlB_2-type transition-metal diborides," *Physical Review B,* vol. 63, p. 045115, 2001.

[67] A. L. Ivanovskii, "Mechanical and electronic properties of diborides of transition 3d–5d metals from first principles: Toward search of novel ultra-incompressible and superhard materials," *Progress in Materials Science,* vol. 57, pp. 184-228, 2012.

[68] B. Post, F. W. Glaser and D. Moskowitz, "Transition metal diborides," *Acta Metallurgica,* vol. 2, pp. 20-25, 1954.

[69] B. Alling, H. Högberg, R. Armiento, J. Rosen, and L. Hultman, "A theoretical investigation of mixing thermodynamics, age-hardening potential, and electronic structure of ternary $M^1_{1-x}M^2_xB_2$ alloys with AlB_2 type structure," *Scientific Reports,* vol. 5, p. 9888, 2015.

[70] B. Basu, G. B. Raju and A. K. Suri, "Processing and properties of monolithic TiB_2 based materials," *International Materials Reviews,* vol. 51, pp. 352-374, 2006.

[71] W. G. Fahrenholtz and G. E. Hilmas, "Oxidation of ultra-high temperature transition metal diboride ceramics," *International Materials Reviews,* vol. 57, pp. 61-72, 2012.

[72] B. R. Golla, T. Bhandari, A. Mukhopadhyay, and B. Basu, "Titanium Diboride," in *Ultra-High Temperature Ceramics: Materials for Extreme Environment Applications*, Edited by W. G. Fahrenholtz*, et al.*, John Wiley & Sons, Inc, Hoboken, New Jersey, pp. 316-360, 2014.

[73] B. Basu and K. Balani, "Bonding, Structure, and Physical Properties," in *Advanced Structural Ceramics*, Edited by B. Basu and K. Balani, John

Wiley & Sons, Inc., Hoboken, New Jersey, pp. 28-29, 2011.

[74] W. Xiao-Bing, T. De-Cheng and W. Li-Long, "The electronic structure and chemical stability of the AlB2-type transition-metal diborides," *Journal of Physics: Condensed Matter,* vol. 6, p. 10185, 1994.

[75] R. G. Munro, "Material Properties of Titanium Diboride," *Journal of Research of the National Institute of Standards and Technology,* vol. 105, pp. 709-720, 2000.

[76] M. M. Opeka, I. G. Talmy, E. J. Wuchina, J. A. Zaykoski, and S. J. Causey, "Mechanical, Thermal, and Oxidation Properties of Refractory Hafnium and zirconium Compounds," *Journal of the European Ceramic Society,* vol. 19, pp. 2405-2414, 1999.

[77] R. Savino, M. De Stefano Fumo, L. Silvestroni, and D. Sciti, "Arc-jet testing on HfB2 and HfC-based ultra-high temperature ceramic materials," *Journal of the European Ceramic Society,* vol. 28, pp. 1899-1907, 2008.

[78] M. M. Nasseri, "The behavior of HfB_2 at neutron irradiation: a simulation study," *Radiation Effects and Defects in Solids,* vol. 171, pp. 252-258, 2016.

[79] W. A. Phelan, S. M. Koohpayeh, P. Cottingham, J. A. Tutmaher, J. C. Leiner, M. D. Lumsden, C. M. Lavelle, X. P. Wang, C. Hoffmann, M. A. Siegler, N. Haldolaarachchige, D. P. Young, and T. M. McQueen, "On the Chemistry and Physical Properties of Flux and Floating Zone Grown SmB6 Single Crystals," vol. 6, p. 20860, 2016.

[80] J. M. Lafferty, "Boride Cathodes," *Journal of Applied Physics,* vol. 22, pp. 299-309, 1951.

[81] C.-H. Chen, T. Aizawa, N. Iyi, A. Sato, and S. Otani, "Structural refinement and thermal expansion of hexaborides," *Journal of Alloys and Compounds,* vol. 366, pp. L6-L8, 2004.

[82] P. I. Loboda, H. P. Kysla, S. M. Dub, and O. P. Karasevs'ka, "Mechanical properties of the monocrystals of lanthanum hexaboride," *Materials Science,* vol. 45, pp. 108-113, 2009.

[83] S. N. Dub, G. P. Kislaya and P. I. Loboda, "Study of mechanical properties of LaB6 single crystal by nanoindentation," *Journal of Superhard Materials,* vol. 35, pp. 158-165, 2013.

[84] B. Huang, Y.-H. Duan, Y. Sun, M.-J. Peng, and S. Chen, "Electronic structures, mechanical and thermodynamic properties of cubic alkaline-earth hexaborides from first principles calculations," *Journal of Alloys and Compounds,* vol. 635, pp. 213-224, 2015.

[85] L. Chao, L. Bao, W. Wei, T. O, and Z. Zhang, "First-principles study on the

electronic structure, phonons and optical properties of LaB_6 under high-pressure," *Journal of Alloys and Compounds,* vol. 672, pp. 419-425, 2016.

[86] R. Iiyoshi, H. Shimoyama and S. Maruse, "A Comparison of Thermionic Emission Current Density and Brightness Evaporation Loss for LaB_6 and Tungsten," *Journal of Electron Microscopy,* vol. 45, pp. 514-517, 1996.

[87] J. D. Buckingham, "Thermionic emission properties of a lanthanum hexaboride/rhenium cathode," *British Journal of Applied Physics,* vol. 16, p. 1821, 1965.

[88] J. I. Goldstein, D. E. Newbury, P. Echlin, D. C. Joy, C. Fiori, and E. Lifshin, "Electron Optics," in *Scanning Electron Microscopy and X-Ray Microanalysis: A Text for Biologist, Materials Scientist, and Geologists*, Edited, Springer US, Boston, MA, pp. 19-51, 1981.

[89] K. N. Leung, "Directly heated LaB6 cathodes for ion source operation," *Vacuum,* vol. 36, pp. 865-867, 1986.

[90] P. Herzig, Z. Fojud, O. J. Żogał, A. Pietraszko, A. Dukhnenko, S. Jurga, and N. Shitsevalova, "Electric-field-gradient tensor and charge densities in LaB_6: B_{11} nuclear-magnetic-resonance single-crystal investigations and first-principles calculations," *Journal of Applied Physics,* vol. 103, p. 083534, 2008.

[91] D. M. Goebel and R. M. Watkins, "Compact lanthanum hexaboride hollow cathode," *Review of Scientific Instruments,* vol. 81, p. 083504, 2010.

[92] X.-h. Zhang, P. Hu, J.-c. Han, L. Xu, and S.-h. Meng, "The addition of lanthanum hexaboride to zirconium diboride for improved oxidation resistance," *Scripta Materialia,* vol. 57, pp. 1036-1039, 2007.

[93] D. D. Jayaseelan, E. Zapata-Solvas, P. Brown, and W. E. Lee, "In situ Formation of Oxidation Resistant Refractory Coatings on SiC-Reinforced ZrB_2 Ultra High Temperature Ceramics," *Journal of the American Ceramic Society,* vol. 95, pp. 1247-1254, 2012.

[94] F. Monteverde, D. Alfano and R. Savino, "Effects of LaB_6 addition on arc-jet convectively heated SiC-containing ZrB_2-based ultra-high temperature ceramics in high enthalpy supersonic airflows," *Corrosion Science,* vol. 75, pp. 443-453, 2013.

[95] T. T. Shen, D. H. Xiao, X. Q. Ou, M. Song, Y. H. He, N. Lin, and D. F. Zhang, "Effects of LaB_6 addition on the microstructure and mechanical properties of ultrafine grained WC–10Co alloys," *Journal of Alloys and Compounds,* vol. 509, pp. 1236-1243, 2011.

[96] V. I. Matkovich, *Boron and refractory borides*: Springer-Verlag, 1977.

[97] T. T. Xu, J.-G. Zheng, A. W. Nicholls, S. Stankovich, R. D. Piner, and R. S.

Ruoff, "Single-Crystal Calcium Hexaboride Nanowires: Synthesis and Characterization," *Nano Letters,* vol. 4, pp. 2051-2055, 2004.

[98] Ö. Balcı, D. Ağaoğulları, İ. Duman, and M. L. Öveçoğlu, "Synthesis of CaB6 powders *via* mechanochemical reaction of Ca/B_2O_3 blends," *Powder Technology,* vol. 225, pp. 136-142, 2012.

[99] S. Otani and T. Mori, "Flux Growth and Magnetic Properties of CaB_6 Crystals," *Journal of the Physical Society of Japan,* vol. 71, pp. 1791-1792, 2002.

[100] J. W. Butler, "Neutron-absorbing bricks made from CaB_6," *Nuclear Instruments and Methods,* vol. 7, pp. 201-203, 1960.

[101] K. G. Schmitt-Thomas, A. Lipp and K. Schwetz, "Process for the production of oxygen-free copper casting and moldings," U.S. Patent 4118256, 1978.

[102] T. Rymon-Lipinski, B. Schmelzer and S. Ulitzka, "Tests on the oxidation-inhibiting effect of CaB_6 in refractory MgO-C materials," *Steel Research,* vol. 65, pp. 234-237, 1994.

[103] D. P. Young, D. Hall, M. E. Torelli, Z. Fisk, J. L. Sarrao, J. D. Thompson, H. R. Ott, S. B. Oseroff, R. G. Goodrich, and R. Zysler, "High-temperature weak ferromagnetism in a low-density free-electron gas," *Nature,* vol. 397, pp. 412-414, 1999.

[104] S. Souma, H. Komatsu, T. Takahashi, R. Kaji, T. Sasaki, Y. Yokoo, and J. Akimitsu, "Electronic Band Structure and Fermi Surface of CaB_6 Studied by Angle-Resolved Photoemission Spectroscopy," *Physical Review Letters,* vol. 90, p. 027202, 2003.

[105] H. Yin, D. Tang, X. Mao, W. Xiao, and D. Wang, "Electrolytic calcium hexaboride for high capacity anode of aqueous primary batteries," *Journal of Materials Chemistry A,* vol. 3, pp. 15184-15189, 2015.

[106] M. Takeda, T. Fukuda, F. Domingo, and T. Miura, "Thermoelectric properties of some metal borides," *Journal of Solid State Chemistry,* vol. 177, pp. 471-475, 2004.

[107] K. Yootaek and H. Tung, "A reflection electron microscopic (REM) study of α-Al_2O_3(0001) surfaces," *Surface Science,* vol. 258, pp. 131-146, 1991.

[108] T. Shirai, H. Watanabe, M. Fuji, and M. Takahashi, "Structural Properties and Surface Characteristics on Aluminum Oxide Powders," *Annual Report of the Ceramics Research Laboratory Nagoya Institute of Technology,* vol. 9, pp. 23-31, 2009.

[109] D. F. Williams, "Contemporary and future biomaterials," in *Essential Biomaterials Science*., Edited, Cambridge University Press, Cambridge, United Kingdom, pp. 497-498, 2014.

[110] B. Yazdani, Y. Xia, I. Ahmad, and Y. Zhu, "Graphene and carbon nanotube (GNT)-reinforced alumina nanocomposites," *Journal of the European Ceramic Society,* vol. 35, pp. 179-186, 2015.

[111] T. Saito, T. Fukuda, H. Maeda, K. Kusakabe, and S. Morooka, "Synthesis of ultrafine titanium diboride particles by rapid carbothermal reduction in a particulate transport reactor," *Journal of Materials Science,* vol. 32, pp. 3933-3938, 1997.

[112] S. H. Kang and D. J. Kim, "Synthesis of nano-titanium diboride powders by carbothermal reduction," *Journal of the European Ceramic Society,* vol. 27, pp. 715-718, 2007.

[113] B. Shahbahrami, F. Golestani Fard and A. Sedghi, "The effect of processing parameters in the carbothermal synthesis of titanium diboride powder," *Advanced Powder Technology,* vol. 23, pp. 234-238, 2012.

[114] R. Thompson, "Production, Fabrication and Uses of Borides," in *The Physics and Chemistry of Carbides, Nitrides and Borides*, Edited by R. Freer, Springer Netherlands, Dordrecht, pp. 113-120, 1990.

[115] C. Subramanian, T. S. R. C. Murthy and A. K. Suri, "Synthesis and consolidation of titanium diboride," *International Journal of Refractory Metals and Hard Materials,* vol. 25, pp. 345-350, 2007.

[116] R. Koc, J. R. Mawdsley and J. D. Carter, "Synthesis of metal borides," U.S. Patent 20120315207, 2012.

[117] D.-W. Ni, G.-J. Zhang, Y.-M. Kan, and P.-L. Wang, "Synthesis of Monodispersed Fine Hafnium Diboride Powders Using Carbo/Borothermal Reduction of Hafnium Dioxide," *Journal of the American Ceramic Society,* vol. 91, pp. 2709-2712, 2008.

[118] J. K. Sonber, T. S. R. C. Murthy, C. Subramanian, S. Kumar, R. K. Fotedar, and A. K. Suri, "Investigations on synthesis of HfB_2 and development of a new composite with $TiSi_2$," *International Journal of Refractory Metals and Hard Materials,* vol. 28, pp. 201-210, 2010.

[119] H. Wang, S.-H. Lee and H.-D. Kim, "Nano-Hafnium Diboride Powders Synthesized Using a Spark Plasma Sintering Apparatus," *Journal of the American Ceramic Society,* vol. 95, pp. 1493-1496, 2012.

[120] Z. Wang, X. Liu, B. Xu, and Z. Wu, "Fabrication and properties of HfB_2 ceramics based on micron and submicron HfB_2 powders synthesized *via* carbo/borothermal reduction of HfO_2 with B_4C and carbon," *International Journal of Refractory Metals and Hard Materials,* vol. 51, pp. 130-136, 2015.

[121] M. Hasan, H. Sugo and E. Kisi, "Low temperature carbothermal and boron carbide reduction synthesis of LaB_6," *Journal of Alloys and*

Compounds, vol. 578, pp. 176-182, 2013.

[122] J. K. Sonber, K. Sairam, T. S. R. C. Murthy, A. Nagaraj, C. Subramanian, and R. C. Hubli, "Synthesis, densification and oxidation study of lanthanum hexaboride," *Journal of the European Ceramic Society,* vol. 34, pp. 1155-1160, 2014.

[123] S. Zheng, G. Min, Z. Zou, H. Yu, and J. Han, "Synthesis of Calcium Hexaboride Powder *via* the Reaction of Calcium Carbonate with Boron Carbide and Carbon," *Journal of the American Ceramic Society,* vol. 84, pp. 2725-2727, 2001.

[124] Z. Lin, M. Guanghui and Y. Huashun, "Reaction mechanism and size control of CaB_6 micron powder synthesized by the boroncarbide method," *Ceramics International,* vol. 35, pp. 3533-3536, 2009.

[125] Ö. Yildiz, R. Telle, C. Schmalzried, and A. Kaiser, "Phase transformation of transient B_4C to CaB_6 during production of CaB_6 from colemanite," *Journal of the European Ceramic Society,* vol. 25, pp. 3375-3381, 2005.

[126] M. Kakiage, S. Shiomi, I. Yanase, and H. Kobayashi, "Low-Temperature Synthesis of Calcium Hexaboride Powder *via* Transient Boron Carbide Formation," *Journal of the American Ceramic Society,* vol. 98, pp. 2724-2727, 2015.

[127] D. Y. Cakta, N. Koç and S. Turan, "Synthesis of Calcium Hexaboride Powder *via* Boro/Carbothermal Reduction with a Gel Precursor," *Journal of Ceramic Science and Technology,* vol. 7, pp. 349-356, 2016.

[128] P. Peshev and G. Bliznakov, "On the borothermic preparation of titanium, zirconium and hafnium diborides," *Journal of the Less Common Metals,* vol. 14, pp. 23-32, 1968.

[129] B. Post, D. Moskowitz and F. W. Glaser, "Borides of Rare Earth Metals," *Journal of the American Chemical Society,* vol. 78, pp. 1800-1802, 1956.

[130] K. Hiebl and M. J. Sienko, "Chemical control of superconductivity in the hexaborides," *Inorganic Chemistry,* vol. 19, pp. 2179-2180, 1980.

[131] W.-M. Guo, Z.-G. Yang and G.-J. Zhang, "Synthesis of submicrometer HfB_2 powder and its densification," *Materials Letters,* vol. 83, pp. 52-55, 2012.

[132] M. M. Hasan, E. Kisi and H. Sugo, "Preparation of lanthanum hexaboride cathodes for thermionic energy generation," in *2013 International Conference on Informatics, Electronics & Vision (ICIEV)*, pp. 1-5, 2013.

[133] M. M. Hasan, H. Sugo and E. H. Kisi, "Low Temperature Synthesis of Rare-Earth Hexaborides for Solar Energy Conversion," *MATEC Web of Conferences,* vol. 13, p. 06005, 2014.

[134] N. Katsuhiro, N. Takanobu, U. Shigenori, S. Hideki, and A. Masahiko,

"Preparation of ultrafine boride powders by metallothermic reduction method," *Journal of Physics: Conference Series,* vol. 176, p. 012043, 2009.

[135] X. Su, F. Fu, Y. Yan, G. Zheng, T. Liang, Q. Zhang, X. Cheng, D. Yang, H. Chi, X. Tang, Q. Zhang, and C. Uher, "Self-propagating high-temperature synthesis for compound thermoelectrics and new criterion for combustion processing," *Nature Communications,* vol. 5, p. 4908, 2014.

[136] U. Demircan, B. Derin and O. Yücel, "Effect of HCl concentration on TiB_2 separation from a self-propagating high-temperature synthesis (SHS) product," *Materials Research Bulletin,* vol. 42, pp. 312-318, 2007.

[137] A. K. Khanra, L. C. Pathak, S. K. Mishra, and M. M. Godkhindi, "Effect of NaCl on the synthesis of TiB2 powder by a self-propagating high-temperature synthesis technique," *Materials Letters,* vol. 58, pp. 733-738, 2004.

[138] N. Chaichana, N. Memongkol, J. Wannasin, and S. Niyomwas, "Synthesis of nano-sized TiB_2 powder by self-propagating high temperature synthesis," *CMU J Nat Sci Special Issue on Nanotechnol,* vol. 7, pp. 51-7, 2008.

[139] A. Nekahi and S. Firoozi, "Effect of KCl, NaCl and $CaCl_2$ mixture on volume combustion synthesis of TiB_2 nanoparticles," *Materials Research Bulletin,* vol. 46, pp. 1377-1383, 2011.

[140] Z.-h. Dou, T.-a. Zhang, Z.-q. Zhang, H.-b. Zhang, and J.-c. He, "Preparation and characterization of LaB_6 ultra fine powder by combustion synthesis," *Transactions of Nonferrous Metals Society of China,* vol. 21, pp. 1790-1794, 2011.

[141] X. Huang, J. Zhong, L. Dou, and K. Wang, "Combustion synthesis of CaB_6 powder from calcium hexaborate and Mg," *International Journal of Refractory Metals and Hard Materials,* vol. 28, pp. 143-149, 2010.

[142] A. Nozari, A. Ataie and S. Heshmati-Manesh, "Synthesis and characterization of nano-structured TiB_2 processed by milling assisted SHS route," *Materials Characterization,* vol. 73, pp. 96-103, 2012.

[143] C. Suryanarayana, "Mechanical alloying and milling," *Progress in Materials Science,* vol. 46, pp. 1-184, 2001.

[144] N. J. Welham, "Formation of Nanometric TiB_2 from TiO_2," *Journal of the American Ceramic Society,* vol. 83, pp. 1290-1292, 2000.

[145] R. Ricceri and P. Matteazzi, "A fast and low-cost room temperature process for TiB_2 formation by mechanosynthesis," *Materials Science and Engineering: A,* vol. 379, pp. 341-346, 2004.

[146] A. Nozari, S. Heshmati-Manesh and A. Ataie, "A facile synthesis of TiB_2

nano-particles *via* mechano-thermal route," *International Journal of Refractory Metals and Hard Materials,* vol. 33, pp. 107-112, 2012.

[147] B. S. B. Reddy, K. Das and S. Das, "A review on the synthesis of in situ aluminum based composites by thermal, mechanical and mechanical–thermal activation of chemical reactions," *Journal of Materials Science,* vol. 42, pp. 9366-9378, 2007.

[148] B. Nasiri-Tabrizi, T. Adhami and R. Ebrahimi-Kahrizsangi, "Effect of processing parameters on the formation of TiB_2 nanopowder by mechanically induced self-sustaining reaction," *Ceramics International,* vol. 40, pp. 7345-7354, 2014.

[149] E. Barraud, S. Bégin-Colin and G. L. Caër, "Nanorods of HfB_2 from mechanically-activated $HfCl_4$ and B-based powder mixtures," *Journal of Alloys and Compounds,* vol. 398, pp. 208-218, 2005.

[150] D. Ağaoğulları, İ. Duman and M. L. Öveçoğlu, "Synthesis of LaB_6 powders from La_2O_3, B_2O_3 and Mg blends *via* a mechanochemical route," *Ceramics International,* vol. 38, pp. 6203-6214, 2012.

[151] D. Ağaoğulları, Ö. Balcı, M. L. Öveçoğlu, and İ. Duman, "Preparation of LaB_6 Powders *via* Calciothermic Reduction using Mechanochemistry and Acid Leaching," *KONA Powder and Particle Journal,* vol. 33, pp. 203-218, 2016.

[152] L. Wang, L. Xu, Z. Ju, and Y. Qian, "A versatile route for the convenient synthesis of rare-earth and alkaline-earth hexaborides at mild temperatures," *CrystEngComm,* vol. 12, pp. 3923-3928, 2010.

[153] I. P. Borovinskaya, A. G. Merzhanov, N. P. Novikov, and A. K. Filonenko, "Gasless combustion of mixtures of powdered transition metals with boron," *Combustion, Explosion and Shock Waves,* vol. 10, pp. 2-10, 1974.

[154] J. B. Holt, "The Use of Exothermic Reactions in the Synthesis and Densification of Ceramic Materials," *MRS Bulletin,* vol. 12, pp. 60-65, 1987.

[155] A. A. Zenin, A. G. Merzhanov and G. A. Nersisyan, "Thermal wave structure in SHS processes," *Combustion, Explosion and Shock Waves,* vol. 17, pp. 63-71, 1981.

[156] D. D. Radev and M. Marinov, "Properties of titanium and zirconium diborides obtained by self-propagated high-temperature synthesis," *Journal of Alloys and Compounds,* vol. 244, pp. 48-51, 1996.

[157] Y. Hwang and J. K. Lee, "Preparation of TiB_2 powders by mechanical alloying," *Materials Letters,* vol. 54, pp. 1-7, 2002.

[158] Y. D. Blum, J. Marschall, D. Hui, B. Adair, and M. Vestel, "Hafnium

Reactivity with Boron and Carbon Sources Under Non-Self-Propagating High-Temperature Synthesis Conditions," *Journal of the American Ceramic Society,* vol. 91, pp. 1481-1488, 2008.

[159] L. S. Volkova, Y. M. Shulga and S. P. Shilkin, "Synthesis of nano-sized titanium diboride in a melt of anhydrous sodium tetraborate," *Russian Journal of General Chemistry,* vol. 82, pp. 819-821, 2012.

[160] S. E. Kravchenko, A. G. Burlakova, I. I. Korobov, Y. M. Shul'ga, N. N. Dremova, L. S. Volkova, G. V. Kalinnikov, S. P. Shilkin, and R. A. Andrievskii, "Preparation of hafnium diboride nanopowders in an anhydrous $Na_2B_4O_7$ ionic melt," *Inorganic Materials,* vol. 51, pp. 380-383, 2015.

[161] S. Xin, X. Han, S. Liu, Z. Liu, B. Xu, Y. Tian, and D. Yu, "CaB_6 single crystals grown under high pressure and hightemperature," *Journal of Crystal Growth,* vol. 313, pp. 47-50, 2010.

[162] D. L. Segal, "Chemical Routes for the Preparation of Powders," in *The Physics and Chemistry of Carbides, Nitrides and Borides*, Edited by R. Freer, Springer Netherlands, Dordrecht, pp. 3-11, 1990.

[163] R. L. Axelbaum, D. P. DuFaux, C. A. Frey, K. F. Kelton, S. A. Lawton, L. J. Rosen, and S. M. L. Sastry, "Gas-phase combustion synthesis of titanium boride (TiB_2) nanocrystallites," *Journal of Materials Research,* vol. 11, pp. 948-954, 1996.

[164] L. Chen, Y. Gu, Y. Qian, L. Shi, Z. Yang, and J. Ma, "A facile one-step route to nanocrystalline TiB_2 powders," *Materials Research Bulletin,* vol. 39, pp. 609-613, 2004.

[165] L. Chen, Y. Gu, L. Shi, Z. Yang, J. Ma, and Y. Qian, "Synthesis and oxidation of nanocrystalline HfB_2," *Journal of Alloys and Compounds,* vol. 368, pp. 353-356, 2004.

[166] S. E. Bates, W. E. Buhro, C. A. Frey, S. M. L. Sastry, and K. F. Kelton, "Synthesis of titanium boride $(TiB)_2$ nanocrystallites by solution-phase processing," *Journal of Materials Research,* vol. 10, pp. 2599-2612, 1995.

[167] Y. Gu, Y. Qian, L. Chen, and F. Zhou, "A mild solvothermal route to nanocrystalline titanium diboride," *Journal of Alloys and Compounds,* vol. 352, pp. 325-327, 2003.

[168] M. Zhang, L. Yuan, X. Wang, H. Fan, X. Wang, X. Wu, H. Wang, and Y. Qian, "A low-temperature route for the synthesis of nanocrystalline LaB_6," *Journal of Solid State Chemistry,* vol. 181, pp. 294-297, 2008.

[169] J. P. Kelly, R. Kanakala and O. A. Graeve, "A Solvothermal Approach for the Preparation of Nanostructured Carbide and Boride Ultra-High-Temperature Ceramics," *Journal of the American Ceramic*

Society, vol. 93, pp. 3035-3038, 2010.

[170] Y. Yuan, L. Zhang, L. Liang, K. He, R. Liu, and G. Min, "A solid-state reaction route to prepare LaB_6 nanocrystals in vacuum," *Ceramics International,* vol. 37, pp. 2891-2896, 2011.

[171] B. Lihong, Wurentuya, W. Wei, and O. Tegus, "A new route for the synthesis of submicron-sized LaB_6," *Materials Characterization,* vol. 97, pp. 69-73, 2014.

[172] L. Shi, Y. Gu, L. Chen, Z. Yang, J. Ma, and Y. Qian, "Low Temperature Synthesis and Characterization of Cubic CaB_6 Ultrafine Powders," *Chemistry Letters,* vol. 32, pp. 958-959, 2003.

[173] L. Bao, X. Qi, Tana, L. Chao, and O. Tegus, "Synthesis, and magnetic and optical properties of nanocrystalline alkaline-earth hexaborides," *CrystEngComm,* vol. 18, pp. 1223-1229, 2016.

[174] H. Wang, S.-H. Lee, H.-D. Kim, and H.-C. Oh, "Synthesis of Ultrafine Hafnium Diboride Powders Using Solution-Based Processing and Spark Plasma Sintering," *International Journal of Applied Ceramic Technology,* vol. 11, pp. 359-363, 2014.

[175] Y. J. Yan, Z. R. Huang, S. M. Dong, and D. L. Jiang, "Carbothermal Preparation of Ultra-Fine TiB_2 Powders Using Solution-Derived Precursors *via* Sol-Gel Method," *Key Engineering Materials,* vol. 336-338, pp. 944-947, 2007.

[176] S. Venugopal, E. E. Boakye, A. Paul, K. Keller, P. Mogilevsky, B. Vaidhyanathan, J. G. P. Binner, A. Katz, and P. M. Brown, "Sol–Gel Synthesis and Formation Mechanism of Ultrahigh Temperature Ceramic: HfB2," *Journal of the American Ceramic Society,* vol. 97, pp. 92-99, 2014.

[177] S. Venugopal, A. Paul, B. Vaidhyanathan, J. G. P. Binner, A. Heaton, and P. M. Brown, "Synthesis and spark plasma sintering of sub-micron HfB_2: Effect of various carbon sources," *Journal of the European Ceramic Society,* vol. 34, pp. 1471-1479, 2014.

[178] P. Ozkalafat, G. Kartal Sireli and S. Timur, "Electrodeposition of titanium diboride from oxide based melts," *Surface and Coatings Technology,* vol. 308, pp. 128-135, 2016.

[179] S. V. Devyatkin, G. Kaptay, V. I. Shapoval, I. V. Zarutskii, V. P. Lugovoi, and S. A. Kuznetsov, "Deposition of Titanium, Zirconium and Hafnium Diboride Coatings by High-Temperature Electrochemical Synthesis from Chloro-Fluoride Melts," in *Refractory Metals in Molten Salts: Their Chemistry, Electrochemistry and Technology*, Edited by D. H. Kerridge and E. G. Polyakov, Springer Netherlands, Dordrecht, pp. 73-80, 1998.

[180] V. I. Taranenko, I. V. Zarutskii, V. I. Shapoval, M. Makyta, and K.

Matiašovský, "Mechanism of the cathode process in the electrochemical synthesis of TiB2 in molten salts—II. Chloride-Fluoride electrolytes," *Electrochimica Acta,* vol. 37, pp. 263-268, 1992.

[181] M. Makyta, V. Daněk, G. M. Haarberg, and J. Thonstad, "Electrodeposition of titanium diboride from fused salts," *Journal of Applied Electrochemistry,* vol. 26, pp. 319-324, 1996.

[182] X. Wang and Y. Zhai, "An electrochemical method for the preparation of CaB6 crystal powder," *Journal of Applied Electrochemistry,* vol. 39, pp. 1797-1802, 2009.

[183] S. Angappan, M. Helan, A. Visuvasam, L. J. Berchmans, and V. Ananth, "Electrolytic preparation of CaB_6 by molten salt technique," *Ionics,* vol. 17, pp. 527-533, 2011.

[184] H. Moissan, *Étude du bore amorphe*. Paris: Gauthier-Villars, 1895.

[185] E. Weintraub, "On the Properties and Preparation of the Element Boron," *Journal of Industrial & Engineering Chemistry,* vol. 3, pp. 299-301, 1911.

[186] W. J. Kroll, O. Corvallis and N. P. Nies, "Production of elemental boron," U.S. Patent 2893842, 1959.

[187] H. Mazza, D. L. Sawyer and R. W. Baier, "Process for producing amorphous boron of high purity," U.S. Patent 2866688, 1958.

[188] N. P. Nies, Pasadena and E. W. Fajans, "Production of elemental boron by magnesium reduction," U. S. Patent 2897056, 1959.

[189] G. I. Yukin, "The mechanism of electroplating with boron," *Metal Science and Heat Treatment,* vol. 13, pp. 662-664, 1971.

[190] M. Makyta, K. Matiašovský and P. Fellner, "Mechanism of the cathode process in the electrolytic boriding in molten salts," *Electrochimica Acta,* vol. 29, pp. 1653-1657, 1984.

[191] M. Makyta, M. Chrenková, P. Fellner, and K. Matiašovský, "Mechanism of the Thermochemical Boriding Process and electrochemical studies in the molten systems based on $Na_2B_4O_7$," *Zeitschrift für anorganische und allgemeine Chemie,* vol. 540, pp. 169-176, 1986.

[192] K. Matiašovský, M. Chrenková-Paučírová, P. Fellner, and M. Makyta, "Electrochemical and thermochemical boriding in molten salts," *Surface and Coatings Technology,* vol. 35, pp. 133-149, 1988.

[193] L. P. Polyakova, G. A. Bukatova, E. G. Polyakov, E. Christensen, J. H. von Barner, and N. J. Bjerrum, "Electrochemical Behavior of Boron in LiF-NaF-KF- Melts," *Journal of The Electrochemical Society,* vol. 143, pp. 3178-3186, 1996.

[194] A. Jain, S. Anthonysamy, K. Ananthasivan, R. Ranganathan, V. Mittal, S. V. Narasimhan, and P. R. Vasudeva Rao, "Characterization of

electrodeposited elemental boron," *Materials Characterization,* vol. 59, pp. 890-900, 2008.

[195] P. R. Taylor and J. C. Gomez, "Synthesis of boron using molten salt electrolysis," U. S. Patent 20100294670, 2010.

[196] R. Pal, S. Anthonysamy and V. Ganesan, "Electrochemistry of Deposition of Boron from KCl-KF-KBF_4 Melts: Voltammetric Studies on Platinum Electrode," *Journal of The Electrochemical Society,* vol. 159, pp. F157-F165, 2012.

[197] A. Jain, S. Anthonysamy, G. S. Gupta, and V. Ganesan, "Processing of enriched elemental boron (^{10}B~65 at.%)," *Materials Chemistry and Physics,* vol. 140, pp. 335-342, 2013.

[198] D. R. Stern and L. Lynds, "High-Purity Crystalline Boron," *Journal of The Electrochemical Society,* vol. 105, pp. 676-682, 1958.

[199] L. Vandenbulcke and G. Vuillard, "Chemical Vapor Deposition of Amorphous Boron on Massive Substrates," *Journal of The Electrochemical Society,* vol. 123, pp. 278-285, 1976.

[200] L. Vandenbulcke and G. Vuillard, "Mass Transfer, Equilibrium, and Kinetics in the Chemical Vapor Deposition of Boron from Impinging Jets," *Journal of The Electrochemical Society,* vol. 124, pp. 1931-1937, 1977.

[201] M. Diana, C. Luponio and G. Russo, "An experimental investigation on the boron trichloride hydrogen plasma reactions at medium and high pressure," *Rev. Phys. Appl. (Paris),* vol. 12, pp. 1237-1242, 1977.

[202] U. Jansson, M. Boman and J.-O. Carlsson, "Kinetics and mechanisms in CVD of boron," *Journal of Crystal Growth,* vol. 94, pp. 171-181, 1989.

[203] E. A. Haupfear and L. D. Schmidt, "Kinetics of boron deposition from BBr_3 + H_2," *Chemical Engineering Science,* vol. 49, pp. 2467-2481, 1994.

[204] J. V. Marzik, R. C. Lewis, M. E. Tillman, Y. Q. Wu, D. K. Finnemore, M. Rindfleisch, M. Tomsic, J. Yue, and W. J. Croft, "Plasma synthesized boron nano-sized powder: The effect of processing conditions on the crystallographic and microstructural properties," *Materials Research Society Symposium Proceedings,* vol. 1148, pp. 214-219, 2008.

[205] Z. Huang, Q. Wu, X. Li, S. Shang, X. Dai, and Y. Yin, "Synthesis and Characterization of Nano-sized Boron Powder Prepared by Plasma Torch," *Plasma Science and Technology,* vol. 12, p. 577, 2010.

[206] D. Ağaoğulları, Ö. Balcı, İ. Duman, and M. L. Öveçoğlu, "Synthesis of α- and β-Rhombohedral Boron Powders *via* Gas Phase Thermal Dissociation of Boron Trichloride by Hydrogen," *Metallurgical and Materials Transactions B,* vol. 42, pp. 568-574, 2011.

[207] A. W. Laubengayer, D. T. Hurd, A. E. Newkirk, and J. L. Hoard, "Boron. I.

Preparation and Properties of Pure Crystalline Boron," *Journal of the American Chemical Society,* vol. 65, pp. 1924-1931, 1943.

[208] D. K. Das and K. Kumar, "Chemical vapor deposition of boron on a beryllium surface," *Thin Solid Films,* vol. 83, pp. 53-60, 1981.

[209] C. Combescure, B. Armas, M. Alnot, and B. Weber, "Kinetic Study of Boron Tribromide Pyrolysis at Low Pressure," *Journal of The Electrochemical Society,* vol. 128, pp. 358-361, 1981.

[210] K. Kamimura, T. Nagaoka, T. Shinomiya, M. Nakao, Y. Onuma, and M. Makimura, "Preparation and properties of boron thin films," *Thin Solid Films,* vol. 343–344, pp. 342-344, 1999.

[211] P. Z. Si, M. Zhang, C. Y. You, D. Y. Geng, J. H. Du, X. G. Zhao, X. L. Ma, and Z. D. Zhang, "Amorphous boron nanoparticles and BN encapsulating boron nano-peanuts prepared by arc-decomposing diborane and nitriding," *Journal of Materials Science,* vol. 38, pp. 689-692, 2003.

[212] H. L. Johnston, H. N. Hersh and E. C. Kerr, "Low Temperature Heat Capacities of Inorganic Solids.1 V. The Heat Capacity of Pure Elementary Boron in Both Amorphous and Crystalline Conditions between 13 and 305°K. Some Free Energies of Formation," *Journal of the American Chemical Society,* vol. 73, pp. 1112-1117, 1951.

[213] J. D. Casey and J. Haggerty, "Laser-induced vapour-phase syntheses of boron and titanium diboride powders," *Journal of Materials Science,* vol. 22, pp. 737-744, 1987.

[214] L. Guo, R. N. Singh and H. J. Kleebe, "Nucleation and Growth of Boron Nanowires on ZrB_2 Particles," *Chemical Vapor Deposition,* vol. 12, pp. 448-452, 2006.

[215] K. Shirai and S. I. Gonda, "Characterization of hydrogenated amorphous boron films prepared by electron cyclotron resonance plasma chemical vapor deposition method," *Journal of Applied Physics,* vol. 67, pp. 6286-6291, 1990.

[216] S. Johansson, J. Å. Schweitz, H. Westberg, and M. Boman, "Microfabrication of three-dimensional boron structures by laser chemical processing," *Journal of Applied Physics,* vol. 72, pp. 5956-5963, 1992.

[217] M. Vignolo, G. Romano, A. Martinelli, C. Bernini, and A. S. Siri, "A Novel Process to Produce Amorphous Nanosized Boron Useful for MgB_2 Synthesis," *IEEE Transactions on Applied Superconductivity,* vol. 22, pp. 6200606-6200606, 2012.

[218] A. A. Chin and C. Hill, "Preparation of boron and sodium from sodium tetrataborate by reduction," European Patent 1887092, 2008.

[219] Z.-h. Dou, T.-a. Zhang, G.-y. Shi, C. Peng, M. Wen, and J.-c. He,

"Preparation and characterization of amorphous boron powder with high activity," *Transactions of Nonferrous Metals Society of China,* vol. 24, pp. 1446-1451, 2014.

[220] N. P. Nies, A. W. Fajans and L. L. Thomas, "Electrolytic production of elemental boron," U.S. Patent 2832730, 1958.

[221] N. P. Nies, "Preparation of Boron by Fused Salt Electrolysis," *Journal of The Electrochemical Society,* vol. 107, pp. 817-820, 1960.

[222] K. U. Nair, D. K. Bose and C. K. Gupta, "The Production of Elemental Boron by Fused Salt Electrolysis," *Mineral Processing and Extractive Metallurgy Review,* vol. 9, pp. 283-291, 1992.

[223] W. Stadlbauer, W. Kladnig and G. Gritzner, "Al_2O_3-TiB_2 composite ceramics," *Journal of Materials Science Letters,* vol. 8, pp. 1217-1220, 1989.

[224] G. Liu, D. Yan and J. Zhang, "Microstructure and mechanical properties of TiB_2-Al_2O_3 composites," *Journal of Wuhan University of Technology-Mater. Sci. Ed.,* vol. 26, pp. 696-699, 2011.

[225] J. Li, L. Gao and J. Guo, "Mechanical properties and electrical conductivity of TiN–Al_2O_3 nanocomposites," *Journal of the European Ceramic Society,* vol. 23, pp. 69-74, 2003.

[226] K. V. Logan, "Shaped refractory products and method of making same," ed: Google Patents, 1990.

[227] S. P. Ray, "Boride-alumina composites: Synthesis and Fabrication," *Metallurgical Transactions A,* vol. 23, pp. 2381-2385, 1992.

[228] L. J. Kecskes, A. Niiler, T. Kottke, K. V. Logan, and G. R. Villalobos, "Dynamic Consolidation of Combustion-Synthesized Alumina-Titanium Diboride Composite Ceramics," *Journal of the American Ceramic Society,* vol. 79, pp. 2687-2695, 1996.

[229] Z. Y. Ma and S. C. Tjong, "In Situ ceramic particle-reinforced aluminum matrix composites fabricated by reaction pressing in the TiO_2 (Ti)-Al-B (B_2O_3) systems," *Metallurgical and Materials Transactions A,* vol. 28, pp. 1931-1942, 1997.

[230] T. D. Xia, T. Z. Liu, W. J. Zhao, Z. A. Munir, and T. M. Wang, "Photo- and Cathodoluminescence of the Combustion-synthesized Al_2O_3–TiB_2 Composites," *Journal of Materials Research,* vol. 15, pp. 1622-1629, 2000.

[231] M. A. Meyers, E. A. Olevsky, J. Ma, and M. Jamet, "Combustion synthesis/densification of an Al_2O_3–TiB_2 composite," *Materials Science and Engineering: A,* vol. 311, pp. 83-99, 2001.

[232] H.-g. Zhu, H.-z. Wang, L.-q. Ge, S. Chen, and S.-q. Wu, "Formation of

composites fabricated by exothermic dispersion reaction in Al-TiO_2-B_2O_3 system," *Transactions of Nonferrous Metals Society of China,* vol. 17, pp. 590-594, 2007.

[233] H. Zhu, H. Wang and L. Ge, "Wear properties of the composites fabricated by exothermic dispersion reaction synthesis in an Al–TiO_2–B_2O_3 system," *Wear,* vol. 264, pp. 967-972, 2008.

[234] C. L. Yeh and R. F. Li, "Formation of TiB_2–Al_2O_3 and NbB_2–Al_2O_3 composites by combustion synthesis involving thermite reactions," *Chemical Engineering Journal,* vol. 147, pp. 405-411, 2009.

[235] R. T. Mousavian, S. Sharafi and M. H. Shariat, "Microwave-assisted combustion synthesis in a mechanically activated Al-TiO_2-H_3BO_3 system," *International Journal of Refractory Metals and Hard Materials,* vol. 29, pp. 281-288, 2011.

[236] S. K. Mishra, V. Gokuul and S. Paswan, "Alumina-titanium diboride in situ composite by self-propagating high-temperature synthesis (SHS) dynamic compaction: Effect of compaction pressure during synthesis," *International Journal of Refractory Metals and Hard Materials,* vol. 43, pp. 19-24, 2014.

[237] E. D. Rodeghiero, B. C. Moore, B. S. Wolkenberg, M. Wuthenow, O. K. Tse, and E. P. Giannelis, "Sol–gel synthesis of ceramic matrix composites," *Materials Science and Engineering: A,* vol. 244, pp. 11-21, 1998.

[238] T. Kimura, "Molten Salt Synthesis of Ceramic Powders," in *Advances in Ceramics - Synthesis and Characterization, Processing and Specific Applications*, Edited by C. Sikalidis, InTechOpen, pp. 75-96, 2011.

[239] S. Zhang, D. D. Jayaseelan, G. Bhattacharya, and W. E. Lee, "Molten salt synthesis of magnesium aluminate ($MgAl_2O_4$) spinel powder," *J. Am. Ceram. Soc.,* vol. 89, pp. 1724-1726, 2006.

[240] D. D. Jayaseelan, S. Zhang, S. Hashimoto, and W. E. Lee, "Template formation of magnesium aluminate ($MgAl_2O_4$) spinel microplatelets in molten salt," *Journal of the European Ceramic Society,* vol. 27, pp. 4745-4749, 2007.

[241] X. Liu and S. Zhang, "Low-Temperature Preparation of Titanium Carbide Coatings on Graphite Flakes from Molten Salts," *Journal of the American Ceramic Society,* vol. 91, pp. 667-670, 2008.

[242] M. E. Ebrahimi, M. Allahverdi and A. Safari, "Synthesis of High Aspect Ratio Platelet $SrTiO_3$," *Journal of the American Ceramic Society,* vol. 88, pp. 2129-2132, 2005.

[243] W. Xie, G. Mobus and S. Zhang, "Molten salt synthesis of silicon carbide

nanorods using carbon nanotubes as templates," *Journal of Materials Chemistry,* vol. 21, pp. 18325-18330, 2011.

[244] Z. Li, S. Zhang and W. E. Lee, "Molten salt synthesis of $LaAlO_3$ powder at low temperatures," *Journal of the European Ceramic Society,* vol. 27, pp. 3201-3205, 2007.

[245] D. Portehault, S. Devi, P. Beaunier, C. Gervais, C. Giordano, C. Sanchez, and M. Antonietti, "A General Solution Route toward Metal Boride Nanocrystals," *Angewandte Chemie International Edition,* vol. 50, pp. 3262-3265, 2011.

[246] S. Ran, H. Sun, Y. n. Wei, D. Wang, N. Zhou, and Q. Huang, "Low-Temperature Synthesis of Nanocrystalline NbB_2 Powders by Borothermal Reduction in Molten Salt," *Journal of the American Ceramic Society,* vol. 97, pp. 3384-3387, 2014.

[247] Z. Liu, Y. n. Wei, X. Meng, T. Wei, and S. Ran, "Synthesis of CrB_2 powders at 800°C under ambient pressure," *Ceramics International,* vol. 43, pp. 1628-1631, 2017.

[248] S. Zhang, M. Khangkhamano, H. Zhang, and H. A. Yeprem, "Novel Synthesis of ZrB_2 Powder *Via* Molten-Salt-Mediated Magnesiothermic Reduction," *Journal of the American Ceramic Society,* vol. 97, pp. 1686-1688, 2014.

[249] G. J. Janz, F. W. Dampier, G. R. Lakshminarayanan, P. K. Lorenz, and R. P. T. Tomkins, "Molten Salts: Volume 1, Electrical Conductance, Density, and Viscosity Data," *National Standard Reference Data,* pp. 48-50, 1968.

[250] G. J. Janz, R. P. T. Tomkins, C. B. Allen, J. R. Downey, G. L. Garner, U. Krebs, and S. K. Singer, "Molten salts: Volume 4, part 2, chlorides and mixtures—electrical conductance, density, viscosity, and surface tension data," *Journal of Physical and Chemical Reference Data,* vol. 4, p. 890, 1975.

[251] L. Nikzad, T. Ebadzadeh, M. R. Vaezi, and A. Tayebifard, "Effect of milling on the combustion synthesis of ternary system B_2O_3, Mg and C," *IET Micro & Nano Letters,* vol. 7, pp. 366-369, 2012.

[252] R. Ebrahimi-Kahrizsangi, M. Alimardani and O. Torabi, "Investigation on mechanochemical behavior of the TiO_2–Mg–C system reactive mixtures in the synthesis of titanium carbide," *International Journal of Refractory Metals and Hard Materials,* vol. 52, pp. 90-97, 2015.

[253] Z.-H. Dou, T.-A. Zhang, S.-G. Fan, Q.-Y. Huang, J.-L. Zhang, H.-Y. Xiao, and N. Fu, "A new method of preparing NdB_6 ultra-fine powders," *Rare Metals,* pp. 1-7, 2015.

[254] R. E. Dinnebier and S. J. L. Billinge, "Principles of Powder Diffraction," in

Powder Diffraction: Theory and Practice, Edited, The Royal Society of Chemistry, pp. 1-19, 2008.

[255] "Crystals and X-Ray," in *Crystallography and the World of Symmetry*, Edited by S. K. Chatterjee, Springer Berlin Heidelberg, Berlin, Heidelberg, pp. 43-56, 2008.

[256] Y. Waseda, E. Matsubara and K. Shinoda, "Fundamental Properties of X-rays," in *X-Ray Diffraction Crystallography: Introduction, Examples and Solved Problems*, Edited, Springer Berlin Heidelberg, Berlin, Heidelberg, pp. 1-20, 2011.

[257] Y. Waseda, E. Matsubara and K. Shinoda, "Diffraction from Polycrystalline Samples and Determination of Crystal Structure," in *X-Ray Diffraction Crystallography: Introduction, Examples and Solved Problems*, Edited, Springer Berlin Heidelberg, Berlin, Heidelberg, pp. 107-167, 2011.

[258] R. Jenkins and R. L. Snyder, "Diffraction Theory," in *Introduction to X-ray Powder Diffractometry*, Edited, John Wiley & Sons, Inc., p. 90, 1996.

[259] X-ray diffraction- Bruker D8 Discover [Online]. Available: https://fys.kuleuven.be/iks/nvsf/experimental-facilities/x-ray-diffraction-2013-bruker-d8-discover

[260] BRIEF INTRODUCTION TO SCANNING ELECTRON MICROSCOPY (SEM) [Online]. Available: http://cfamm.ucr.edu/documents/sem-intro.pdf

[261] W. Zhou, R. Apkarian, Z. L. Wang, and D. Joy, "Fundamentals of Scanning Electron Microscopy (SEM)," in *Scanning Microscopy for Nanotechnology: Techniques and Applications*, Edited by W. Zhou and Z. L. Wang, Springer NY, New York, pp. 1-40, 2007.

[262] M. A. Sutton, N. Li, D. C. Joy, A. P. Reynolds, and X. Li, "Scanning Electron Microscopy for Quantitative Small and Large Deformation Measurements Part I: SEM Imaging at Magnifications from 200 to 10,000," *Experimental Mechanics,* vol. 47, pp. 775-787, 2007.

[263] J. I. Goldstein, D. E. Newbury, P. Echlin, D. C. Joy, C. E. Lyman, E. Lifshin, L. Sawyer, and J. R. Michael, "Electron Beam–Specimen Interactions," in *Scanning Electron Microscopy and X-ray Microanalysis: Third Edition*, Edited by J. I. Goldstein*, et al.*, Springer US, Boston pp. 61-98, 2003.

[264] L. Reimer, "Imaging with Secondary and Backscattered Electrons," in *Scanning Electron Microscopy: Physics of Image Formation and Microanalysis*, Edited, Springer Berlin Heidelberg, Berlin, Heidelberg, pp. 227-271, 1985.

[265] L. Reimer, "Introduction," in *Scanning Electron Microscopy: Physics of Image Formation and Microanalysis*, Edited, Springer Berlin Heidelberg, Berlin, Heidelberg, pp. 1-12, 1998.

[266] L. Reimer, "Elemental Analysis and Imaging with X-Rays," in *Scanning Electron Microscopy: Physics of Image Formation and Microanalysis*, Edited, Springer Berlin Heidelberg, Berlin, Heidelberg, pp. 379-447, 1998.

[267] J. I. Goldstein, D. E. Newbury, P. Echlin, D. C. Joy, C. E. Lyman, E. Lifshin, L. Sawyer, and J. R. Michael, "X-Ray Spectral Measurement: EDS and WDS," in *Scanning Electron Microscopy and X-ray Microanalysis: Third Edition*, Edited by J. I. Goldstein*, et al.*, Springer Science+Business Media, New York, pp. 297-353, 2003.

[268] Scanning Electron Microscopy (SEM) [Online]. Available: https://www.gla.ac.uk/schools/ges/researchandimpact/researchfacilities/isaac/services/scanningelectronmicroscopy/

[269] D. B. Williams and C. B. Carter, "The Transmission Electron Microscope," in *Transmission Electron Microscopy: A Textbook for Materials Science*, Edited, Springer US, Boston, MA, pp. 3-22, 2009.

[270] D. B. Williams and C. B. Carter, "Lenses, Apertures, and Resolution," in *Transmission Electron Microscopy: A Textbook for Materials Science*, Edited, Springer US, Boston, MA, pp. 91-114, 2009.

[271] D. B. Williams and C. B. Carter, "The Instrument," in *Transmission Electron Microscopy: A Textbook for Materials Science*, Edited, Springer US, Boston, MA, pp. 141-171, 2009.

[272] Brent Fultz and J. M. Howe, "The TEM and its Optics," in *Transmission Electron Microscopy and Diffractometry of Materials*, Edited by B. Fultz and J. M. Howe, Springer-Verlag, Berlin, pp. 61-118, 2008.

[273] TEM manual JEM-2100 [Online]. Available: https://www.aphys.kth.se/polopoly_fs/1.190438!/Menu/general/column-content/attachment/TEM_manual_JEOL2100.pdf

[274] R. M. Brydson and C. Hammond, "Generic Methodologies for Nanotechnology: Characterization," in *Nanoscale Science and Technology*, Edited by R. W. Kelsall*, et al.*, John Wiley & Sons, Ltd, England, pp. 57-82, 2005.

[275] E. Bilgi, H. E. Çamurlu, B. Akgün, Y. Topkaya, and N. Sevinç, "Formation of TiB2 by volume combustion and mechanochemical process," *Materials Research Bulletin,* vol. 43, pp. 873-881, 2008.

[276] J. Wypartowicz, T. Østvold and H. A. Øye, "The solubility of magnesium metal and the recombination reaction in the industrial magnesium electrolysis," *Electrochimica Acta,* vol. 25, pp. 151-156, 1980.

[277] R. Hovhannisyan, H. Alexanyan, M. Hovhannisyan, B. Petrosyan, and V. Harutyunyan, "Phase Diagramm, Cristallization Behavior and Ferroelectric Properties of Stoichiometric Glass Ceramics in the

BaO-TiO2-B2O3 System," in *Ferroelectrics - Physical Effects*, Edited by M. Lallart, InTechOpen, pp. 49-76, 2011.

[278] W. Xie, Z. Mirza, G. Möbus, and S. Zhang, "Novel Synthesis and Characterization of High Quality Silicon Carbide Coatings on Carbon Fibers," *Journal of the American Ceramic Society,* vol. 95, pp. 1878-1882, 2012.

[279] X. Li, Z. Dong, A. Westwood, A. Brown, S. Zhang, R. Brydson, N. Li, and B. Rand, "Preparation of a titanium carbide coating on carbon fibre using a molten salt method," *Carbon,* vol. 46, pp. 305-309, 2008.

[280] J. Ye, S. Zhang and W. E. Lee, "Novel low temperature synthesis and characterisation of hollow silicon carbide spheres," *Microporous and Mesoporous Materials,* vol. 152, pp. 25-30, 2012.

[281] K. Ouchi, Y. Kobayashi, R. Endo, and M. Susa, "Promotion of Solid TiO_2 Reduction by Molten Magnesium from the Perspective of Reaction Mechanisms," *Tetsu-to-Hagane,* vol. 99, pp. 433-438, 2013.

[282] M. Ito and K. Morita, "The Solubility of MgO in Molten $MgCl_2$-$CaCl_2$ Salt," *Materials Transactions, JIM,* vol. 45, pp. 2712-2718, 2004.

[283] R. L. Martin and J. B. West, "Solubility of magnesium oxide in molten salts," *Journal of Inorganic and Nuclear Chemistry,* vol. 24, pp. 105-111, 1962.

[284] H. Hayashi and K. Minato, "Stability of lanthanide oxides in LiCl–KCl eutectic melt," *Journal of Physics and Chemistry of Solids,* vol. 66, pp. 422-426, 2005.

[285] M.-l. Zhang, P. Cao, W. Han, Y.-d. Yan, and L.-j. Chen, "Preparation of Mg–Li—La alloys by electrolysis in molten salt," *Transactions of Nonferrous Metals Society of China,* vol. 22, pp. 16-22, 2012.

[286] C. Caravaca, P. Diaz Arocas, J. A. Serrano, C. Gonzalez, R. Bermejo, M. Vega, A. Martinez, and Y. Castrillejo, "Solubilization studies of rare earth oxides and oxo halides, application of electrochemical techniques in pyrochemical processes," *6th Information Exchange Meeting,* vol. 32, pp. 625-636, 2001.

[287] H. Kobayashi, M. Katoh, Y. Kamiyama, and T. Mitamura, "Preparation of ZrB2 Fine Powders Using Thermite Method by Reduction with Mg," *Journal of the Ceramic Society of Japan,* vol. 100, pp. 172-177, 1992.

[288] H. Kobayashi, K. Shimosaka and T. Mitamura, "Preparation and formation process of HfB_2 fine powders by Mg-thermite method," *Journal of the Ceramic Society of Japan. International ed.,* vol. 101, pp. 446-450, 1993.

[289] S. Wang, F. Zhang, X. Liu, and L. Zhang, "CaO solubility and activity coefficient in molten salts CaCl2–x (x = 0, NaCl, KCl, $SrCl_2$, $BaCl_2$ and

LiCl)," *Thermochimica Acta,* vol. 470, pp. 105-107, 2008.

[290] R. Schmid-Fetzer, A. Kozlov, B. Wiese, C. L. Mendis, D. Tolnai, K. U. Kainer, and N. Hort, "Thermodynamic Description of Reactions between Mg and CaO," in *Magnesium Technology 2016*, Edited, John Wiley & Sons, Inc., pp. 67-72, 2016.

[291] S.-H. Ha, J.-K. Lee and S. K. Kim, "Effect of CaO on Oxidation Resistance and Microstructure of Pure Mg," *MATERIALS TRANSACTIONS,* vol. 49, pp. 1081-1083, 2008.

[292] C. W. Bale, P. Chartrand, S. A. Degterov, G. Eriksson, K. Hack, R. Ben Mahfoud, J. Melançon, A. D. Pelton, and S. Petersen, "FactSage thermochemical software and databases," *Calphad,* vol. 26, pp. 189-228, 2002.

[293] G. Jiang, J. Xu, H. Zhuang, and W. Li, "Fabrication of B_4C from $Na_2B_4O_7$ + Mg + C by SHS method," *Ceramics International,* vol. 37, pp. 1689-1691, 2011.

[294] Z.-K. Liu, Y. Zhong, D. G. Schlom, X. X. Xi, and Q. Li, "Computational thermodynamic modeling of the Mg-B system," *Calphad,* vol. 25, pp. 299-303, 2001.

[295] M. Vignolo, G. Bovone, D. Matera, D. Nardelli, C. Bernini, and A. S. Siri, "Nano-sized boron synthesis process towards the large scale production," *Chemical Engineering Journal,* vol. 256, pp. 32-38, 2014.

[296] Y. Safaei-Naeini, F. Golestani-Fard, F. Khorasanizadeh, M. Aminzare, and S. Zhang, "LOW TEMPERATURE MOLTEN SALT SYNTHESIS OF NANO CRYSTALLINE $MgAl_2O_4$ POWDER," *Iranian Journal of Materials Science & Engineering,* vol. 8, pp. 23-28, 2011.

[297] A. Chakrabarti, T. Xu, L. K. Paulson, K. J. Krise, J. A. Maguire, and N. S. Hosmane, "Synthesis of Boron Nanorods by Smelting Non-Toxic Boron Oxide in Liquid Lithium," *Journal of Nanomaterials,* vol. 2010, p. 5, 2010.

[298] V. Sundaram, K. V. Logan and R. F. Speyer, "Aluminothermic reaction path in the synthesis of a TiB_2–Al_2O_3 composite," *Journal of Materials Research,* vol. 12, pp. 1681-1684, 1997.

[299] C. F. Feng and L. Froyen, "On the reaction mechanism of an Al-TiO_2-B system for producing in-situ (Al_2O_3+TiB_2)/Al composites," *Scripta Materialia,* vol. 39, pp. 109-118, 1998.

[300] S. Hashimoto and A. Yamaguchi, "Synthesis of $MgAl_2O_4$ (Spinel) Powder Using $MgCl_2$," *Journal of the Ceramic Society of Japan,* vol. 109, pp. 894-896, 2001.

[301] K. Bao, C. Liu, B. Yazdani Damavandi, and S. Zhang, "Low-Temperature Preparation of Lanthanum Hexaboride Fine Powder *via* Magnesiothermic

Reduction in Molten Salt," *Journal of Ceramic Science and Technology* vol. 7, pp. 403-408, 2016.

[302] K. Bao, Y. Wen, M. Khangkhamano, and S. Zhang, "Low-temperature preparation of titanium diboride fine powder *via* magnesiothermic reduction in molten salt," *Journal of the American Ceramic Society,* vol. 100, pp. 2266-2272, 2017.

[303] D. Horlait, S. Grasso, A. Chroneos, and W. E. Lee, "Attempts to synthesise quaternary MAX phases $(Zr,M)_2AlC$ and $Zr_2(Al,A)C$ as a way to approach Zr_2AlC," *Materials Research Letters,* vol. 4, pp. 137-144, 2016.

[304] K. V. Logan and J. D. Walton, "TiB_2 Formation Using Thermite Ignition," in *Proceedings of the 8th Annual Conference on Composites and Advanced Ceramic Materials: Ceramic Engineering and Science Proceedings*, Edited, John Wiley & Sons, Inc., pp. 712-738, 1984.

[305] M. H. Rowell, "Liquid-Liquid Extraction in the Sodium Oxide-Boron Oxide-Sodium Chloride System," *Inorganic Chemistry,* vol. 4, pp. 1802-1806, 1965.

[306] A. Silny and T. A. Utigard, "Interfacial Tension between Aluminum and Chloride−Fluoride Melts," *Journal of Chemical & Engineering Data,* vol. 41, pp. 1340-1345, 1996.

[307] T. A. Utigard, R. R. Roy and K. Friesen, "The Roles of Molten Salts in the Treatment of Aluminum," *Canadian Metallurgical Quarterly,* vol. 40, pp. 327-334, 2001.

[308] M. Mobin, A. U. Malik and S. Ahmad, "High temperature interactions of metal oxides with NaCl," *Journal of the Less Common Metals,* vol. 160, pp. 1-14, 1990.

[309] J. N. Balaraju, V. Ananth and U. Sen, "Studies on Low Temperature Al Electrolysis Using Composite Anodes in NaF - KCl Bath Electrolyte," *Journal of The Electrochemical Society,* vol. 142, pp. 439-444, 1995.

[310] V. N. Baumer, S. S. Galkin, L. V. Glushkova, T. P. Rebrova, and Z. V. Shtitelman, "Solubility of Al_2O_3 in Some Chloride−Fluoride Melts," *Inorganic Chemistry,* vol. 45, pp. 7367-7371, 2006.

[311] Y. Xiao, C. R. Mambote, G. A. Wierink, and A. van Sandwijk, "Solubility of Al_2O_3 in NaCl-KCl Based Molten Salt System," in *Molten Salts and Ionic Liquids*, Edited, John Wiley & Sons, Inc., pp. 389-395, 2010.

[312] E. Elssfah and C. Tang, "From $Al_4B_2O_9$ Nanowires to $Al_{18}B_4O_{33}$:Eu Nanowires," *The Journal of Physical Chemistry C,* vol. 111, pp. 8176-8179, 2007.